

High-pressure and high-temperature structural and electronic properties of (Mg,Fe)O and FeO

Von der Fakultät für Biologie, Chemie and Geowissenschaften
der Universität Bayreuth

zur Erlangung der Würde eines
Doktors der Naturwissenschaften
- Dr. rer. nat. -

genehmigte Dissertation

vorgelegt von
Diplom-Geochemiker Innokentiy Kantor
aus Moskau

Bayreuth, 2007

Prüfungsausschuß:

Prof. K. Bitzer, Universität Bayreuth	(Vorsitzender)
PD Dr. L. Dubrovinsky, Universität Bayreuth	(1. Gutachter)
Prof. H. Keppler, Universität Bayreuth	(2. Gutachter)
Prof. J. Breu, Universität Bayreuth	
Prof. D. Rubie, Universität Bayreuth	

Tag der Einreichung: 29 Martz 2007

Tag der wissenschaftlichen Kolloquiums: 10.Juli 2007

**Dedicated to the memory
of my grandfather,
Israel Kantor**

Contents

Zusammenfassung.....	3
Abstract.....	7
I. Introduction.....	10
MgO and FeO compounds.....	10
Periclase and wüstite minerals.....	14
Chemical composition of the Earth's mantle:	
planet formation and the meteorite record.....	15
Geophysical record: seismic structure of the mantle.....	21
Mineralogical model of the mantle.	
Ferropericlase in the Earth's deep interior.....	26
Motivation.....	31
II. Methods and instrumentation.....	34
Diamond anvil cells.....	34
Basic principles.....	34
DAC heating.....	37
Cryogenic gas loading.....	41
Pressure measurements.....	42
X-ray diffraction.....	44
Neutron diffraction.....	47
X-ray absorption spectroscopy.....	49
Mössbauer spectroscopy.....	50
Theoretical ab-initio calculations.....	56
III. Results and discussion.....	60
III.1. Phase diagrams of FeO and MnO at moderate pressures:	
relations between structural and magnetic properties.....	60
III.2. Quasi-single crystal X-ray diffraction and Mössbauer	
study of FeO: close view to the high-pressure polymorphism.....	73

III.3. Mössbauer spectra and short-range order in (Mg,Fe)O ferropericlase: evidence for Fe clusterization under high pressure.....	81
III.4. Pressure-induced trigonal distortion in Mg _{0.8} Fe _{0.2} O ferropericlase.....	99
III.5. Pressure-induced spin crossover in ferropericlase.....	115
IV. Conclusions.....	131
Bibliography.....	137

Zusammenfassung

Magnesiumreiche MgO-FeO-Mischkristalle, die als Ferroperiklas bezeichnet werden, sind als zweithäufigstes Mineral des unteren Erdmantels nach (Mg,Fe)SiO₃-Perowskit maßgeblich am Aufbau des Erdinneren beteiligt. In einer Kombination aus experimentellen und theoretischen Studien wurden strukturelle und elektronische Eigenschaften von Ferroperiklas über einen weit gespannten Druck- und Temperaturbereich untersucht.

Um in den Versuchen stabile Druckbedingungen einzustellen, wie sie im unteren Erdmantel herrschen, wurden Diamantstempelzellen (DAC) eingesetzt; die entsprechenden hohen Temperaturen wurden mit Hilfe einer neu entwickelten, sehr kleinen internen Widerstandsheizung erreicht. Das neue Heizungsbauteil für DACs ermöglicht die Einstellung und Aufrechterhaltung von Temperaturen bis zu 1000 K über einen Zeitraum von mehr als 12 Stunden. Unterschiedliche, mit der DAC-Technologie kompatible experimentelle Methoden wurden eingesetzt, um verschiedenartige Eigenschaften des untersuchten Probenmaterials zu bestimmen. Aus Röntgen- und Neutronenbeugungsmessungen stammen Daten zur periodischen Fernordnung der Kristallstruktur mit Neutronenbeugungsmessungen ließ sich weiterhin die magnetische Struktur erfassen. Spektroskopische Verfahren (Röntgenabsorption, Mößbauer-Spektroskopie) lieferten Informationen über elektronische Eigenschaften, Wertigkeit und Spin-Zustand des Eisens.

Das Phasendiagramm von FeO (Wüstit), einem Endglied der (Mg,Fe)O-Mischkristallreihe, hat sich als viel komplexer erwiesen, als bisher angenommen. Es zeigte sich, dass der Übergang der magnetischen Ordnung („Néel transition“) nicht mit der Symmetrieänderung (kubisch → trigonal) in der Kristallstruktur von nicht-stöchiometrischem FeO übereinstimmt. Über den gesamten untersuchten Druckbereich, d.h. bis hin zu 40 GPa, trat der Néel-Übergang stets bei höheren Temperaturen auf als der Wechsel in der Kristallstruktur. Die durch Pulver-Röntgendiffraktometrie ermittelte Grenze des Strukturübergangs wird durch die Gleichung $P_{tr}(\text{GPa}) = -4.7(\pm 0.2) + 0.056(\pm 0.005) \times T(\text{K})$ festgelegt. Sie stimmt recht gut mit der von Fei (1996) vorgestellten Gleichung $P_{tr}(\text{GPa}) = -5.0 + 0.070(\pm 0.003) \times T(\text{K})$ überein, die für quasi-hydrostatische Bedingungen gültig ist. Die bestehende Diskrepanz lässt sich auf das Fehlen hydrostatischer Bedingungen sowie die unterschiedliche Probenzusammensetzung zurückführen. Die Grenzlinie des Strukturwechsels weicht möglicherweise bei geringen Drücken (unterhalb von 2-3 GPa) von der Linearität ab, jedoch sollte diese Annahme noch näher untersucht werden.

Der Übergang in der magnetischen Ordnung wurde durch eine Kombination von Mößbauer-Spektroskopie und Neutronendiffraktometrie zum ersten Mal bestimmt. Die Ergebnisse beider Methoden zeigen vollständige Übereinstimmung, woraus für FeO abgeleitet werden kann, dass Mößbauer-Spektren die großräumliche magnetische Ordnung widerspiegeln. Die Néel-Temperatur steigt mit zunehmendem Druck und wird durch die Gleichung $T_N(\text{K}) = 200(\pm 5) + 20.8(\pm 0.5) \times P$ (GPa) definiert. Aus der Tatsache, dass der strukturelle und magnetische Phasenübergang getrennt voneinander auftreten, ergibt sich, dass die Ursache der Kristallverzerrung nicht in der Wechselwirkung mit magnetischen Momenten des Fe^{2+} liegt. Eine ergänzende Neutronenbeugungsstudie wurde an MnO durchgeführt; es weist eine zu FeO analoge Struktur auf und zählt zur selben Gruppe der gut korrelierten Monoxid-Übergangsmetalle. Die Untersuchung bestätigte die Unabhängigkeit von Kristallstrukturänderung und Übergängen in der magnetischen Ordnung. Für MnO stimmen bei geringen Drücken unterhalb von ~ 3.5 GPa beide Übergänge überein; bei höheren Drücken tritt jedoch der Phasenübergang bei höheren Temperaturen auf als der Wechsel in der magnetischen Ordnung. Die trigonal verzerrte Modifikation existiert daher im paramagnetischen Zustand.

Die Beziehung zwischen strukturellen und magnetischen Übergängen in FeO und MnO kann durch eine fehlende Kugelform der d-Elemente erklärt werden, was dazu führt, dass die verformte Struktur dichter als die ideale, kubisch-dicht gepackte NaCl-Kristallstruktur ist. Ähnliches wird für elementare Lanthanid-Kristalle unter hohen Drücken beschrieben (Dmitriev et al., 2003).

Röntgenbeugungsstudien an quasi-Einkristallen aus FeO zeigen im Vergleich mit früheren Untersuchungen (Shu et al., 1998-I; Jacobsen et al., 2005), dass der für den Phasenübergang nötige Druck nicht nur vom Spannungszustand abhängig ist, sondern auch von der Zusammensetzung von Wüstit; möglicherweise ist auch der Grad des Übergangs (zweiter Ordnung oder schwacher erster Ordnung) ebenfalls spannungsabhängig. Oberhalb von ~ 70 GPa ergibt das Röntgenbeugungsmuster für FeO nach der Laser-Aufheizung eine monokline Struktur die zur Raumgruppe $P2_1/m$ gehört. Die Existenz einer monoklinen Phase, ähnlich der hier beobachteten, aber nicht mit ihr identisch, wurde schon für niedrige Temperaturen und normalen Umgebungsdruck für nahezu stöchiometrischen Wüstit beschrieben (Fjellvag et al., 2002). Die Hypothese, dass FeO bei hohen Drücken eine monokline Phase bildet, wurde schon früher aufgestellt (Zou et al., 1980; Fei, 1996), konnte jedoch erst mit der hier vorliegenden Arbeit experimentell bestätigt werden.

Mischkristalle der (Mg,Fe)O-Reihe wurden über einen breiten Druck- und Temperaturbereich und mit sehr unterschiedlichen FeO-Gehalten (zwischen 5 und 20 mol % of FeO) untersucht. Feinauswertungen der Mößbauer-Spektren von (Mg,Fe)O liefern einen klaren Beweis für die Verteilung des hyperfeinen Parameters (Quadrupol Aufspaltung Δ), einer Schlüsselgröße zur Bestimmung der lokalen Struktur. Durch Analysen der Δ -Verteilung kann ein Parameter für die Nahbereichsordnung für (Mg,Fe)O-Mischkristalle mit niedrigem Fe-Anteil abgeschätzt werden. Von hohen Temperaturen bei Umgebungsdrücken abgeschreckte Proben zeigen nach vorangegangenen Beschreibungen (Waychunas et al., 1994) fast zufällige lokale Kationen-Verteilungsmuster. Nach der Kompression wurde jedoch eine schnelle Zunahme der Nahbereichsordnung mit der Tendenz zur Clusterbildung von Eisen beobachtet. Es wurde gezeigt, dass diese nicht-regellose Verteilung der Atome sowohl bei hohen Drücken als auch bei hohen Temperaturen stabil ist. Ursache der Mischbarkeitslücke in der (Mg,Fe)O-Mischkristallreihe bei hohen Drücken und Temperaturen, die auch experimentell beobachtet wurde (Dubrovinsky et al., 2000-I; 2005), könnte somit die festgestellte Tendenz der Fe-Ionen zur Absonderung sein.

Bei der Kompression von (Mg_{0.8}Fe_{0.2})O-Ferropentlandit bei Drücken über 35 GPa unter nicht-hydrostatischen Bedingungen und bei Raumtemperatur wurde mit Röntgenbeugungsmethoden eine trigonale Kristallverzerrung beobachtet, sowie auch feine Veränderungen in den Mößbauer- und XANES-Spektren unter diesen Druckbedingungen. Die trigonal verzerrte Phase konnte durch nicht-hydrostatische Spannungen stabilisiert werden; dass ein derartig niedriger Fe-Gehalt eine trigonale Verzerrung in (Mg,Fe)O hervorrufen kann, wurde bisher nicht beschrieben. Hohe Temperaturen und höhere hydrostatische Spannungen sollten die kubische, NaCl-ähnliche Phase stabilisieren; demzufolge ist diese Verzerrung der Kristallstruktur im Erdmantel wohl nicht maßgeblich. Dennoch ist die Beobachtung für eine korrekte Interpretation der Ergebnisse aus Hochdruck-Experimenten bei Raumtemperaturen von Bedeutung.

Bei Drücken über 50 GPa wurde ein Spin-Paar-bildender Übergang von Fe²⁺ beobachtet. Deutlich ausgeprägte Veränderungen in den Mößbauer-Spektren stimmen sehr gut mit einem Spin-Übergang von hoch zu niedrig überein: die zentrale Verschiebung nimmt ab, was auf eine Zunahme der Elektronendichte im Kern hindeutet. Die Quadrupol Aufspaltung geht ebenfalls in Richtung Null und weist somit auf die deutliche Ausbildung einer kugelförmigen Symmetrie der Valenzelektronen sowie die Aufhebung des Gradienten

im elektrischen Feld hin. Die absolute Magnitude aller Veränderungen stimmt sehr gut mit den im Rahmen dieser Studie angestellten *ab initio*-Kalkulationen überein.

Der Beginn des Spin-Übergangs ist bei allen untersuchten Proben ähnlich, die Breite des Übergangsbereiches wird jedoch stark von der chemischen Zusammensetzung beeinflusst. Je höher der Fe-Gehalt ist, desto breiter zeigt sich der Übergang, der im Fall der $(\text{Mg}_{0.8}\text{Fe}_{0.2})\text{O}$ -Probe ungefähr 50 GPa erreicht. Ein derartig weit gespannter Übergang ist für Phasenwechsel mit starkem Volumeneinbruch eher untypisch. Die Auswertung von Literaturdaten (Speziale et al., 2005; Lin et al., 2005) führen zusammen mit Ergebnissen der vorliegenden Arbeit zu einer Interpretation des Spin-Übergangs als einem Prozess zur Einstellung des thermischen Gleichgewichts ohne Phasenübergang. Die Abhängigkeit des Spin-Übergangs in Ferroperiklas von Temperatur und chemischer Zusammensetzung kann mit diesem Modell recht gut beschrieben werden, wenn man die lokale Struktur des Mischkristalls in Betracht zieht. Die mit diesem Modell erzielten Ergebnisse wurden auch durch *ab initio*-Simulationen bestätigt.

Das in der vorliegenden Arbeit vorgeschlagene Modell prognostiziert, der Spin-Übergang in Ferroperiklas über einen großen Tiefenbereich im unteren Erdmantel auftritt. Es werden im Gegensatz zu früheren Annahmen (Lin et al., 2005) keine Diskontinuitäten bezüglich Dichte und elastischer Eigenschaften im unteren Erdmantel erwartet, die durch Spin-Übergänge in Ferroperiklas hervorgerufen werden.

Abstract

Magnesium-rich MgO-FeO solid solution, known as the mineral ferropericlasite, constitutes a significant part of the Earth as the second most abundant mineral in the lower mantle after (Mg,Fe)SiO₃ perovskite. A combined experimental and theoretical study was carried out in order to determine structural and electronic properties of ferropericlasite over a broad pressure and temperature range.

Static high pressures relevant to the Earth's lower mantle were achieved using the diamond anvil cell (DAC) technique, and high temperature was reached using a newly developed miniature internal resistive heater. This new heating assembly for the DAC allows the attainment and maintenance of temperatures up to 1000 K for times more than twelve hours. Several experimental techniques that are compatible with the DAC were used to characterize different properties of the studied materials. X-ray and neutron diffraction provided information about long-range periodic structure and the latter is also sensitive to the magnetic ordering. Spectroscopic techniques (X-ray absorption and Mössbauer spectroscopy) provide information regarding electronic, valence and spin state of Fe.

The phase diagram of FeO (wüstite), the end member of the (Mg,Fe)O solid solution, was found to be more complex than previously thought. It was discovered that the magnetic ordering (Néel) transition does not coincide with the structural cubic-to-trigonal symmetry breaking transition in non-stoichiometric FeO. In the entire pressure range studied, i.e., up to 40 GPa, the Néel transition was found to occur at a higher temperature than the structural distortion. The structural transition boundary, traced by powder X-ray diffraction, is given by $P_{tr}(\text{GPa}) = -4.7(\pm 0.2) + 0.056(\pm 0.005) \times T(\text{K})$, which agrees reasonably well with that reported by Fei (1996) for nearly hydrostatic conditions $P_{tr}(\text{GPa}) = -5.0 + 0.070(\pm 0.003) \times T(\text{K})$. The discrepancy can be explained by different degrees of non-hydrostaticity and different samples compositions. The structural transition boundary probably deviates strongly from linearity at low pressures (below 2-3 GPa), but this fact should be further investigated.

The magnetic ordering transition was determined for the first time by a combined Mössbauer spectroscopy and neutron diffraction study. A full agreement between these two methods was observed, indicating that in the case of FeO the Mössbauer spectra reflect long-range magnetic ordering. The Néel temperature increases with pressure and is given by $T_N(\text{K}) = 200(\pm 5) + 20.8(\pm 0.5) \times P(\text{GPa})$. The fact that these two transitions occur independently suggests that the cause of structural distortion is not the interaction of Fe²⁺ magnetic

moments. A complementary neutron diffraction study of MnO, a close structural analogue of FeO belonging to the same group of strongly correlated transition metal monoxides, also confirmed the independence of structural distortion and magnetic ordering transitions. In MnO at pressures below ~ 3.5 GPa these two transitions coincide, but at higher pressures the structural distortion occurs at higher temperatures than magnetic ordering, so that the trigonally distorted phase exists in the paramagnetic state.

The relationship between the structural and magnetic transitions in FeO and MnO can be explained by a non-spherical effective shape of d-elements, resulting in the distorted structure being denser than ideal NaCl-like cubic close packing, similar to elementary lanthanide crystals under high pressure (Dmitriev et al., 2003).

A quasi-single crystal X-ray diffraction study of FeO compared with previous results (Shu et al., 1998-I; Jacobsen et al., 2005) shows that the transition pressure depends not only on stress conditions, but also on wüstite composition, and probably the order of the transition (second- or weak first-order) is also stress dependent. Above ~ 70 GPa after laser annealing the X-ray diffraction pattern of FeO could not be explained as a trigonal structure, but as a monoclinic structure with space group $P2_1/m$. The existence of a monoclinic phase, close but not identical to the one observed here, was already shown to exist at low temperatures and ambient pressure for nearly stoichiometric wüstite (Fjellvag et al., 2002). The hypothesis that monoclinic FeO exists at high pressures was suggested before (Zou et al., 1980; Fei, 1996), but is confirmed here experimentally for the first time.

(Mg,Fe)O solid solution was studied over a wide pressure and temperature range and over a compositional range from 5 to 20 mole % of FeO component. The detailed analysis of (Mg,Fe)O Mössbauer spectra shows clear evidence for the distribution of the hyperfine parameter quadrupole splitting (Δ), which provides a key to determining its local structure. It is shown that by analyzing the Δ distribution, a short-range order parameter could be estimated for the low-Fe (Mg,Fe)O solid solution. Samples quenched from high temperature at ambient pressure during synthesis show local cation distribution close to randomness, as was reported previously (Waychunas et al., 1994). Upon compression, however, a rapid increase of short-range order with the tendency for Fe clusterization was observed. This non-random atomic distribution was shown to be stable at high pressures and also at high temperatures. Such a tendency for Fe ions to separate could lead to the miscibility gap in the (Mg,Fe)O solid solution series at high pressures and temperatures, as was observed experimentally (Dubrovinsky et al., 2000-I; 2005).

When compressing ferropericlase ($\text{Mg}_{0.8}\text{Fe}_{0.2}\text{O}$) above 35 GPa under non-hydrostatic conditions and room temperature, a trigonal distortion was observed by X-ray diffraction and also subtle changes in Mössbauer and XANES spectra were observed at this pressure. The trigonally distorted phase could be stabilized by non-hydrostatic stress; however this is the lowest Fe content ever reported that could produce a trigonal distortion in $(\text{Mg,Fe})\text{O}$. High temperature and more hydrostatic stress conditions should stabilize the cubic NaCl-like phase; hence this structural distortion is likely not relevant for the Earth's mantle. However, this observation is important for the correct interpretation of experimental room-temperature high-pressure results.

At pressures higher than 50 GPa a spin-pairing transition of Fe^{2+} was observed. Clear and pronounced changes in the Mössbauer spectra are fully consistent with a high- to low-spin transition: the centre shift decreases, indicating an increase of electron density at the nuclei. Quadrupole splitting also vanishes to zero, indicating significant spherical symmetrisation of the valence electrons and electrical field gradient disappearance. The absolute magnitude of these changes is in full agreement with *ab initio* calculations made in this study.

The onset of the spin transition is similar for all the samples studied, but the width is strongly composition dependent. The higher the iron content, the broader the transition width, which reaches about 50 GPa for the $(\text{Mg}_{0.8}\text{Fe}_{0.2})\text{O}$ sample. Such a broad transition range is not typical for phase transitions with significant volume collapse. Analysis of literature data (Speziale et al., 2005; Lin et al., 2005) together with the results of this study lead to an interpretation of spin crossover as a thermal equilibrium process without phase transition. The compositional and temperature dependence of spin crossover in ferropericlase can be described fairly well within such a model, taking into account the local structure of the solid solution. The results of this model were also confirmed by *ab initio* simulations.

The model proposed in this work predicts that spin crossover in ferropericlase will occur over a large depth range of the lower mantle. No discontinuities in density or elastic properties are expected to be produced in the lower mantle due to spin crossover in ferropericlase, contrary to previous suggestions (Lin et al., 2005).

I. Introduction

MgO and FeO compounds

The oxide MgO is one of the simplest binary compounds known. At ambient conditions MgO is isostructural with NaCl, which consists of cubic packing of oxygen ions and produces cubic and octahedral crystals. There are no polymorphs of MgO known to exist from experimental work, both at high- or low-temperatures and at high pressures up to at least 227 GPa (Duffy et al., 1995). MgO is believed to be mainly an ionic crystal, and there are many examples of ionic crystals with the NaCl (B1) structure which transform at high pressure into the CsCl (B2) structure. From theoretical calculations, this transition in MgO is expected at very high pressures, not yet accessed by experiments. The main controversy between different calculations has been the exact value of the transition pressure, with estimates ranging from 200 to over 1000 GPa. Calculations with the most accurate approximations give transition pressures of ~ 510 GPa (Jaffe et al., 2000; Oganov and Dorogokupets, 2003). MgO is one of the best studied materials. Its thermodynamic, vibrational and elastic properties have been precisely measured experimentally (eg. Saxena et al., 1993) and also well reproduced by *ab initio* calculations (eg., Oganov and Dorogokupets, 2003). MgO is also often used as an internal pressure marker in high-pressure experiments, and its P,T equation of state and elasticity were determined and refined several times (eg., Chen et al., 1998; Zha et al., 2000; Speziale et al., 2001).

FeO has a more complicated crystal chemistry compared to MgO. In many ways this “simple” binary compound remains enigmatic even after several decades of intense experimental and theoretical studies (Mao et al., 1996). If an ideal sample of stoichiometric wüstite, FeO, could be prepared at ambient pressure, it would presumably have the rock-salt B1 structure similar to MgO. However, at ambient pressure and temperature ideal FeO is unstable, presumably because Fe^{2+} can be very easily oxidized to Fe^{3+} . FeO synthesized at ambient pressures never has a stoichiometric composition, but always a certain iron deficit is observed, and its chemical formula is written as Fe_{1-x}O . Fe_{1-x}O is a typical example of a non-stoichiometric compound with variable composition.

The phase diagram of Fe_{1-x}O has been studied for many years and has undergone various revisions which always seem to reveal more complexities (Long and Grandjean, 1991). A simplified compositional phase diagram of the Fe-O system in the Fe_{1-x}O region is shown in Fig. 1.1.

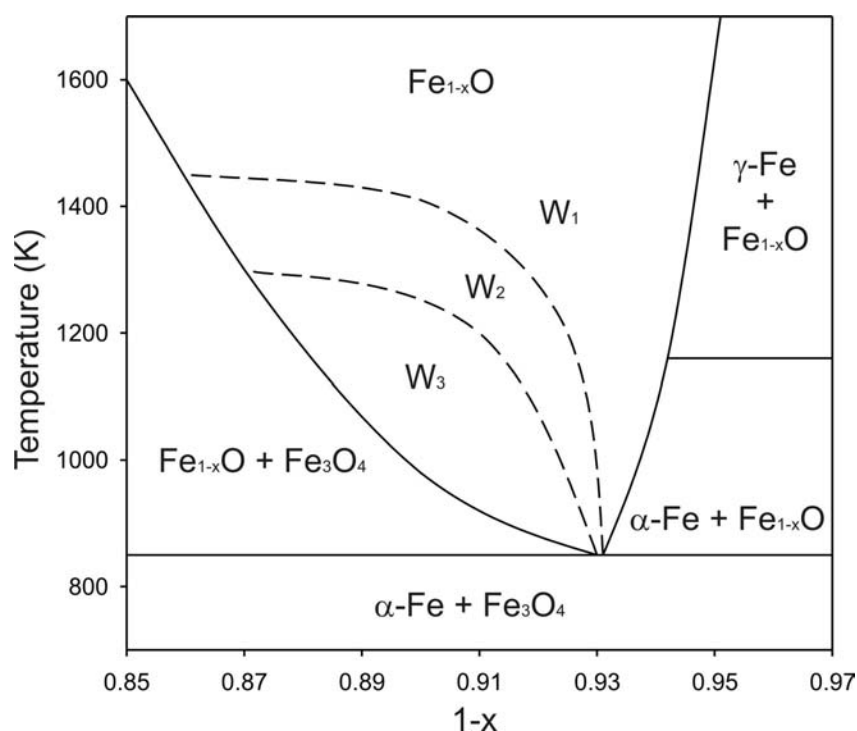


Fig. 1.1. The temperature-composition phase diagram for Fe_{1-x}O . W_1 , W_2 and W_3 are hypothetical phases of Fe_{1-x}O where these subdivisions are based on thermochemical properties. Modified from Long and Grandjean, 1991.

From Fig. 1.1 it is immediately seen that below 840 K Fe_{1-x}O is not stable and decomposes into metallic iron and Fe_3O_4 magnetite. At high temperatures Fe_{1-x}O is stable over a relatively broad compositional range. Fig. 1.1 indicates the presence of three subdivisions of the Fe_{1-x}O phase as proposed by several authors (eg., Molenda et al., 1987) on the basis of equilibrium high-temperature studies. However, this subdivision was not confirmed by other studies (Mrowec and Podgorecka, 1987). The difference in thermochemical properties between the W_1 , W_2 and W_3 phases could be attributed to different defect structures in Fe_{1-x}O .

Incorporation of ferric iron into the FeO structure is charge-balanced by Fe vacancies. The simplest charge balance reaction can be written as $3\text{Fe}^{2+(o)} = \square^{(o)} + 2\text{Fe}^{3+(o)}$, where $3\text{Fe}^{2+(o)}$, $\square^{(o)}$, and $\text{Fe}^{3+(o)}$ represent ferrous iron in an octahedral position, an iron vacancy, and ferric iron in an octahedral position, respectively. However, Fe_{1-x}O always contains a certain amount of Fe^{3+} ions in tetrahedral interstitial position of the *fcc* (face-centered cubic) oxygen sublattice (Long and Grandjean, 1991).

Introducing an interstitial Fe^{3+} ion results in a strong local charge misbalance, and to compensate for it, the four nearest iron octahedral positions become vacancies. Thus, a 4:1 (Roth, 1960) cluster (the 4:1 notation is used to show 4 vacancies and 1 interstitial) can be

formed (Fig. 1.2.a). It is the 4:1 cluster that is believed to be the main building block for various possible defect clusters in FeO.

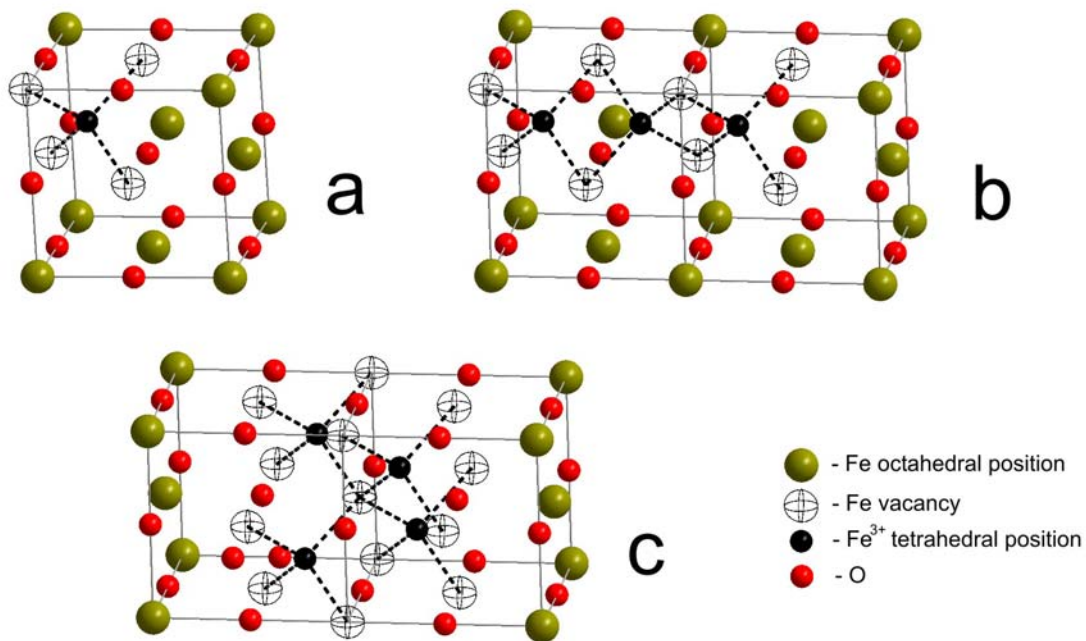


Fig. 1.2. Defect clustering in FeO. a – elementary 4:1 cluster, b – 8:3 chain cluster, c – 13:4 Koch-Cohen cluster. Modified after Long and Grandjean (1991).

A large range of different defect clusters can be constructed from the 4:1 building block. For example, three edge-sharing clusters could form a 8:3 chain (fig. 1.2.b), and so on. Different defect clusters can be characterized by the vacancy to interstitial ratio ρ , which usually varies between 2.7 and 3. The minimum possible value for ρ is 1.5 (full charge compensation of interstitials and vacancies). Some measurements suggest ρ to have a value as high as 3.2, which is compatible with the proposed 13:4 cluster (Koch and Cohen, 1969), Fig. 1.2.c. Different defect clusters could exist in the FeO structure, and cluster geometry also varies with the composition and, perhaps, temperature. The defect structure of FeO is further complicated by relative arrangement of defect clusters in the crystal structure. Based on the analysis of diffuse scattering around incommensurate diffraction peaks, it was shown that the defect cluster distribution is not random, and a significant correlation between clusters was suggested (Welberry and Christy, 1997). At high pressures and in equilibrium with metallic Fe the degree of FeO nonstoichiometry decreases (McCammon, 1993), implying that the stability of defect clusters changes significantly with pressure. Direct evidence for pressure-induced changes in the FeO defect structure were obtained from single crystal X-ray diffraction diffuse scattering observations (Ding et al., 2005).

The defect structure of FeO significantly influences its physical properties. It is known from many systematic studies that the lattice parameter varies linearly as a function of x in the Fe_{1-x}O formula (Simons, 1980; McCammon and Liu, 1984). It is believed that the isothermal bulk modulus also depends on x , and this dependence is non monotonous (Zhang, 2000; McCammon, 1993). Data on K and K' from different studies are strongly scattered, however. Virtually nothing is known about the effect of ρ and defect cluster geometry and distribution on the elastic properties of FeO. Some atomistic semi-empirical simulations show that such correlations do exist (Haavik et al., 2000). These calculations imply that FeO samples with different synthesis temperatures and history (cooling rate, etc.) could show different elastic properties due to variations in ρ and cluster ordering even for similar x values. This could explain disagreements between different studies of FeO compressibility.

At low temperature near 90 K the FeO X-ray diffraction pattern is no longer consistent with ideal cubic symmetry, and a small degree of trigonal distortion has been observed (Willis and Rooksby, 1953). Later a magnetic ordering (Néel) transition was also observed in FeO around 195 K, and structural distortion was assumed to be a magnetostriction effect, similar to MnO, CoO and NiO (Smart and Greenwald, 1951). The exact value of the Néel temperature varies depending on Fe_{1-x}O composition (McCammon, 1992). The magnetic structure of FeO at low temperature was one of the first structures solved by neutron diffraction (Shull, 1951). Fe ions with parallel spins form flat sheets perpendicular to the $\langle 111 \rangle$ direction and the alternating sheets are antiparallel. A more recent high-resolution neutron diffraction study revealed that the crystal symmetry of nearly stoichiometric FeO is even lower (namely, monoclinic), which was attributed to the deviation of the spin orientation from the $\langle 111 \rangle$ direction (Fjellvag et al., 2002).

At high pressures a trigonal distortion and electronic transformations occur at room temperature. A trigonal distortion was observed at pressures from 9 to 24 GPa (Zou et al., 1980; Jacobsen et al., 2005). The strongest effect on the transition pressure is when non-isotropic stress conditions are present in the sample: more hydrostatic conditions result in higher transition pressures (Dubrovinsky et al., 2000-II). Although Fei (1996) claimed that the FeO composition does not affect transition pressure, it could also be a factor (see Chapter III.2). The Néel transition was observed in high-pressure Mössbauer experiments (Nasu, 1994; Pasternak et al., 1997), but the exact transition pressure at room temperature is not known so far.

At pressures above 90 GPa a structural phase transformation from the trigonal NaCl-related structure to a NiAs-like hexagonal phase was observed (Fei and Mao, 1994). Later it

was discussed whether the observed diffraction pattern is consistent with a NiAs-like or an inverse NiAs-like structure (where Fe occupies the position of As and O occupies the position of Ni), or even polytypical stacking of NiAs- and inverse NiAs-like layers (Mazin et al., 1998). The phase boundary between the trigonal NaCl-like structure and NiAs polymorphs was later revised by Murakami et al. (2004-II).

Based on an ultra-high pressure Mössbauer spectroscopic study of FeO a high- to low-spin transition was suggested in FeO at pressures above 100 GPa (Pasternak et al., 1997). Later, however, a diamagnetic state of FeO was not confirmed by X-ray emission spectroscopy (Badro et al., 1999) and it was shown that the Mössbauer spectra could be also interpreted as an antiferromagnetic to paramagnetic transition. It is not clear if the transition to the NiAs-like phase is coupled directly to the spin changes or metallization. A recent study of MnO, a close structural and electronic analogue of FeO, shows that these changes occur at different pressures (Yoo et al., 2005).

Relations between the structural and electronic states of FeO in the high-pressure and high-temperature region still remain unclear.

Periclase and wüstite minerals

Periclase is the mineral name of MgO. Periclase is relatively scarce and is found mainly in marbles, and is usually formed during contact metamorphism of dolomites and magnesites. $\text{CaMg}(\text{CO}_3)_2$ dolomite dissociates into MgO (periclase), CaCO_3 (calcite) and CO_2 fluid. If the periclase-rich marbles are exposed to weathering, periclase easily alters to either brucite, $\text{Mg}(\text{OH})_2$ or hydromagnesite, $\text{Mg}_5(\text{CO}_3)_4(\text{OH})_2 \times 4\text{H}_2\text{O}$. Pure MgO is colorless and transparent; however, natural crystals are usually yellow brown or black due to the presence of iron. In marble periclase, iron is usually present in the form of magnetite Fe_3O_4 small particles. Specimens of periclase can be very attractive as brightly lustered, smoothly faceted crystals projecting out of the otherwise formless rough marble host rock. Notable occurrences of periclase include Monte Somma, Vesuvius, Italy; Crestmore, California, USA and Nordmark, Varmland, Sweden. Periclase is an important industrial material, because it is formed in cements and is the basis of many high-temperature ceramics for a wide range of applications.

Wüstite (FeO) is a rare mineral of iron(II) oxide found in meteorites with native iron and is isostructural to MgO at ambient conditions. Natural wüstite was discovered in 1927 in Echterdingen, Stuttgart, Baden-Wurttemberg, Germany, and was named for Ewald Wüst

(1860-1938), German metallurgist and Director for Iron Research of the Kaiser Wilhelm Institute in Düsseldorf. In addition to the type locality in Germany, it has been reported from Disko Island, Greenland, the Jharia coalfield, Bihar, India and as inclusions in diamonds in a number of kimberlite pipes. It is also reported from deep sea manganese nodules. Wüstite is a rather rare mineral, occurring in highly reducing environments. Under oxidizing conditions wüstite can be easily oxidized to various Fe^{3+} and mixed Fe^{2+} and Fe^{3+} oxides or hydroxides: magnetite Fe_3O_4 , hematite Fe_2O_3 , goethite $\text{FeO}(\text{OH})$, and so on. As mentioned above, wüstite never has the ideal FeO stoichiometry. In most natural and synthetic samples there is always a certain iron deficit that results in the chemical formula Fe_{1-x}O . Due to the presence of Fe^{3+} in the wüstite structure, strong charge transfer bands appear in the band structure, and bulk wüstite samples are opaque and black in color, while thin sections of wüstite are transparent (Anthony et al., 1997).

At ambient conditions both MgO and FeO have a similar crystal structures, formal valence states and very close lattice parameters (about 4.212 Å for MgO and about 4.25 Å for FeO , depending on its stoichiometry). As a result, a complete series of $(\text{Mg,Fe})\text{O}$ solid solutions can be formed. The corresponding mineral form of $(\text{Mg}_x\text{Fe}_{1-x})\text{O}$ is called ferropericlase for $x > 0.5$ and magnesiowüstite for $x < 0.5$ compositions. If the composition of $(\text{Mg,Fe})\text{O}$ is not specified, the term “magnesiowüstite” has traditionally been used. Natural samples of $(\text{Mg,Fe})\text{O}$ are rarely found in nature, usually as inclusions in diamonds from kimberlitic xenoliths (Harte and Harris, 1994). Although $(\text{Mg,Fe})\text{O}$ natural samples are rare on the Earth's surface, $(\text{Mg,Fe})\text{O}$ is believed to be one of the main constituents of the lower mantle and probably the most abundant oxide (non-silicate) phase on our planet according to current mineralogical models of the Earth.

A mineralogical model of the Earth predicts which phases (minerals), their chemical compositions and abundances are present in different regions of the Earth's interior. A mineralogical model is the result of combining cosmochemical constraints with models of the Solar system and Earth formation, our understanding of the Earth's history, experimental and theoretical studies of thermodynamic phase stabilities over a wide pressure and temperature range, and geophysical (mostly seismological) data of elastic and other properties of the Earth's deep interior.

Chemical composition of the Earth's mantle: planet formation and the meteorite record

According to the current concepts, the formation of our solar system followed the collapse and fragmentation of a dense interstellar molecular cloud (O'Neill and Palme, 1998). Due to angular momentum of this matter, a rotating disk was initially formed. Material within the disc lost its initial angular momentum through viscous dissipation of other processes, leading ultimately to the growth of a central star, our Sun. Only a tiny fraction of the mass of the solar system, about 0.1%, was left behind in the disc to form planets and asteroids. The mixture of gas and grains that made up the proto-solar accretion disk is called the solar nebula.

The growth of solid bodies in the solar nebula began with the accretion of tiny dust grains. Initially micrometer-size grains gradually formed centimeter-size bodies that in turn grew to metre- and kilometre-size blocks by collisional coagulation (Weidenschilling, 1988). Once the diameter of the planetesimals had reached 1-10 km, gravitational forces controlled further growth. Three major conclusions derived from this model are most important for constraining bulk chemical composition of the Earth:

- Planetesimals appear to grow from small particles through a range of increasingly larger bodies – an evolving size distribution. Planetesimals and planets do not grow by accreting dust onto a single nucleus.

- Bodies up to kilometre size are composed of the material derived from local matter sources and thus possess the chemical signatures characteristic to the heliocentric distance at which they formed.

- At some point there was a “cleaning” of the nebula through intense activity of the Sun, which removed gas and fine dust. This is the most probable mechanism for the removal of volatile elements. Earth group planets (Mercury, Venus, Earth and Mars) that are closer to the Sun lost a major part of their volatile elements, while more distant and heavy gas giants contains a much larger amount of volatile elements.

At the next step the inner planets were formed by accumulation of embryos. At this stage some mixing of embryos from different heliocentric distances occurred, and the material formed far out in the asteroid belt may have contributed significantly to the growing Earth and its chemistry.

The major deduction from the hypothesis of a well-mixed nebula is that all solar-system material, including that forming the Earth, was derived from a nebula material with a uniform, characteristic, chemical and isotopic composition. This is the solar composition as

observed in the solar photosphere. This deduction is supported by many experimental observations. Some information on the chemical composition can be obtained remotely via spectroscopic methods; however, direct analysis is even more interesting. Samples from the Earth and Moon surface are available directly for laboratory analysis. Recent successful Mars expeditions also provide results of direct measurements of the Mars surface. However, a large group of samples of a wide range of solar-system materials are also available for study, namely meteorites.

Some rare types of meteorites come from the Moon and Mars, while most are thought to be derived from asteroids (Wood and Morfill, 1988). Asteroids are small planetary bodies, or planetesimals, many of which are concentrated in the gap between Mars and Jupiter. They are remnants from the era during which the planets of the solar system, including the Earth, formed.

There are many different types of meteorites, as well as different principles of their classification. The fundamental distinction among meteorites is between those derived from parent bodies that have undergone igneous differentiation and metal segregation, and those derived from essentially undifferentiated parent bodies. The first group provides important samples from different parts and from different stages of planetesimal differentiation. These are products of partial melting (basaltic meteorites, such as eucrites), residues from partial melting (lodranites and ureilites), the metallic cores of planetesimals (the ‘magmatic’ irons), samples from the core-mantle boundaries of the planetesimals (the pallasite stony irons) and so forth. The meteoritic record probably samples a continuum of the differentiation of planetesimals, ranging from the completely undifferentiated, through those that had just begun to melt, to the completely differentiated.

Among different types of meteorites probably the most important for the reconstruction chemical composition of the bulk Earth are chondrites. Chondrites are the meteorites from undifferentiated bodies. Initially the term “chondrites” comes from chondrules, the name given to near-spherical objects in a homogenous matrix, typically of sub-millimeter to millimeter dimensions that are interpreted to be agglomerations of nebula dust that were melted by rapid heating and then were rapidly cooled. Indeed, most chondrites contain a significant amount of chondrules. However, in many chondrites it is difficult to recognize chondrules due to subsequent recrystallization (O’Neill and Palme, 1998). Carbonaceous chondrites do not contain chondrules – they are composed mostly of matrix material.

During the formation of the solar system a certain heating and fractionation of chemical elements occurred. The cosmochemical behavior of an element depends mostly on two properties: its volatility in a gas of solar composition, and its affinity for metallic versus silicate or oxide phases. The cosmochemical classification of elements must include gas/solid or gas/liquid equilibria during initial condensation of the solar nebular (the element volatility) and metal/silicate or sulphide/silicate equilibria during metallic core formation. The latter type of partitioning divides elements into lithophile (preferentially partition to silicate/oxide phase), siderophile (partition into Fe-rich metal) and chalcophile (partition into sulphide). The distinction between the last two groups is of minor importance, since above the Fe-FeS eutectic temperature sulphide and metal melt to form a single S-containing metallic liquid.

Refractory elements have condensation temperatures higher than the major phases in meteorites (Mg silicates and FeNi metal) and make up about 5% of the condensable matter of the solar nebula. Condensation temperatures of refractories vary from 1800 to 1400 K. The most abundant are the refractory lithophile elements (RLEs) Al, Ca and Ti which form oxides and silicates. Large numbers of trace elements (rare-earth elements, Nb, Ta, U, Th, and so on) are expected to condense together with the refractory phases. The most refractory elements Hf, Zr, Sc, and Y condense as separate phases. Refractory metals (Re, Os, Ir, Ru, Pt) will condense as alloys (Palme and Boynton, 1993). The most important observation from the meteoritic record is the constant ratio of RLEs in all chondritic meteorites. It is a central postulate in reconstructing planetary bulk compositions.

The common or major elements Mg, Si, Cr, Fe, Ni, and Co have condensation temperatures only slightly lower than those of refractory elements (1300 – 1350 K), but condense in different phases. Mg and Si form forsterite Mg_2SiO_4 and enstatite $MgSiO_3$; whereas Fe, Ni, and Co condense as alloys. Silicate and metal phases together are the most important components forming planetesimals, accounting for as least 90% of chondritic meteorites. It is important that forsterite and metallic alloy have similar condensation temperatures, which explains the limited fractionation of metal and silicate phases in the solar nebula. Cr, according to recent thermodynamic data, mostly condenses to olivine and pyroxene as Cr_2SiO_4 and $CrSiO_3$ components. Mg and Si can be considered to be slightly volatile, relative to the refractory elements. Chondritic meteorites show differences within a factor of 2 in their abundances of Mg + Si. Several possible mechanisms for the differentiation of refractories and Mg and Si have been proposed; however, this problem has not been completely resolved. That the variation in the RLE/Si or RLE/Mg ratio in chondrites is primarily due to the volatility of Si and Mg and not to some silicate fractionation process is

proved by the remarkable correlation of Ir/Au with Al/Si. Nevertheless, the variation in RLE/Si or RLE/Mg is surprisingly poorly correlated with the depletion of moderately volatile elements. It seems that there were different volatility-related processes in the solar nebula (O'Neill and Palme, 1998).

Volatile elements are those having condensation temperatures lower than those of Mg silicates and FeNi alloy. Volatiles can be lithophile, siderophile and chalcophile elements. They are usually divided into moderately volatile elements with condensation temperatures between 1300 and 650 K (P, Li, Mn, Rb, K, Na, F, Zn, Au, As, Ag, Sb, Sn, Te, S, Se, Cu) and highly volatile elements with condensation temperatures between 400 and 500 K (Cl, Br, I, Cs, In, Tl, Bi, Pb). Both the moderately volatile elements and the highly volatile elements are depleted, relative to CI chondrites (the most chemically primitive meteorites), in every other meteorite (i.e. in all the other chondrite groups, as well as in meteorites from differentiated parent bodies, Martian meteorites, and every group of iron meteorites). There are no known examples of solar-system material with concentrations of volatile elements higher than the CI concentrations. This indicates that the depletion was not a simple local redistribution (i.e., vaporization-recondensation) and also that it was fundamentally different to the siderophile-element fractionation discussed in the preceding section, because the latter resulted in both metal-rich and metal-poor materials. Low volatile-element abundances are characteristic of the inner solar system, and the Earth should be no exception (Palme et al., 1988). The observed volatile depletion pattern in meteorites is best explained by progressive removal of the nebular gas during cooling, so that the fractions of condensable elements gradually decreased with decreasing condensation temperatures.

Ice-forming elements condense at temperatures below 300 K; these are H, C, N, and the rare gases. Only tiny fractions of the solar abundance of these elements are contained in even the most volatile-rich meteorites. The mechanism of ice-forming element depletion in the Earth is probably the same as for volatiles, but the degree of depletion is much higher.

Oxygen has a unique status in cosmochemical classification due to its unique behavior. Some O was among the first material to condense with the refractory elements (for example, as Al_2O_3), and more condensed with Mg and Si. Next, more O condensed through oxidation of Fe metal, forming the FeO component of silicates and oxides. However, the amount of O condensing in this way is only ~15% of the solar nebula oxygen content. The remaining 85 % of O is predicted to have condensed as H_2O in the ice-forming regime.

Although the meteoritic record provides a relatively well constrained bulk chemical composition of the Earth, the most important differentiation event inside the planet must be

considered to understand its constitution. The fundamental division in the Earth is between its outer silicate portion, consisting of the mantle plus the crust which is usually called the Bulk Silicate Earth (BSE) and its Fe-rich metal core, which is 32% of the Earth by weight. An important issue regarding the principal divisions of the Earth is that the core is probably chemically isolated from the BSE and has been for most of the Earth's history. The justification for this view is the absence of any noticeable change in the siderophile-element content of mantle-derived rocks with time over the entire geological record (i.e., from nearly 4.0 billion years ago).

The isolation of the core from the mantle means that the chemistry of the core is not accessible for direct investigation, except by imposing broad-scale constraints from geophysical observations such as density and seismic velocities. Rather, the chemistry of the core must be inferred from a global mass balance between the composition of the entire Earth, deduced from cosmochemical principles, and the composition of the BSE. The principle is straightforward: if the abundance of an element in the bulk Earth can be deduced from cosmochemical constraints, then the difference between that deduced value and its abundance in the BSE will give the amount of the element in the core. It is therefore necessary first to determine the composition of the BSE.

Table 1.1. Major-element composition of the bulk silicate Earth (BSE).

Element	O'Neill and Palme		Jagoutz et al.		Palme and Nickel		Hart and Zindler		McDonough and Sun
	(1998)	Ringwood (1975)	Ringwood (1979)	et al. (1979)	Wänke et al. (1984)	(1985)	(1986)	(1995)	
MgO	36.33	38.1	38.1	38.3	36.8	35.5	37.8	37.8	
Al ₂ O ₃	4.73	4.6	3.3	4.0	4.1	4.8	4.1	4.4	
SiO ₂	45.56	45.1	45.1	45.1	45.6	46.2	46.0	45.0	
CaO	3.75	3.1	3.1	3.5	3.5	4.4	3.2	3.5	
FeO _t	8.17	7.9	8.0	7.8	7.5	7.7	7.5	8.1	
Total	98.54	98.8	97.6	98.7	97.5	98.6	98.6	98.8	

_t – total iron content, is written as 'FeO'

There are a number of independent estimations of BSE abundance of the elements (Table 1.1). For most elements, agreement among these estimates is good. The nature of the BSE composition determination is the following. The BSE is composed of a number of geochemical reservoirs: the continental crust; the sub-continental lithospheric mantle; the

oceanic crust; the sub-oceanic lithosphere; the depleted, well-stirred upper mantle, which is the source region for mid-ocean-ridge basalt (MORB); the enriched, heterogeneous, source regions for ocean-island basalt (OIB), which may include subducted oceanic crust; and, possibly, primitive mantle that has never been differentiated. For a few extremely incompatible elements such as hydrogen, the noble gases, and Cl, Br, and I, the oceans and atmosphere also need to be included. The choice of what to define as a geochemical reservoir is somewhat arbitrary. For each element there is a mass balance that should be solved. Currently the BSE composition is known relatively well, and agreement between different workers is quite good (see Table 1.1).

It is remarkable that only five components constitute more than 98% of the bulk silicate Earth. This implies that a relatively simple model with a limited number of phases could be a relative good approximation for the bulk mantle composition. This idea is realized, in particular, in the well known pyrolite model of the mantle. The term ‘pyrolite’ was chosen by Ringwood (1962) as the name for a chemical composition of the mantle consisting predominantly of pyroxene and olivine. The pyrolite model is the most used and has been subsequently developed over the last few decades (Green and Fallon, 1998).

Geophysical record: seismic structure of the mantle

Seismological techniques have provided much of the currently available information on the internal structure of the Earth, and in particular on the mantle. Seismic waves, originating mainly from earthquakes, pass through the Earth while bouncing and refracting at seismic boundaries (Fig. 1.3). Analyzing and comparing seismograms from the same event recorded at different seismological stations allows the determination of many physically important properties of the Earth: location of seismic boundaries and determination of seismic wave velocities, and pressures and densities in the deep interior. Early studies revealed the need for an increase in seismic velocity with depth in the Earth, and by 1915 Gutenberg was able to make a good estimate of the radius of the core based on seismic wave propagation through the Earth. Knowledge of the Earth's internal structure was refined by iterative improvement of earthquake locations and the travel times for seismic phases through the Earth, so that in 1940 Jeffreys and Bullen were able to publish an extensive set of travel-time tables based on a model of both P-wave and S-wave velocities in the mantle. Their velocity profile was intentionally as smooth as possible, but it was necessary to introduce a sharp change in velocity gradient near depths of 410 km and 660 km to account for the

distinct change in slope of travel-time curves at a distance of approximately 20° from the source for both P and S waves. Subsequent studies have refined our conception of mantle structure to reveal the presence of discontinuities in velocity and zones of strong velocity gradients which have been correlated with mineralogical phase changes.

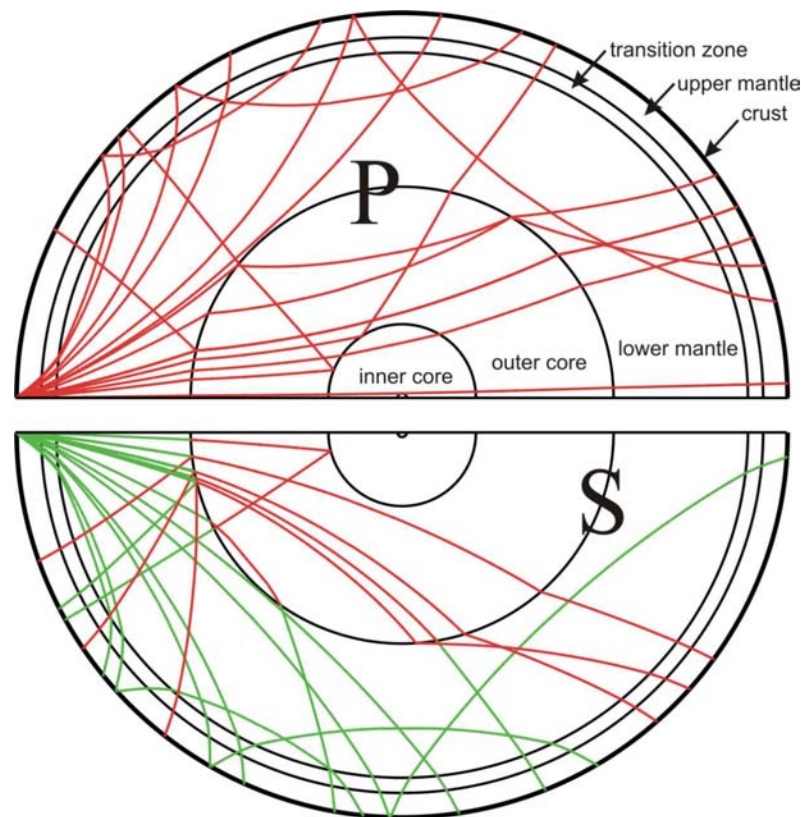


Fig. 1.3. Scheme of different P- (upper hemisphere) and S- (lower hemisphere) seismic waves propagation paths through the Earth.

The presence of three-dimensional variations in the Earth's structure became apparent through regional differences in seismic travel times, and they became better understood once surface-wave observations demonstrated significant differences in surface-wave dispersion between oceanic and continental regions. Surface-wave studies revealed the presence of a zone of decreased shear-wave velocity at depth and showed significant variations in the thickness of the overlying high-velocity zone between different regions. The differences between the characteristics of the upper mantle in oceanic and continental regions led Dziewonski et al. (1975) to develop models with allowances for oceanic and continental character as well as an average radial model for the entire Earth.

In last decades the quality and quantity of seismological data have improved sufficiently that it is possible to begin to resolve the three-dimensional structure within the Earth using a combination of information from the travel times for seismic phases, the free oscillations of the Earth, and long-period seismic waveforms. A consensus is developing regarding the largest-scale features in the aspherical structure. In particular, the upper mantle is a zone of major variability and relatively strong horizontal gradients in seismic properties. Subducted slabs are associated with large, localized contrasts in velocity. Detailed P-wave tomography based on the inversion of seismic travel times has revealed the complex patterns of subduction in many regions. The influence of subduction is largest in the upper mantle, but in many places subducted material appears to have penetrated directly or indirectly into the lower mantle. The high seismic velocities associated with the colder subducted material seem to be the dominant mode of smaller-scale heterogeneity in the lower mantle, which otherwise appears to be characterized by relatively low gradients of heterogeneity. However, the degree of variability increases as the core-mantle boundary is approached, and the D" layer in the 300-km zone at the base of the mantle shows considerable variability on a wide range of scales revealed by studies with many different types of probes.

The variation of seismic properties within the Earth is inferred from the analysis of seismograms in a variety of ways and is dominated by a radial dependence. However, three-dimensional variations are manifest in the crust and in all parts of the mantle; currently the most effective representation of such three-dimensional structure is as a perturbation to a reference radial model. For this radial reference model, the major sources of information come from the travel times for seismic phases and from the free oscillations of the Earth. The travel times provide constraints on the seismic wave speeds within the Earth, and the frequencies of normal modes provide additional information on the density distribution and attenuation profile for seismic waves.

The zones of greatest heterogeneity lie in the uppermost part of the mantle (depths shallower than about 250 km) and near the core-mantle boundary. In such zones, horizontal gradients in velocities can approach the radial gradients, so it is difficult to define a representation of an "average" structure in those parts of the Earth. Various techniques are currently being employed to build up a body of information on the three-dimensional structure of the Earth. To determine the distribution of velocities for compressional (P) waves, the dominant approach is the use of traveltimes tomography, primarily based on the impressive collection of arrival-time data for different seismic phases assembled by the International Seismological Centre (ISC). Recently, additional information on travel times has become available from analyses of long-period seismograms by correlation techniques (e.g., Woodward and Masters, 1991).

At present, nearly all the techniques designed to assess the three-dimensional structure of the Earth are based on a representation in terms of deviations from a reference model (which normally is a spherically symmetrical model). The nature of the reference model is therefore of considerable importance. These reference spherical models are also called one-dimensional (1D) models. Dziewonski et al. (1975) introduced a new style of representation for such reference models with the PEM model, which was defined in terms of a limited number of radial segments, within each of which the seismic velocities and densities were defined by polynomials (up to cubic) in radius. The advantage of such a form of representation is that the entire model is defined by a relatively small number of parameters.

Such parameterized models have been used extensively since 1975, notably in the PREM model of Dziewonski and Anderson (1981) which endeavored to take account of a very wide range of information from the free oscillations of the Earth, dispersion of surface waves, travel times for the major seismic phases, and differential travel times. The PREM model allowed for the frequency dependence of seismic velocities associated with anelastic attenuation within the Earth, and it also introduced the concept of transverse isotropy in the uppermost mantle to try to reconcile the dispersion characteristics of Rayleigh and Love waves. The PREM model has been extensively used in work involving the normal modes of the Earth, and it is frequently used as a reference model in global studies.

The same style of parametrization has been adopted in the recent models *iasp91* (Kennett and Engdahl, 1991) and *sp6* (Morelli and Dziewonski, 1993) for P and S velocities derived from travel-time information. With these improved velocity models, it is possible to refine the locations of seismic events and thus obtain an updated set of empirical travel times for a wide range of seismic phases. Kennett, Engdahl, and Buland (1995) have constructed a new model, *ak135*, for the seismic velocities using such improved travel times, and in order to fit the observed behaviour they were forced to employ a more complex parametrization in the lower mantle and core.

The main difference between different spherical seismic models of the Earth exist in the upper mantle and transition zone with considerable regional variability, but in the lower mantle beneath about 750 km there is much greater consistency between the velocities for different reference models (Fig. 1.4-1.5).

The bottom 200 km of the lower mantle (the D" layer) is a zone of relatively strong heterogeneity, as shown by a wide range of studies. This zone, just above the core-mantle boundary, may well have heterogeneity comparable to that near the Earth's surface and may serve as a repository for the debris from mantle processes that potentially can be remobilized

by the heat emerging from the core. There are different possible explanations for the anomalous elastic properties of D" layer, including partial melting or the appearance of new phases.

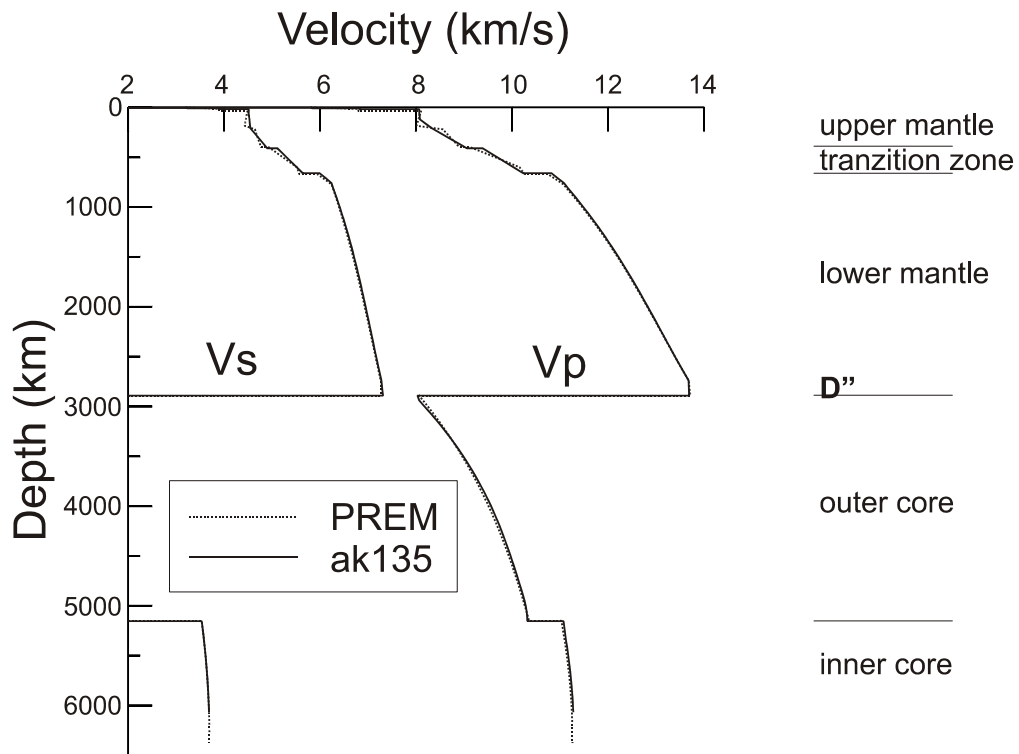


Fig. 1.4. PREM (Dziewonski and Anderson, 1981) and *ak135* (Kennett et al., 1995) spherical models for P- and S-waves velocities in the Earth.

Seismic boundaries (areas of discontinuous gradients of elastic properties) play a key role in our understanding of the mineral (phase) constitution of the Earth. The most important boundary – the core-mantle boundary – separates two chemically absolutely distinct regions, the silicate/oxide mantle and the metallic core. The boundary between the inner and outer core is a phase boundary between an outer liquid and an inner solid region, while other discontinuities exist in solid regions of relatively uniform chemical composition. These latter boundaries therefore reflect phase transitions in major rock-forming minerals (see below).

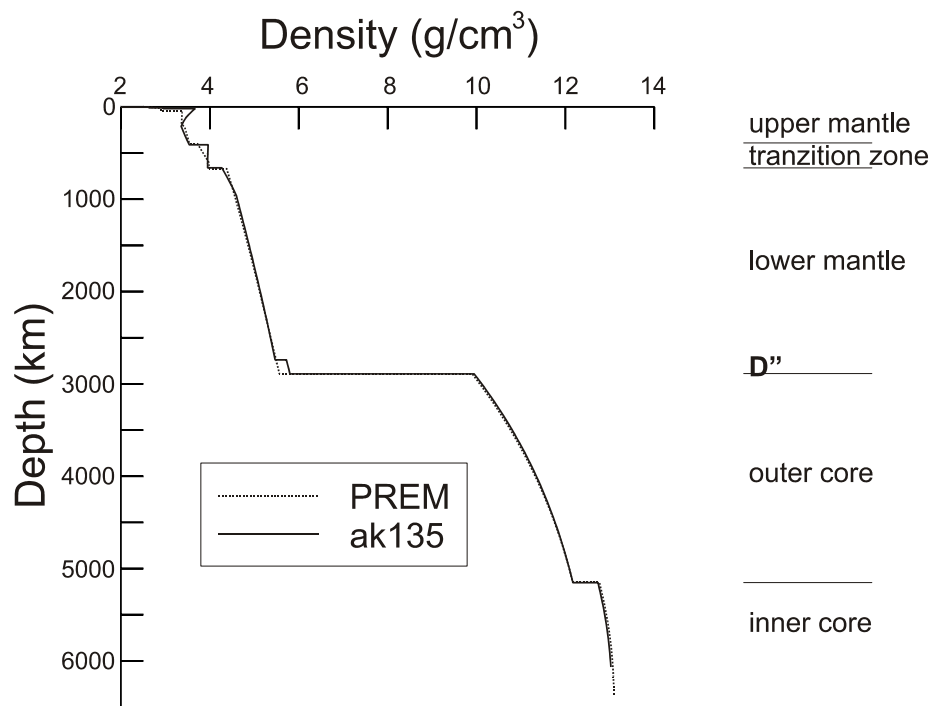


Fig. 1.5. PREM (Dziewonski and Anderson, 1981) and *ak135* (Kennett et al., 1995) spherical models for density in the Earth.

One great advantage of seismological observations is that they constrain pressure and density well for the deep Earth's interior. However, the temperatures in the Earth's interior are much more controversial. There are several constrains for the depth-temperature profile, called the geotherm. They are the temperature at the inner-outer core boundary which is the melting temperature of iron-nickel alloy at ~ 329 GPa, thermoelasticity of the major phases in the mantle, and the Clapeyron-Clausius slope of phase transitions associated with seismic discontinuities (see below). All these constrains have significant uncertainty that propagates to the final temperature uncertainty; however it is generally agreed that temperature in the lower mantle varies from about 1800-1900 K at the top to 2200-2500 K at the bottom.

Mineralogical model of the mantle. Ferropericlase in the Earth's deep interior.

As shown above, there are strong pressure and temperature variations in the Earth's interior. Phase transformations in the main minerals are therefore quite possible and indeed are expected. Such transformations would have effects on density (particularly in the mantle transition zone, where phase changes and reactions have been identified as functions of depth) and/or on elastic properties. The potential consequences of density changes in terms of

the dynamics of the Earth's mantle have been matters of active debate for at least 30 years (Ringwood, 1975).

There are formidable complexities in laboratory investigations of the mechanisms and kinetics describing transformations of mantle phases, as well as in the consequent geophysical interpretations. Nevertheless, many impressive successful studies have been made and are summarized briefly below. As mentioned above, the composition of bulk silicate Earth can be described fairly well as a mixture of olivine $(\text{Mg,Fe})_2\text{SiO}_4$ and pyroxene $(\text{Mg,Fe})\text{SiO}_3$ (pyrolite model), and phase transitions in these phases should be of the utmost importance.

$(\text{Mg,Fe})_2\text{SiO}_4$.

Ringwood and Major (1966) experimentally transformed the α phase (olivine) of $(\text{Mg,Fe})_2\text{SiO}_4$ into its cubic spinel polymorph, now known as either the γ -phase or ringwoodite (mineral name). In doing so, they noted the existence of a spinel-related phase, later named the β phase and given the mineral name wadsleyite. From crystal-structure determinations for these phases (e.g., Morimoto et al., 1970), it was shown that the β and γ phases are quite closely related, and both are significantly different from the α phase. In olivine Mg and Fe occupy octahedral positions with two topologically slightly different sites M1 and M2. Silicon is 4-coordinated and $[\text{SiO}_4]$ tetrahedra are isolated from each other (Fig. 1.6.a).

Ringwoodite has a cubic spinel crystal structure with $[\text{SiO}_4]$ tetrahedra and $[\text{MgO}_6]$ octahedra (Fig. 1.6.c). This structure is denser compared to the α phase due to more effective space packing of $[\text{MgO}_6]$ octahedra. The wadsleyite crystal structure is almost identical to the γ phase, but silicon tetrahedra forms isolated pairs that share a common apex (Fig. 1.6.b). Wadsleyite is also often called a “modified spinel” phase, compared to the “spinel” γ phase. All three phases have been shown to be thermodynamically stable in the Mg-Fe system with stability fields that are now experimentally well established. By combining thermodynamic calculations and experimental observations of temperature and composition effect on the transition pressures, it is absolutely clear that the $\alpha \rightarrow \beta$ transformation is responsible for the strong 410-km seismic discontinuity and the $\beta \rightarrow \gamma$ transition is responsible for the weaker 520-km discontinuity.

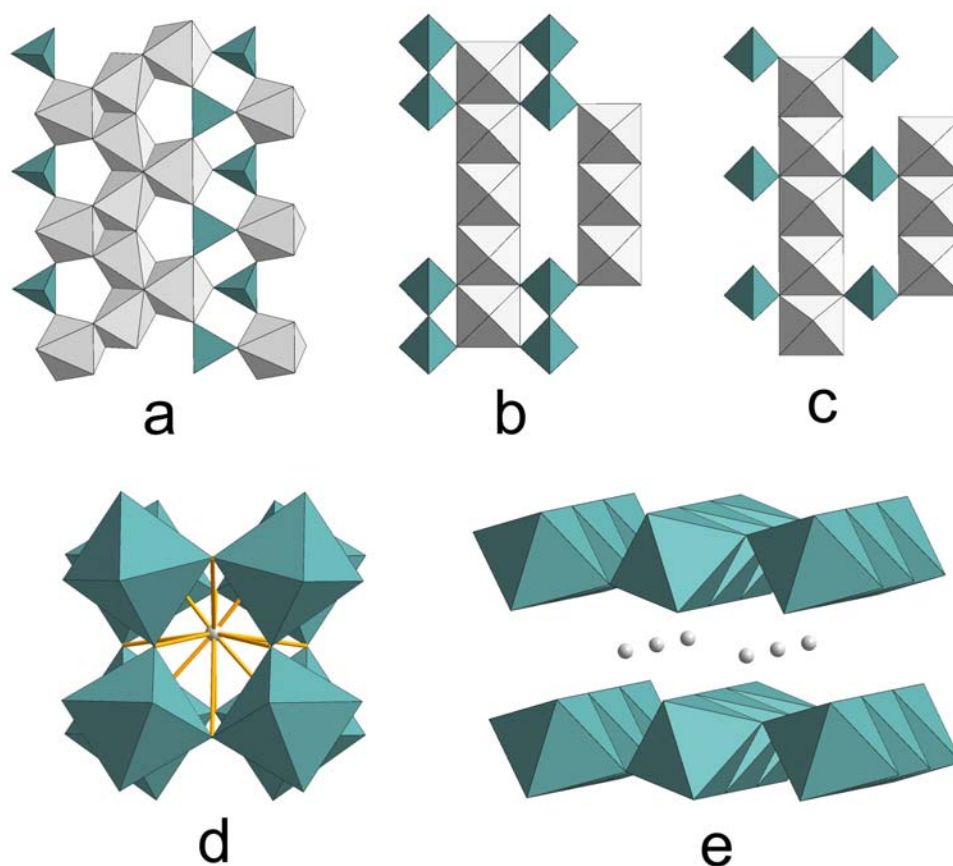


Fig. 1.6. Polyhedral model of the crystal structures of Mg_2SiO_4 olivine (a), wadsleyite (b), ringwoodite (c) and MgSiO_3 perovskite (d) and “post-perovskite” (e).

The close relations between the β and γ phases have led many to conclude that the transition between these two phases can be accomplished by a diffusionless martensitic transformation (e.g., Price, 1983). In contrast, the transition from α to either β or γ must involve a major reconstruction of the polyhedral groupings and cation arrangements. The mechanisms of the transitions among the three polymorphs have been studied in numerous transmission-electron-microscopy investigations of experimental products and their natural equivalents preserved in meteorites. Initially, experimental investigations used analogue materials such as Mg_2GeO_4 (Vaughan and Coe, 1981) because the phase transitions were more accessible using the apparatus available at that time. The γ phase is intrinsically somewhat stronger (dislocation glide requires higher stress) than the α phase. Of course some analogue systems are inappropriate for comparison with $(\text{Mg,Fe})_2\text{SiO}_4$ – for example there is no stable β phase of Mg_2GeO_4 ; Co_2SiO_4 is a better analogue in this regard (Remsberg and Liebermann, 1991).

The nature of the phase-transition mechanisms likely to occur in $(\text{Mg,Fe})_2\text{SiO}_4$ within the mantle above 660 km depth are fairly well understood. Our knowledge is now approaching the point where the kinetics of these transitions can be reasonably predicted and

applied to the dynamics of subducted slabs. By reference to the equilibrium phase diagram it was pointed out that $(\text{Mg,Fe})_2\text{SiO}_4$ in cool subducting slabs would undergo transitions at shallower depths and initially in a different sequence (due to the $\alpha \rightarrow \gamma$ field) than in the warmer surrounding mantle. The situation becomes more complicated if rates of phase transitions and slab heating are considered. At the same time the sluggish kinetics (at $T < 700^\circ\text{C}$) of the transition from α - $(\text{Mg,Fe})_2\text{SiO}_4$ should result in a metastable field of olivine. Using a simple rate model allowing only grain-boundary nucleation, Sung and Burns (1976) calculated that metastability could extend more than 200 km below the approximately 400-km depth of equilibrium transition in the form of a wedge of relict peridotite. The mantle phases coexisting with olivine could also have some influence over the transitions. Sharp and Rubie (1995) have identified a catalytic effect of clinoenstatite on the $(\text{Mg,Fe})_2\text{SiO}_4$ transitions into the γ phase and possibly the β phase and have speculated on the consequent implications for reaction kinetics; i.e., that such a catalytic effect could reduce the metastability depth even further.

The most important phase transition that is responsible for the 660-km discontinuity is the decomposition of ringwoodite into $(\text{Mg,Fe})\text{SiO}_3$ with the perovskite structure and $(\text{Mg,Fe})\text{O}$ oxide. It is an important observation that equilibrium coexistence of these two phases is possible only above the transition pressure. Natural samples with coexisting $(\text{Mg,Fe})\text{O}$ and $(\text{Mg,Fe})\text{SiO}_3$ (as pyroxene) in diamond inclusions are therefore concluded to have a lower mantle origin (Harte and Harris, 1994).

In the perovskite ABX_3 structure cite the A site is 12-coordinated and the B site is six-coordinated (octahedral) by X anions (Fig. 1.6.d). $[\text{BX}_6]$ octahedra form a three-dimensional framework and share common apices. The A-cation occupies a large cavity in this framework. Perovskites can possess cubic symmetry or can be tetragonal, trigonal, orthorhombic or even monoclinic. In the latter cases, the A position is usually strongly distorted and its coordination number is more correctly written as $8 + 4$, which means 8 X anions at somewhat shorter distances from the central A cation and 4 X anions at longer distances.

The term “perovskite” as applied to lower-mantle magnesium silicate is in some ways an unfortunate terminological choice. Perovskite is a relatively rare mineral with the chemical formula CaTiO_3 . However there is an extremely broad range of chemical compounds that adopt the same or closely related crystal structures. There are several hundred synthetic compounds with the perovskite structure (for example, LaMnO_3), and many of them have important technological applications. Hence the term perovskite is often used to denote a certain type of crystal structure. When it is applied to MgSiO_3 , it could be somewhat confusing. Nevertheless, until natural samples of Mg,Si-perovskite are found and a

mineralogical name can be given to this phase, we use the term “perovskite phase”, similar to the term “spinel phase” which is often used for ringwoodite.



The second most abundant mineral in the pyrolite mantle model is pyroxene with the nominal formula $(\text{Mg,Fe})\text{SiO}_3$. The pyroxene family features many textbook transformations that have long fascinated mineralogists. Angel and Hugh-Jones (1994) reviewed the volume changes and phase relations among the ortho, high-clino, and low-clino polymorphs of enstatite. Hogrefe et al. (1994) investigated the kinetics of transformation of MgSiO_3 at pressures of 16-21 GPa and reported that at 1000°C the high-clino polymorph of enstatite can undergo a nonequilibrium transition directly to a MgSiO_3 polymorph with the ilmenite (FeTiO_3) structure.

At moderate pressures in the presence of Al and Ca (which is the case for the mantle) pyroxene transforms to garnet. At the bottom of the upper mantle pyroxene is no longer stable, but only a mixture of garnet and CaSiO_3 perovskite. Not much is known about the mechanical aspects of phase transitions in the garnet family at high pressure. There is a possible cubic-tetragonal transition in MgSiO_3 majorite garnet as identified by microstructural effects (Wang et al., 1993), and the large volume change of about 16.9% for the MgSiO_3 end member (Yusa et al., 1993) associated with the garnet- to-perovskite transition at the base of the mantle transition zone may be important. Again, however, the mechanical effects of this ultra-high-pressure transition have not been investigated. There is evidence for possible cubic-tetragonal-orthorhombic transitions in $(\text{Mg,Fe})\text{SiO}_3$ perovskite that could occur in the upper part of the lower mantle (Wang, Guyot, and Liebermann, 1992); however, information is limited, particularly for the effects of stress on the fields of phase stability and for the controls of transformation on rheology. Because of the crystallographic complexities of some of the lower-pressure members of the $(\text{Mg,Fe})(\text{Si,Al})\text{O}_3$ family and the relatively high pressures of many of the transformations relevant to the deeper mantle, it is likely that detailed knowledge about transformations and their geophysical effects will remain limited, compared with those for the $(\text{Mg,Fe})_2\text{SiO}_4$ minerals (Drury and Fitz Gerald, 1998).

The discovery of another reconstructive phase transition that occurs in MgSiO_3 perovskite at pressures close to the core-mantle boundary provides more promising possibilities (Murakami et al., 2004-I; Oganov and Ono, 2004). This new phase has the CaIrO_3 layered structure which is not typical for high-pressure polymorphs in general. $[\text{SiO}_6]$ octahedra share a common edge, which creates columns and these columns are formed into layers by connecting through common apices. Mg and Fe ions are located in between

adjacent Si-O layers (Fig. 1.6.e). Many speculations have been made regarding the possible implications of this transition on D'' layer anomalies at the core-mantle boundary.

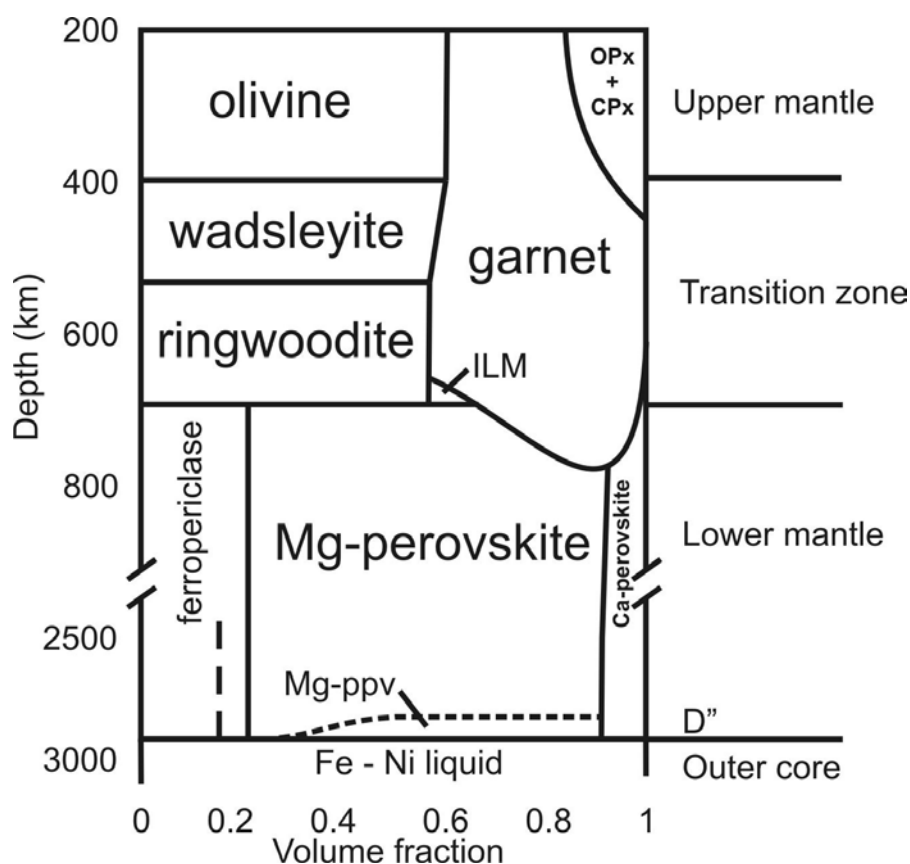


Fig. 1.7. Volume fraction of the main rock-forming minerals of the Earth's mantle. OPx and CPx are ortho- and clinopyroxenes, ILM is MgSiO_3 with the ilmenite structure, Mg-perovskite and Ca-perovskite are $(\text{Mg,Fe})(\text{Si,Al})\text{O}_3$ and CaSiO_3 silicates with perovskite-like crystal structures, Mg-ppv is a post-perovskite CaIrO_3 -like phase of $(\text{Mg,Fe})(\text{Si,Al})\text{O}_3$. Vertical dashed line in the ferropicroclase field indicates possible decomposition of $(\text{Mg,Fe})\text{O}$ into Fe-rich and Fe-poor phases due to miscibility gap.

For $(\text{Mg,Fe})\text{O}$ ferropicroclase there are no structural phase transitions expected under mantle conditions. Although the FeO end-member of the solid solution undergoes certain phase transformations (see chapter III.1 and III.2), the dilute $(\text{Mg,Fe})\text{O}$ solution has been assumed to exist in the cubic NaCl structure over the entire lower mantle P, T range (Lin et al., 2003). The reconstructive phase transition from the NaCl-like structure to an NiAs-like structure in FeO at high pressures (Fei and Mao, 1994) could have a strong influence on the miscibility of MgO and FeO. In particular, at high pressures it could decompose into a Mg-rich cubic phase and a Fe-rich NiAs-like phase. Some experimental evidence for the decomposition of magnesiowüstite at high pressures and temperatures exist (Dubrovinsky et

al., 2000-I). Surprisingly, the decomposition into two isostructural NaCl-like phases was observed, and the reason for MgO-FeO immiscibility was not clear. Moreover, some controversy still exists (Lin et al., 2003).

A schematic diagram showing the relative abundance of the different phases in the Earth's mantle summarizes all the abovementioned observations (Fig. 1.7).

Motivation

As seen from Fig. 1.7, ferropericlase (Mg,Fe)O is the second most abundant mineral of the lower mantle, formed by the dissociation of (Mg,Fe)₂SiO₄ (ringwoodite) into (Mg,Fe)SiO₃ (perovskite) and (Mg,Fe)O (ferropericlase). MgO shows no phase transitions up to at least 227 GPa (Duffy et al., 1995), which is also confirmed by *ab initio* simulations (Oganov et al., 2003). FeO wüstite undergoes a number of pressure-induced transitions as mentioned above. First, there is a structural transition from the cubic to a trigonally distorted structure (Zou et al., 1980), and the transition pressure strongly depends on the hydrostaticity (Dubrovinsky et al., 2000-II), and probably also on the stoichiometry (Shu et al., 1998-I; Jacobsen et al., 2005). At higher pressures, around 90-100 GPa, FeO transforms from the NaCl-related structure to an NiAs-like hexagonal structure (Fei and Mao, 1994). There are also several pressure-induced electronic transformations in FeO: antiferromagnetic ordering at about 5.5 GPa (Kantor et al., 2004-II; Nasu, 1994) and a possible high- to low-spin transformation at approximately 100 GPa (Pasternak et al., 1997), although this transition was not confirmed by X-ray emission study (Badro et al., 1999).

Structural phase transitions are not expected to occur in low-Fe containing ferropericlase. MgO is the dominant component in lower-mantle ferropericlase, and it is extremely stable in the NaCl-like B1 structure. The minimum iron content for which a trigonal distortion has been observed in magnesiowüstites under high pressure is more than 50 mole % (Mao et al., 2002; Kondo et al., 2002, 2004). Transformation to the B8 structure is even less probable for low-iron ferropericlase. Magnetic ordering also requires a significant iron concentration in order to propagate long-range spin orientation throughout the entire crystal. In addition, high temperature in the Earth's mantle should suppress any possible magnetic ordering. A spin-pairing transition, however, does not require a high iron concentration and could occur in iron-bearing minerals under high-pressure conditions in the lower mantle. An iron spin-pairing transition in the mantle was first predicted more than 40 years ago (Fyfe, 1960). The effective radius of the high-spin electronic state is generally smaller than that of the low-spin state, and the pressure-induced bond length reduction and

phase transitions to dense polymorphs would stabilize the low-spin state of Fe^{2+} . Pressure also increases crystal field splitting and, at the same time, the covalency of the chemical bonding (the Racah parameter B decreases), and all these changes would also shift the thermodynamic equilibrium to the low-spin configuration (Burns, 1993).

There are several possible consequences of a spin transition in the mantle. The first and the most trivial is the loss of magnetism. For Fe^{2+} there are four unpaired electrons in the high-spin state, and no unpaired electrons in the low-spin state. Differences in macroscopic properties between paramagnetic and diamagnetic states are not so important for geophysics. The second and much more important is the possible change in density and compressibility due to a spin-pairing transition. Such a change would be of great importance for Earth modeling, because it would directly affect the seismological profile. Third, a pressure-induced contraction of interatomic distances could lead to an enrichment of low-spin Fe^{2+} ions of host phases in the mantle. If two compounds contain cations of the same charge, the one with the larger cation generally has the lower melting point. At low pressures, the Fe end-members of ferromagnesian silicate solid solution series have lower melting points than the Mg end-members, with the result that crystallization leads to enrichment of Mg in the mineral and Fe in the liquid. At pressures above the spin-pairing transition point, however, low-spin Fe^{2+} may have a smaller ionic radius than Mg^{2+} , and could possibly lead to a reversal of melting point relationships (Burns, 1993). The same effect could also result in significant changes of the partitioning of iron between the main iron-bearing phases, namely ferropericlase and Mg-Si perovskite (Badro et al., 2003). Finally, a spin-pairing transition would also shift absorption bands in minerals due to changes in the electronic configuration. Since the main mechanism of thermal transport in the mantle is radiation, a spin transition could also significantly affect thermal transport properties of the mantle (Goncharov et al., 2005).

This study is generally focused of high-pressure and high-temperature behavior of ferropericlase and FeO end member for better understanding the constitution of the Earth deep interior. It addresses some of the abovementioned problems regarding structural and electronic states of (Mg,Fe)O and the FeO end member under high pressures and temperatures and explores the implications for the Earth sciences.

II. Methods and instrumentation

Diamond anvil cells

Basic principles

There are numerous types of high-pressure devices used both for sample synthesis and for *in situ* studies of materials under high pressures (Spain, 1977). Between them only two main classes can create static pressures relevant to the Earth's mantle: multi-anvil large-volume presses and diamond anvil cells (DACs) (Spain, 1977). Multi-anvil assemblies have several clear advantages: relatively large sample volume and stable electrical resistive heating up to several thousand Kelvin for sufficiently long time periods (hours). However, they are quite limited in the highest possible pressure (up to 25-30 GPa) and to the number of *in situ* techniques that can be applied. In contrast, diamond anvil cells can reach a maximum possible static pressure above 300 GPa. Diamond anvils are transparent for photons in a broad energy range, including optical, near-infrared region and X-rays. This makes DACs unique tools for *in situ* studies of materials under high pressures.

The basic principle of the DAC is very simple. Pressure is defined as a ratio of a force over the area over which it is applied. Therefore if the anvil surface is small enough, even moderate force could produce extremely high pressure. The limiting part of the system is the anvil material: it should be hard enough, mechanically very stable, as incompressible as possible and it should not plastically deform during compression (when the force is applied). Probably the best material is single-crystal diamond, which is one of the hardest materials with very high bulk modulus and it is transparent. The main part of any DAC assembly is the following: a metal gasket with a small hole is squeezed between two diamond anvils (Fig. 2.1). Diamond culet diameter can normally vary from 1 mm to 60 μm , and the sample chamber thickness from 500 to 15 μm . Sample chamber diameter is usually chosen to be from one half to two thirds of the culet size. The higher the desired pressure is, the smaller the culet size and sample volume are. The sample can be loaded in a pressure-transmission medium to minimize pressure gradients and non-hydrostatic stresses on the sample.

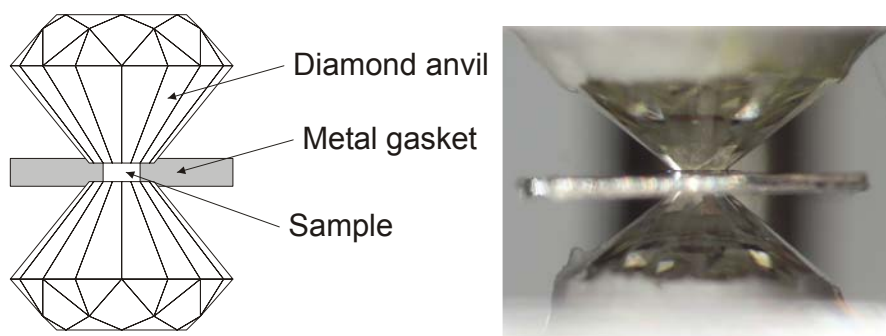


Fig. 2.1. Schematic (left) and actual (right) images of opposed diamond anvil assembly, the main part of the DAC.

Diamond anvil cutting for the high-pressure experiments can be different. The culet shape can be eight- to 64-sided. The most common is the normal diamond design, as is shown

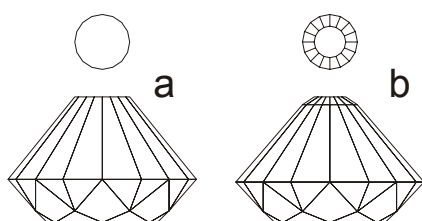


Fig. 2.2. Simple (a) and beveled (b) diamond anvil design.

in Fig. 2.1 and 2.2a. For ultrahigh studies so-called beveled diamonds can be used (Fig. 2.2b). Upon compression incredible pressure gradients develop in the diamond anvil: at the culet pressure can reach several megabars, while at the outer surface pressure is just a few GPa. Moreover, pressure (or, to be more precise, stress) changes non-linearly within the bulk

diamond and major gradients exist within the first millimeter or a fraction of millimeter. Diamond beveling redistributes stresses and diamonds can provide higher pressure without cracking or damaging (Bruno and Dunn, 1984). Not only single-beveled, but also double- or even triple-beveled anvils could be used. For some specific applications more complex designed anvils exist, such as perforated diamonds with decreased anvil thickness (Dadashev et al., 2001) or diamonds with build-in electrodes for electrical conductivity and magnetic susceptibility measurements (Jackson et al., 2003), and so on. Typical size of the whole anvil is 1.5 – 2 mm in height and mass varies from $\frac{1}{4}$ to $\frac{1}{3}$ carat.

A diamond anvil cell should simply be able to push two anvils to each other with a sufficient force, while keeping the anvils perfectly aligned. A large number of different DAC designs exist, with various sizes, angular access and so on (Jayaraman 1983). All of them can be divided into two groups: piston-cylinder and opposed-plates types (Fig. 2.3).

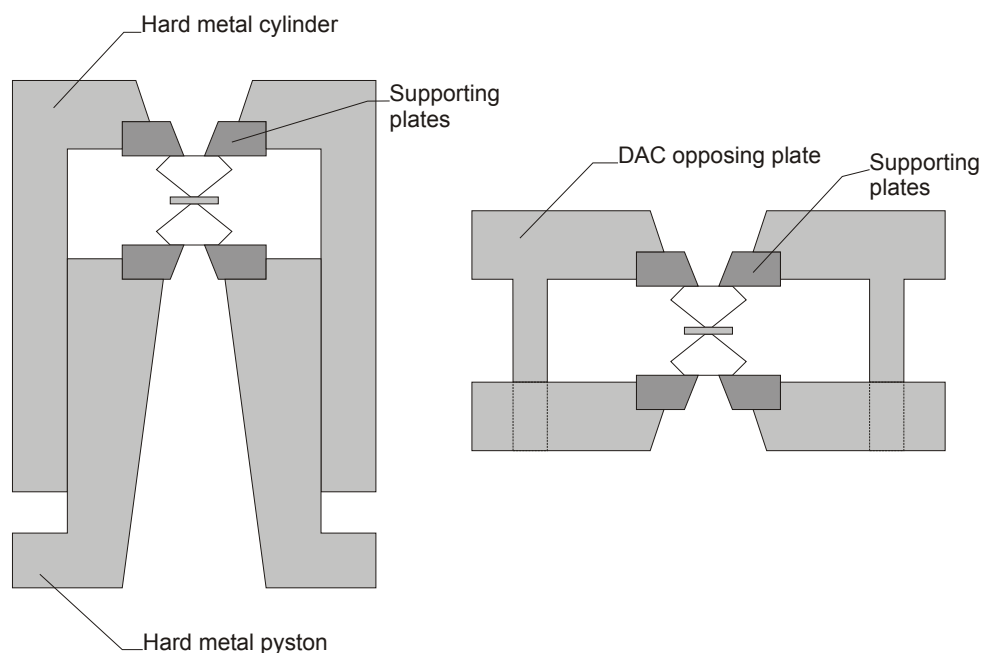


Fig. 2.3. Piston-cylinder (left) and opposed-plates (right) types of diamond anvil cells.

Diamonds are fixed on supporting plates (seats), and the DAC is equipped with an alignment mechanism for translational alignment (usually with screws) and sometimes angular alignment (with hemispherical or hemi cylindrical rockers). Supporting plates could be made from hard metal or from X-ray transparent materials (Be alloys, cubic boron nitride and so on). In the latter case the assembly is less stable: beryllium and its alloys are relatively soft, and diamond anvils can be pressed into the supporting plate during the experiment, while cubic boron nitride plates are relatively fragile and can be easily cracked. The compression mechanism can also be different. Most cells use a simple screw-driven mechanism or a combination of screw drives with various arms. Another common possibility is a gas-membrane cell. In the latter case the piston or plate of the DAC is pushed by a metal membrane filled with gas under high pressure. Gas membranes allow fine pressure adjustment without manipulating the cell, only by changing gas pressure in the membrane. This is a major advantage for synchrotron studies, when a significant fraction of beam time can be saved from DAC positioning in the beam after every pressure change. A disadvantage of the gas-membrane cell is the complexity of the whole system in comparison with mechanically driven DACs, difficulties with low-temperature (the gas inside the membrane could start to condense) and high-temperature (expanding gas in the membrane could cause unpredictable pressure changes in the DAC) experiments. Some examples of most popular DAC designs are shown in Fig. 2.4.

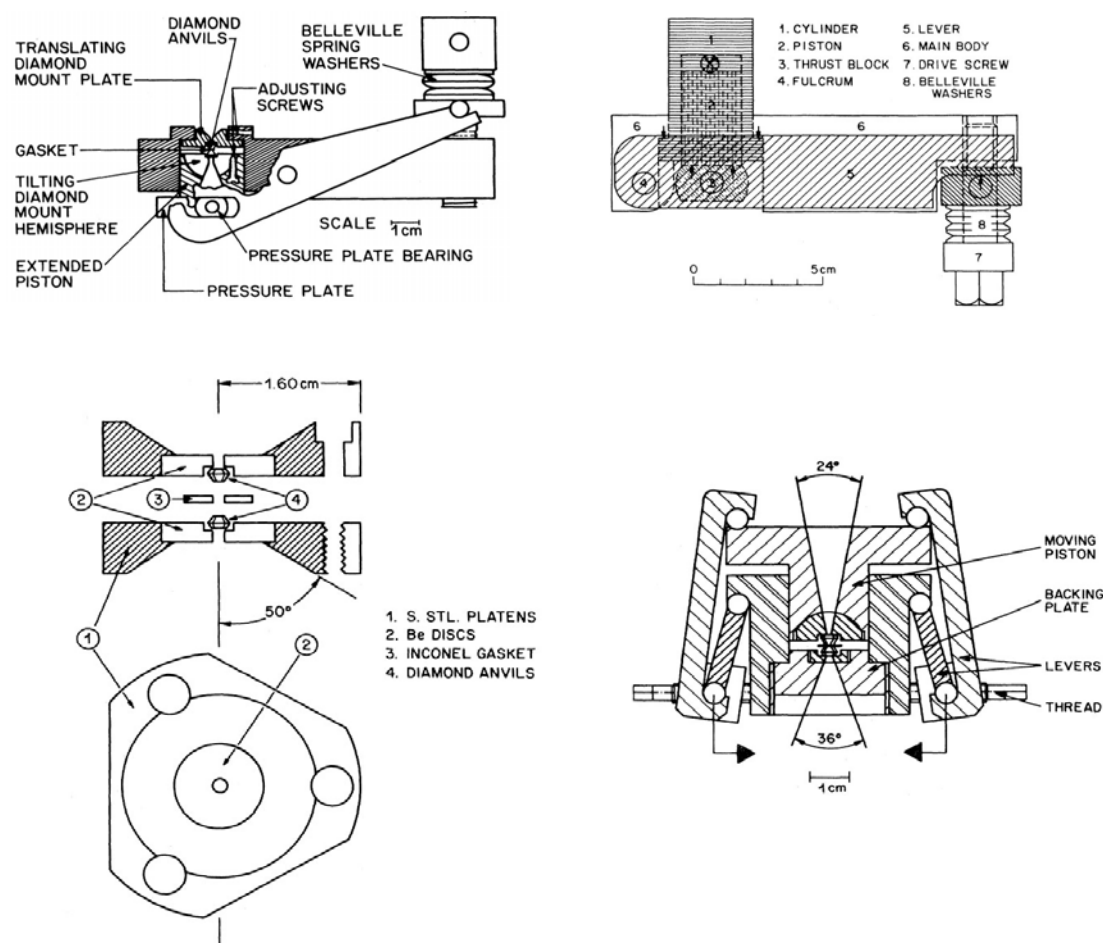


Fig. 2.4. Some types of DAC designs. Top left – National Bureau of Standards ultrahigh-pressure DAC (Piermarini and Block, 1975). Top right – Mao-Bell piston-cylinder DAC (Mao *et al.*, 1979). Bottom left – compact Merrill-Bassett type DAC (Merrill and Bassett, 1974). Bottom right – Syassen-Holzapfel cell (Huber *et al.*, 1977). Figures after Jayaraman (1983).

DAC heating

DACs can create pressures equal to those in the inner core of the Earth, but generating high temperatures is also very important. There are two ways of DAC heating: external electrical resistive and internal laser or electrical wire heating. External resistive heating of the whole DAC or only the interior volume (around the pressure chamber) has clear advantages. First, temperature gradients in the sample chamber are relatively small, and heating is very homogeneous. Second, temperature measurement is straightforward, since conventional thermocouples can be used. Third, high temperature can be maintained for sufficient time periods (hours or days), which could be necessary for kinetically frozen processes and some long-collecting time measurements (like Mössbauer spectroscopy).

Samples of any nature and any loading design (with or without pressure medium) can be heated. External electrical heating, however, is limited in temperature, and the maximum temperature that can be reached routinely is about 1000 °C. Higher temperatures are possible in principle but require a special design for cooling the DAC itself, isolating diamond anvils from the atmosphere to prevent diamond oxidation, and so on. Laser heating, in contrast, can produce temperatures up to several thousand degrees Kelvin, which is its major advantage. In contrast to resistive heating, laser heating of the DAC introduces additional thermal stresses on the sample. Extremely high temperature gradients develop upon laser heating, in both radial (in the plane of the sample) and axial (along the main axis of the DAC) directions. Temperature measurement during laser heating is also complicated. Normally a radiometry method is used, where the thermal radiation of the hot spot is collected and then fitted to the Plank's black- or grey-body emission model. However, there is still a question of what temperature is actually measured (maximum or average in the spot), and special care should be taken to avoid optics aberration that also affects the emission spectra. Another problem is the difficulty of the fine temperature adjustment and special requirements of the sample. If the sample does not absorb laser radiation (i.e., it is transparent in the given spectral range), it would not heat. The absorbing sample should be isolated from the diamond culet surface; otherwise due to extremely high thermal conductivity of the diamond the sample will still not be heated. Therefore a special loading design is frequently used for laser heating under high pressure, when the sample is "sandwiched" between two thin layers of a thermal insulator, such as sodium chloride or potassium bromide. Double-sided laser heated DAC (two laser beams come to both sides of the sample through two anvils) improves the temperature distribution making axial temperature gradients smaller (Meng et al., 2006). The radial temperature distribution can be made more flat by changing the laser beam power distribution. For example, for samples with good thermal conductivity a donut shaped laser beam combined with a Gaussian laser power profile can provide quite flat (20-40 μm in diameter with temperature variation within 50 K) temperature profiles.

One critical issue for both laser and resistive heated DACs is *in situ* pressure determination under high temperature. A commonly used routine (especially for the laser heated DAC) is pressure measurement at room temperature, and then heating assuming isobaric heating. In reality during heating the cell body itself is also heated. In long-time or high-temperature laser heating experiments the DAC body can be heated to 100 °C or higher. Heating of the DAC and its screws results in thermal expansion. The loading force therefore

decreases and pressure drops down. Our experience shows that pressure can be decreased by 20% or more depending on pressure, temperature and the particular cell design. Pressure calibration under high temperature remains a very important issue and should always be done to obtain reliable results. As was mentioned above, in a gas-membrane driven mechanism the thermal expansion of the cell results in pressure decrease, while the thermal expansion of gas inside the membrane can increase pressure. The competition of these contributions could give unpredictable pressure evolution during the heating.

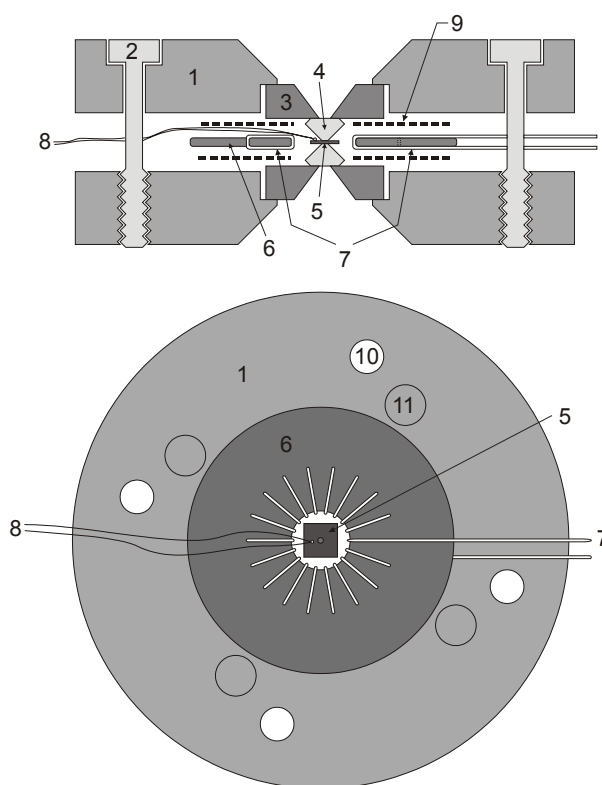


Fig. 2.5. Schematic diagram of the four-pin modified Merrill-Bassett DAC equipped with the internal resistive heater used in this study. Upper figure – cross-sectional view, lower figure – top-view of one DAC plate with the heater. 1 – opposed plate of the cell (temperature stable non-magnetic alloy); 2 – pressurizing screws; 3 – hard metal diamond supporting plate; 4 – diamond anvils; 5 – rhenium gasket with the sample; 6 – fired pyrophyllite heater body; 7 – platinum heater wires (0.3 to 0.5 mm in diameter); 8 – ultra thin R-type Pt-Pt:Rh thermocouple; 9 – mica insulation plate; 10 – screw holes; 11 – guiding pins.

Resistive heaters for the DAC are either miniature heaters that heat only relatively small volumes inside the cell and external heaters, like a small oven for the whole cell (Dubrovinskaia and Dubrovinsky, 2003). Such a design ensures the most homogeneous heating with minimum temperature gradients. However, such a large assembly is not

compatible with many experimental techniques and is not always applicable. Miniature heaters produce higher temperature gradients but practically does not increase DAC size, so it can be applied at any experimental setup, suitable for conventional diamond anvil cells. In our studies many different experimental *in situ* techniques were used, so internal heaters were favored. I used miniature platinum internal resistive heaters mounted inside modified three- (30 mm in diameter) or four-pin Merrill-Bassett DACs (50 mm in diameter, Fig. 2.5). The DAC is made of either Republica or Nimonic alloys, which are non-magnetic and stable for heating in air. The internal resistive heater consists of a ceramic (fired pyrophyllite) ring that fits into the cell, and has ~ 0.5 mm diameter holes for wire loops. I tested Pt, Pt-Ir and Nichrome wires, and found that the best performance was obtained with pure Pt wire of 0.3 to 0.5 mm in diameter. Mica rings are used as an electrical thermal insulator. A fine R- or S-type thermocouple was fixed using high temperature Ceramobond (Amerco Inc.) at a distance of less than 0.5 mm from the pressure chamber, allowing direct and precise temperature measurements. Temperature distribution is rather homogeneous within the DAC sample chamber, and varies no more than ± 15 K at 800 K within a 2 mm diameter circle around the anvils. The internal heater for the three-pin DAC (DAC diameter is 30 mm) is very similar, and differs only in its size (Kantor et al., 2005-II), Fig. 2.6.

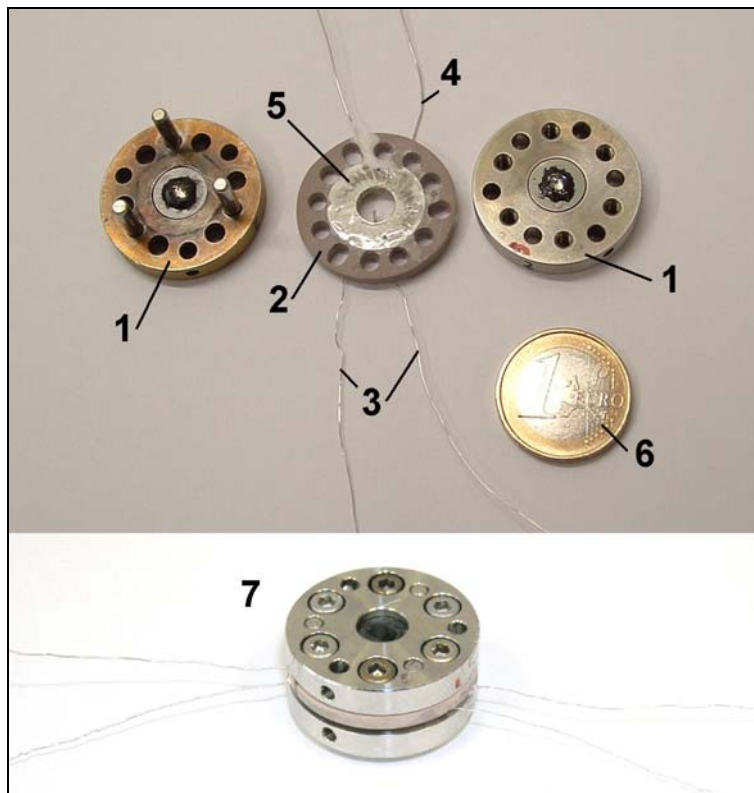


Fig. 2.6. Heating assembly for high P, T Mössbauer measurements: 1 – diamond anvil cell, 2 – ceramic (pyrophyllite) heater, 3 – thermocouple, 4 – platinum wires, 5 – mica for electrical isolation, 6 – one Euro coin for scale, 7 – entire assembly.

The gasket material was chosen to be rhenium for its stable mechanical properties. A rhenium gasket, in contrast to the commonly used steel gaskets for “medium” pressure range studies, does not contain iron and would not contaminate ^{57}Fe Mössbauer spectra.

Cryogenic gas loading

The most favorable conditions for the high-pressure experiments are so-called hydrostatic conditions. If a sample is immersed in a gas or liquid, external pressure is homogeneous and is truly a classical thermodynamic parameter. In the case of hydrostatic conditions no additional stresses develop in the sample; single-crystals are not destroyed within the stability field of the material, etc. In order to produce hydrostatic conditions in the diamond anvil cell a pressure-transmitting medium should be used. Up to now the highest known solidification pressure at room temperature is around 11-12 GPa (for mixtures of ethanol, methanol and water or for liquid helium), if we consider materials that can be used in the DAC. In this pressure range hydrostatic experiments are conducted routinely. The simplest and cheapest is the usage of an ethanol:methanol:water mixture in the proportion 16:3:1. The main disadvantage of alcohol-based mixtures is their temperature instability – upon heating: even to several hundred degrees they can decompose or react with the sample and gasket material. In a solid material stress introduced by the diamond anvils produces non-homogeneous strains, depending on the elastic properties of the material. If the pressure transmitting medium is a polycrystalline material, the non-hydrostatic uniaxial stress it transmits to the sample depends mostly on the shear modulus of the pressure transmitting medium. There are a variety of materials with relatively small shear moduli, such as solid helium and other noble gases, nitrogen, oxygen, and alkali halides (NaCl, KBr, LiF and so on). Experiments with solid helium or neon are often called quasi-hydrostatic experiments (sometimes the term “hydrostatic” is misused in the literature, since above approximately 12 GPa helium is no longer liquid at room temperature). Gases cannot be loaded in the DAC in an appropriate amount, and should be either compressed or liquefied to fill the sample chamber so that the sample is immersed in liquid or compressed gas. In order to load helium or neon high-pressure bombs are used, but argon, oxygen and some other gases can be loaded using cryogenic liquefying. The simplest cryogenic gas-loading device is shown in Fig. 2.7. When the DAC is prepared and the sample is loaded in the sample chamber, the cell is opened by 10-20 μm and is placed inside an aluminum or copper vessel. The vessel is closed hermetically with a transparent plastic cover and an O-ring. Argon or other gas flows through a gas feed connector in the side part of the vessel. Everything is then placed in an open

reservoir filled with liquid nitrogen. Upon vessel cooling Ar slowly condenses, and the vessel is filled with the liquid. During slow gas condensation there are no strong turbulence flows in the liquid, and therefore no risk of losing the sample or ruby chips from the sample chamber. The process is controlled visually through the upper transparent cover. When the vessel is filled with liquid, covering the whole DAC, the upper cover is opened and the DAC screws are tightened to trap the liquid medium inside the sample chamber. Then the DAC can be warmed up and ready for further compression.

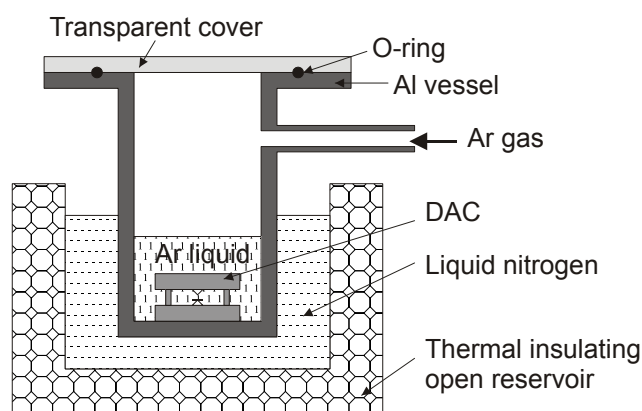


Fig. 2.7. Cryogenic liquid-gas loading device.

Pressure measurements

There are several methods to measure pressure inside the DAC. Usually pressure is determined indirectly using some known pressure standard. In the case of an X-ray diffraction study, almost any material with a known equation of state could be used as an internal pressure standard. The overlapping of X-ray diffraction peaks of the sample and pressure medium should be avoided, so usually high-symmetry cubic materials are used, such as gold, platinum, sodium chloride, etc. For many of these pressure calibrants thermal equations of state are determined, so pressure can be calculated easily from the known temperature and lattice parameters of the material. However, X-ray diffraction is not always available, and the most fast, simple and widely used method is the ruby fluorescence pressure scale. Ruby (Cr-doped Al_2O_3) has a very strong luminescence with two main peaks (R_1 and R_2), Fig. 2.8.

Upon compression fluorescence lines shift to higher wavenumbers. In a hydrostatic or soft pressure medium the lines remain relatively narrow and clearly distinguishable. There is also a rapid intensity growth of the R_3 line, and above 100 GPa it could become dominant in the

spectra. Ruby can be loaded as a powder, a small piece of a single crystal or a small sphere. Ruby spheres of 1-5 μm in diameter are available commercially and show very homogenous chromium distribution and strong fluorescence spectra. Ruby spheres should not be bridged between two diamonds or between the sample and the diamonds, because in this case the spectrum shape is strongly distorted and pressure determination is no longer reliable. The best recommendation is the usage of several as small as possible ruby spheres, placed in different parts of the sample chamber. In such a design not only the average pressure, but also the radial pressure gradients can be monitored.

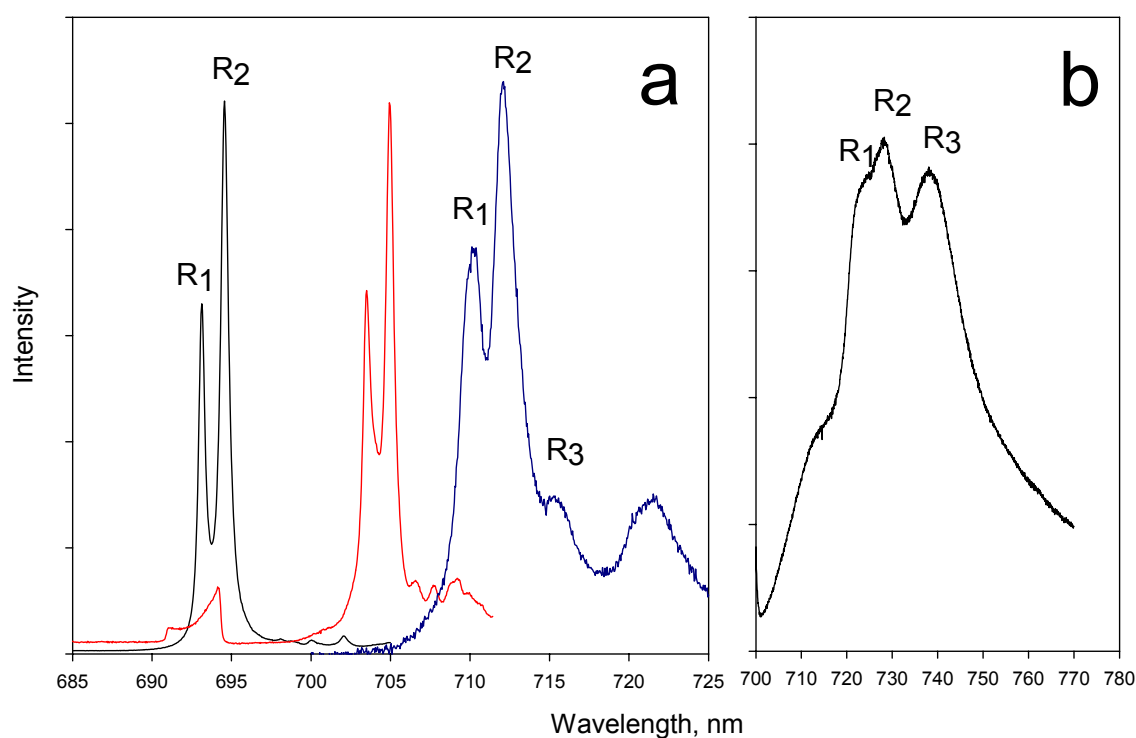


Fig. 2.8. Ruby fluorescence spectra. a) – spectra recorded at ambient pressure (black), 30.4 GPa (red) and 51.6 GPa (blue) in a soft (LiF) pressure medium. b) – ruby spectra at 102 GPa in strongly non-hydrostatic MgO pressure medium.

The pressure dependence of the R_2 line position was calibrated several times, using the functional form

$$P(\text{GPa}) = (A/B) \left[\left(\frac{\lambda}{\lambda_0} \right)^B - 1 \right] \quad (2.1),$$

where λ and λ_0 are measured under pressure P and at ambient pressure for the R_2 line position; and A and B are refined coefficients. The absolute value of λ could vary for different ruby crystals, depending on the total chromium concentration. The classical ruby pressure

scale was determined by Mao and co-authors (Mao et al., 1986) using the gold equation of state, with $A = 1904$ and $B = 5$ for non-hydrostatic conditions and $B = 7.665$ for quasi-hydrostatic conditions (He pressure medium), Fig. 2.9. Recently this scale was refined by Zha et al. (2000) using MgO Brillouin scattering combined with single-crystal X-ray diffraction measurements, which is truly a primary pressure scale. The refined value of B was 7.715; virtually the same as given by Mao et al. (1986), Fig. 2.9.

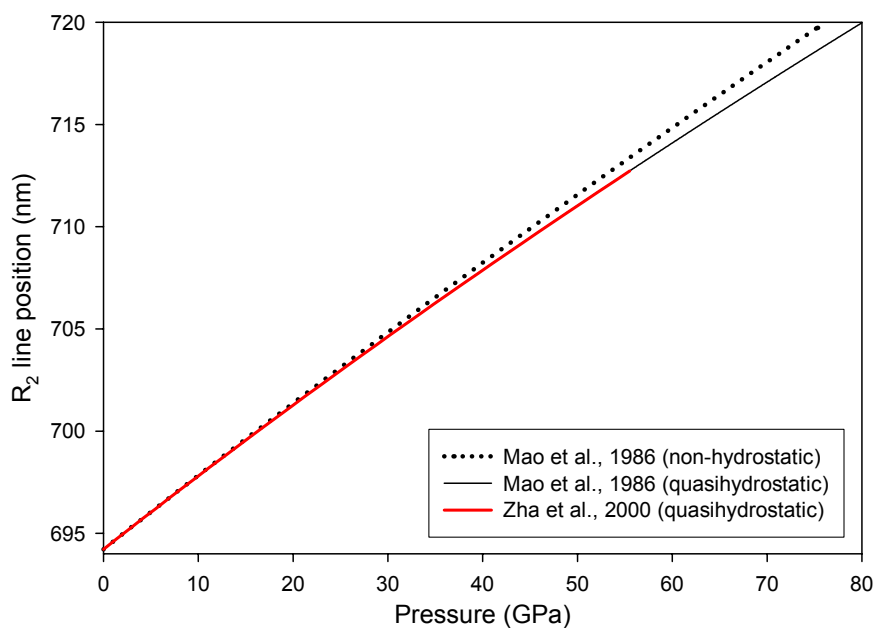


Fig. 2.9. Pressure dependence of the R2 ruby fluorescence line. Dotted line – non-hydrostatic scale of Mao et al. (1986), black solid line – quasi-hydrostatic scale of Mao et al. (1986); red line – refined quasi-hydrostatic scale of Zha et al. (2000).

The internal precision of the ruby pressure scale is quite high, and its fluorescence spectra also contain information concerning uniaxial non-hydrostatic stresses in the sample chamber (line width, $R_1/R_2/R_3$ intensity ratio, and so on). Ruby fluorescence is also temperature dependent, and temperature corrections should be applied for high- or low-temperature measurements. There are several studies of the temperature correction (Vos and Schouten, 1991; Rekhi et al., 1999) under ambient pressure. One of the most important future developments of the ruby pressure scale is to perform simultaneous high-pressure and high-temperature calibration to obtain more realistic temperature correction under high pressure.

X-ray diffraction

X-ray diffraction is the most direct and widely used technique for crystal structure probing of the material. X-rays are scattered elastically by electrons, and in the case of

regular three-dimensional atoms arrangements a diffraction pattern is produced. X-ray diffraction occurs whenever Bragg's law is satisfied:

$$2d \sin(\theta) = \lambda \quad (2.2);$$

where d is the interplanar distance, λ is the X-ray wavelength and θ is the half angle between the initial and diffracted beams. It is obvious that every regular atomic plane would give a diffracted X-ray beam and that crystallites should be in a special orientation with respect to the initial beam. In the case of single-crystal diffraction using a monochromatic X-ray beam, the crystal should be rotated on a goniometer in order to collect all possible reflections. In the case of a powder sample there are always some crystallites in the diffraction position, and the diffracted beam forms a cone (Fig. 2.10).

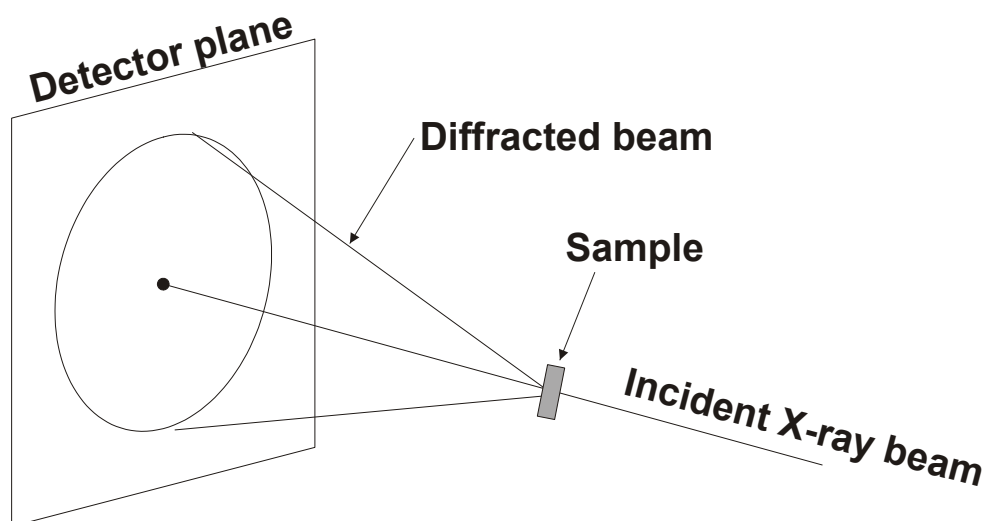


Fig. 2.10. Basic principle of monochromatic (angle-dispersion) powder diffraction. In the case of the detector plane normal to the initial beam, the diffraction peak forms a circle (Debye-Scherrer ring), while in the case of any inclination, the diffraction peak forms an ellipse.

Single-crystal diffraction in the DAC is restricted to hydrostatic conditions and to the phase under investigation being in its stability field. Under non-hydrostatic conditions a single crystal becomes a mosaic and is eventually destroyed, and pressure-induced phase transitions also usually destroy single crystals. For this reason in the present study only powder X-ray diffraction was employed. Diamonds are almost transparent to X-rays, but the diamond support seats are usually not transparent, and the opening angle of seats and DACs limits the maximum 2θ angle. From Bragg's equation it is obvious that short wavelengths should be used in order to observe the maximum number of reflections in the limited 2θ range. The conventional X-ray source (X-ray tubes or rotating anode machines) wavelength

is the characteristic emission of the anode material, and Mo radiation with the shortest wavelength ($\lambda = 0.71 \text{ \AA}$) is often used. Synchrotron radiation sources have many clear advantages with respect to conventional sources. First, the intensity of the X-ray beam is higher by several orders of magnitude, which allows very short exposure time (seconds) even for extremely small samples. Second, the wavelength can be tuned to the desired value and the X-ray beam can be strongly focused. Nowadays on high-pressure diffraction beamlines at synchrotrons a wavelength of about 0.4 \AA is used and the initial beam is focused to about 10 \mu m FWHM. As a detector a charge-coupled devices (CCD) or image plates are usually used. CCD scanning time is much shorter, but the total resolution and dynamical range is poor with respect to the image plates. Probably the best commercially available image plate is the MAR345 detector with a plate of 300 mm in diameter. An example of a raw MAR image is shown in Fig. 2.11.

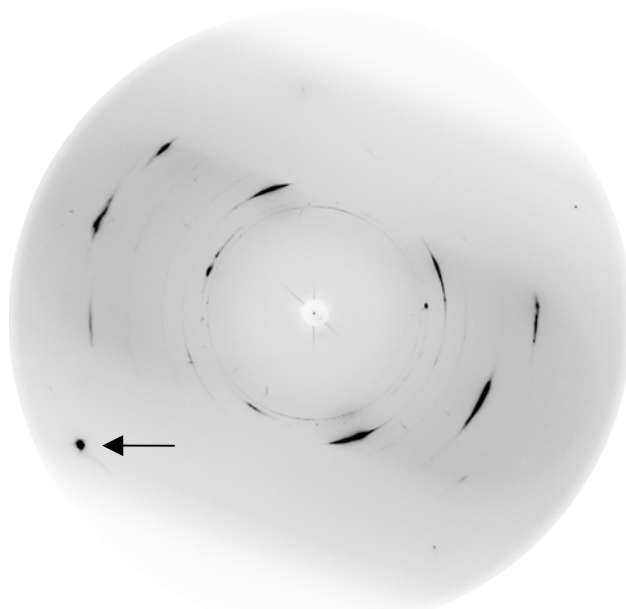


Fig. 2.11. An example of a MAR345 X-ray diffraction image of the sample in the DAC. A rectangular shadow from the diamond seats and dark diffraction spot from the diamonds (shown by an arrow) are seen.

The raw image is further transformed to the ordinary one-dimensional powder diffraction pattern using the Fit2D software. It applies geometry and intensity corrections, allows the masking of some areas (for example, diamond diffraction spots), and much more. The obtained powder diffraction pattern can then be analyzed as an ordinary pattern: lattice parameters of the sample can be extracted, and a full-profile model refinement (Rietveld or Le Bail method) can be applied. There are several peculiarities of powder diffraction under high pressures. First is poor crystalline statistics. The sample is usually very small, and the number of irradiated crystallites could be relatively small (if the powder is not fine-grained).

As a result, the intensity distribution over the Debye-Scherrer ring is not smooth, but spotty. Second, there is a strong preferred orientation. Under non-hydrostatic conditions individual crystallites tend to adopt special orientations with respect to the main stress direction (usually the loading direction of the cell). This results in the changing of the relative intensities of different diffraction rings and in non-uniform intensity distribution along a single ring. Due to pressure gradients and non-uniform stresses in the crystallites, diffraction lines can be significantly broadened and individual lines are often non-resolved. Moreover, due to elastic anisotropy of the material, different crystallites experience different deformation, and different diffraction line positions slightly deviate from their ideal positions, calculated from the lattice parameters. All these factors could significantly complicate full-profile or intensity analysis of the diffraction patterns.

Neutron diffraction

The basic principle of neutron diffraction is generally similar to X-ray diffraction. The main difference is that neutrons are scattered by the neutrons in the atomic nuclei, and therefore the neutron diffraction pattern reflects the three-dimensional arrangement of atomic nuclei. For example, hydrogen ions are almost invisible for X-ray diffraction, but can be easily located in the crystallographic unit cell by means of neutron diffraction. Another very important difference between X-ray and neutron diffraction is that neutron scattering is sensitive to the spin orientation of neutrons in nuclei. In the case of magnetically ordered compounds, the electron density of spin-up and spin-down atoms are equal, but magnetic neutron scattering amplitudes are not. The main consequence is the appearance of superstructural diffraction reflections that characterize the magnetic ordering of the material. Neutron diffraction is probably the most direct method for probing the magnetic structure of the material (Shull et al., 1951).

In order to get a neutron beam, a neutron source (reactor) is necessary. There are many difficulties with transmitting, reflecting and focusing of neutrons, because they are not charged and do not interact with magnetic or electric fields, unlike electrons. The main experimental challenge for high-pressure neutron diffraction studies is to produce small and intense monochromatic beams. Some of these problems could be solved with different efficiency, and neutron beams of several millimeters in diameter are probably the best that can be obtained today. The sample volume should be much higher compared to X-ray diffraction, so generally only lower pressures can be reached in neutron diffraction experiments. Coherent neutron scattering amplitude has no simple z-number dependence; for

example hydrogen scatters much better than oxygen or magnesium. Even neighboring chemical elements (like Mn and Fe) can have significantly different scattering amplitudes and therefore diffraction peak intensities from the same sample volume.

An example of high-pressure powder neutron diffractometer G6.1 at Laboratoire Léon Brillouin (LLB) is shown in Fig. 2.12. A monochromatic neutron beam is selected by a graphite monochromator. The typical incident wavelength is 4.74 Å. The contamination of the second harmonics ($\lambda/2$, $\lambda/3$, ...) is suppressed by inserting a beryllium filter (cooled down to liquid nitrogen temperature) in the incident beam path. The diffractometer is equipped with a linear (banana-type) 400-cell multidetector covering 80 degrees of scattering angle. The multidetector and its protection can rotate around the sample axis, covering a total angle of 150 degrees. A special design piston-cylinder sapphire anvil cell can be cooled down to 1.5 K in a liquid helium cryostat (Goncharenko, 2004). The typical scattering sample volume of the studied oxides is several mm^3 , and the highest possible pressure is limited to ~ 12 GPa.

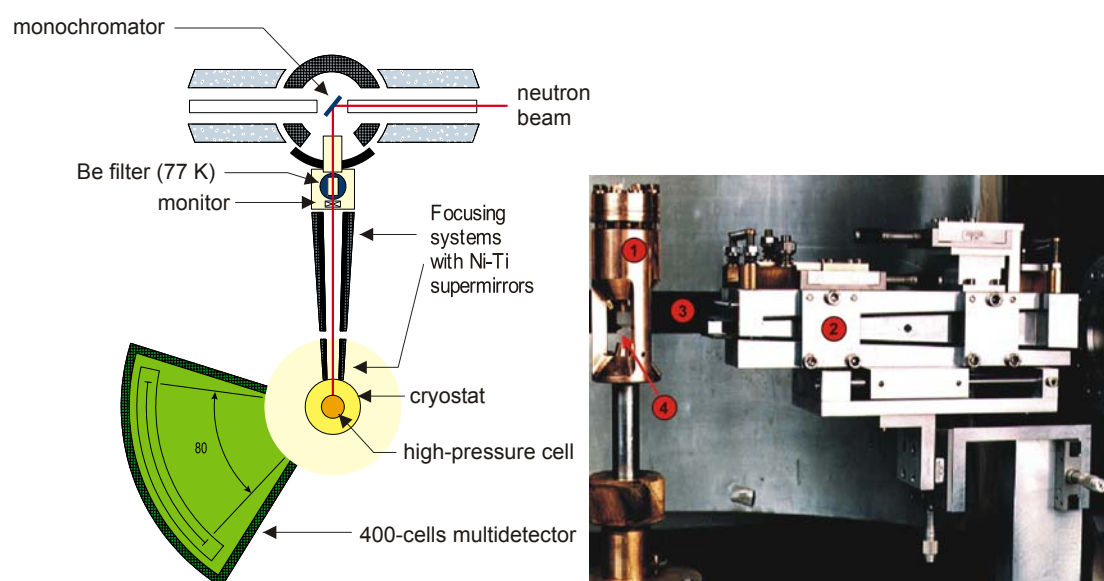


Fig. 2.12. Schematic layout of the cold-neutron G6.1 powder diffractometer at LLB (top view), compatible with the high-pressure cells. At the right is the photo of the high-pressure neutron diffraction setup (horizontal view): 1 – piston-cylinder sapphire anvil high-pressure cell, 2 – focusing system, 3 – linear multidetector, 4 – sapphire anvils with the sample in between.

X-ray absorption spectroscopy

X-ray absorption spectroscopy (XAS) has found extensive application in determining the local atomic and electronic structure of the absorbing centers (atoms) in materials science, physics, chemistry, biology, and geophysics. Rapid advance in the XAS method is caused by appearance of synchrotron sources, as well as by considerable achievement in the theory and its practical realization. XAS can provide information that substantially complements the results of other experimental methods, such as the diffraction (scattering) of x-rays and neutrons, photoelectron, and emission x-ray spectroscopy. The basic XAS advantages are (i) selectivity in the chemical-element type (in some cases, also in the location of an element in a material), which enables one to acquire information on pair and multiatomic distribution functions for the local environment of each element of the material under investigation; (ii) sensitivity to the partial densities of vacant states near the Fermi level; (iii) high density sensitivity (10–100 particles per mole) and relatively short times (from milliseconds to tens of minutes) of detecting experimental spectra when synchrotron radiation is used; and (iv) a small required sample volume.

When x-rays of energies close to the electron binding energies are absorbed, features known as absorption edges are observed. The typical x-ray absorption spectrum for the iron K edge in a (Mg,Fe)O polycrystal is shown in Fig. 2.13. It exhibits an oscillating fine structure, which extends far from the absorption edge. For convenient interpretation, two regions are often separated in the absorption spectra: (i) the x-ray absorption near-edge structure (XANES), and (ii) the extended x-ray absorption fine structure (EXAFS). It is agreed that the XANES region extends for 50-100 eV beyond an absorption edge and is determined by the local density of vacant states in an absorbing atom, as well as by multiple-scattering effects, i.e., scattering of an excited photoelectron on several atoms. The EXAFS region is dominated by single scattering processes and extends up to 2000 eV from an edge. Its upper bound is determined by the signal-to-noise ratio and/or another absorption edge (Aksenov et al., 2001).

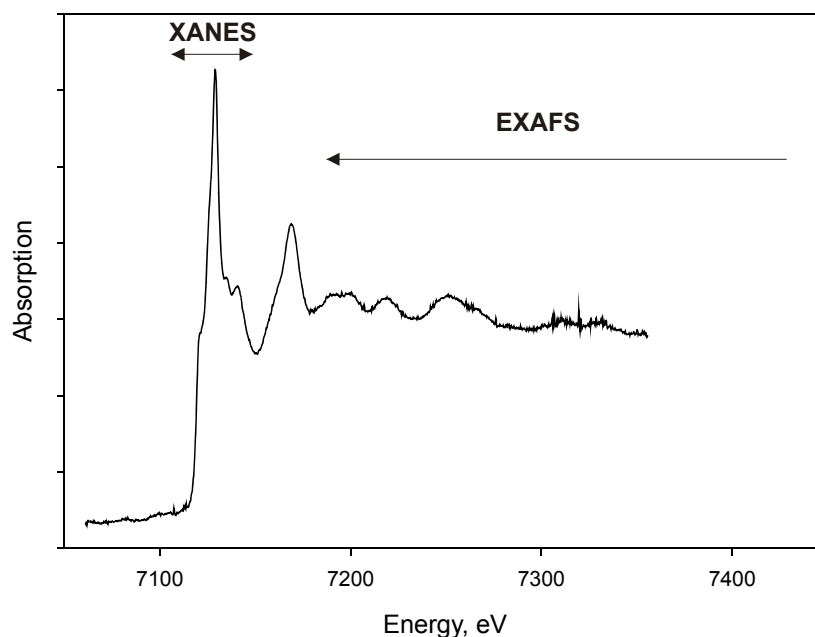


Fig. 2.13. Fe *K*-edge X-ray absorption spectrum of (Mg,Fe)O powder sample. XANES and EXAFS regions are shown.

The EXAFS part of the spectrum contains information of the local structure around the absorbing atom, and a radial distribution function can be obtained via Fourier transform and model fitting EXAFS analysis. Under high pressures in the DAC in our experiments only the XANES part of the spectra were good enough, while the EXAFS part was too noisy for qualitative analysis. The XANES part of a spectrum contains information on the electronic structure of the absorbing atom, covalency of the chemical bonding with the nearest ligands, and characteristics of the coordination polyhedron. The only problem is that all this information could not be extracted directly from the XANES spectra, and mostly the comparison between XANES spectra and theoretical calculations was performed in order to determine possible structure or electronic transformations in the material. All XANES spectra presented in this study were collected at ID24 of the ESRF.

Mössbauer spectroscopy

The Mössbauer effect is the recoilless nuclear resonant absorption of γ -rays. When a gamma-quantum falls to the nucleus and its energy exactly coincides with the energy level difference of two nuclear energy states, it can be absorbed and the absorbing nucleus would be transformed to its excited state. The measured resonance absorption line position therefore gives directly the energy difference between the different nuclear levels, characterizing many

important properties of the absorbing atom from hyperfine parameters. If nuclear recoil occurs during absorption, no resonance is possible. The probability f that no lattice excitation (energy transfer) takes place during the γ -emission of absorption process is called the recoil-free fraction. It is given by

$$f = 1 - k^2 \langle x^2 \rangle \quad (2.3);$$

where $\langle x^2 \rangle$ is the expectation value of the squared vibrational amplitude in the x -direction and k is the propagation vector. The recoil-free fraction in Mössbauer spectroscopy increases with decreasing recoil energy, decreasing temperature and increasing Debye temperature Θ_D . Stronger absorption is observed at lower temperatures (and from the temperature changes of the recoil-free fraction the partial (Mössbauer) Debye temperature can be calculated), and materials with stronger bonding have stronger absorption. The f parameter is also called the Debye-Waller factor or the Lamb-Mössbauer factor. The characteristic f value for the ^{57}Fe 14.4 keV gamma transition (the most popular Mössbauer transition) is about 0.91. Another important application of the recoil-free fraction is that f vanishes to zero in a liquid or gaseous state, and melting could be in principle determined by the disappearance of the Mössbauer absorption spectrum.

In order to observe resonant absorption, the energy of the initial γ -quantum should exactly match that of the absorbing nucleus. The natural line width of the nuclear transition is so small (for ^{57}Fe it is about 4.5×10^{-9} eV) that only the excited atom of the same kind (not only the same element, but the same isotope) could be a source for Mössbauer spectroscopy. This is a general limitation of MS applications. The excited nucleus can be formed during radioactive decay. For example, radioactive ^{57}Co produces a proton and ^{57}Fe in the excited state after decay. Therefore, the ^{57}Fe Mössbauer effect can be studied. The parental isotope should be on the one hand sufficiently radioactive to produce enough intensity of the γ radiation, and on the other hand it should not have too short a half life. Among geologically relevant elements, there are several Mössbauer isotopes (^{57}Fe , ^{119}Sn , ^{197}Au and some others), but ^{57}Fe is the most popular. Its excited lifetime is not too long and the transition width is sufficient, f is usually quite large, and a ^{57}Co source has a half-life of approximately 6 months, making experiments and source operations (production, transportation) relatively simple. Fe is also the most important element in the Earth that can adopt different valence, electronic and magnetic states, making Mössbauer spectroscopy a unique instrument for the geosciences.

As mentioned above, the initial γ -quantum energy should almost exactly coincide with the energy transition in the absorbing nucleus, but this is usually not the case, since emitting and absorbing atoms can be in a different valence, magnetic state and in different crystallographic positions. In order to tune the source energy within certain limits, a Doppler effect is applied. If the source is moving towards or backwards relative to the absorber, energy shifts to a higher or lower value. By recording transmission as a function of Doppler velocity of the source, a Mössbauer spectrum can be recorded. The number and position of the absorbance peaks is defined by the hyperfine parameters of the studied material. They are centre shift, quadrupole splitting and hyperfine magnetic field.

There are always electrostatic Coulomb interactions between the nuclear charge and electrons inside the nucleus volume. The major contribution comes from the inner s -electrons, and the s electron density on the core produces an energy shift, which is called the isomer shift δ . The origin of the isomer shift is shown in Fig. 2.14. The relationship between s -electron density and isomer shift is given by

$$\delta = \frac{2}{3} \pi Z e^2 \left\{ |\psi_s(0)_E|^2 - |\psi_s(0)_A|^2 \right\} \left\{ \langle R_e^2 \rangle - \langle R_g^2 \rangle \right\} \quad (2.4)$$

where $\langle R_g^2 \rangle$ and $\langle R_e^2 \rangle$ are the mean squared radii of the ground and excited nuclear states, $|\psi_s(0)_E|^2$ and $|\psi_s(0)_A|^2$ are the electron densities at the emitting and absorbing nuclei and Z is the atomic number (Greenwood and Gibb, 1971).

The electric monopole interaction does not change the degeneracy of electron levels, and in the case of pure monopole interactions there is only one absorption line in the Mössbauer spectrum.

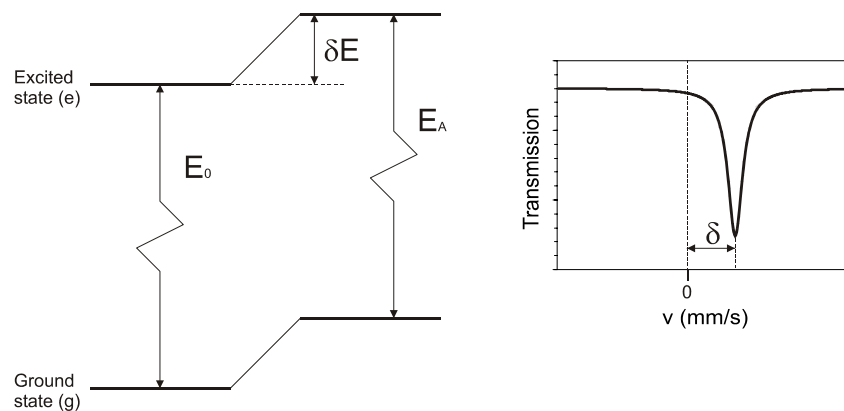


Fig. 2.14. Origin of the isomer shift. Electric monopole interaction between the nuclear charge and electrons at the nucleus shifts nuclear energy levels without changing the degeneracy. At the right a schematic of the resulting Mössbauer spectrum is shown.

The isomer shift depends on the valence and spin state of iron, and also on the sample density, so it should also vary with changing pressure and temperature due to compression and thermal expansion. At non-zero temperatures there is also another contribution to the Mössbauer spectrum. Due to thermal motions of the atoms, a second-order Doppler shift (SOD) also occurs, and is added to the source Doppler velocity. By definition the SOD energy shift is given by

$$\frac{\delta E}{E} = -\frac{\langle v^2 \rangle}{2c^2} \quad (2.5),$$

where $\langle v^2 \rangle$ is the mean square particle velocity. It depends on the absolute temperature and Debye temperature of the solid. The experimentally measured quantity (energy shift of the absorbance peak) is therefore a sum of the isomer shift δ and the second-order Doppler shift SOD. This sum is called the centre or chemical shift CS. Usually at room temperature the SOD is almost identical for different compounds, and differences in CS are assumed to be equal to the differences in δ . A large database of CS values for different iron compounds is available, and possible CS ranges for different spin and valence states of iron are defined (Gütlich et al., 1978; Greenwood and Gibb, 1971). The obtained CS value is given in units of Doppler velocity, and usually its value is given with respect to the CS of a standard, normally α -Fe under ambient conditions.

A nucleus that has a spin quantum number $I > \frac{1}{2}$ has a non-spherical charge distribution. The magnitude of the charge deformation is called Q , and it is negative when the nucleus is flattened (pancake-like shape) and positive when the nucleus is elongated (cigar-like shape) along the spin axes. If the charge distribution around the nucleus is asymmetric, it produces an electric field gradient (EFG) ∇E . An interaction between the nuclear moment and ∇E produces quadrupole splitting in the nuclear energy levels (Fig. 2.15). It is important to note that a quadrupole interaction occurs only when the EFG is non-zero; the nuclear moment itself is not enough. The absolute value of the quadrupole splitting can be calculated theoretically with the different degrees of accuracy, but generally its changes with temperature, electronic state, ligand coordination and so on are not obvious. Isomer shift, central shift and quadrupole splitting are given in the units of Doppler velocity; normally in mm/s.

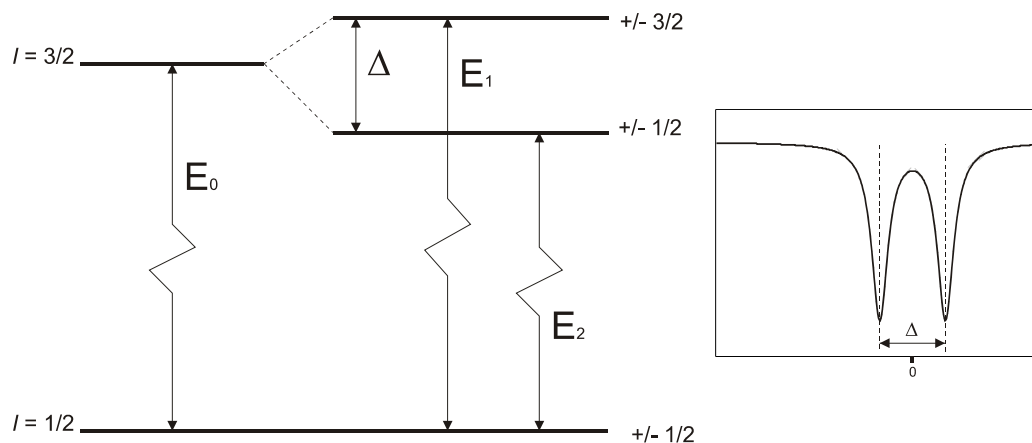


Fig. 2.15. Origin of quadrupole splitting in the Mössbauer spectrum (shown at the right).

Magnetic hyperfine splitting is caused by the dipole interaction between the nuclear spin moment and a magnetic field. The effective magnetic field experienced by the nucleus is a combination of fields from the atom itself, from the lattice through crystal field effects and from external applied fields. The hyperfine magnetic field removes the energy level degeneracy, giving rise to a total of 6 non-equivalent levels (Fig. 2.16). Taking into account the selection rule $\Delta m_I = 0, \pm 1$ for the transition, there are a total of six lines in the Zeeman split spectrum. The intensity of each line depends on the probability of a corresponding transition, and for a randomly oriented powder the peak intensities ratio should be 3:2:1:1:2:3. In the case of preferred orientation or external applied field the relative intensities can change. Magnetic or Zeeman splitting is given either in mm/s, or as a value of magnetic hyperfine field B_{HF} in Tesla. Units conversion for the ^{57}Fe Mössbauer transition is $1 \times (\text{T}) = 0.06897 \times (\text{mm/s})$. In a real material all contributions can occur at the same time (isomer shift, SOD, quadrupole splitting and hyperfine Zeeman splitting).

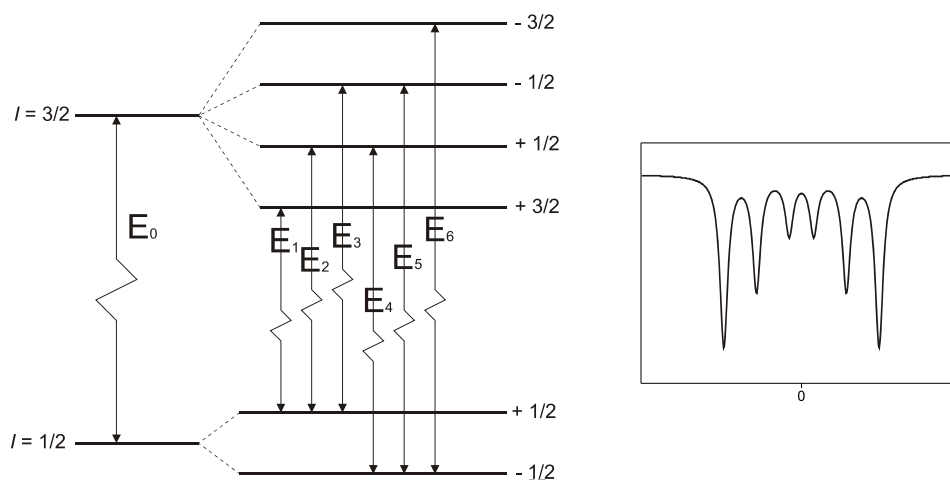


Fig. 2.16. Hyperfine Zeeman splitting of ^{57}Fe nuclear levels. At the right the schematic Mössbauer spectrum is shown.

There are several additional factors that contribute to the Mössbauer spectrum. First is the geometry effect. The source moves relative to the sample, and at some moments it is closer to the detector, while at others it is more distant. As a result the total intensity varies in a sine-like way as a function of the channel number. Normally the analyzing software routinely corrects for this effect during spectrum folding. Another important contribution is the thickness effect. Since the sample has a finite thickness, there are a finite number of Fe atoms in the path of the gamma quanta. It can undergo multiple absorption events, and the probability of additional absorption in the given energy range (counter channel) is proportional to the number of quanta passing through the sample. The thickness effect makes strong peaks look smaller and small peaks look stronger. It also results in a more Gaussian contribution to the nominally Lorentzian shape of the absorption peaks, and increasing width of the resonance lines. The thickness effect can be corrected using a full transition integral analysis, which is incorporated into many of the Mössbauer analysis software packages. In order to account for this effect properly, the knowledge of sample thickness, composition, iron content and ^{57}Fe isotopic content are necessary. Fortunately, the thickness effect in conventional Mössbauer spectroscopy does not affect hyperfine parameters of the spectrum (centre shift, quadrupole splitting and hyperfine magnetic field). If the ratio between different subspectral components is not important, the full transmission integral analysis is not strictly necessary, and a simple Voigt function for the line shape can be applied to better match the experimental spectrum.

A typical Mössbauer spectrometer consists of three principal parts: vibrating drive with the ^{57}Co source, sample holder and the detector. In the DAC the sample size is extremely small, and therefore the radiation source should also be small (Fig. 2.17). I used a so-called “point” high-specific activity source of ^{57}Co in a Rh-matrix. The source size is 0.5x0.5 mm, and it is usually placed as close as possible to the outer diamond surface of the DAC. The samples for the high-pressure DAC studies should be enriched with ^{57}Fe , especially in low-Fe containing materials.

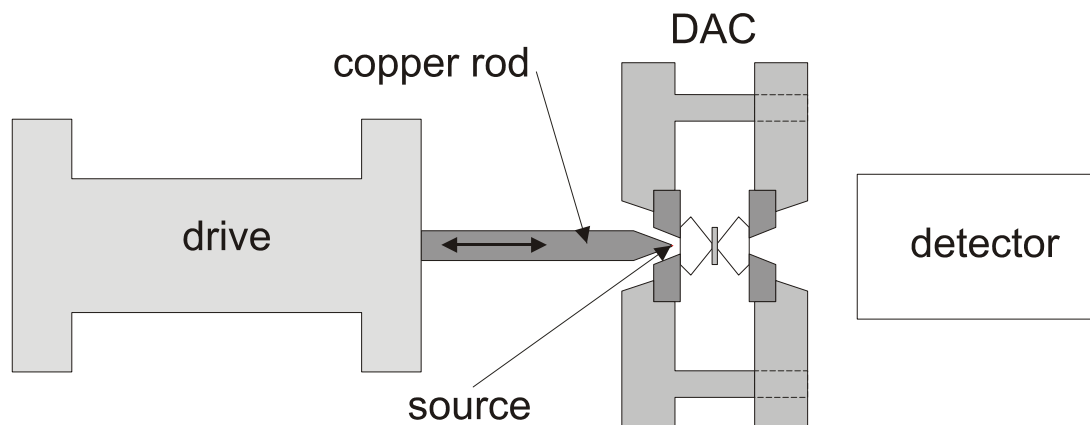


Fig. 2.17. Schematic layout of a high-pressure Mössbauer spectrometer.

Theoretical *ab-initio* calculations

The main task of any theoretical science is the explanation of known and the prediction of unknown facts. For crystal chemistry this is the task of predicting structure, properties, and stability fields of all possible modifications for a given compound. The last 20 years have seen an enormous progress towards this goal, yet we are still far from it. Nearly all modern methods start with a given topology of the crystal structure, which is then refined to the theoretically optimal structure. Knowing just the structural topology, for most compounds it is possible to accurately predict many properties and behavior at high pressure (and in some cases at high temperature). There is a huge variety of theoretical methods for such calculations, and they can be divided into (semi-)empirical and *ab-initio* methods. Any computer simulation is based on some physical and mathematical model. Some models have an empirical base. Such models include some potentials or equations that require parameterization. A typical example is pair-potential simulation methods, when a matter (gas, liquid or solid, crystalline or amorphous) is considered as a combination of particles with some effective potentials of interactions. These pair- or many-body potentials include some empirical coefficients. The latter could be determined in many ways (Urusov and Dubrovinsky, 1989); for example to reproduce experimentally observed physical properties of a compound. The major problem of semiempirical methods is the extrapolation of the model to the conditions outside the range for which the model was parameterized. The other group of methods does not require any “external” data for parameterization allowing calculations *ab initio* (from first principles). The overwhelming majority of physical properties of matter are controlled by electronic interactions, and nuclear processes are

negligible. A single electron is described exactly with the Schrödinger equation. The Hamiltonian of the wavefunction for a many-electron system is explicitly difficult for calculations, making a pure many-electron solution of the Schrödinger equation practically impossible. Different quantum-mechanical methods choose different ways of approximating the Hamiltonian and representing the wavefunction. All modern computational methods are based on approximate one-electron theories, reducing the total Hamiltonian to a set of similar coupled equations for separate one-electron orbitals. Apart from making the wavefunction tractable, one-electron theories gain another advantage: they yield one-electron energy spectra, which enable an understanding of chemical bonding and give a first approximation to the excitation spectra. In many respects, one-electron theories can be exact. A great breakthrough in computational physics and chemistry occurred with the appearance of density functional theory (DFT). It formulates quantum mechanics in terms of the observable and tractable electron density instead of the extremely complicated and unobservable wavefunction. Currently DFT is the main method used in quantum-mechanical studies of solids. The most impressive achievements of computational mineral physics are associated with DFT. Hohenberg and Kohn (1964) and their followers formulated and proved two remarkable theorems:

- The electron density $\rho(r)$ determines (within an additive constant) the external potential, i.e., the potential due to the nuclei.
- In the ground state the total energy of a system varies with respect to the electron density, i.e., the exact $\rho(r)$ provides the minimum possible energy for the ground state.

The only remaining problem is the consideration of exchange correlations between individual electrons. There are several widely used approximations of the DFT. The simplest is the local density approximation (LDA). Briefly, it considers all electrons in the system as a homogeneous electron gas, and the total electronic density at a given point is an effective value for the exchange effect on the given electron. This approximation does not give accurate exchange-correlation holes for atoms, but gives reasonable spherical averages for these holes – luckily, it is only the spherically-symmetric part of the multipole expansion that is important. The shortcomings of the LDA include the following:

1. Underestimation of the energies occurs in isolated atoms – LDA treats well the valence electrons, but significantly underbonds the core electrons,
2. Overbonding (by ~20%) occurs in molecules and crystals,
3. Bond lengths are usually ~1% too short,

4. Reaction barriers are usually too low compared to experiment,
5. Large errors occur for weakly bonded systems (e.g., hydrogen bonds),
6. van der Waals bonding cannot be treated correctly within the LDA,
7. Sometimes the energy difference between polymorphs are inaccurate,
8. Often a wrong ground state is predicted,
9. Serious errors occur for many Mott insulators,
10. In many cases, the dissociation products are not neutral atoms, but atoms with non-physical fractional charges.

The most obvious way to construct an improved function is to expand the exchange-correlation energy in powers of the density gradients, which is the main feature of the generalised gradient approximation (GGA). GGA is constructed in such a way as to preserve all the correct features of the LDA and add some more. There are several popular GGA functions, the best of which seem to be the PW91 function (Wang & Perdew, 1991) and a very similar function PBE (Perdew et al., 1996). GGA significantly improves the description of atomic core electrons and to some extent the valence electrons as well. Exchange energies of atoms are reproduced with a typical error of only 0.5%; the typical error for the correlation energy is 5%. The main faults of the GGA approximation are the following:

1. Bond lengths are usually overestimated by ~1%,
2. Like in the LDA, but less often, the electronic ground states of atoms, molecules, and solids can sometimes be incorrect,
3. Sometimes the energy differences are incorrect,
4. GGA is particularly inaccurate for the heavy transition metals (e.g., Au). For bond lengths the GGA ‘overcorrects’ the LDA (Oganov, 2002).

For some compounds with strong correlations (a typical example is FeO), neither LDA nor GGA gives satisfactory results, and even the ground state is not reproduced correctly. They predict an antiferromagnetic, metallic ground state for FeO; whereas it is actually an insulator with an optical band gap of 2.4 eV (Bowen et al. 1975). This discrepancy arises from the fact that the local Coulomb repulsion is not taken explicitly into account in LDA and GGA methods, and is therefore underestimated. The LDA+U or GGA+U method (Anisimov et al. 1991) is designed to remedy this situation through the application of an orbital-dependent potential between correlated states, and then subtraction of a correction for the double-counting of these interactions. This approach reproduces high-pressure properties, and gives insulating behavior in reasonable agreement with experiment. There are several functional forms to include exchange interactions, among which the

Dudarev approach (Dudarev et al. 1998) is the most useful, since it treats only a single parameter instead of two (exchange integral J and exchange energy U). The value of Dudarev's U is estimated to be around 4-5 eV for FeO, based either on reproducing the experimentally observed band gap and ground state, or on some self-consistent methods of U evaluations.

III. Results and discussion

III.1. Phase diagrams of FeO and MnO at moderate pressures: relations between structural and magnetic properties.

Mössbauer spectroscopic studies were carried out on a ^{57}Fe -enriched $\text{Fe}_{0.94(1)}\text{O}$ sample with initial cell dimension $a = 4.307(7)$ Å synthesized by reducing Fe_2O_3 in a gold capsule at 1000°C in a CO-CO_2 gas mixture with $\log(f_{\text{O}_2}) = -14.6$ for 16 h. X-ray and neutron diffraction studies were carried out on a $\text{Fe}_{0.92(1)}\text{O}$ sample with initial lattice parameter $a = 4.2980(3)$ Å synthesized by oxidation of pure iron in a CO-CO_2 gas flowing furnace at 900°C with $\log(f_{\text{O}_2}) = -13.5$. The MnO sample was chemically pure (99.99%) synthetic powder, available commercially.

The magnetic phase boundary in FeO was studied by two techniques – Mössbauer spectroscopy and neutron diffraction, while the structural phase boundary was followed by X-ray diffraction. High-pressure and high-temperature Mössbauer spectroscopic (MS) and X-ray diffraction (XRD) studies were performed in the diamond-anvil cell (DAC), equipped with a miniature resistive internal heater (Kantor et al., 2005-II). Diamonds with culet size of 250-300 μm were used in the experiments. The Re gasket was pre-indented to 20-30 μm and a 125 μm diameter hole was drilled for the sample. In MS experiments liquid Ar was cryogenically loaded as a pressure transmitting medium while NaCl was used in XRD experiments. Angle-dispersive XRD measurements with a 0.3738 Å wavelength were performed at ID27 at the European Synchrotron Radiation Facility. The MAR 345 image-plate system at 324 mm distance from the sample was used as a detector. Data processing was performed using the FIT2D software package (Hammersley et al., 1996). The size of the beam on the sample was approximately 10 μm x 9 μm FWHM. Pure NaCl powder was added to the FeO sample in 1:1 proportion as a pressure transmitting medium and as a pressure calibrating standard (Brown, 1999; Sata et al., 2002).

Powder neutron diffraction studies were performed on a G6-1 cold neutron two-axis diffractometer in Laboratoire Léon Brillouin, Saclay, France. A monochromatic neutron beam was selected by a graphite monochromator with initial wavelength of 4.741 Å. A beryllium filter cooled to liquid nitrogen temperature was used to select the second harmonic with 2.3705 Å wavelength. The diffractometer was equipped with a linear 400-cell BF3 multidetector and a liquid helium cryostat, compatible with the high-pressure cells. High-pressure experiments were performed in a sapphire anvil high-pressure cell (Goncharenko,

2004). The anvil culet size was 3.5 mm. An aluminium gasket was preindented to 0.5 mm and a 1.7 mm hole was drilled. Approximately 5.7 mm^3 of sample powder together with a small amount of ruby powder for pressure calibration was loaded in the sample chamber.

The magnetic (Néel) transition boundary of FeO was tracked by neutron diffraction and MS up to 1100 K and 73 GPa, as is shown in Fig. 3.1. The low-temperature part of the wüstite magnetic phase boundary (up to 5 GPa) was studied by the neutron diffraction technique with three sets of experiments: at ambient pressure, at $3.9(\pm 0.1)$ GPa, and at $5.0(\pm 0.1)$ GPa were performed at various temperatures. One structural diffraction line of FeO (111) and the intense $3/2 \ 1/2 \ 1/2$ magnetic peak below the Néel temperature were observed clearly even at the highest pressure (Fig. 3.2). Since neutron diffraction patterns were collected at different temperatures and constant pressure, estimation of the Néel temperature is quite straightforward – the integrated intensity of the magnetic reflection (which is proportional to total

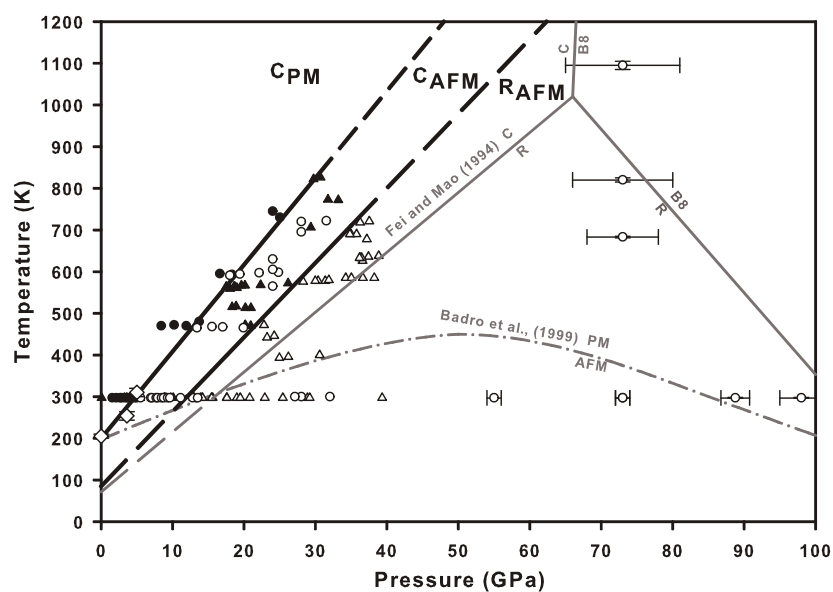


Fig. 3.1. Phase diagram of non-stoichiometric wüstite. Black lines – phase boundaries between cubic paramagnetic (C_{PM}), cubic antiferromagnetic (C_{AFM}), and rhombohedral antiferromagnetic (R_{AFM}) phases obtained in this study. Circles – Mössbauer spectroscopic runs: solid circles – paramagnetic phase, open circles – magnetically ordered phase. Triangles – X-ray diffraction studies: solid triangles – cubic phase, open triangles – rhombohedral phase. Diamonds are Néel temperature values obtained from neutron diffraction studies. The structural phase boundary by Fei and Mao (1994) and magnetic phase boundary proposed by Badro et al. (1999) are also shown for comparison in grey. C, R, and B8 are cubic, rhombohedral and NiAs-like hexagonal phases, respectively, and PM and AFM are paramagnetic and antiferromagnetic phases, respectively.

magnetization M/M_0) is fitted in the vicinity of magnetic ordering to the simple Ising equation

$$\frac{M}{M_0} \sim \left(\frac{T_N - T}{T_N} \right)^{2\beta} \quad (3.1),$$

where T_N , T , and β are the Néel temperature, temperature and empirical exponent parameter, respectively (Fig. 3.2, inset). The Néel temperatures at ambient pressure, $3.9(\pm 0.1)$ and $5.0(\pm 0.1)$ GPa were found to be 201 ± 1 K, 270 ± 10 K and 300 ± 10 K, respectively (diamonds in Fig. 3.1), which supports our linear magnetic phase boundary, obtained from high pressure and temperature Mössbauer studies.

Mössbauer spectra of FeO are not as straightforward to interpret in comparison with neutron diffraction patterns.

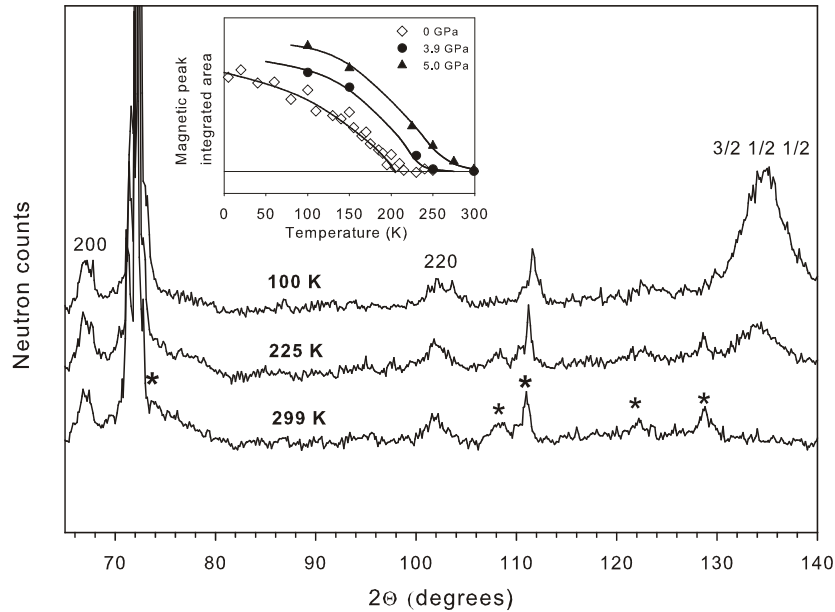


Fig. 3.2. Selected neutron diffraction patterns collected at $5.0(\pm 0.1)$ GPa. Asterisks indicate diffraction lines from the shields and cryostat equipment. Inset – integrated area of the $3/2\ 1/2\ 1/2$ magnetic peak. Diamonds – ambient pressure, circles – $3.9(\pm 0.1)$ GPa, triangles – $5.0(\pm 0.1)$ GPa. Lines are guides for the eye.

Due to the complex defect structure and different local surrounding for different iron ions in the FeO structure, Mössbauer spectra of both paramagnetic and antiferromagnetic states can be analyzed in different ways, implying several subspectral positions (Long and Grandjean, 1991). A typical example is shown of the antiferromagnetic Mössbauer spectra of FeO at low temperature and ambient pressure (Fig. 3.3.a) and at high pressure and room temperature (Fig. 3.3.b). There is a considerable difference between those two types of spectra, and even with a naked eye the Mössbauer spectrum at high pressure looks much more simple: six main

lines due to Zeeman splitting are clearly seen, in contrast to the low-temperature ambient pressure spectrum with multiple closely overlapping components due to different magnetic Fe positions. Multiple Fe positions at ambient pressure appear due to defect clustering. The charge deficit due to iron vacancies in wüstite is compensated in two ways. First is the replacement of Fe^{2+} with Fe^{3+} for charge compensation according to the equation $3\text{Fe}^{2+} = 2\text{Fe}^{3+} + \square_{\text{Fe}}$. In addition, some of Fe^{3+} ions occupy interstitial tetrahedral positions, becoming the core of the defect cluster formed by $\text{Fe}^{3+(\text{IV})}$ and surrounding vacancies. There is a large number of different defect clusters of various size and geometry (Long and Grandjean, 1991). The main implication for Mössbauer spectroscopy is the existence of Fe ions with different local environment in defect clusters, resulting in quite complex spectral structure.

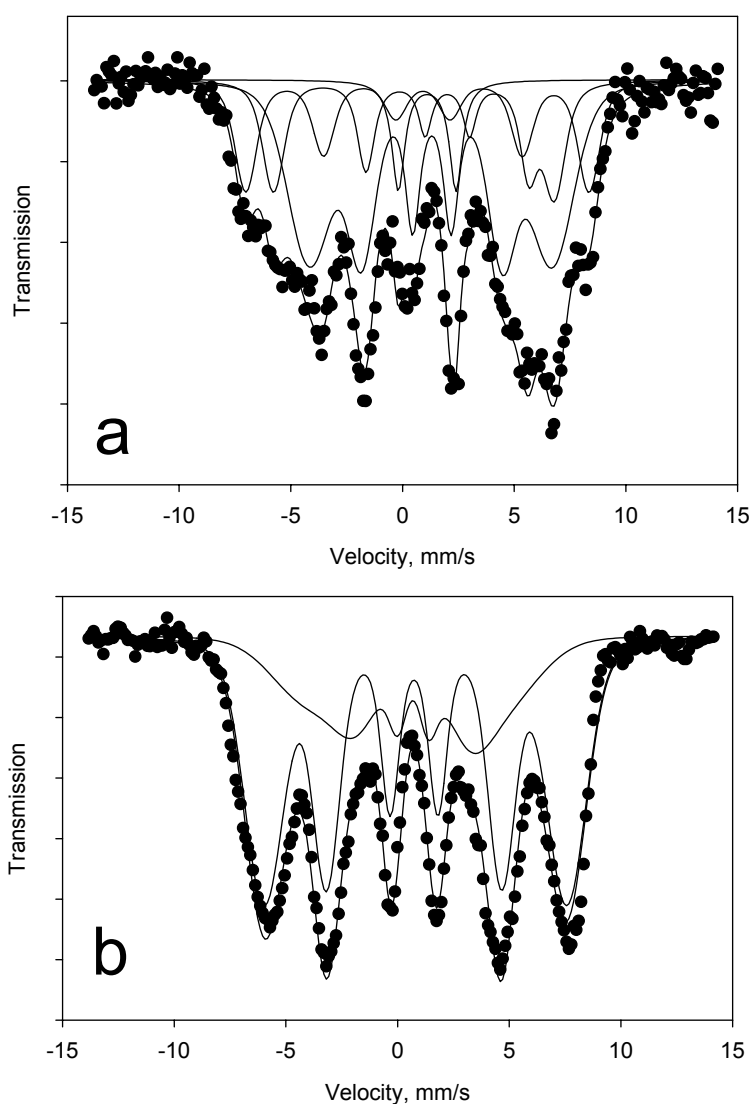


Fig. 3.3. a) – Mössbauer spectrum of $\text{Fe}_{0.92}\text{O}$ wüstite at ambient pressure and 80 K. b) – Mössbauer spectrum of $\text{Fe}_{0.94}\text{O}$ wüstite at room temperature and 37 GPa.

At high pressure the defect clusters seem to dissociate in the wüstite structure. In particular, very strong X-ray diffuse scattering in wüstite disappears at high pressures (Ding et al., 2005). Our Mössbauer spectroscopic observations are in agreement with the X-ray diffuse scattering results.

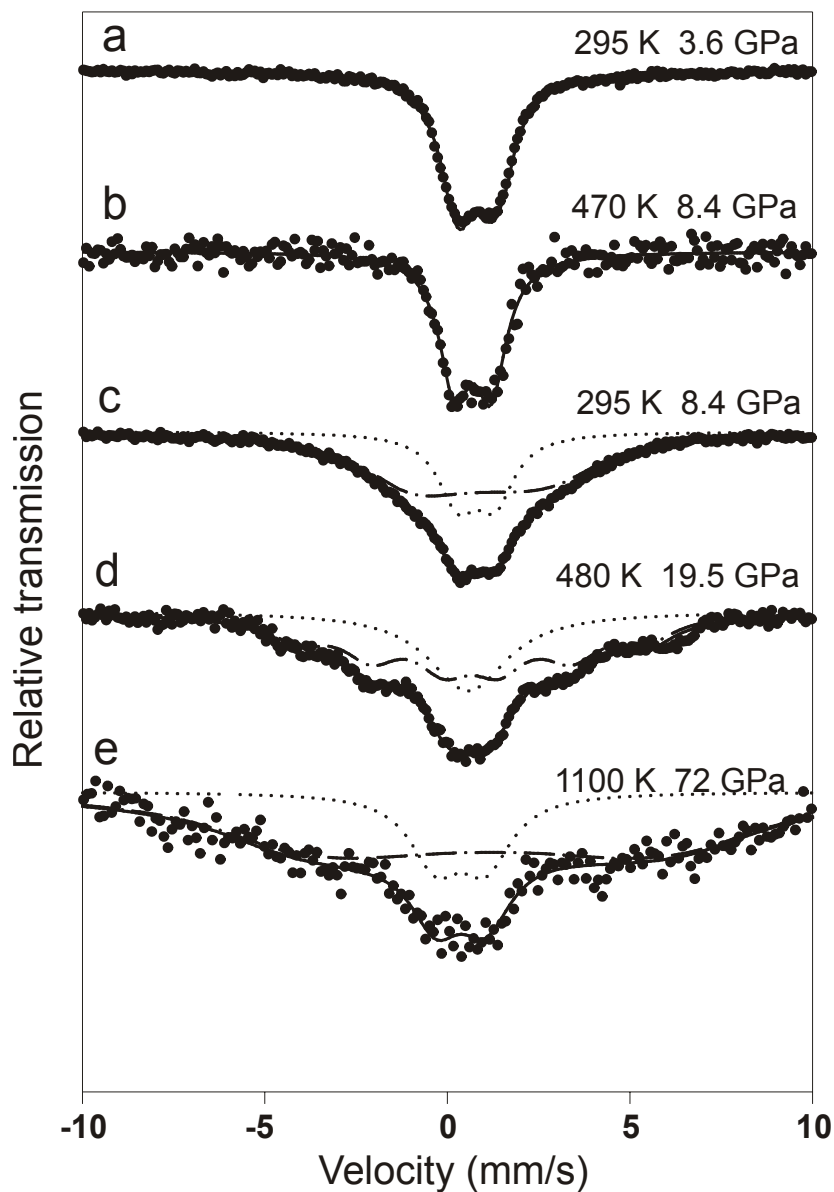


Fig. 3.4. Selected Mössbauer spectra of $\text{Fe}_{0.94}\text{O}$ wüstite in the vicinity of the Néel transition: a and b are from the paramagnetic phase; c, d and e are taken below T_N . The dotted line shows the paramagnetic doublet, while the dashed-dotted line represents the magnetic sextet subspectral component.

Examples of FeO MS spectra in different magnetic states at different P, T conditions are shown in Fig. 3.4. It is worth noticing that in the vicinity of the Néel transition some paramagnetic absorption is present in the spectrum together with the magnetically ordered

absorption, and the effect is more pronounced at high pressures. This implies that some fraction of Fe ions exist in magnetically disordered surroundings in some P, T -range in the antiferromagnetic (AFM) phase. Such behaviour is called ‘superparamagnetic’ and is explained by the existence of small (~ 100 Å) AFM particles with thermally fluctuating magnetic moment directions. Superparamagnetism should not be misunderstood as a type of paramagnetic state, because long-range AFM order exists. Since Mössbauer spectroscopy is sensitive to the local state of Fe ions, while the neutron diffraction pattern shows superstructural magnetic reflections for long-range order, these two methods could give slightly different results. I compared the low-temperature results of Mössbauer spectroscopy with neutron diffraction of a similar FeO sample at ambient pressure. The agreement of the normalized average hyperfine field BHF obtained from MS measurements and the integrated intensity of magnetic reflections in the neutron diffraction pattern was excellent (Fig. 3.5), indicating that MS shows the actual Néel transition (not just short-range magnetic order) in the case of FeO. Experimental MS data for the PM and AFM states of FeO are shown as filled and open circles, respectively, in Fig. 3.1. The magnetic transition boundary of FeO appears to be linear and the Néel temperature is given by $T_N(\text{K})=200(\pm 5) + 20.8(\pm 0.5) \times P$ (GPa).

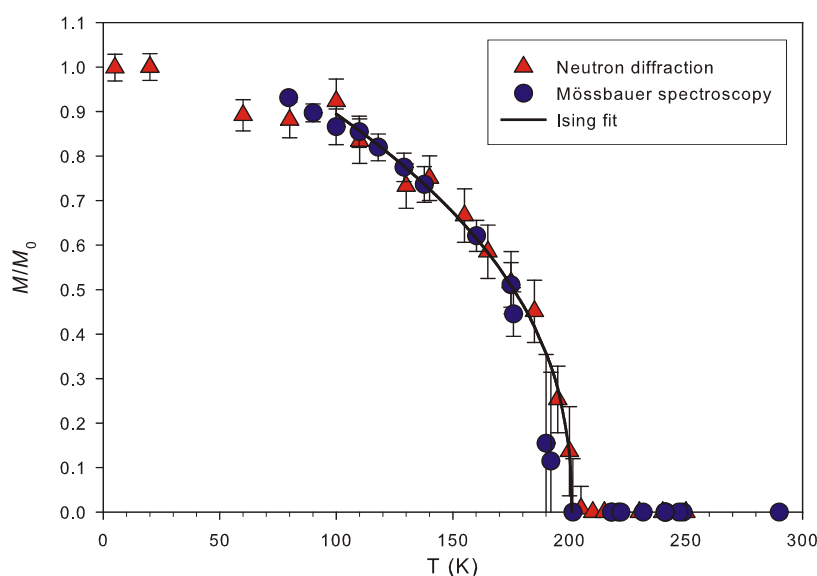


Fig. 3.5. Magnetization (M/M_0) of $\text{Fe}_{0.92}\text{O}$ at ambient pressure, obtained by Mössbauer spectroscopy (circles) and powder neutron diffraction (triangles). The solid line is the Ising fit used for the Néel temperature determination.

The pressure dependence of the Néel temperature of wüstite obtained in this study differs from the only previous study, Okamoto et al. (1967), who give $T_N(\text{K})=198 +$

$6.5 \times P$ (GPa) in the pressure range 0-0.6 GPa. This could be due to a strong nonlinearity of the magnetic transition boundary in the very low pressure region, but in the paper of Okamoto et al. neither sample characterization nor the description of experimental procedure (including pressure calibration) were given, so other reasons for the discrepancy cannot be excluded.

The magnetic phase boundary of wüstite proposed by Badro et al. (1999) is also plotted in Fig. 3.1 for comparison. As is seen from Fig. 3.1, this line differs significantly from our data. Note that the magnetic Mössbauer spectrum collected at about 73 GPa and 1100 K in this study (Fig. 3.4.e) lies significantly above the highest Néel transition point suggested by Badro et al. (1999) (Fig. 3.1). The possibility of decreasing Néel temperature at very high pressures cannot be excluded, but it is not observed in this study.

The structural phase boundary of FeO was tracked by means of powder X-ray diffraction. The cubic-to-rhombohedral distortion results in splitting of some of the diffraction lines (hereafter we use the subscripts 'c' and 'r' after the Miller indices to denote cubic and rhombohedral indices of FeO, respectively): the 111_c reflection splits into 101_r and 003_r ; 220_c splits into 110_r and 104_r and 311_c splits into 021_r , 113_r and 015_r . The most intense 200_c reflection remains unsplit. In the vicinity of the structural transition the degree of the distortion is small and line splitting can be seen as reflection broadening. In the studied pressure range, only the 111_c and 200_c wüstite reflections do not overlap with various NaCl reflections. The rhombohedral distortion in wüstite thus was estimated by asymmetric broadening of the 111_c reflection. In the rhombohedral phase the latter splits into two, where 101_r is expected to be at lower angles and three times lower in intensity compared with the 003_r reflection (for FeO; in MnO it would be the opposite). Fitting of the 111_c reflection as two peaks (Fig. 3.6) gives the degree of splitting (as a difference between the two peak positions), which is a good criterion of the rhombohedral transition (Fig. 3.6, inset). The resulting structural phase boundary is shown in Fig. 3.1 together with our experimental P, T points. At room temperature the rhombohedral distortion was observed at 12(1) GPa, in good agreement with previous reports (Dubrovinsky et al., 2000-II; Zou et al., 1980; Yagi et al., 1985). It is known that the pressure of this transition in wüstite is affected by the degree of hydrostaticity (Dubrovinsky et al., 2000-II). When no medium is used the transition is observed already at 9-10 GPa (Zou et al., 1980). In a Ne or He pressure transmitting medium (almost pure hydrostatic conditions) the transition is observed at 16 to 23 GPa (Fei, 1996; Shu et al., 1998-I; Jacobsen et al., 2005). Thus, the transition pressure in NaCl transmitting medium is intermediate, virtually the same as was obtained by Haavik et al. (2000) in a

nitrogen pressure transmitting medium. The P, T boundary of the structural transition obtained in this study ($P_{tr}(\text{GPa}) = -4.7(\pm 0.2) + 0.056(\pm 0.005) \times T(\text{K})$) differs from that reported by Fei (1996) for nearly hydrostatic conditions ($P_{tr}(\text{GPa}) = -5.0 + 0.070(\pm 0.003) \times T(\text{K})$; grey line in Fig. 3.1). We can propose several reasons for this discrepancy: first and probably the most important is the difference in hydrostatic environment, as discussed above. The second reason could be the different method of pressure calibration: we used a NaCl pressure standard, while Fei (1996) used the ruby fluorescence scale together with a gold pressure standard. The third possible reason is the different detection method: we used a constant wavelength angle dispersive technique, while Fei (1996) used an energy dispersive diffraction. Finally, the difference in chemical compositions of the samples could contribute to the difference of results, although Fei (1996) reported that no difference in phase boundary was observed between $\text{Fe}_{0.92}\text{O}$ and $\text{Fe}_{0.98}\text{O}$ samples. An additional argument for the latter possibility is that single-crystal diffraction studies of FeO in similar hydrostatic conditions (using a He pressure medium) show ~ 5 GPa difference (Shu et al., 1998-I; Jacobsen et al., 2005) for samples of different composition.

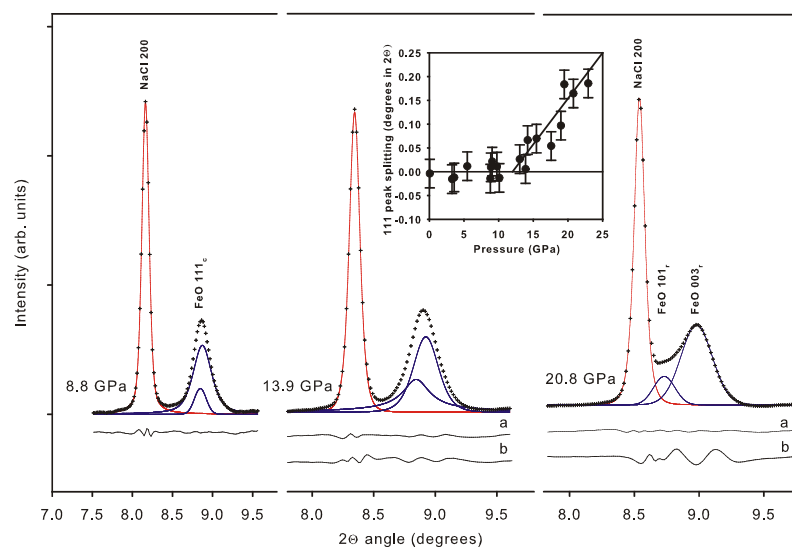


Fig. 3.6. Selected parts of the X-ray diffraction patterns of $\text{Fe}_{0.92}\text{O}$ collected at room temperature and various pressures. The strong NaCl 200 reflection together with FeO 111_c are shown. Fitting of FeO 111_c reflections as two peaks below the rhombohedral distortion (8.8 GPa) gives equal peak positions. Above the transition (at 13.9 GPa and 20.8 GPa), 101_r and 003_r have different positions. Residuals a and b are for double-peak (shown in figure) and for single-peak fitting of FeO 111_c, respectively. Inset: FeO 111_c line splitting (difference between the two peak positions) as a function of pressure. Below 12 ± 1 GPa the splitting is equal to zero, indicating a cubic structure. Above 12 ± 1 GPa the splitting starts to grow rapidly. Lines are given as guides for the eye.

Extrapolation of the cubic-to-rhombohedral phase transition temperature to ambient pressure gives $71(\pm 2)$ K for the data of Fei (1996) and $84(\pm 2)$ K for this study, which are reasonably consistent with each other. It is important to note that the experimentally measured structural transition temperature at ambient pressure for the FeO sample studied here was 160 K (Kantor et al., 2005-III): this implies a strong non-linearity of the structural transition boundary at low pressures (below 3 GPa); the same could be true for the magnetic transition boundary as discussed above.

Neutron diffraction patterns of MnO, similar to FeO, contain a structural 111 reflection and magnetic $3/2 \ 1/2 \ 1/2$ reflection below the Néel transition. The magnetic transition in MnO was determined from neutron powder diffraction patterns in the same way as in FeO. The resulting values of the Néel temperature at various pressures are shown as circles in Fig. 3.7. The pressure dependence of the magnetization (Néel) temperature is remarkable: the pressure slope abruptly changes from positive to negative at about 3.5 GPa where the Néel temperature reaches its maximum (ca. 170 K). Such a feature is not unique and was reported before for EuO, the structural analogue of MnO (Abd-Elmeguid and Taylor, 1990). The explanation of the non-monotonous pressure dependence of the magnetization temperature is relatively simple. Magnetic interactions in materials with a face-centered cubic (fcc) lattice can be described at least by two exchange integrals: J_1 , interaction with the 12 nearest metal neighbours (so-called antiferromagnetic interaction), and J_2 , superexchange interaction with the 6 next-nearest neighbours (so-called ferromagnetic interaction). These two integrals determine, in particular, the type of magnetic structure (Seehra and Giebultowicz, 1988) and the magnetization (Néel or Curie) temperature. There are several approximations for the Néel temperature determination. The simplest is given within the mean-field approximation and gives for cubic *fcc* type II antiferromagnets

$$T_N = 4S(S+1)|J_2| \quad (3.2);$$

where S is the spin number. In fact, this expression could be expanded to the form

$$T_N = \frac{2}{3}S(S+1)(x_1J_1 + x_2J_2) \quad (3.3);$$

where x_1 and x_2 are the number of first- and second- shell neighbours in the cationic sublattice taking into account spin orientation. In particular, there are 12 first neighbours; six of them have parallel spins and six have antiparallel spin orientation. The resulting value of x_1 is, therefore, zero, and in the cubic cell J_1 does not contribute to the Néel temperature. However, when the structure becomes trigonal, six parallel-spin neighbours are at slightly different

distances from the central atom as six antiparallel-spin neighbours. The effective value of x_1 now deviates from zero, and J_1 contributes to the Néel temperature. The higher is the trigonal distortion, the stronger is the J_1 effect on the Néel temperature. Depending on the absolute value of J_1 and the direction of the trigonal distortion, this effect could be either positive or negative (lowering the magnetization temperature), which is probably the case for MnO. This effect is also sometimes described as a splitting of J_1 into two non-equivalent components: $J_1^{\uparrow\uparrow}$ for the in-planar ferromagnetic interactions and $J_1^{\uparrow\downarrow}$ for the inter-planar antiferromagnetic interactions.

A non-monotonous pressure dependence of the magnetization temperature could be also caused by other reasons, such as a non-uniform pressure dependence of the J_2 integral by itself, or a competing exchange interaction and an outer shell hybridization changes with pressure, such as was observed in EuO (Abd-Elmeguid and Taylor, 1990).

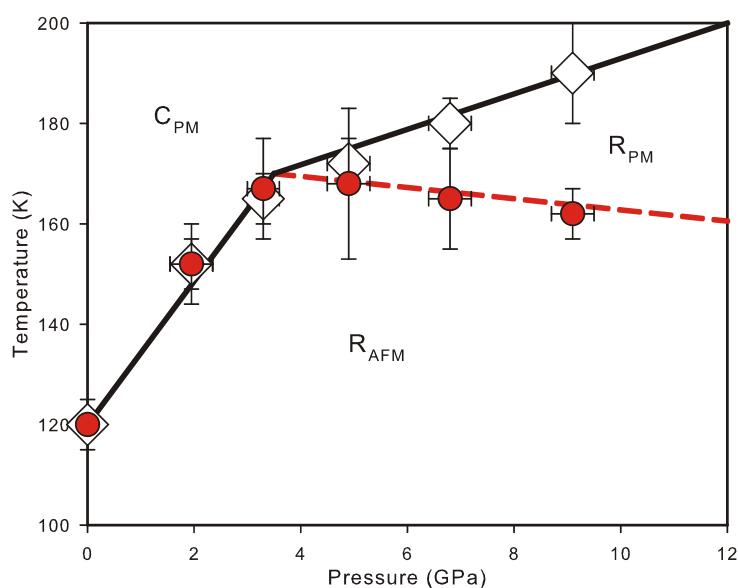


Fig. 3.7. Phase diagram of MnO. Open diamonds and the solid line are the phase boundary between cubic (C) and rhombohedral (R) phases. The circles and the dashed line are the boundary between paramagnetic (PM) and antiferromagnetic (AFM) phases.

The experimental geometry of the neutron powder diffraction measurement of MnO was the following: the high-pressure cell was arranged vertically, so that the loading direction and uniaxial stress vector were vertical. A one-dimensional linear detector was in the horizontal plane. In such a geometry the diffraction reflections could be detected only from vertical atomic planes. When a cubic crystallite with vertical $\langle 111 \rangle_c$ directions of MnO transforms to the rhombohedral phase, it will always contract in the main stress direction, i.e.,

a 100% preferred orientation in the $\langle 111 \rangle$ direction is formed. This implies that the rhombohedral 101_r reflection cannot be seen in the experimental design we used. The structural transition in MnO can nevertheless be easily recognized from collected diffraction patterns. In the high temperature cubic phase d_{111} (d-spacing of the 111_c reflection) is proportional to the lattice parameter and unit cell volume, and decreases continuously with decreasing T due to thermal contraction. Below the temperature of the structural distortion d_{101} increases slightly with decreasing temperature due to the lattice distortion. The temperature of the structural transition could be, therefore, easily determined (Fig. 3.8). The structural transition temperature (diamonds in Fig. 3.6) continuously increases with pressure, but not monotonously: above ~ 3.5 GPa its pressure slope becomes somewhat smaller. Extrapolation of the high-pressure trend of the structural transition boundary to room temperature gives a transition pressure of ~ 40 GPa, which is fairly close to what was reported by Yoo et al. (2005) (between 30 and 40 GPa), and Kondo et al. (2000) (between 30 and 36 GPa).

The main general conclusion from the phase diagrams of FeO and MnO is that the magnetic ordering transition is not necessarily coupled with the structural distortion transition. There are not just cubic paramagnetic (C_{PM}) and rhombohedral antiferromagnetic (R_{AFM}) phases, but also R_{PM} (in the case of MnO) and C_{AFM} (in the case of FeO) phases. What could be the driving force of the structural distortion?

The cubic B1 structure of TMMs consists of two *fcc* sublattices; one is formed by oxygen ions, and the other by metal ions. The *fcc* lattice is a cubic close packing of particles. In the case of spherical particles it is the densest way of arrangement in space. O^{2-} ions could be considered as spherical particles, giving rise to numerous oxide structures based on cubic or hexagonal close packing of oxygen ions. The outer electron shell of Fe^{2+} and Mn^{2+} is a 3d shell; therefore the effective shape is not spherical. The close packing of non-spherical particles would be distorted, and the resulting symmetry becomes lower than cubic. This mechanism was also proposed for lanthanide element crystals, which adopt several low symmetry structures under pressure due to the ovaloid effective shape of the 4f electronic shell (Dmitriev et al., 2003). In FeO and MnO (as well as in CoO and NiO) there is a competition between oxygen and metal sublattices, where the former favors an ideal cubic lattice, while the latter favors a distorted lattice.

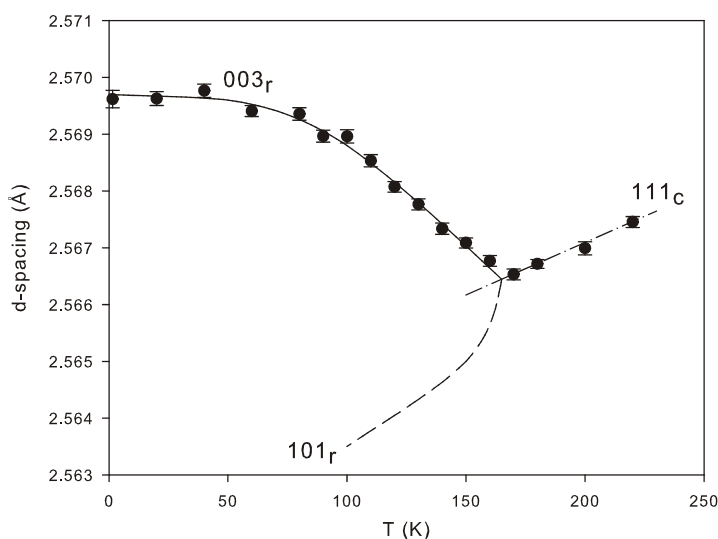


Fig. 3.8. Temperature evolution of the 111_c reflection d-spacing of MnO at 3.3 GPa. Below 165 K it splits into two, but the 101_r reflection does not appear in the diffraction pattern due to ~100% preferred orientation of crystallites along the <111> direction.

Upon compression the cation to anion radius ratio increases, and the contribution from the metal sublattice becomes more important, resulting in a pressure-induced symmetry-breaking transition in TMMs. We can denote the total energy benefit of lattice distortion for simplicity as a ΔH_d term (which includes also changes in lattice energy at zero pressure), although the pressure effect does not only change the volume, but also affects the relations between electronic shells and oxygen/metal sublattices. It is obvious that the entropy of a cubic phase is higher than that of a distorted phase in the case of displacive transitions. Therefore the $T\Delta S_d$ term favours the cubic lattice. This explains the general topology of the B1-rB1 transition boundary: high pressure stabilizes the distorted structure, while high temperature stabilizes the cubic structure. The transition condition is given in this way simply by $\Delta H_d - T\Delta S_d = 0$. The real situation is, however, also affected by antiferromagnetism. Type II magnetic ordering (which exists in TMMs) has essentially rhombohedral symmetry even if the lattice shape remains perfectly cubic. This immediately implies that magnetic ordering should stabilize the low-symmetry phase with respect to the cubic one. If we denote the effect of magnetic ordering on the free energy difference between cubic and distorted structures as ΔG_M , we now have three main parts, and the four possible relations between them are:

- (i) $\Delta H_d - T\Delta S_d > 0$; $\Delta G_M = 0$ – cubic paramagnetic state. Exists both in FeO and MnO at ambient conditions;
- (ii) $\Delta H_d - T\Delta S_d < 0$; $\Delta G_M = 0$ – rhombohedral paramagnetic state. Exists in MnO at 10 GPa and 170 K;

(iii) $\Delta H_d + \Delta G_M - T\Delta S_d > 0$ – magnetically ordered cubic state. Exists in FeO at 7 GPa and 300 K;

(iv) $\Delta H_d + \Delta G_M - T\Delta S_d < 0$ – magnetically ordered rhombohedral state. Exists both in MnO and FeO at low temperature and/or high pressure.

In the case when the cubic structure is only slightly stable relative to the rhombohedral one and the Néel transition occurs, structural distortion could be induced, which happens in MnO at pressures below 3.5 GPa. In such cases these two transitions are coupled, and magnetism indeed induces lattice distortion as was suggested before for TMMs (Smart and Greenwald, 1951), although magnetic interactions alone are not enough to induce lattice distortion.

Our considerations imply that the displacive transition in TMMs is not a magnetostriction effect. Experimental observations of elastic constant softening in the vicinity of structural transitions in TMMs (Kantor et al., 2004-I; Sumino et al., 1980) allow the suggestion that the transition is driven by the phonon instability. Ab-initio calculations also support our general conclusion: it was shown by static calculations that even in the paramagnetic state the rhombohedral lattice is stable relative to the cubic one for both FeO and MnO (Fang et al., 1999).

III.2. Quasi-single crystal X-ray diffraction and Mössbauer study of FeO: close view to the high-pressure polymorphism.

In order to get a better understanding of the pressure-induced symmetry-breaking transitions in FeO, I performed a quasi-single crystal X-ray diffraction study of wüstite FeO. “Quasi-single crystal” means that an initially single crystal sample was partially destroyed during compression and formed a kind of mosaic crystal with a strong preferred orientation of individual crystallites. On the diffraction image a single Bragg-reflection spot becomes a strip, however remains quite sharp in 2Θ FWHM. Such an experiment gives much better resolution with respect to normal powder diffraction. It allows resolution of closely overlapping Bragg peaks, which is crucial for exact symmetry determination. On the other hand, quasi-single crystal diffraction could not give the correct relative intensities of the reflections, and a full-profile structural refinement is not possible. X-ray diffraction data were collected at the high-pressure ID09 beam line at ESRF. A single crystal of $\text{Fe}_{0.94}\text{O}$ was loaded in the diamond anvil cell between two thin (few microns) layers of NaCl. Sodium chloride acts in this experiment as an internal pressure standard, pressure transmitting medium and as a thermal insulator for the laser heating.

In order to get a diffraction pattern from a single crystal, one should rotate the sample relative to the X-ray beam to put corresponding interatomic planes into reflective positions. However, the wavelength of the synchrotron radiation is so short (in this case 0.41 Å) and the radius of the Ewald sphere is so high, that it is possible to get zone-diffraction patterns even without cell rotation. The observed peak positions in this case should be corrected and the real d-spacing is calculated as

$$d_{\text{real}} = \frac{d_{\text{measured}}}{\cos(\Theta_{\text{measured}})} \quad (3.4);$$

where d_{measured} is the d-spacing obtained from the measured diffraction angle $2\Theta_{\text{measured}}$ (Ding et al., 2005).

At low pressures strong diffuse X-ray scattering around some Bragg reflections was observed (Fig. 3.9).

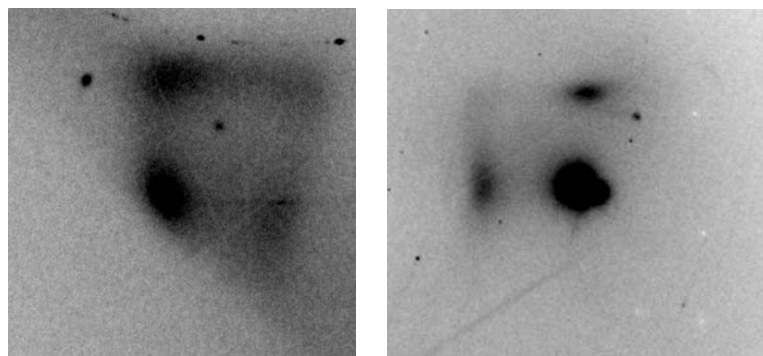


Fig. 3.9. X-ray diffuse scattering around 200 (left) and 220 (right) Bragg reflections for $\text{Fe}_{0.94}\text{O}$ at 2 GPa.

Upon compression, diffuse scattering disappears, as was shown also by Ding et al. (2005), indicating dissociation of the defect clusters. Defect clusters in wüstite are built from one block formed by Fe^{3+} tetrahedral interstitials surrounded by four cation vacancies (Long and Grandjean, 1991). I suggest that with increasing pressure ferric iron cations move from tetrahedral positions to one of the neighbouring octahedral vacant sites. Defect clusters, therefore, disappear. The tendency for coordination number increase with increasing pressure is the general tendency in high-pressure polymorphism, and, probably, shown by ferric iron behaviour in wüstite.

Between 11.7 and 13.5 GPa a trigonal distortion ($\text{B1} \rightarrow \text{rB1}$ transition) was observed. A clear splitting of the diffraction reflection is seen, both in X-ray diffraction images (Fig. 3.10) and in integrated patterns.

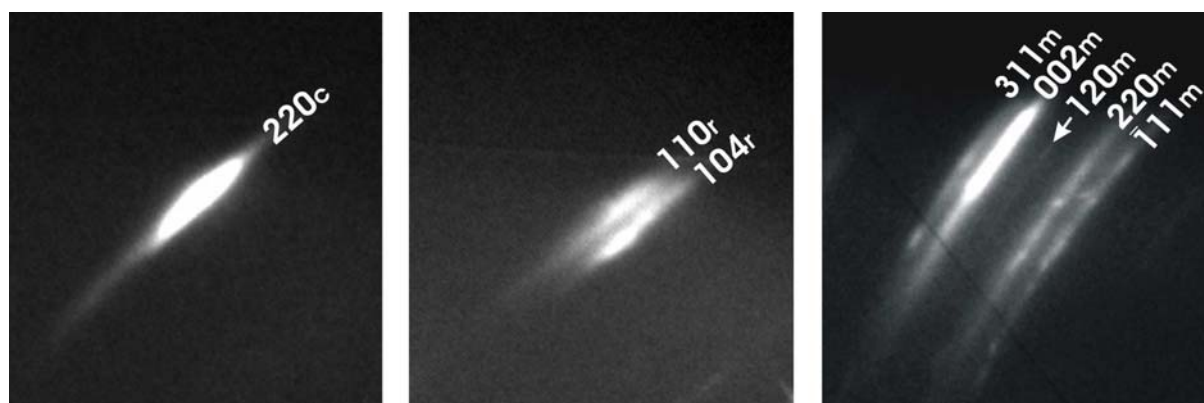


Fig. 3.10. Pressure evolution of the cubic 220 reflection. Left – cubic phase at 11.6 GPa (just below trigonal distortion). Middle – trigonal phase at 24.6 GPa with two reflections (104 and 110 in trigonal setting). Right – monoclinic phase at 74.5 GPa with five reflections (-111, 220, 120, 002, and 311 in monoclinic rational ($\gamma \neq 90^\circ$) cell setting).

Pressure dependence of the FeO lattice parameters in the hexagonal setting is shown in Fig. 3.11.

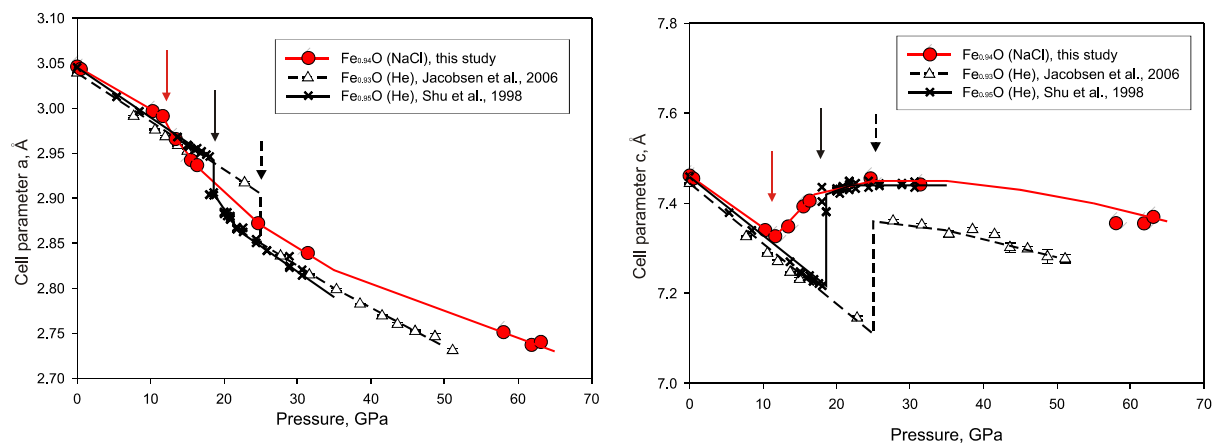


Fig. 3.11. Pressure evolution of the lattice parameters a and c of FeO (in the hexagonal setting). Circles – this study; for comparison other single-crystal diffraction data are shown – $\text{Fe}_{0.93}\text{O}$ in helium pressure medium (Jacobsen et al., 2005) and $\text{Fe}_{0.95}\text{O}$ in helium pressure medium (Shu et al., 1998-I). Lines are given as guides for the eye. Vertical arrows shows the transition pressure.

As shown in Fig. 3.11, the hydrostaticity strongly affects the $\text{B1} \rightarrow \text{rB1}$ transition pressure, in full agreement with previous studies (Dubrovinsky et al., 2000-II). An important and new result is that the nature of this distortional transition changes with hydrostaticity. Under strongly non-hydrostatic conditions the transition is second order-like: there is no discontinuity in volume and lattice parameters upon transition. In contrast, in experiments with helium as a pressure transmitting medium (Jacobsen et al., 2005; Shu et al., 1998-I), the transition is weak first-order: a clear discontinuity in lattice vectors and small discontinuity in volume is observed. Although under hydrostatic conditions the transition is first order, no pressure hysteresis is observed, because it is a displacive transition with no kinetic barrier between high-symmetry (cubic) and low-symmetry (trigonal) states. An interesting observation is that just above the transition pressure the hexagonal c lattice parameter increases with increasing pressure, especially for the non-hydrostatic experiment (Fig. 3.11). This means that no ordinary equation of state could describe wüstite compressibility in the vicinity of a phase transition due to strong spontaneous strain effects. Finally, there is a clear compositional dependence of the transition pressure. In two experiments with similar hydrostatic conditions (He pressure medium), the transition pressure was about 25 GPa for the $\text{Fe}_{0.93}\text{O}$ sample (Jacobsen et al., 2005) and less than 19 GPa for the $\text{Fe}_{0.95}\text{O}$ sample. Non-stoichiometry strongly stabilizes the high-symmetry structure (cubic versus trigonal). This also coincides with the low-temperature observations: the monoclinic structure was observed for nearly stoichiometric wüstite (Fjellvåg et al., 1996), while samples with more defects

show only the trigonal structure, and the degree of trigonal distortion is lower for less stoichiometric samples (Willis and Rooksby, 1953).

The main purpose of the “quasi- single-crystal” diffraction study was to synthesize the high-pressure polymorph (B8 or iB8) of wüstite (Fei and Mao, 1994). The sample was compressed to 80 GPa and then laser heated at about 2000 K. These P,T conditions correspond to the stability field of the B8 phase, as was reported by Kondo et al., (2004). After laser heating, diffraction peaks become sharper, and some new peaks appear in the diffraction pattern (Fig. 3.12). These new peaks, however, could be described in terms of a monoclinic structure, instead of a mixture of rB1 + B8 phases, and monoclinic line indexing gives better agreement than the latter case. The monoclinic phase is topologically equal to those reported by Fjellvåg et al. (1996), although not exactly the same.

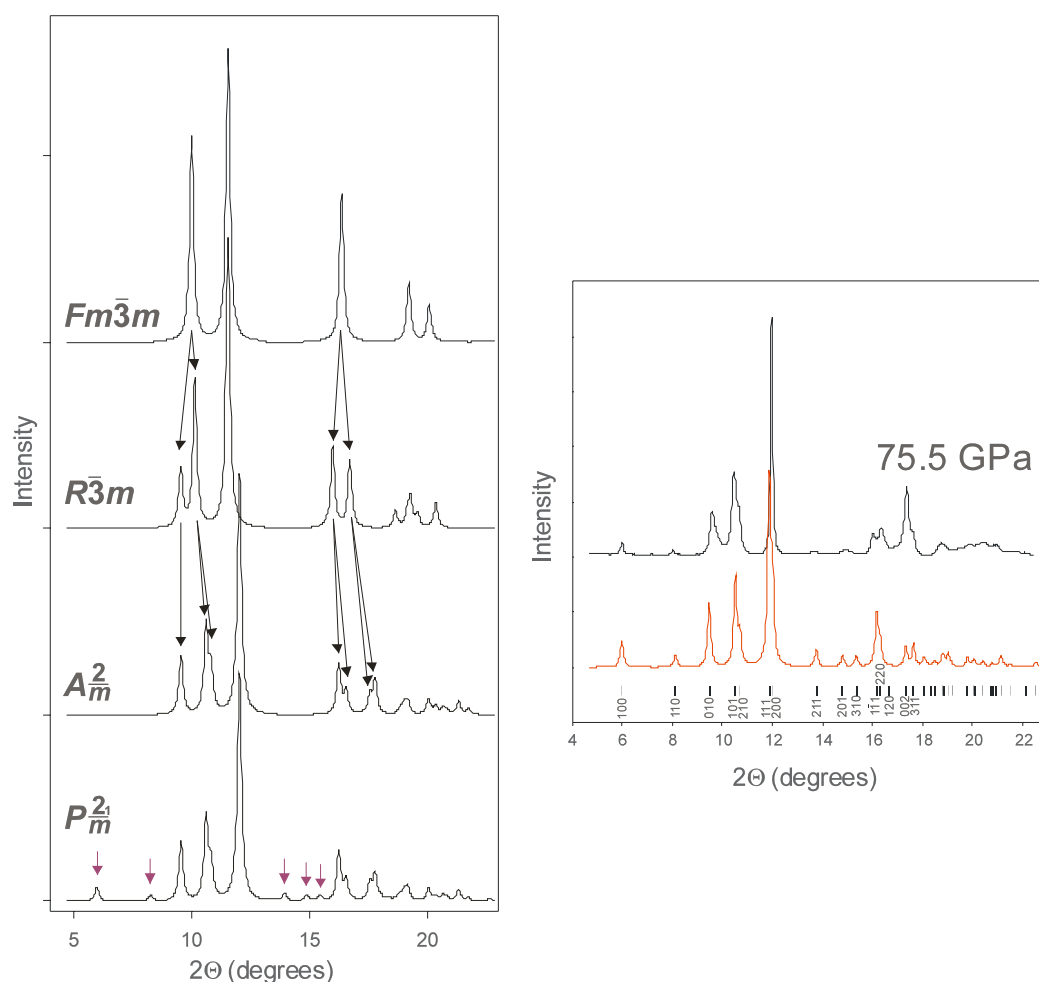


Fig. 3.12. Left – simulated X-ray diffraction patterns of FeO for cubic cell ($Fm\bar{3}m$), trigonal cell ($R\bar{3}m$), and two different monoclinic cells ($A\frac{2}{m}$ and $P\frac{2}{m}$). Vertical arrows

show extra peaks that appear only in the case of atomic displacements in addition to the monoclinic cell distortion. Right – integrated observed X-ray diffraction patterns of FeO at 75.5 GPa (upper graph) and simulated with the monoclinic space group $P\frac{2_1}{m}$ (lower graph).

Relations between cubic, trigonal and monoclinic unit cells in FeO are shown in Fig. 3.13. Trigonal distortion could be described as an elongation along one of the cubic three-fold axes. Further distortion to monoclinic symmetry is the introduction of two additional strains: distortion of the trigonal γ -angle (it deviates from 120 degrees) and tilting of the trigonal c-axis in the (110) plane. These lattice distortions do not imply shifts of atoms from their regular positions in the NaCl-like structural motif.

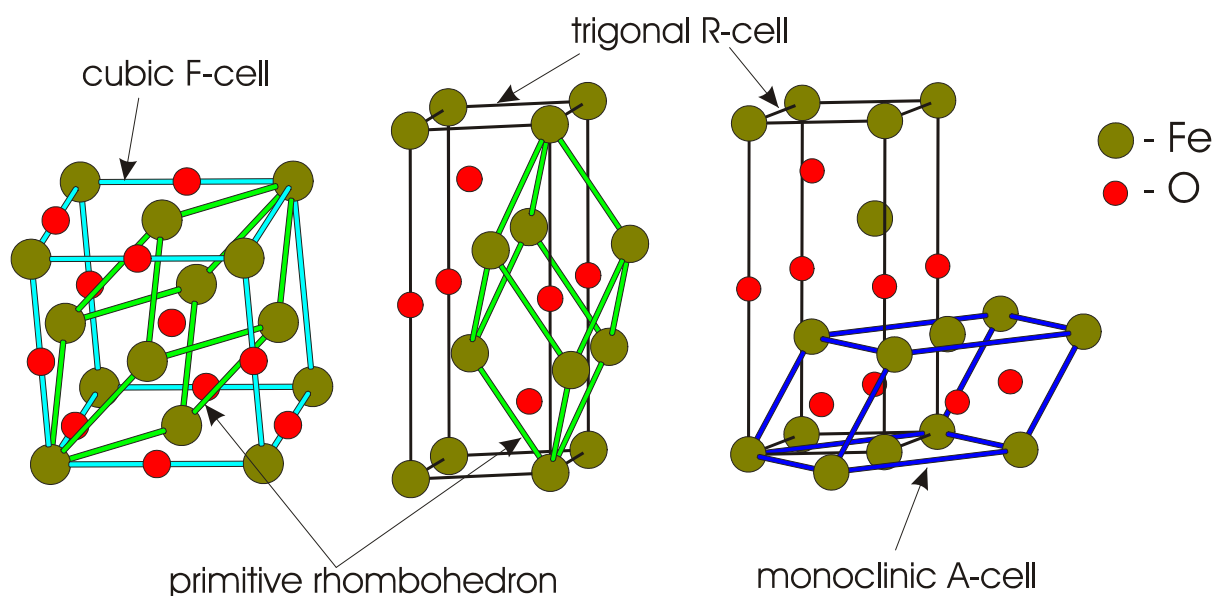


Fig. 3.13. Relations between cubic, trigonal, and monoclinic unit cells in FeO.

The observed X-ray diffraction pattern of FeO at 75.5 GPa after laser heating (Fig. 3.12) contains also some additional peaks that are not allowed in a pure $A\frac{2}{m}$ symmetry. These prohibited peaks could appear only if atoms shift from their regular positions, and some symmetry operations disappear (Fig. 3.14). It is not possible to determine the exact direction and magnitude of atomic shifts from their regular positions from the diffraction pattern, especially when relative peak intensities are not exact, which is the case in the present study. In principle there is another possibility for the appearance of prohibited reflections other than symmetry reduction. In the case of very large defect and impurity concentrations, the long-range order could be significantly violated and prohibited reflections

could appear (the process is somewhat similar to diffuse X-ray scattering at low pressures). However, this possibility is unlikely since no diffraction peak broadening was observed.

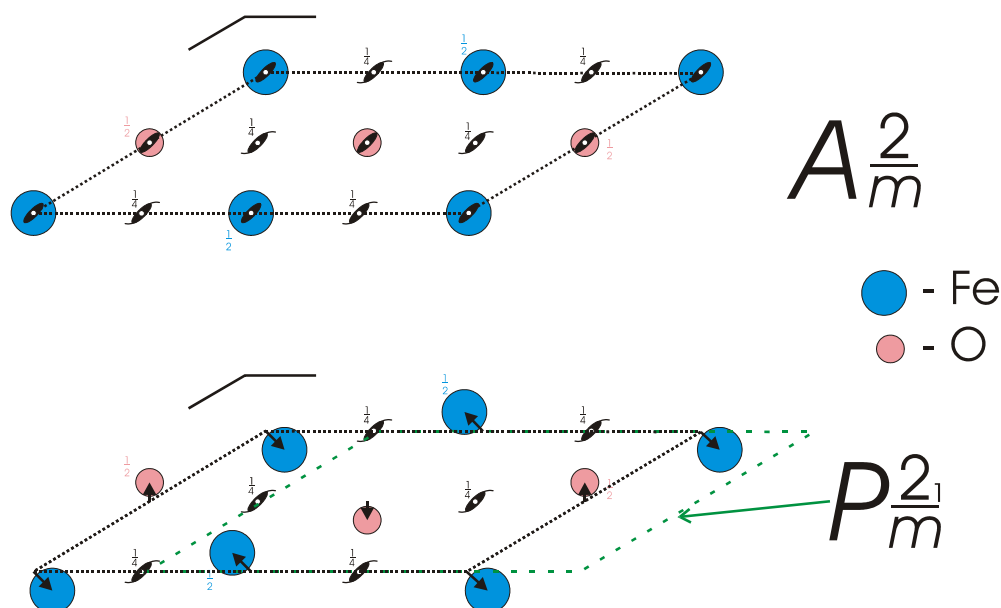


Fig. 3.14. Two possible monoclinic structures of FeO in a (110) projection. If Fe and/or O atoms are shifted from their regular positions, two-fold axes and inversion centers disappear as well as lattice A -translational vectors. The space group is then reduced from $A\frac{2}{m}$ to $P\frac{2_1}{m}$. The unit cell origin is shifted to $\frac{1}{4}$ in the y and z directions. A monoclinic unit cell parameter refinement for FeO at 75.5 GPa is presented in Table 3.1.

Table 3.1. Observed and calculated X-ray diffraction pattern of FeO at 75.5 GPa.

h	K	l	d_{obs}	d_{calc}^*	$d_{\text{obs}} - d_{\text{calc}}$
1	0	0	3.9352	3.9415	-0.0063
1	1	0	2.9385	2.9055	0.0330
0	1	0	2.4638	2.4932	-0.0294
1	0	1	2.2575	2.2473	0.0102
2	1	0	2.2143	2.2099	0.0044
1	1	1	1.9754	1.9707	0.0047
2	1	1	1.7312	1.7354	-0.0042
3	1	0	1.5862	1.5990	-0.0128
-1	1	1	1.4796	1.4654	0.0142
2	2	0	1.4496	1.4528	-0.0031
0	0	2	1.3656	1.3678	-0.0021
3	1	1	1.3445	1.3442	0.0004

*Monoclinic unit cell: space group $P2_1/m$, $a = 4.630(41)$ Å, $b = 2.929(26)$ Å, $c = 2.735(4)$ Å, and $\gamma = 58.4(7)^\circ$.

The exact stability field of the monoclinic FeO phase is not known. Unfortunately, decompression of the DAC was not performed due to diamond breakage. No differences between the Mössbauer spectra of trigonal (rB1) and monoclinic (mB1) FeO were observed. However, some small changes in the pressure dependence of the average hyperfine splitting in FeO can be seen (Fig. 3.15): the BHF rapidly increases above the magnetic ordering transition, up until it reaches a plateau at about 60 GPa. Above 75-80 GPa a small decrease in magnetic field can be seen, indicating a possible reduction of effective Fe magnetic moments in the monoclinic phase.

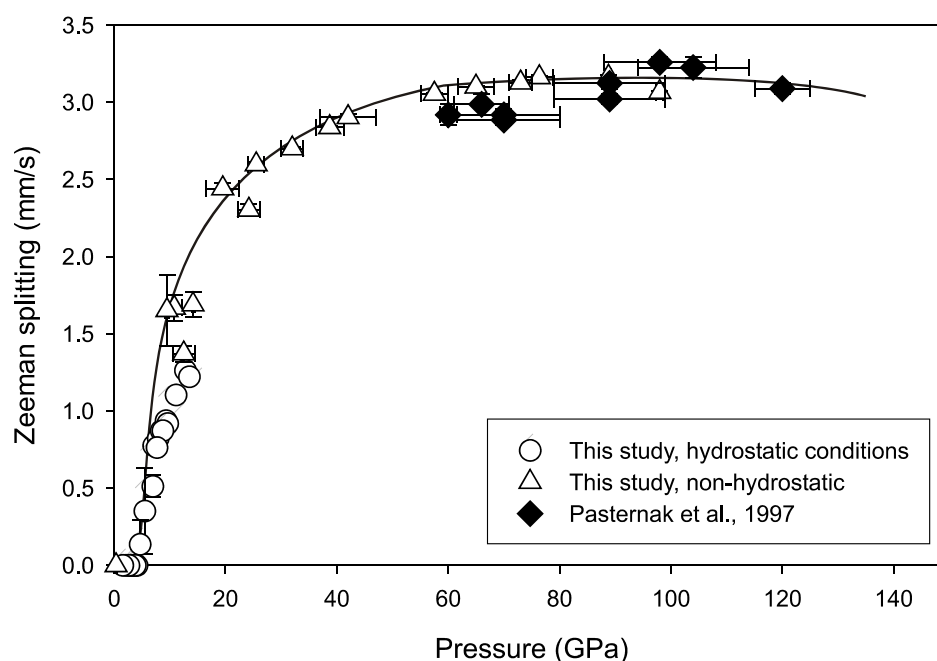


Fig. 3.15. Pressure dependence of the magnetic Zeeman splitting of FeO at room temperature. Circles – results from the experiment under hydrostatic conditions (in ethanol:methanol:water mixture), triangles – results from non-hydrostatic conditions. Data from Pasternak et al. (1997) are also shown for comparison. Line is given as guide for the eye.

The relations between the hypothetical B8 (NiAs structural type) and monoclinic mB1 phases are also not known. The first discovery of the high-pressure B8 polymorph of FeO was made in an energy-dispersive X-ray diffraction experiment (Fei and Mao, 1994). The resolution of the diffraction pattern was rather low, but new peaks were observed and indexed for a hexagonal cell of NiAs-like structure. The relative intensities, however, were not fully consistent with the B8 structure, and a discussion appears in the literature for a possible inverse-B8 structure (where Fe occupies As positions and O occupies Ni positions). Further analysis of relative peak intensities suggests possible polytypism in FeO with stacking layers of B8, iB8 and rB1 structure (Mazin et al., 1998). I note, that the positions of peaks of the hypothetical B8 phase roughly coincide with the peak positions of the mB1 phase, described

above. In particular, the 002_{B8} reflection is close to 010_{mB1} , 100_{B8} is close to 010_{mB1} , 101_{B8} to 111_{mB1} , 102_{B8} to 211_{mB1} , and so on. It is almost impossible, therefore, to detect the mB1 phase if the B8 and rB1 phases also coexist. There is also a possibility that the high-pressure mB1 phase of FeO was misinterpreted as a B8 phase. Recent angle-dispersive X-ray diffraction studies of FeO under high pressure with much better resolution also show the appearance of new peaks in addition to the rB1 phase, interpreted as an appearance of the B8 or iB8 phase (Murakami et al., 2004-II). However, even at pressures well above the hypothetical transition pressure and at high temperatures with *in situ* laser heating experiments, the pure B8 phase was never observed, and the diffraction patterns were interpreted as a mixture of B8 and rB1 or B1 phases (Murakami et al., 2004-II; Sata 2002). These facts are indirectly also in accordance with the possibility of single mB1 phase existence instead of mixtures of rB1, B8 or iB8 polymorphs.

III.3. Mössbauer spectra and short-range order in (Mg,Fe)O ferropericlaase: evidence for Fe clusterization under high pressure.

Ferropericlaase (Mg,Fe)O is one of the most important minerals of the Earth. The solid Earth consists of two principal layers – inner metal and outer oxide (silicate) layers. The composition of the latter can be roughly described as (Mg,Fe)₂SiO₄. This formula corresponds to the mineral olivine, which together with its high-pressure modifications forms the major part of the Earth down to the lower mantle. One of the main seismic boundaries separates the upper and lower mantle regions of the Earth. This seismic discontinuity is attributed to the dissociation of (Mg,Fe)₂SiO₄ into (Mg,Fe)SiO₃ (magnesium-silicate perovskite) and (Mg,Fe)O – ferropericlaase. Ferropericlaase is the second mineral of the lower mantle, forming likely almost one third of its volume. For these reasons a knowledge of the high-pressure and high-temperature physical properties of ferropericlaase is essential for creating a model of the Earth and understanding its evolution and current structure and composition. Sections III.3, III.4 and III.5 of this work consider the high pressure and high-temperature structural and electronic states of the ferropericlaase.

Three samples were used in this study, containing 5, 13, and 20 mole % of iron (samples Fe5, Fe13 and Fe20, respectively). The samples were synthesized in a CO/CO₂ gas-flowing furnace at 1200 °C and $\log f_{\text{O}_2} = -17.4$. Starting materials for the synthesis were pure MgO and ⁵⁷Fe-enriched Fe₂O₃ powders, which were carefully ground, mixed together and compressed in dense pellets to provide better intergranular connection.

The samples were annealed for ~100 hours and during this period twice crushed and re-ground in order to achieve full chemical heterogeneity. Samples then were rapidly quenched into a cold reservoir with the same gas mixture to prevent possible surface oxidation. Sample purity was checked with X-ray diffraction, Mössbauer spectroscopy and microprobe analysis, and no chemical heterogeneities were observed down to 1 μm. The Fe³⁺/ΣFe ratio was about 3.2 % for the Fe20 sample, 2.5 % for the Fe13 sample and 1.5 % for the Fe5 sample. High-pressure Mössbauer spectroscopic measurements were performed using a diamond anvil cell (DAC) technique at pressures up to 20 GPa at room temperature. Diamond anvils with 300 to 400 μm culet sizes were used in the DACs. The final Re gasket thickness was 15 or 30 μm and the sample chamber was 125 to 150 μm in diameter. A constant-acceleration Mössbauer spectrometer with transmission geometry was equipped

with a high-specific activity ^{57}Co point source in a Rh matrix. Two types of experiments were done: (1) under purely hydrostatic conditions using an ethanol:methanol:water (16:3:1) mixture as a pressure transmission medium up to 11 GPa; and (2) under non-hydrostatic conditions without a pressure medium up to 20 GPa. Small ruby chips were loaded in the DAC together with the sample for pressure determination (Mao et al., 1986).

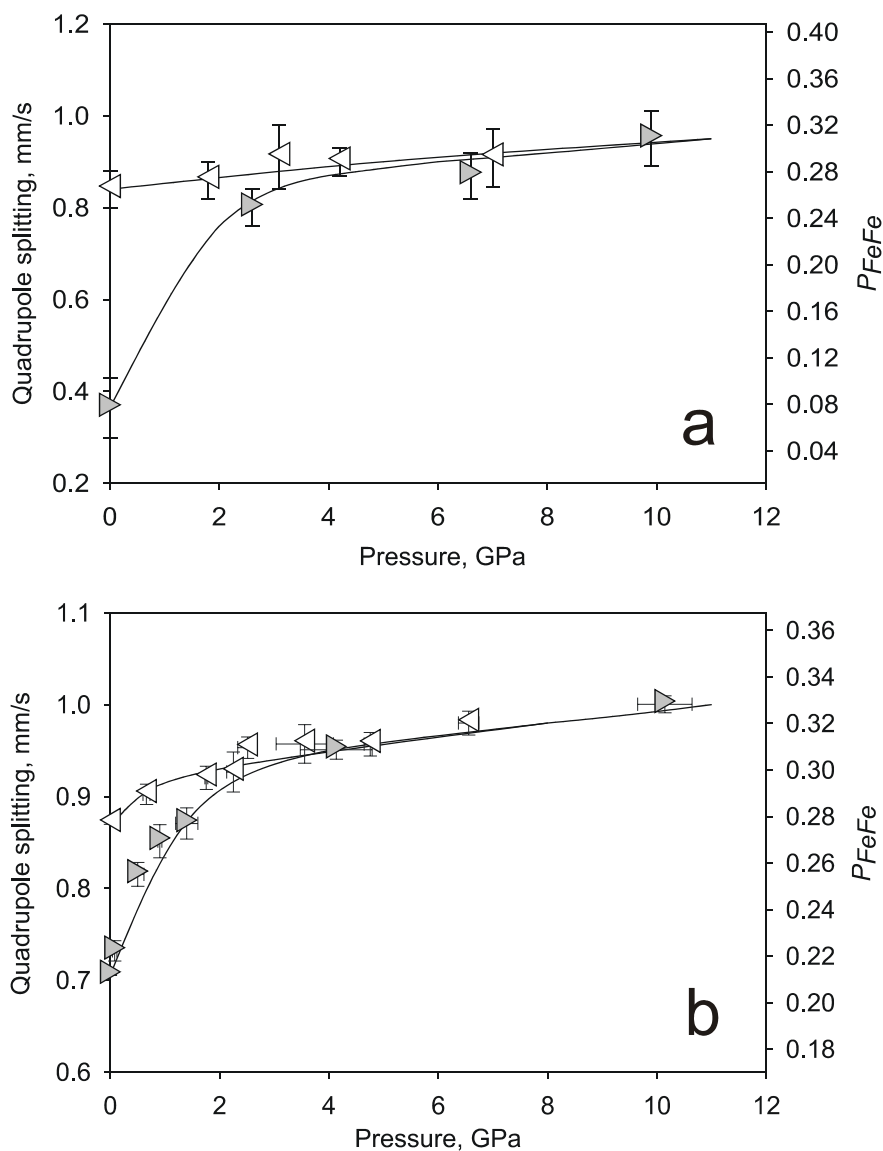


Fig. 3.16. Pressure dependence of the quadrupole splitting of Fe5 and Fe20 samples (a and b, respectively). Grey triangles pointing to the right are compression points, while white triangles pointing to the left are decompression points. Lines are given as a guide for the eye. Axes on the right show corresponding P_{FeFe} values according to Eq. (3.8).

Under ambient conditions ferroperriclinic Mössbauer spectra consist of a main quadrupole split absorption line corresponding to paramagnetic high-spin Fe^{2+} , and a small additional doublet of Fe^{3+} absorption (with negligible area for the low-Fe samples), in

agreement with previous studies (Dobson et al., 1998). Quadrupole splitting (QS) increases with increasing Fe content, which is also consistent with previous studies (Waychunas et al., 1994). Upon compression (Mg,Fe)O Mössbauer spectra show an unusual behavior. In the relatively low-pressure region (up to 2-3 GPa) QS significantly increases and then increases more slowly to a “plateau” (Fig. 3.16). This effect was observed both in hydrostatic and non-hydrostatic experiments, and in the latter case QS increases more rapidly. QS changes are more pronounced in the Fe5 sample. Upon decompression QS decreases but does not return to its initial value, and Mössbauer spectra of the samples quenched from high pressure differ significantly from those quenched from high-temperature synthesis (Fig. 3.17, 3.18).

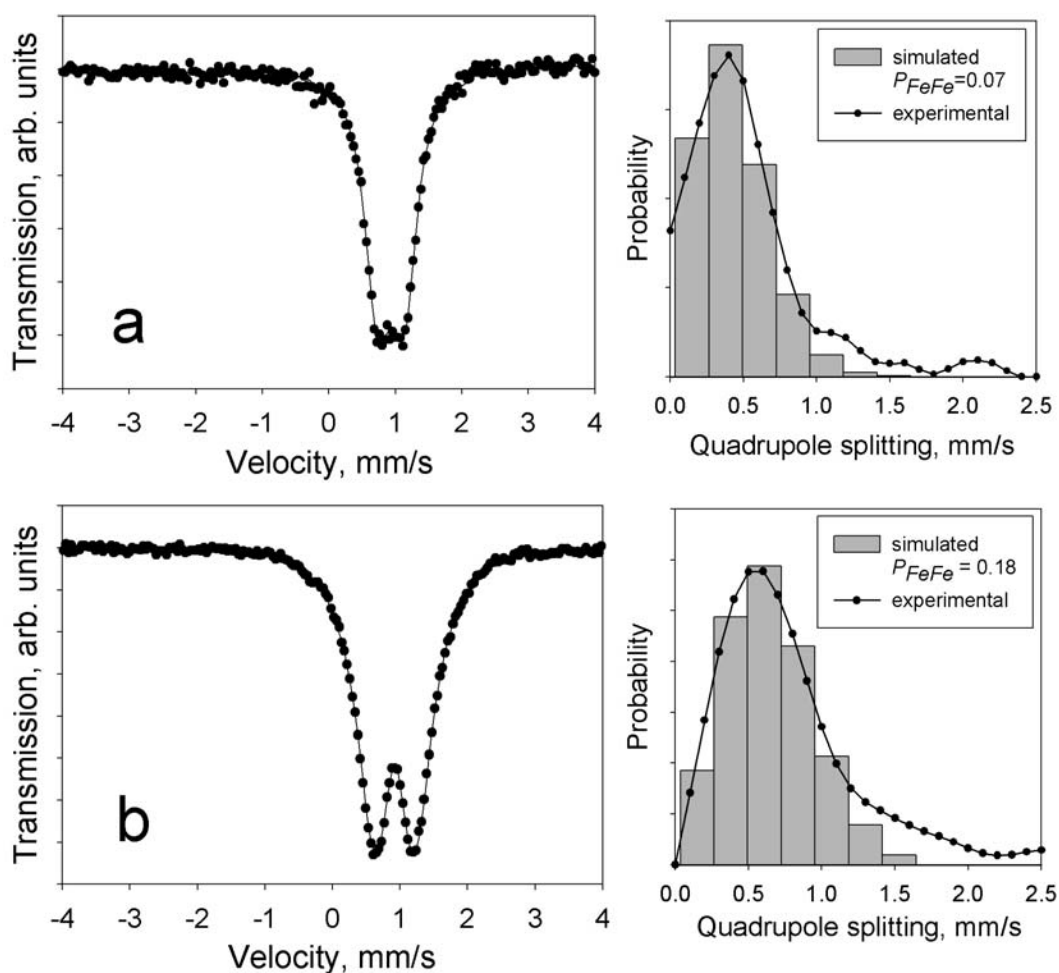


Fig. 3.17. Mössbauer spectra of the Fe5 ($\text{Mg}_{0.95}\text{Fe}_{0.05}\text{O}$) sample at ambient conditions before (a) and after (b) hydrostatic compression to 10 GPa at room temperature. On the right the experimental quadrupole splitting distribution is shown together with the simulated distribution with $P_{\text{FeFe}} = 0.07$ and 0.18 for figures (a) and (b), respectively.

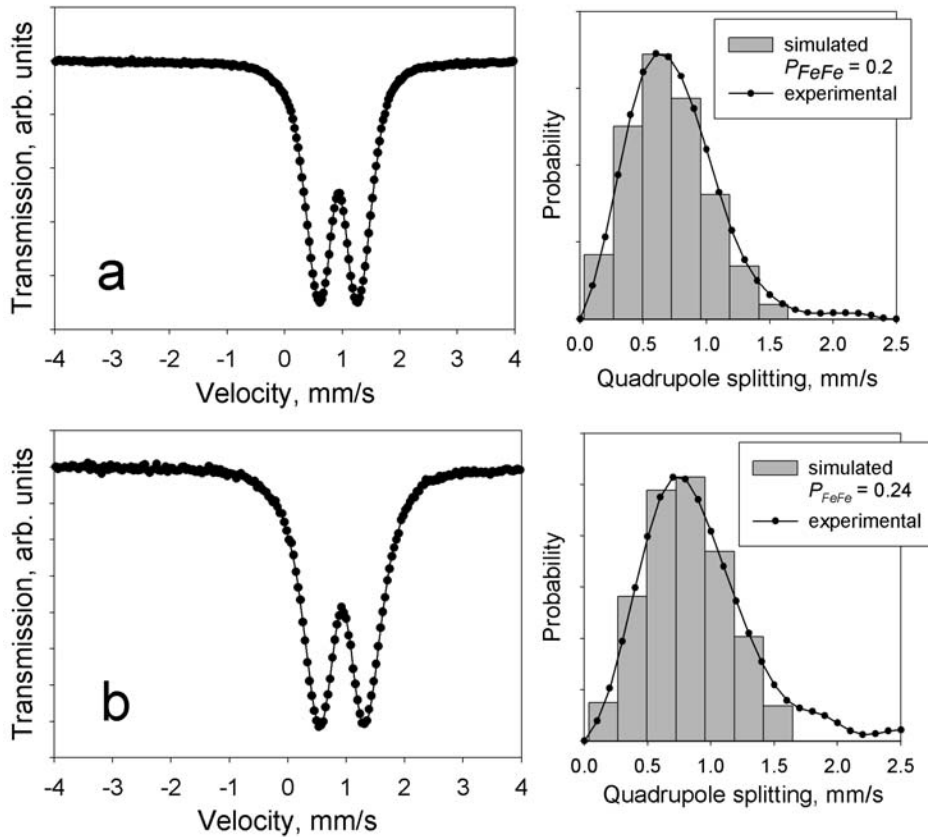


Fig. 3.18. Mössbauer spectra of the $(Mg_{0.8}Fe_{0.2})O$ sample at ambient conditions before (a) and after (b) hydrostatic compression to 10 GPa at room temperature. On the right the experimental quadrupole splitting distribution is shown together with the simulated distribution with $P_{FeFe} = 0.20$ and 0.24 for figures (a) and (b), respectively.

No phase transitions occur in ferropericlase at these pressures, and no changes in iron oxidation state or unit cell parameters were observed for the samples before and after compression. However, some properties should have changed according to the observed changes in Mössbauer hyperfine parameters.

If one considers Mössbauer spectra of ferropericlase at ambient conditions in more detail, an interesting observation is made: the Mössbauer spectra cannot be fitted sufficiently well with simple Lorentzian lines as shown by the dashed line in Fig. 3.19. This effect is well known for some disordered Fe alloys and implies a certain distribution of hyperfine parameters. In these cases, Mössbauer spectra of ferropericlase can be described with a quadrupole splitting distribution model. In such a model a probability distribution of QS is extracted from the experimental spectra (Fig. 3.19). In order to understand the reason of varying quadrupole splitting, one should consider the nature of QS in ferropericlase.

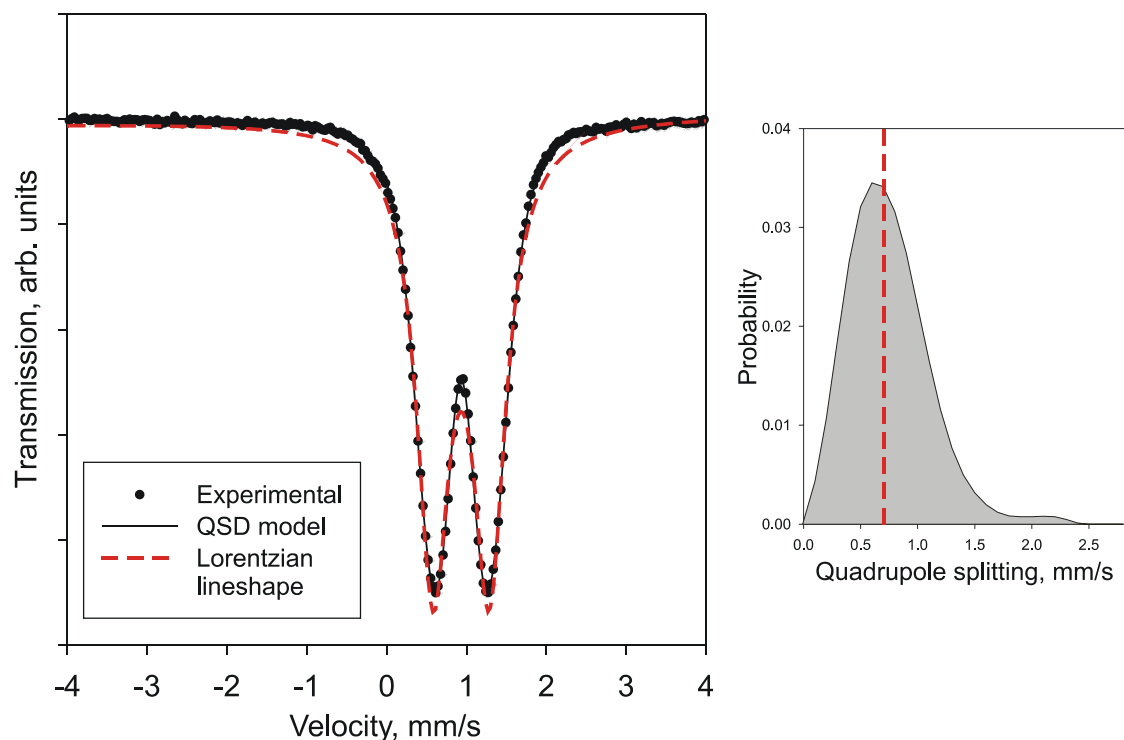


Fig. 3.19. Left – experimental Mössbauer spectrum at ambient conditions of the Fe20 sample (circles), model Lorentzian lineshape spectrum (dashed red line), and quadrupole splitting distribution (QSD) model (solid line). Right – quadrupole splitting distribution probability obtained from the QSD model. The dashed red line shows the QS value from the Lorentzian lineshape analysis.

Mössbauer quadrupole splitting Δ is directly proportional to the electrical field gradient (EFG) ∇E . The latter can be described in terms of two principal parts – lattice contribution and valence electron contribution. The lattice contribution to the EFG can be understood as a result of superposition of the electrical fields generated by surrounding ions, which could be modelled as point charges or dipoles. (Mg,Fe)O has a cubic NaCl-type crystal structure. Nominally cations occupy an octahedral position which has perfect cubic symmetry O_h . In such a case there is no lattice contribution to the electric field gradient for the Fe^{2+} nuclei. In a real solid solution the ideal crystal structure is locally distorted due to different types of atoms occupying one type of crystallographic site; hence the lattice contribution can be non-zero in the case of ferropericlase. However, the lattice contribution to the EFG is usually much smaller compared to the valence electron contribution. As confirmed by *ab-initio* calculations, the EFG lattice contribution in ferropericlase is indeed negligible, and the main reason for the quadrupole splitting is the valence electron contribution. In the case of a homogeneous environment of Fe^{2+} in the cubic lattice, the valence d-electronic shell produces only a small EFG, mainly due to the small Jahn-Teller distortion. In almost pure stoichiometric FeO (Broussard, 1969) or in highly diluted (Mg,Fe)O (0.5 mol % of Fe,

Waychunas et al., 1994), where the local cation environment of the Fe ion is essentially homogeneous (all neighbors are Fe in the case of FeO, and Mg in the case of highly diluted (Mg,Fe)O), the quadrupole splitting is quite small, namely less than 0.2 mm/s. In all other cases (Mg,Fe)O Mössbauer spectra shows a clear quadrupole splitting (Waychunas et al., 1994, Dobson et al., 1998). The appearance of the EFG is caused by the non-equivalent next-nearest neighbor coordination, and therefore the analysis of quadrupole splitting in ferroperricite gives information on the local environment of iron. Fe ions have strong electronic exchange interactions, while at the same time there is no Fe-Mg electronic exchange. In the case of both Mg and Fe surrounding the central Fe ion, its valence d-shell would be distorted, causing a stronger EFG and hence Mössbauer quadrupole splitting.

Every solid solution or alloy can be characterized not only by its composition (in our case Fe content), but also by the relative positions of the two elements distributed over one or more crystallographic sites. Two components could form either a random solution, or a solution with a certain degree of long-range or short-range order. The phenomenon of long-range order (LRO) and short-range order (SRO) has been studied in detail in many metallic alloy systems (see, for example, Newkirk et al., 1951). Atomic ordering affects many physical properties and the degree of short-range order acts as one of the thermodynamic parameters that define the total free energy and the entropy of the system. SRO could be relatively easily studied experimentally in the case when alloying components occupy two or more non-equivalent positions. In such a case the relative populations of different structural sites could be determined using many conventional methods, namely X-ray diffraction, Mössbauer spectroscopy, etc. Typical examples of such a system are the silicate mineral olivine $(\text{Mg,Fe})_2\text{SiO}_4$ and orthopyroxene $(\text{Mg,Fe})\text{SiO}_3$, which both have two slightly different octahedral sites M1 and M2, and the relative population of Fe/Mg between these positions changes with temperature (Morozov et al., 2005; Yang and Ghose, 1994). If two or more components occupy one crystallographic position, only the experimental methods sensitive to the local atom environment can be used to study SRO, which makes the experimental observation of short-range cation ordering quite difficult.

Up to now, (Mg,Fe)O was always regarded as a disordered solid solution with no SRO. Indeed, (Mg,Fe)O at ambient pressure shows continuous miscibility and no evidence for the ordered structural compound formation was ever observed. Waychunas et al. (1994) showed the absence of SRO in (Mg,Fe)O samples of different compositions synthesized at ambient pressure and high temperatures based on a combined extended X-ray absorption fine structure (EXAFS) and Mössbauer spectroscopic study. However in the laser-heated diamond

anvil cell (Mg,Fe)O decomposes into Fe-rich and Mg-rich components, implying the appearance of a miscibility gap under high pressure (Dubrovinsky et al., 2000-I, 2005). The miscibility gap existence suggests that Fe ions tend to separate from Mg, and therefore under high pressures SRO in the (Mg,Fe)O solid solution could deviate from a random distribution towards Fe clustering.

In the *fcc* lattice of ferroperricline every Fe ion has 12 next-nearest cation neighbors (NNN). We assume that in the case that all NNNs are of the same kind (12Mg or 12Fe) there are minimal distortions of electronic orbitals on the central site and the smallest quadrupole splitting should be observed. In the case that one NNN differs from the others (11Mg+1Fe or 11Fe+1Mg) some additional EFG appears and the QS is slightly higher, and so on, up to the 6Mg+6Fe configuration with the highest QS. The probability of any configuration can be easily calculated from the known pair correlation function P_{FeFe} (that is, the probability to find a Fe ion in the NNN coordination shell of another Fe ion):

$$P(n) = P_{FeFe}^n \left[(1 - P_{FeFe})^{12-n} \right] \frac{12!}{n!(12-n)!} \quad (3.5);$$

where $P(n)$ is the probability of a Fe ion to have n Fe ions in its NNN coordination shell. In the case of a random cation distribution P_{FeFe} is equal to the Fe concentration $x(\text{Fe})$. In the case of clusterization $P_{FeFe} > x(\text{Fe})$ a long-range ordered distribution $P_{FeFe} < x(\text{Fe})$ is usually assumed; however this is not necessarily true and a superstructural cation arrangement should be described by more than one pair correlation function (not only the first coordination shell, but also the second, third, and so on). For disordered and clusterized solutions consideration of only the first cation coordination shell (NNN) is enough and the short-range order parameter σ is given by

$$\sigma = \frac{P_{FeFe} - x(\text{Fe})}{1 - x(\text{Fe})} \quad (3.6).$$

In such a definition σ coincides with the Warren-Cowley short-range order parameter (Warren, 1968). From Eq. 3.6 it is obvious that $\sigma = 0$ for the random (disordered) solution, $\sigma > 0$ in case of clusterization, and $\sigma = 1$ in the case of complete decomposition of the solid solution into pure MgO and FeO.

The correlation between the local environment of a Fe ion and its quadrupole splitting is not trivial. We assume a linear relationship between quadrupole splitting Δ and number of non-equivalent NNN cations as

$$\Delta = aN + b \quad (3.7);$$

where N is an integer varying between 0 and 6 showing the number of non-equivalent NNN cations (for example, $N = 3$ for the $3\text{Fe}+9\text{Mg}$ and $3\text{Mg}+9\text{Fe}$ configurations), and a and b are fitted parameters. In order to obtain the a and b coefficients one should fit experimentally the observed QS distribution to the histogram calculated from Eq. (3.5) assuming a certain P_{FeFe} value. It is known that ferropericlase samples quenched from high temperature at ambient pressure are random solutions (Waychunas et al., 1994), and P_{FeFe} therefore is equal to the Fe concentration. We use the Fe20 sample (which has the most broad QS distribution) to calibrate a and b (Fig. 3.20), and obtain $a = 0.23$ mm/s and $b = 0.15$ mm/s. Note that the value $\Delta = 0.15$ mm/s obtained here for a homogeneously surrounded Fe ion is quite close to the value of ~ 0.19 mm/s obtained by Waychunas et al. (1994) using a significantly different analysis method.

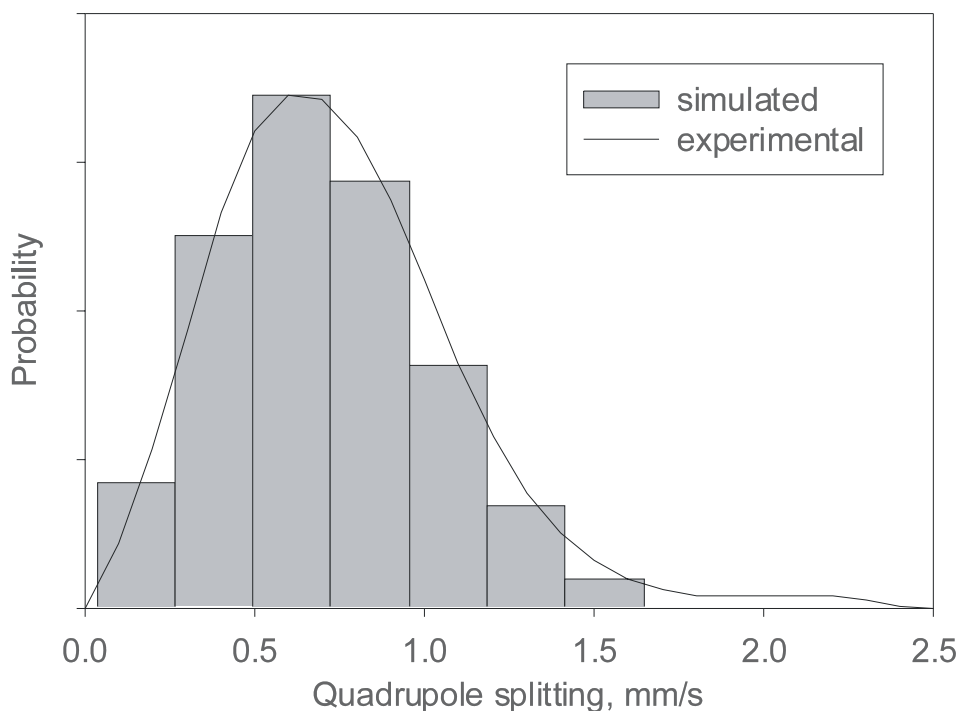


Fig. 3.20. Experimental (solid line) and simulated quadrupole splitting distribution according to Eq. 3.5 and 3.7 (grey bars) in the Fe20 sample assuming random Fe-Mg distribution.

After the a and b coefficients are determined, the inverse procedure could be applied to the experimentally observed QS distribution in order to obtain P_{FeFe} and the short-range order parameter σ . For Fe5 and Fe13 samples the obtained P_{FeFe} values are 0.077 and 0.170, respectively, which are quite close to the nominal values of 0.05 and 0.13 for the random distribution. The difference is probably due to the higher Fe^{3+} content in the Fe20 sample, which introduces an additional source of QS with respect to Fe5 and Fe13 samples. It could

be also that a certain degree of short-range order exists in the samples quenched from high temperature. Mössbauer spectra collected inside the DAC have a significantly smaller signal to noise ratio and additional line broadening due to the high sample thickness and relatively high line width of the point ^{57}Co source. Therefore the QS distribution could not be extracted precisely, but the mean value of QS could be obtained instead, which still provides a reasonable measure of P_{FeFe} and σ . From Eq. 3.5 and 3.7 an approximate relation can be deduced as

$$P_{\text{FeFe}} = 0.3948 \times \Delta(\text{mm/s}) - 0.0667 \quad (3.8);$$

for $0 \leq P_{\text{FeFe}} \leq 0.4$. Note that all the abovementioned conclusions are valid only for (Mg,Fe)O solid solution with no Fe^{3+} , and are not applicable for ferropericlasite with more than ~30% of Fe, where the ferric iron content usually cannot be neglected.

As shown above the observed high-pressure behavior of the quadrupole splitting in ferropericlasite (Fig. 3.16) reflects changes in the cationic short-range order. Such an observation has several important implications. Different short-range order states of the same material could be quenched to ambient conditions, but only one state would be thermodynamically stable. This means that interatomic diffusion at ambient temperature and pressure is slow and SRO is kinetically frozen. In order to establish a certain short-range order, Fe and Mg ions need to move between octahedral positions in the oxygen close-packed network. The most probable mechanism of this process is probably cation diffusion along grain boundaries, small-angle boundaries, screw dislocations, etc. Such processes could be accelerated dramatically by means of shear stresses or intergranular sliding during compression. In other words, even under hydrostatic conditions in a powder sample there are sufficient plastic deformations that could significantly increase the diffusion rate and allow equilibrium SRO formation.

A second important observation is that SRO under high pressure significantly deviates from zero, and Fe ions form local clusters. This agrees with the observed decomposition of ferropericlasite under high pressure and temperature. Fe cluster formation also could affect significantly many physical properties of the solid solution, especially those related to Fe electronic properties (magnetic and spin state). In particular, the local environment of Fe^{2+} (and, therefore, Fe-Fe exchange and superexchange interactions) in the Fe5 sample under pressure is almost identical to that in the randomly distributed Fe20 solution.

In order to verify the suggested Fe clustering in ferropericlasite, we performed *ab-initio* calculations of (Mg,Fe)O oxide with various relative Fe arrangements. *Ab-initio* calculations

were performed within the generalized gradient approximation (GGA) of the density functional theory (DFT). The frozen-core all electron projector augmented wave (PAW) method was used, as implemented in the *ab-initio* total-energy and molecular-dynamics program VASP (Vienna *ab-initio* simulation program) (Kresse and Furthmüller, 1996). The GGA+ U formalism formulated by Dudarev et al. (Dudarev et al., 1998) was used to account for the strong on-site Coulomb repulsion amongst the rather localized d-electrons of iron. In this approach only the difference between U and J is significant (Dudarev et al., 1998), and consequently we will henceforth treat them as one single parameter, for simplicity labeled as U . In this study the explicit spin (S) reference in the L(S)DA+ U abbreviation was omitted, i.e., it will be denoted as LDA+ U . For the supercell calculations a 4x4x4 Monkhorst-Pack k point mesh was used (Monkhorst and Pack, 1976) (2 irreducible k-points) and Gaussian smearing with a smearing parameter of 0.20 eV. In order to assure accurate results a plane-wave cut-off energy of 600 eV was used for all calculations. The (Mg,Fe)O solid solution was modeled using a 2x2x2 supercell (64 atom sites) derived from the ideal NaCl structure. Different concentrations of iron were modeled by changing the number of iron atoms in the supercell. For the chosen supercell changing one Mg for a Fe atom corresponds to a concentration of 3.125 % Fe. For the Fe atom 8 electrons were treated as being in the valence shell. Test calculations showed that inclusion of the semi-core Fe p-states into the calculation did not noticeably change the results in the pressure range considered here.

In the 2x2x2 supercell used in our calculations there are 32 cation positions. When one Mg atom is replaced with Fe, Fe ions are located quite far away from each other and are not interacting. In this case the composition of the supercell corresponds to (Mg_{0.96875}Fe_{0.03125})O. All the symmetrization was switched off in the calculation, allowing ions to shift from their regular positions. Although the local Fe surrounding is perfectly cubic in this case, the FeO₆ octahedron shows a small Jahn-Teller distortion. Fe-O distances are non-equivalent: four oxygen ions are at 2.176 Å from the central Fe ion and two oxygen ions are at 2.130 Å.

Mössbauer quadrupole splitting can be obtained from the electrical field gradient at the nucleus that is obtained from the *ab-initio* calculations performed with the Wien2K program. The EFG is described by three principal components: V_{zz} , V_{yy} and V_{xx} . The eigenvalues of V_{zz} , V_{yy} and V_{xx} axes are chosen in order of decreasing absolute EFG magnitude. The direction associated with V_{zz} is called the principal direction of the EFG. The eigenvectors can be averaged according to the scheme

$$V^* = |V_{zz}| \sqrt{1 + \frac{\eta^2}{3}} \quad (3.9),$$

with the asymmetry parameter $\eta = \frac{V_{xx} - V_{yy}}{V_{zz}}$.

The quadrupole splitting Δ is given as

$$\Delta = \frac{1}{2} e^2 Q V^* \quad (3.10);$$

where Q is the nuclear quadrupole moment of the first excited state of the absorber nucleus (Evans et al., 2005). For the ^{57}Fe isotope $Q = 0.16$ barn (Dufek et al., 1995). In the case where the EFG is given in atomic units (au), simply multiplying the EFG by 1.62 therefore gives Δ in mm/s. In SI units, the EFG is given in the units of V/m^2 , and the conversion factor is $1 \text{ au} = 9.7174 \times 10^{21} \text{ V}/\text{m}^2$. For an isolated Fe ion in a MgO matrix at zero pressure the calculated Δ value was 1.35 mm/s. This value is significantly higher than experimentally was observed for the low-Fe ferroperricline sample Fe5 (average Δ about 0.4 mm/s). This difference could be partially explained with the temperature effect. I performed low-temperature Mössbauer spectroscopic measurements of the Fe5 and Fe20 samples down to 80 K. The calculated Δ value for $T = 0$ K falls in between the values of these two samples, extrapolated to zero temperature (Fig. 3.21). Even in the Fe5 sample there is a significant amount of non-isolated Fe ions that increases the quadrupole splitting compared to that for an isolated Fe ion. This implies that the GGA+U calculations used in this study overestimate the Jahn-Teller effect of Fe^{2+} ion, and EFG calculations can be treated only semi-quantitatively. However, the principal results of these calculations are reliable. The pressure effect on the quadrupole splitting is negligible: as shown by the calculations compression of ferroperricline to 38 GPa would decrease Δ by less than two percent.

If we replace another Mg by Fe, the bulk composition would be $(\text{Mg}_{0.9375}\text{Fe}_{0.0625})\text{O}$, fairly close to the Fe5 sample composition. Inside the chosen supercell we can locate a second Fe ion in the first (NNN position), second, third, fourth or sixth cation coordination shell. All these possibilities were calculated for two different volumes with lattice parameters a equal to 4.25 and 4.00 Å, which corresponds to pressures of approximately 0 and 40 GPa, respectively. The calculated energy difference between these two configurations is remarkable (Fig. 3.22). The energy difference is given per one oxygen atom, and the absolute values are shifted to produce a zero value for the configuration with two Fe ions as the closest (NNN) neighbors.

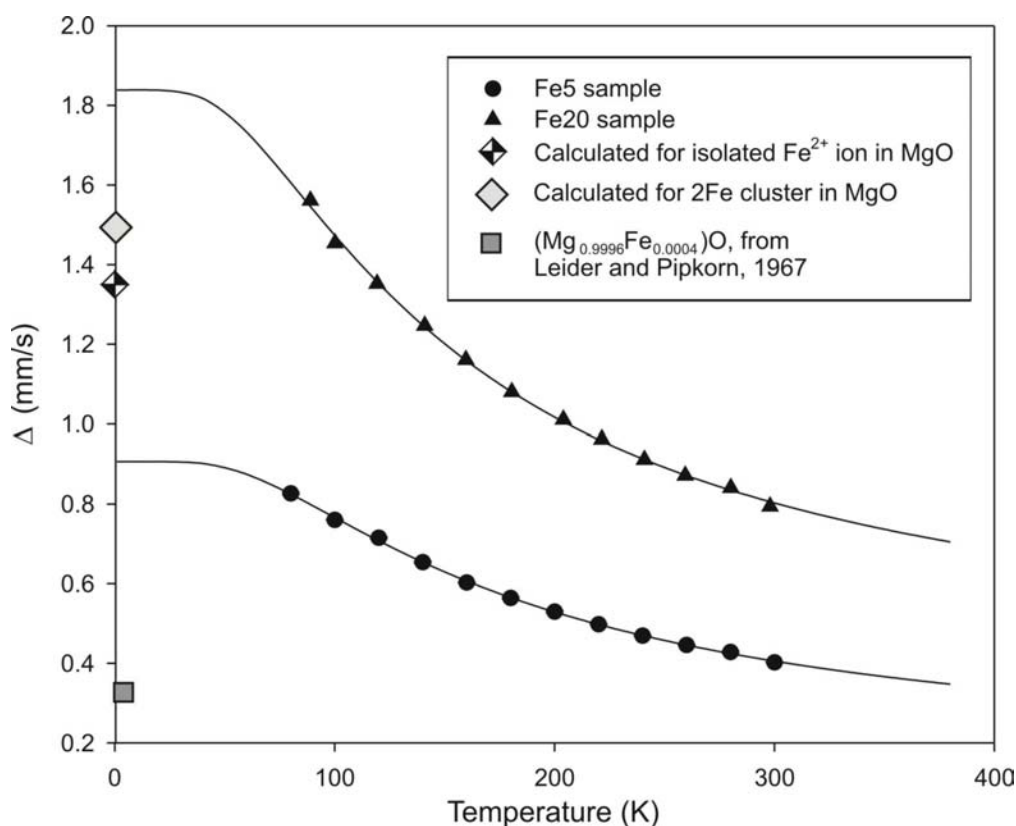


Fig. 3.21. Temperature dependence of the average quadrupole splitting of Fe5 and Fe20 samples. Solid lines show the fit using the crystal-field approach (Eeckhout et al., 2000). Diamonds show the calculated Δ value for $T = 0$ K for an isolated Fe^{2+} and 2Fe cluster substituting in a MgO matrix. Square shows experimental value measured at 14 K for $(\text{Mg}_{0.9996}\text{Fe}_{0.0004})\text{O}$ sample (Leider and Pipkorn, 1967).

The configuration with two Fe ions forming a pair cluster is much more favorable compared to all other configurations. There is almost no energy difference when the second Fe ion is in the third or more distant coordination shells, implying almost no Fe-Fe interactions at a distance of more than $\sim 5 \text{ \AA}$. However, the second coordination shell is energetically in between the first (NNN) shell and more distant coordination shells. This implies that for an accurate description of the $(\text{Mg,Fe})\text{O}$ solid solution (for example, within the cluster variation approach CVA), at least the second correlation function should also be included into the model. The second conclusion that can be made directly from Fig. 3.22 is that increasing pressure increases ΔH_{SRO} : when pressure increases from 0 to 40 GPa, the energy difference between NNN and non-interacting configurations increases by about 30 %.

It is interesting to look at the local distortion of the cubic lattice around Fe ions, a quantity which is almost impossible to observe experimentally. In analyzing 2Fe and 3Fe cluster geometries unexpected conclusions were found. The Fe-Fe distances are smaller than they should be in the idealized structure; and Fe ions are shifted towards each other and

bridging oxygen ions are shifted away, resulting in strong FeO_6 octahedral distortion (Fig. 3.23). From a general crystallographic point of view an opposite effect should be expected. The effective radius of Fe^{2+} at ambient conditions is larger than that of Mg^{2+} , and the FeO lattice parameter is about 3% higher than that for MgO. In the dilute solid solution Fe would tend to “push away” oxygen ions and cation neighbors to produce a higher polyhedron volume. The only source of the attraction force between neighboring Fe ions is electronic exchange interactions. Therefore, ab-initio calculations give us evidence for strong electronic exchange between neighboring Fe ions which distorts electronic d-orbitals and produces an electrical field gradient and hence Mössbauer quadrupole splitting. It is also interesting to compare the 2Fe cluster calculation for the high-spin and low-spin Fe states. It is clear from an Fe-O distance analysis that low-spin Fe^{2+} at ambient conditions (not stable relative to high-spin state) is slightly smaller than Mg^{2+} . The distortion of FeO_6 octahedra is even higher for the low-spin state than for high-spin Fe, but at the same time the electrical field gradient is negligible (two orders of magnitude smaller than for the high-spin state). These considerations give direct evidence that the lattice contribution to the EFG is much smaller than the valence contribution and can be neglected.

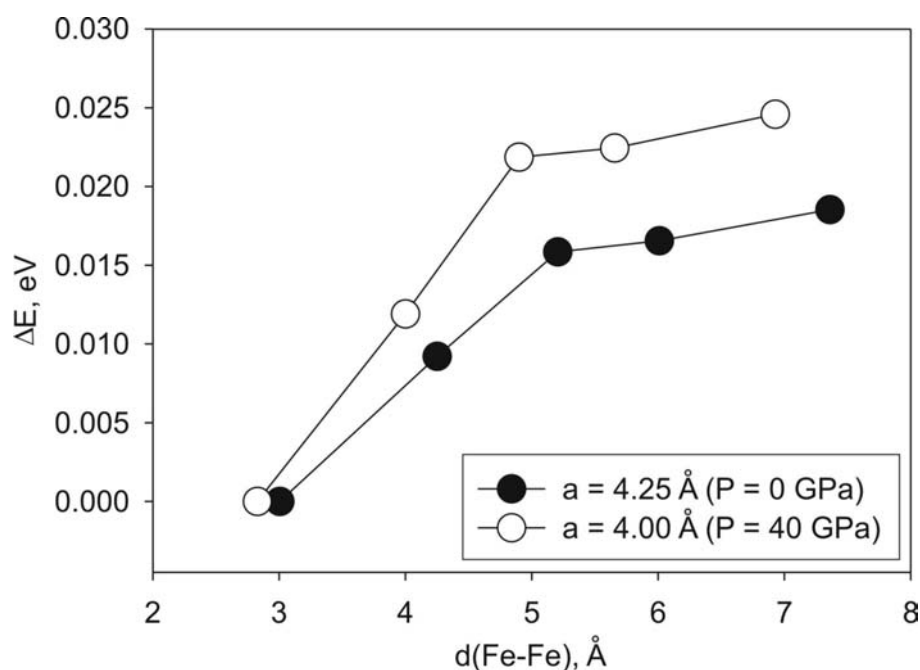


Fig. 3.22. Calculated enthalpy difference for the $(\text{Fe}_2\text{Mg}_{30})\text{O}_{32}$ supercell as a function of Fe-Fe distance. Black circles are for $a = 4.25 \text{ \AA}$ (pressure about 0 GPa) and open circles are for $a = 4.00 \text{ \AA}$ (pressure about 40 GPa).

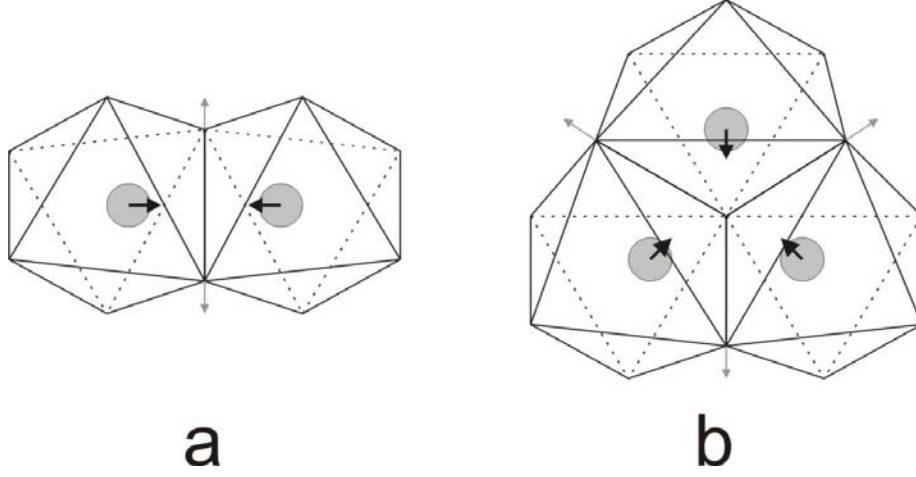


Fig. 3.23. Local distortions of Fe octahedra in 2Fe cluster (a) and 3Fe cluster (b), as obtained from *ab-initio* calculations. Fe ions (grey circles) are shifted towards each other as shown with black arrows. Grey arrows show schematically the shifts of bridging oxygen ions.

Although there is a clear enthalpy contribution for the clusterization at $T = 0$ K, an entropy contribution should also be taken into account. High temperature usually favors disordered cation distribution due to the size of the entropy effect. Entropy, in principle, is a function of short-range order. Excess SRO entropy contains two main components: configurational and excess vibrational entropy. Excess vibrational entropy can be either positive and negative, and is extremely difficult to predict theoretically. In contrast, configurational entropy can be easily estimated, and for the *fcc* cation lattice considering only first-term (NNN) correlations can be written as follows (Tsatskis, 1998):

$$\Delta S_{conf} = -3k_B \sigma^2 \quad (3.11),$$

where k_B is the Boltzmann constant and σ is the SRO parameter. In our experiment, we found that SRO is higher in low-Fe samples, and is maximum for the Fe5 sample. Under high-pressure the pair correlation function P_{FeFe} is about 0.28, and the corresponding σ value is 0.242. Therefore, at room temperature the $-T\Delta S_{conf}$ contribution to the Gibbs free energy (relative to a random cation distribution) is about 4.55×10^{-3} eV. The vibrational entropy contribution as a function of SRO is not clear. However, if the upper limit of clusterization is taken to be complete decomposition ($\sigma = 1$) and the lower limit as a disordered solution ($\sigma = 0$), the excess vibrational entropy is given simply as (Urusov et al., 1997):

$$\Delta S_{vibr} = 3k_B \ln \left(\frac{\theta_D}{\theta'_D} \right) \quad (3.12),$$

where θ_D and θ'_D are the Debye temperatures of the mechanical mixture of the components and of the random solid solution, respectively. This Debye temperature ratio is not lower than 0.93 for Mg-rich ferroperricite (Jacobsen et al., 2002), and at room temperature the $-T\Delta S_{vibr}$ contribution does not exceed 5×10^{-3} eV. For $0 < \sigma < 1$ this contribution should be smaller, but still has the same order of magnitude as the configurational entropy contribution for the Fe5 sample. This implies that the enthalpy increase due to short-range ordering (ΔH_{SRO}) should be on the order of -10^{-3} eV or -10^2 J/mol, which is a significant value. The nature of ΔH_{SRO} is clear: if the energy of an Fe-Mg bond E_{Fe-Mg} is lower than $\frac{1}{2}(E_{Fe-Fe} + E_{Mg-Mg})$, then Fe ions would tend to separate from each other and the solid solution would tend to form an ordered superstructural compound (such as in CuAu alloys). In the case when $E_{Fe-Mg} \approx \frac{1}{2}(E_{Fe-Fe} + E_{Mg-Mg})$, there is no tendency to ordering and a disordered random solution is formed due to the entropy contribution. Finally, if $E_{Fe-Mg} > \frac{1}{2}(E_{Fe-Fe} + E_{Mg-Mg})$, then Fe ions would prefer to be surrounded by Fe ions only and a tendency for clusterization and further possible decomposition of the solid solution is favoured. According to our experimental observations, the latter case exists at least near the low-Fe composition end of (Mg,Fe)O solid solutions.

Our calculation results are not sufficient to treat them within the CVA due to very small number of configurations considered. However, we can perform estimations using a type of simplified CVA for highly dilute solid solutions. For the 6.25 %Fe composition in the random solution more than 80 % of Fe ions are either isolated from each other, or form pairs. If we assume that only these two configurations are possible, then a random solution can be described as 25 % isolated Fe ions and 75 % of Fe ions having another Fe as its NNN. The configuration with all Fe forming NNN pairs would have $P_{FeFe} = 1/12$ and $\sigma = 0.0222$. In this case $\Delta H_{SRO} = -3.75 \times 10^{-3}$ eV, and at room temperature $-T(\Delta S_{conf} + \Delta S_{vibr})$ is on the order of 1×10^{-3} eV. In other words, the enthalpy effect dominates and equilibrium SRO is even higher, implying the formation of a significant amount of three-, four- and higher numbers of atoms in Fe clusters in the solid solution. This estimation strongly supports our experimental observations concerning the significant SRO especially in the low-Fe members of the (Mg,Fe)O solid solution.

Another interesting result of our experimental study is that changes in short-range order are much higher for the Fe5 sample with respect to the Fe20 sample. From Fig. 3.17 it is clear that in the Fe5 sample before compression the maximum probability corresponds to the two-atom 2Fe cluster. After compression, most frequent are three-atom 3Fe clusters. We can assume that the 3Fe cluster is the most energetically stable, and dilute Fe ions tend to

form 3Fe clusters. The most probable configuration of the 3Fe cluster is a Fe triangle in the $\langle 111 \rangle$ plane (inside a close-packing layer), in which every Fe ion has two NNNs (for comparison, in a 3Fe linear chain only the central ion has 2 NNNs). In the Fe₂₀ sample in the random solution most of the Fe ions are in 3Fe clusters; therefore changes in the SRO are much smaller. The enthalpy benefit of formation of four and higher numbers of atoms in Fe clusters is probably much smaller, and the enthalpy penalty suppresses strong SRO in higher Fe content compositions.

All of the thermodynamic calculations shown above are only estimations, so we are interested in additional experimental constraints to understand the P, T limits for significant SRO in ferropericlasite. The only way is to equilibrate the ferropericlasite sample at different conditions and to compare the Δ distribution of the quenched samples. Three experiments with the Fe₂₀ sample were performed: compression at room temperature up to 30 GPa; annealing in the multianvil large-volume press at 18 GPa and 1000 °C; and a laser-heating experiment in the DAC at 40 GPa and ~ 1800 °C. The latter two spectra were taken from McCammon et al. (1998). In the laser-heating experiment the temperature was not measured, so the value of 1800 °C is a rough estimation. The resulting Δ distributions are shown in Fig. 3.24. The starting material (annealed at ambient pressure and 1200 °C), and the sample, annealed at 18 GPa and 1000 °C, show very similar Mössbauer spectra which are assigned to the disordered cation distribution. In contrast, the sample laser heated at 40 GPa is almost identical to those treated at room temperature and 30 GPa. This means that a significant SRO should exist also at mantle conditions, since pressure strongly stabilizes clusterization in ferropericlasite. This could be not only due to the increasing excess enthalpy, but also due to decreasing of the excess vibrational entropy, because the relative difference in the Debye temperature (see Eq. 3.12) probably decreases with increasing pressure.

Additional evidence for the changes in short-range order come from XANES spectroscopy. I measured XANES spectra of Fe₅, Fe₁₃ and Fe₂₀ samples quenched from high pressure, and also XANES spectra of the starting Fe₁₃ sample and also of pure FeO. There are clear composition dependent changes in the edge structure of (Mg,Fe)O solid solutions (Fig. 3.25). An inflection point at about 7123 eV becomes smaller with increasing Fe content, and completely disappears in the FeO XANES spectrum. In XANES spectra a single-scattering process dominates, so these changes reflect the local iron concentration around the absorbing Fe atom. There is a clear difference in the XANES spectrum of the Fe₁₃ sample before and after compression (curves e and b in Fig. 3.25). The local Fe

concentrations in the Fe13 and Fe20 samples after compression are almost identical. The Fe5 sample after compression show a XANES spectrum almost identical to that of the Fe13 sample before compression (curves a and e), which implies more than a two-fold increase of local Fe concentration around the Fe atom, in full agreement with the Mössbauer spectroscopic data.

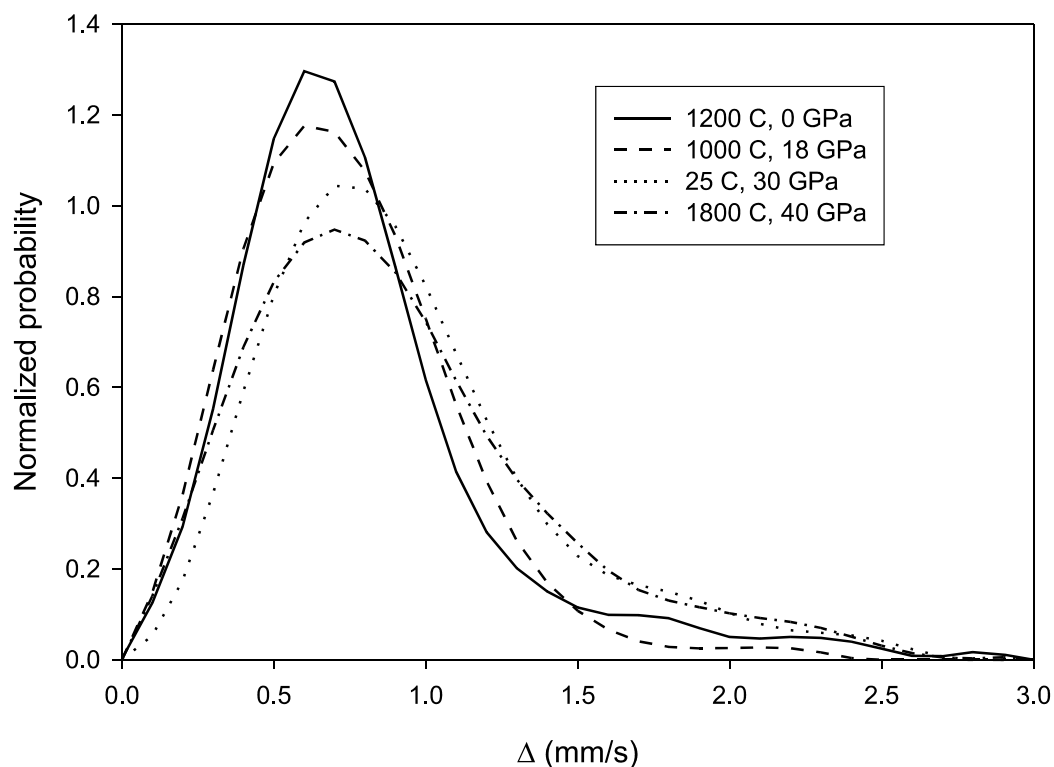


Fig. 3.24. Quadrupole splitting distribution of Fe20 samples with different history. Solid line – starting material, equilibrated at 1200 °C and ambient pressure. Dashed line – sample, annealed at 1000 °C and 18 GPa in a large-volume multianvil press. Dotted line – sample after compression to about 30 GPa at room temperature. Dashed-dotted line – laser-heated sample (approximately 1800 °C) at 40 GPa.

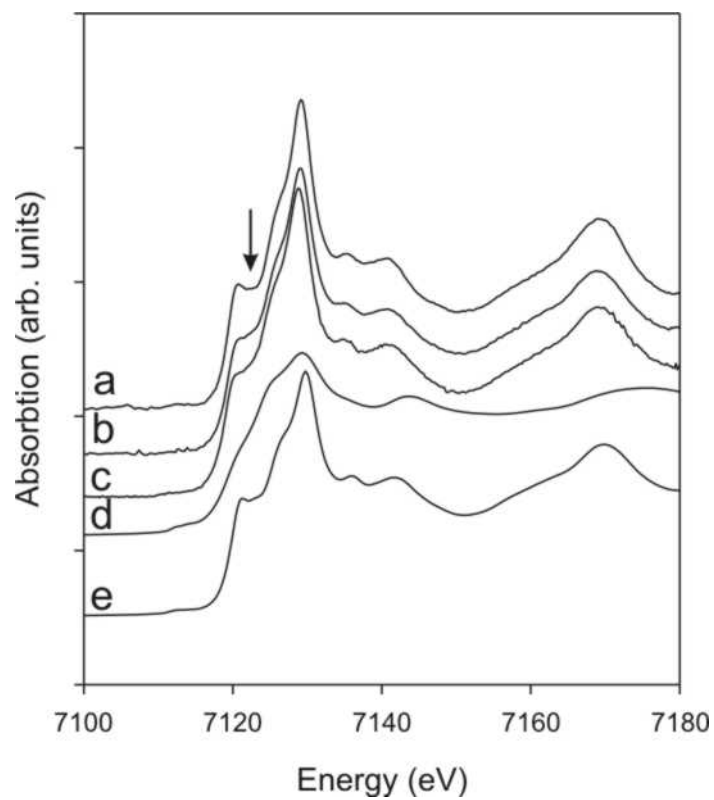


Fig. 3.25. Fe K-edge XANES spectra of ferropericlasite samples and wüstite. a) Fe5 sample after compression; b) Fe13 sample after compression; c) Fe20 sample after compression; d) FeO wüstite sample. e) starting Fe13 material. The arrow indicates the region of major changes in the XANES spectra.

III.4. Pressure-induced trigonal distortion in $\text{Mg}_{0.8}\text{Fe}_{0.2}\text{O}$ ferropericlase

Transition metal monoxides (MnO , FeO , CoO , NiO) are of great interest for solid-state physics and technology due to their magnetic, electronic and structural properties. Phase transitions from cubic to distorted structures with lower symmetries are known to occur in all of these oxides (Rooksby, 1948; Willis and Rooksby, 1953; Saito et al., 1966; Morosin, 1970). At ambient pressure, structural transition temperatures appear to coincide with Néel temperatures. It was suggested (Smart and Greenwald, 1951) that these crystallographic deformations are a consequence of the exchange interactions which result from antiferromagnetic ordering. Also, *ab initio* calculations of FeO and MnO show that a magnetically ordered state stabilizes trigonal structures relative to cubic structures at zero temperature and atmospheric pressure (Fang et al., 1999; Gramsch et al., 2003). At elevated pressures, MnO , FeO , and CoO also undergo the same type of rhombohedral distortion: MnO at ca. 35 GPa (Yoo et al., 2005), FeO at ca. 16 GPa (Shu et al., 1998-I) and CoO at ca. 43 GPa (Guo et al., 2002). The rhombohedral distortion of FeO is thought to be a second-order transition with negligible volume change at the transition, where the space group of the trigonal phase is a subgroup of the high-symmetry cubic phase (Shu et al., 1998-I); however it could also be a weak first-order transition. High-pressure Mössbauer spectroscopic studies of FeO at widely spaced pressure intervals showed the Néel transition to occur in a similar pressure range (Nasu, 1994), and suggested that these structural transitions resulted from an increase of the Néel temperature with pressure. However a recent high-pressure Mössbauer and ultrasonic elasticity study of FeO revealed a magnetic transition in FeO at about 5 GPa, which differs significantly from the structural transition pressure (Kantor et al., 2004-I,II). One approach to elucidate the relation between the magnetic and structural transitions is to eliminate magnetic interactions by diluting FeO in a non-magnetic isostructural compound (for example MgO , the mineral periclase). MgO is extremely stable in the rock-salt structure and is not observed to undergo any structural transitions up to at least 227 GPa at ambient temperature (Duffy et al., 1995). The rhombohedral distortion in $(\text{Mg}_x\text{Fe}_{1-x})\text{O}$ solid solution (the mineral ferropericlase when $x > 0.5$ and magnesiowüstite when $x \leq 0.5$) was observed over a relatively wide composition range (Kantor et al., 2005-I; Kondo et al., 2002; Mao et al., 2002; Shu et al., 1998-II). Some controversy exists regarding the minimum iron content that allows lattice distortion in ferropericlase: it was recently reported (Lin et al., 2003) that no phase transition occurs in $(\text{Mg}_{0.39}\text{Fe}_{0.61})\text{O}$ up to 102 GPa.

(Mg_xFe_{1-x})O ferropericlase with $x \sim 0.8$ is believed to be the second most abundant phase in the Earth's lower mantle after (Mg,Fe)SiO₃ perovskite, and therefore its properties and stability field are important for geophysical and geochemical models of the Earth's deep interior (Badro et al., 2003; Dubrovinsky et al., 2000-II; Lin et al., 2003; Wentzkovitch et al., 2004). I performed an *in situ* investigation of the behavior of (Mg_{0.8}Fe_{0.2})O at elevated pressure in diamond anvil cells (DACs) using Mössbauer spectroscopy (MS) as a direct method to probe magnetic properties of the material at high pressures, X-ray Fe K_α-edge absorption spectroscopy (XANES) as a method to probe the local environment of iron atoms, and X-ray powder diffraction (XRD) to provide information about long-range order and symmetry of the material.

Two samples, FP-1 and FP-2, with nominal composition Mg_{0.8}Fe_{0.2}O were used in the experiments as starting material, and are the same as used in previous experiments (McCammon et al., 1998). The two samples have the same nominal composition, and differ only in ferric iron content. The first sample was synthesized by mixing stoichiometric amounts of MgO and Fe₂O₃ (50% enriched with ⁵⁷Fe), heating overnight at 1200°C in reducing conditions ($\log fO_2 = -17.4$) using a CO/CO₂ gas-flow furnace and quenching into water. This low ferric iron sample ($Fe^{3+}/\Sigma Fe = 0.043$) is hereafter referred to as FP-1. A high ferric iron sample (FP-2) was synthesized by re-equilibrating part of sample FP-1 at higher oxygen fugacity ($\log fO_2 = -8.9$) and 1200°C, and quenching into water ($Fe^{3+}/\Sigma Fe = 0.074$). Lattice constants are $a=4.2389(5)$ and $4.2348(5)$ Å for samples FP-1 and FP-2, respectively. After the experiments, the chemical composition of the quenched samples was checked by scanning electron microscopy and X-ray microprobe: no changes in chemical composition were detected, and no evidence for chemical inhomogeneity on the length scale of the measurements (ca. 1 μm) was observed.

High-pressure measurements were performed in a three-pin (Mössbauer spectroscopy) or four-pin (X-ray absorption and X-ray diffraction) modified Merrill-Basset design diamond anvil cell (DAC) (Dubrovinskaia and Dubrovinsky, 2003), mounted with gem-quality diamonds with 250 μm culets. A rhenium gasket with initial thickness 260 μm was preindented to about 40-60 μm, and a 125 μm diameter hole was drilled in the gasket and filled with sample powder. Several small ruby chips were also loaded in the sample chamber for pressure measurements and estimations of pressure gradients (Mao et al., 1986). No pressure transmitting medium was used. To relieve stresses at high pressure, samples were scanned for about 30 seconds at several stages during the experiment using an infrared laser at low power at temperatures below 1000 K. Thermal radiation from the sample was detected

by an infrared-sensitive camera, confirming that the sample in the DAC was indeed heated. Laser heating was performed at several pressures: 25, 36, 49, and 55 GPa.

⁵⁷Fe Mössbauer spectra (MS) of samples FP-1 and FP-2 were recorded at room temperature in transmission mode on a constant acceleration Mössbauer spectrometer using a high specific activity ⁵⁷Co point source in a Rh-matrix. The beam diameter (> 500 μm) was larger than the sample diameter, so absorption was measured from the entire sample volume. The velocity scale was calibrated relative to a 25-μm α-Fe foil. Collection time for each spectrum varied from 12 to 24 hours. Pressure was measured before and after each run and then averaged. The typical pressure drift during Mössbauer measurements was less than or about 1 GPa.

The XAS measurements were carried out on the dispersive XAS beamline ID24 at the ESRF. The gap of the undulator was optimized to have the maximum of the first harmonic in the energy range 7000 – 7500 eV. The optics comprised a pair of curved SiC mirrors in a Kirkpatrick Baez geometry at a grazing incidence angle of 3 mrad, followed by a Si(111) polychromator crystal in the Bragg geometry and an additional vertically focusing Si mirror at a grazing incidence of 3.5 mrad (Pascarelli et al., 2004). The size of the beam on the sample was approximately 10 μm x 10 μm FWHM. Spectra were recorded using a CCD-based position sensitive detector in the energy range 7070 – 7330 eV. Pixel - energy calibration was obtained by measuring spectra on a reference Fe foil sample.

Angle-dispersive X-ray diffraction measurements (XRD) were made at beamline ID30 at the European Synchrotron Radiation Facility (ESRF). The MAR 345 image-plate system at 450 mm distance from the sample was used as a detector. The size of the beam on the sample was approximately 10 μm x 9 μm FWHM. All samples measured with XAS were also studied at the same pressures by X-ray powder diffraction.

Theoretical calculations of the x-ray absorption spectra were based on an *ab initio* self-consistent real space multiple scattering method (Ankudinov et al., 1998; Ankudinov et al., 2002; Rehr and Albers, 2000; Zabinsky et al., 1995) for a cluster of atoms centered on the absorbing ion. The electric-dipole approximation was employed, meaning that only the transitions between the atomic core wave functions with orbital angular momentum *l* to the *l*+1 components of the normalized continuum wave functions were considered. The Hedin-Lundqvist (Hedin and Lindqvist, 1971) self-energy model was used for the exchange correlation potential. The computed XANES spectra were consistent with the final-state rule (von Barth and Grossman, 1982), where a core-hole is present in the charge density. Absorption Fe K-edge spectra were calculated for the MgO rock salt structure where 20% of

the Mg atoms were randomly substituted by the Fe ions. All the multi-scattering calculations were conducted on a spherical atomic cluster of radius of 10 Å.

In a solid solution, atoms are normally shifted from their regular positions due to the non-homogeneous environment. I calculated relaxed atomic coordinates in the $(\text{Mg}_{0.8}\text{Fe}_{0.2})\text{O}$ solid solution using a simple pair potentials method incorporating the GULP (Gale, 1997) code. A $4 \times 4 \times 4$ *fcc* supercell containing 512 ions with randomly distributed Mg and Fe in the cation sublattice was used for relaxation calculations and the resulting equilibrium atomic coordinates were transferred into the cluster for further *ab-initio* XANES spectra calculations. Parameters of the Buckingham interatomic pair potentials for Fe-O and O-O interactions were taken from Minervini and Grimes (Minervini and Grimes, 1999); and parameters of Mg-O short-range potential were fitted to reproduce the experimental structure and elasticity of MgO (Zha et al., 2000), resulting in $A_{\text{Mg-O}}=805.54$ eV and $\rho_{\text{Mg-O}}=0.3246$ Å. The presence of ferric iron in the ferropiclasite structure, as well as charge-compensating vacancies, was ignored in these calculations.

Mössbauer spectra of samples FP-1 and FP-2 were collected at pressures up to 56 GPa. The spectra are consistent with single-phase $(\text{Mg,Fe})\text{O}$, and no evidence for chemical inhomogeneity (e.g. FeO-rich regions) was found. A typical Mössbauer spectrum of sample FP-1 at 47 GPa is shown in Fig. 3.26 (inset). I deconvoluted the Mössbauer spectra according to the model, incorporating two Lorentzian quadrupole doublets, one for Fe^{2+} and one for Fe^{3+} sites (Dobson et al., 1998), where the amount of Fe^{2+} and Fe^{3+} was determined based on the absorption area of the relevant doublet. Within the pressure range from 3 to 56 GPa, the proportion of Fe^{3+} in each sample remains essentially constant: the $\text{Fe}^{3+}/\Sigma\text{Fe}$ ratio fluctuates around 4.7 % for sample FP-1 and 7.7 % for sample FP-2 within the estimated error of 0.4%. I did not observe any significant difference in the high-pressure behavior between the FP-1 and FP-2 samples within the uncertainty of the measurements. The isomer shift of the main doublet depends linearly on pressure with a slope of about -0.003 mm/s per GPa within the studied pressure range. I observed a strong non-monotonous pressure dependence of the quadrupole splitting: it increases up to pressures of about 36-37 GPa and decreases at higher pressures (Fig. 3.26). No difference between compression and decompression paths was observed, and the quadrupole splitting changes described above were completely reversible. Quadrupole splitting is a sensitive indicator of the distortion of the local iron environment. For example, in FeSiO_3 clinoferrosilite the distortion of the $M2(\text{Fe}^{2+})$ octahedron is coupled to a rapid decrease of quadrupole splitting (McCammon and Tennant, 1996). I infer that the changes in quadrupole splitting of samples FP1 and FP2 are also due to changes in the

distortion of the local Fe^{2+} environment. No evidence of magnetic ordering or line broadening in Mössbauer spectra were observed up to the highest pressure reached in this study (56 GPa). As was shown for FeO (Kantor et al., 2004-II), even when magnetic ordering is incomplete and the Mössbauer spectrum does not show a resolved six-line structure, magnetic ordering can be easily detected by significant broadening of absorption lines: neither effect was observed in the high-pressure Mössbauer spectra of the ferropericlyase samples.

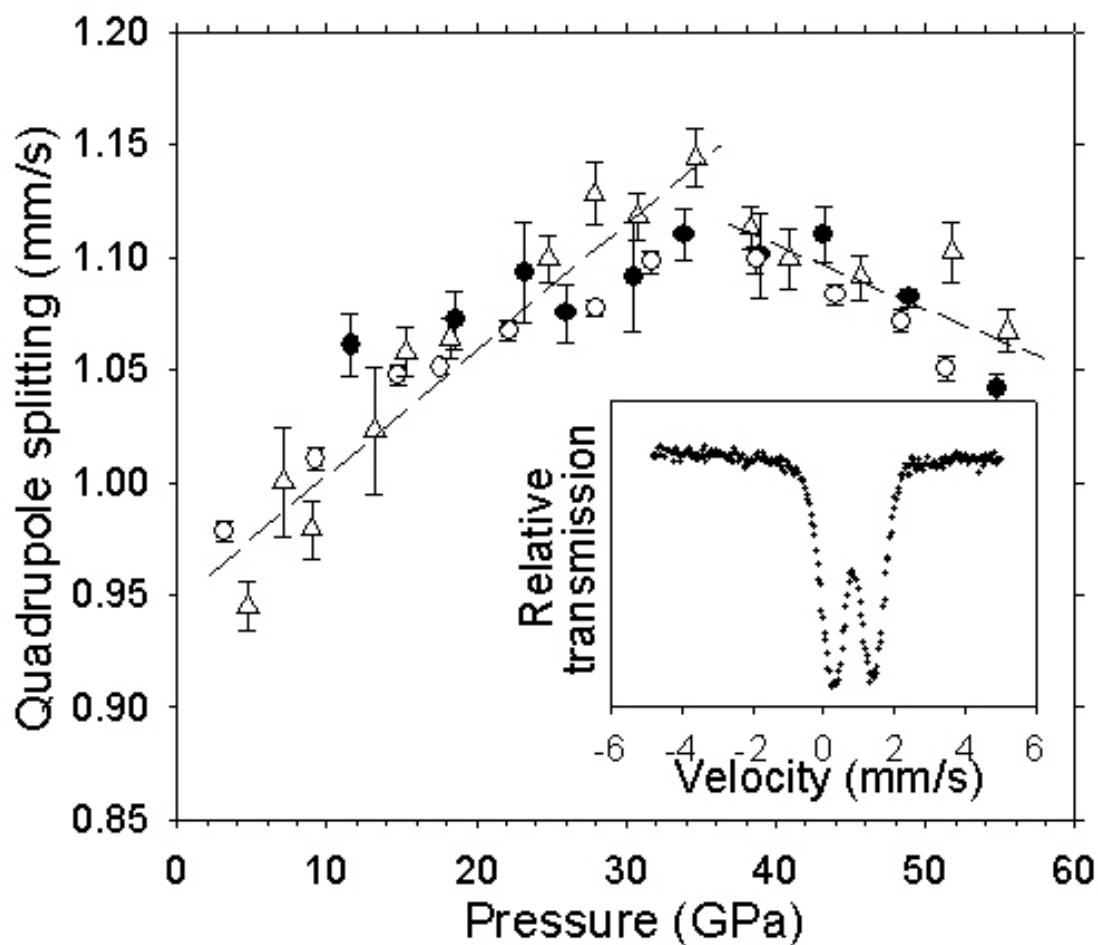


Fig. 3.26. Quadrupole splitting of the dominant doublet derived from room temperature Mössbauer spectra as a function of pressure. Solid circles – compression path of sample FP-1, open circles – decompression path of sample FP-1, triangles – compression path of sample FP-2. Dashed lines are guides for the eye. Inset: Mössbauer spectra of sample FP-1 at 47(1) GPa. The velocity scale is relative to α -Fe.

X-ray absorption spectra were collected from 0 to 59 GPa at room temperature in the DAC. Selected spectra at different pressures are shown in Fig. 3.27. In general, Fe K-edge XANES spectra of ferropericlyase are similar to Co and Ni K-edge XANES spectra of

(Co,Mg)O and (Ni,Mg)O solid solutions (Kuzmin et al., 1997). Upon compression the peaks in the XANES spectra of sample FP-1 shift to higher energies, mainly due to increasing electron density at the Fe nucleus (no XANES or XRD spectra were collected for sample FP-2 due to time constraints and the observed lack of significant influence of Fe^{3+} concentration on the transition seen in Mössbauer data). Changes in the spectra as a function of pressure can be highlighted using $\delta\mu/\delta E$ derivatives (Fig. 3.28), and show that, in particular, the intensity minimum at ~ 7127 eV disappears near 36 GPa. One of the most important characteristics of XANES spectra is the position of the absorption edge (usually defined as a maximum of the first derivative), which is sensitive to the valence state and chemical bonding of the absorbing atom (Srivastava and Nigam, 1973; Lytle et al., 1988). The absorption-edge position of ferropericlase increases with increasing pressure, but not monotonously (Fig. 3.29). If all data that are clearly below ($P < 30$ GPa) and above ($P > 40$ GPa) the transition are fitted separately to linear models, the lines intersect at 34 GPa. I observed that all changes to the spectra were completely reversible and showed no pressure hysteresis, and the XANES spectrum of the recovered sample was identical to that of the starting material.

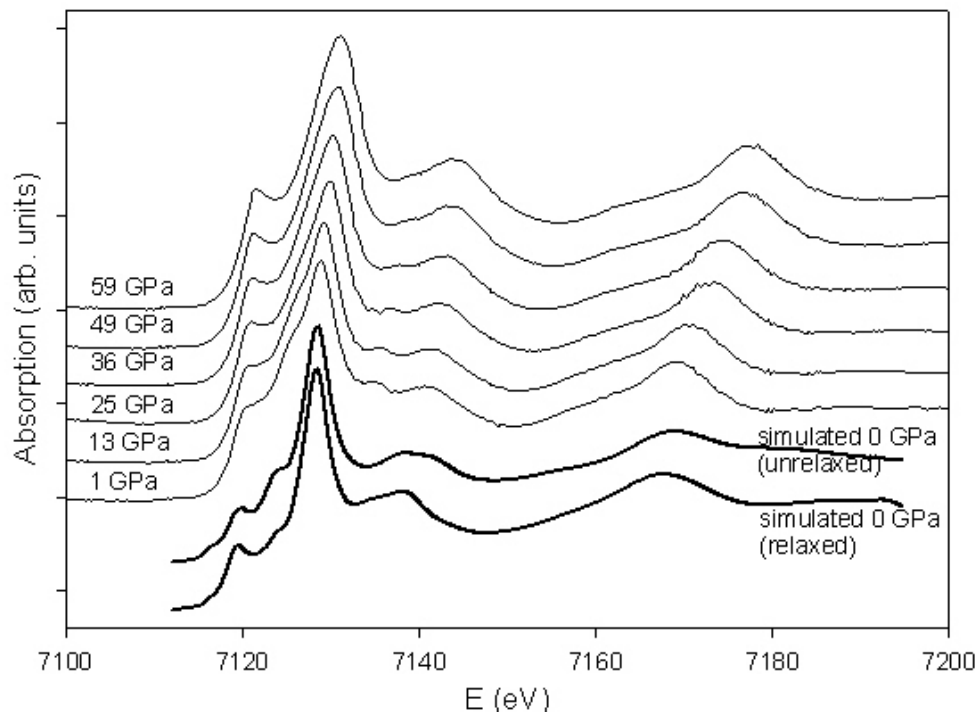


Fig. 3.27. Experimental XANES spectra of sample FP-1 at various pressures (six upper curves) and simulated XANES spectra at zero pressure with relaxed and unrelaxed atomic coordinates (two lower curves - see text for details). Spectra are shifted vertically for clarity.

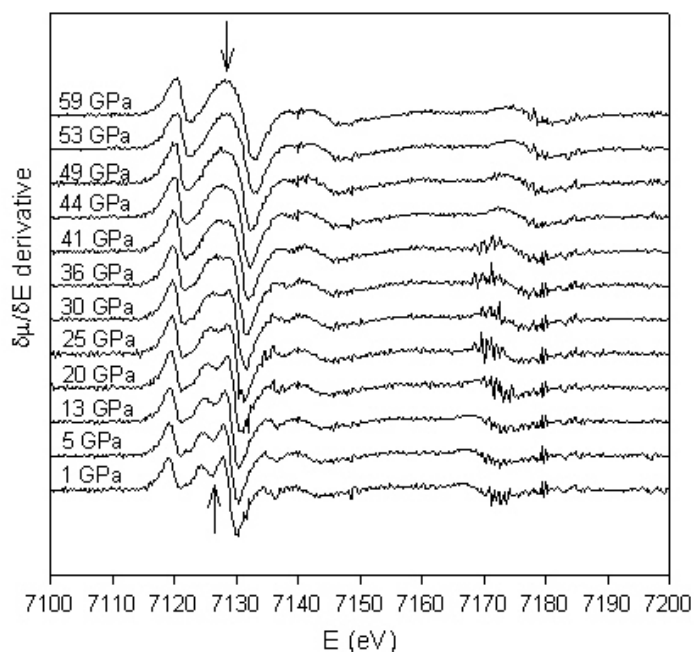


Fig. 3.28. $\delta\mu/\delta E$ derivatives of experimental XANES spectra from sample FP-1. Arrows indicate the region in which changes are observed at about 36 GPa.

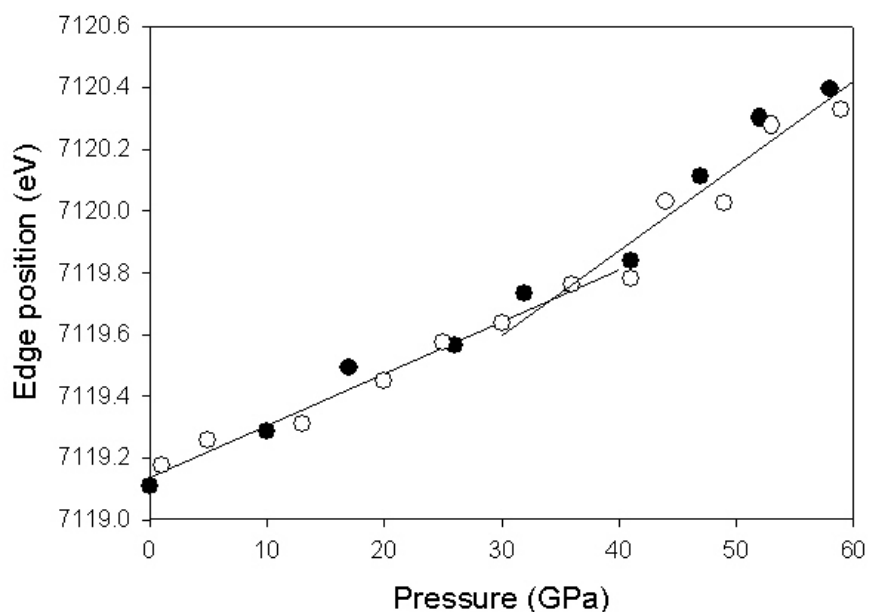


Fig. 3.29. X-ray Fe K- α edge position derived from experimental XANES spectra of sample FP-1 as a function of pressure. Solid and open symbols represent compression and decompression paths, respectively. Lines are least-square linear fits to the high- and low-pressure data with intersection at 34 GPa.

We performed *ab initio* calculations of the XANES spectra in order to compare them with those from the experiments. Due to the difficulty of *ab initio* calculations to account for

the strong electron correlations in these types of oxides, I do not expect the calculated positions of all spectral features to be correctly determined, but it is instructive to investigate if at least the topological features can be reproduced. The first calculation was made assuming that all ions are located in the regular positions of the cubic lattice. With this assumption, the “unrelaxed” Fe K-edge absorption spectrum is in generally good qualitative agreement with the experimental data, where the most significant qualitative deviation is a small feature at about 7135 eV that is absent in the calculated spectrum (Fig. 3.27). In order to improve our calculations, I modelled a more physically realistic case when atoms are shifted from their regular positions. I calculated relaxed coordinates of atoms using simple pair atomic potentials, and then used these relaxed coordinates for *ab initio* calculations of the XANES spectrum. Although the average shift of atoms from their regular positions was small (about 0.03 Å), the qualitative agreement of the calculated XANES spectrum with the experimental spectra is improved (Fig. 3.27, 3.26). P. Kizler (1992) described a mathematical procedure to treat XANES spectra to make features of the spectra more pronounced, that is taking a difference between the initial curve and a 5-eV running average (Fig. 3.30). As seen from Fig. 3.30, the relaxed spectrum is in better agreement with the experimental spectra, and the feature at ~7135 eV appears as indicated by the arrow.

The X-ray diffraction data of sample FP-1 can be fit perfectly to a cubic rock-salt structure up to 35 GPa. At pressures higher than 36 GPa, some of the diffraction peaks rapidly start to become broadened. The transition from a cubic to a rhombohedral structure should result in the splitting of 111_c , 220_c , and 311_c cubic reflections, while the most intense 200_c cubic reflection remains unsplit (Mao et al., 2002; Shu et al., 1998-I). From the X-ray diffraction images I can clearly see the splitting of the 220_c reflection (Fig. 3.31), although in the integrated pattern the line splitting is less pronounced (Fig. 3.32). Generally in this system (FeO-MgO) the deviation from cubic symmetry is small, and the transition pressure of powder samples is determined by the increase of the full width at half maximum (FWHM) of the 220_c peak compared to the FWHM of the 200_c peak (Mao et al., 2002). Figure 3.33 shows the pressure variation of the FWHM of the 220_c and 200_c peaks normalized to zero-pressure values. Rapid broadening of the 220_c reflection starts at 35(1) GPa, that I believe to be the transition pressure.

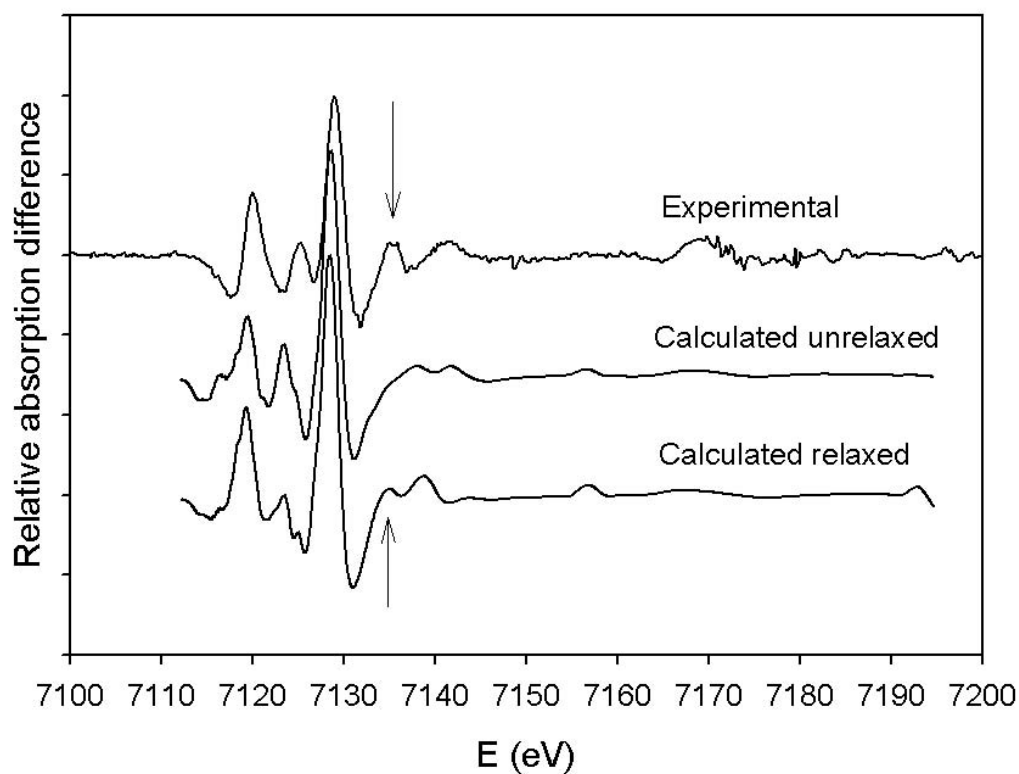


Fig. 3.30. Difference between XANES spectra and 5-eV running averages (see text) for experimental and calculated spectra at zero pressure. The arrows indicate the feature at ~ 7135 eV discussed in the text.

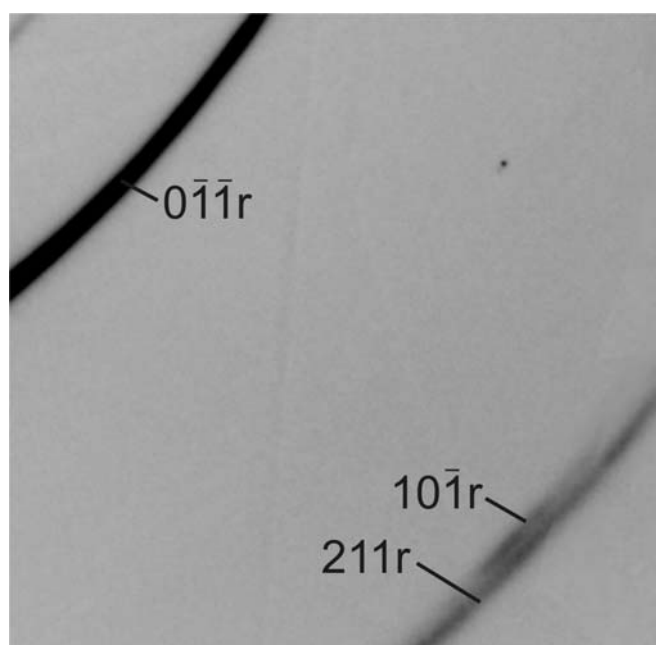


Fig. 3.31. Part of MAR345 diffraction image of sample FP-1 at 44(1) GPa. Reflection indices are for a rhombohedral lattice ($a = b = c$, $\alpha = \beta = \gamma \neq 60^\circ$).

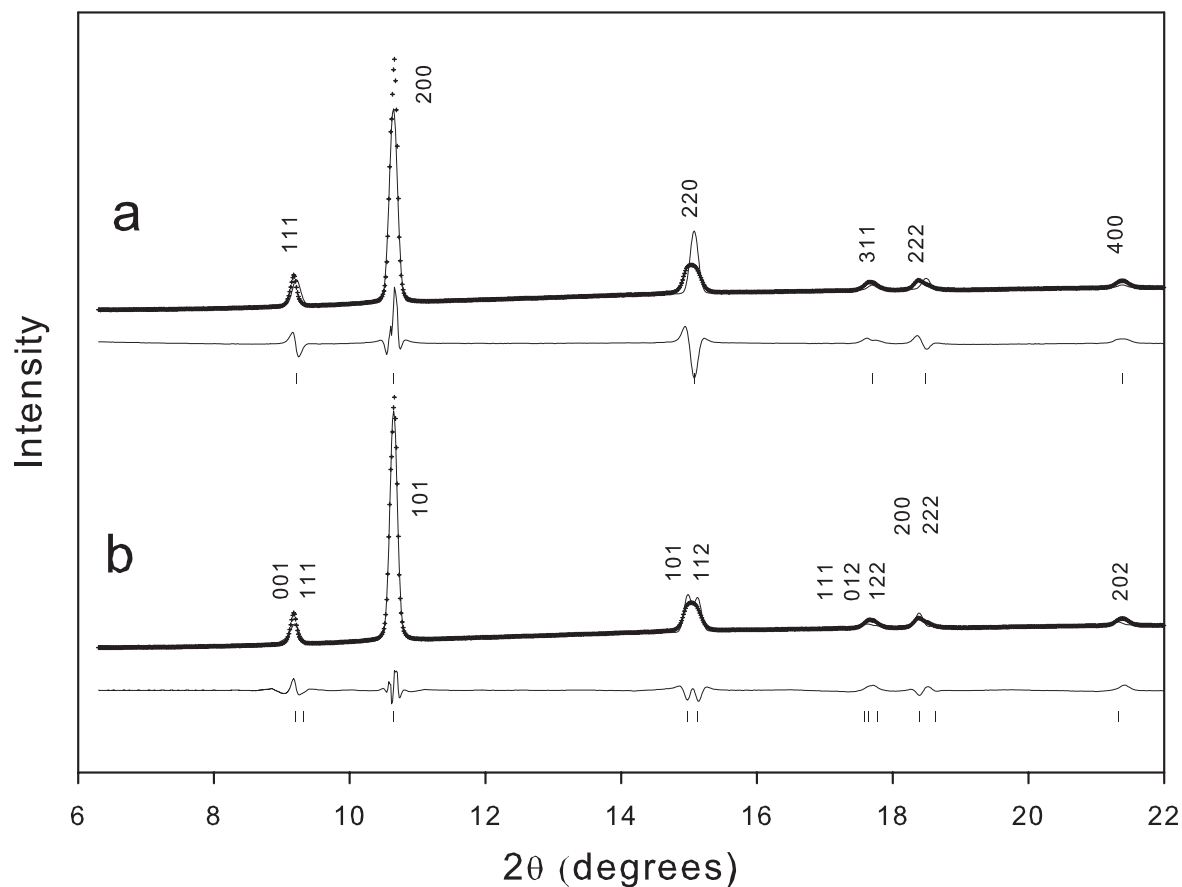


Fig. 3.32. Full-profile Rietveld refinement of rhombohedral and cubic structures at 41 GPa ($\lambda=0.3738 \text{ \AA}$).

(a) – cubic structure (space group $Fm\bar{3}m$) with cell parameter $a = 4.029(4) \text{ \AA}$ (crosses – experimental data, solid line – simulated). Final R-factors are $R_p=0.0554$, $R_{wp}=0.0253$, $\chi^2(\text{reduced})=4.163$.

(b) – rhombohedral structure (space group $R\bar{3}m$) with cell parameters $a = 2.810(5) \text{ \AA}$ and $\alpha = 60.70(1)^\circ$. Final R-factors are $R_p=0.0273$, $R_{wp}=0.0145$, $\chi^2(\text{reduced})=1.038$.

In both cases all fractional atomic coordinates are fixed by symmetry. Mg and Fe atoms were in the same position with occupancies of 0.8 and 0.2, respectively.

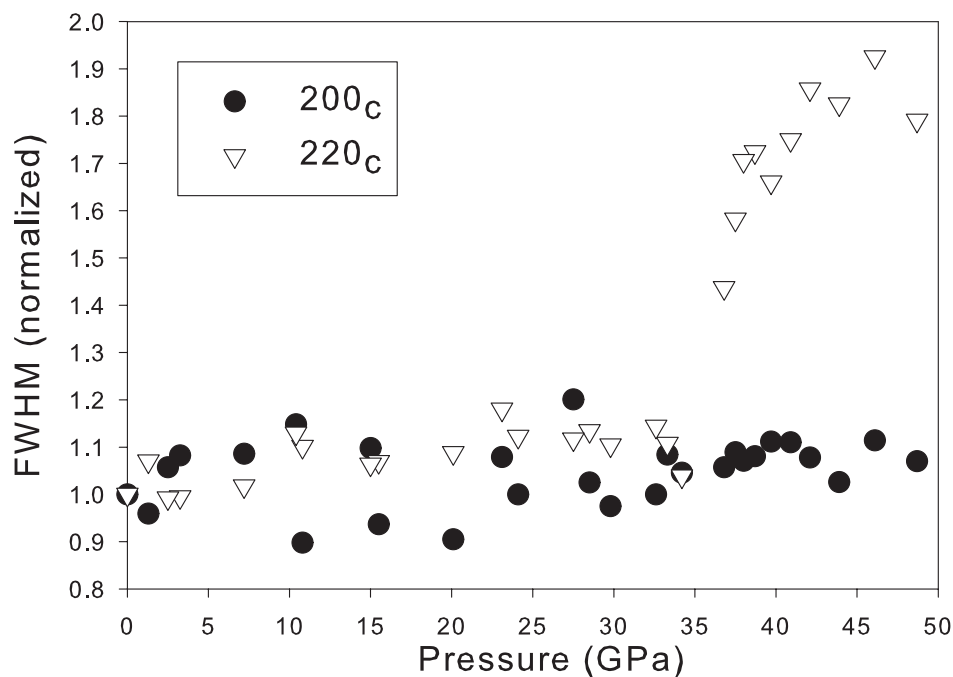


Fig. 3.33. Full width at half maximum (FWHM) of 200_c and 220_c reflections of $(\text{Mg}_{0.8}\text{Fe}_{0.2})\text{O}$ (normalized to the zero-pressure value) as a function of pressure.

There are several complications in analyzing powder diffraction data under high and non-hydrostatic pressure. The first is a pronounced stress development in the sample chamber of the DAC. On non-hydrostatic compression of a powder sample two principal types of stress develop: uniaxial stress caused by compression between two opposing diamonds, and local stresses that are generated by mismatches in the shapes of neighboring grains in the sample. In angle-dispersive XRD, only crystallites with one particular orientation contribute to the intensity of a particular reflection. This means that each Debye-Scherrer ring is formed by crystallites with different orientations with respect to the stress ellipsoid; hence each reflection is distorted in different way. As a result a set of integration parameters to transform 2D XRD images to a single-dimension dataset will be correct for one reflection (i.e. the Debye-Scherrer ring is circular), but not for others (the Debye-Scherrer rings are ellipses). Theories of angle-dispersive XRD under non-hydrostatic conditions predict that uniaxial stress affects diffraction line positions (Dubrovinsky and Dubrovinskaya, 2004; Funamori et al., 1997; Singh et al., 1998). Systematic shifts of d -spacings for different reflections appear due to inhomogeneous compression of the crystalline solid, which ideally requires the complete elastic tensor and uniaxial stress components to account for this effect. Local stress mainly produces broadening of some of the X-ray diffraction lines (Funamori et al., 1997). The second complication is a strong preferred orientation of powder crystallites, which

affects the relative peak intensities and also results in intensity variation along each of the Debye-Scherrer rings. For all of these reasons, a full-profile Rietveld refinement is not successful in reproducing the splitting of peaks (see Fig. 3.32). Instead, I performed an integration of separate peaks over a small area of the image plate with the most pronounced line splitting and without bright spots. The resulting patterns at 42(1) GPa are shown in Fig. 3.34, which shows clearly that the observed line splitting is consistent with a rhombohedral structure. The rhombohedral angle α , determined from all split reflections, is 60.5 ± 0.3 degrees. According to theories for XRD under non-hydrostatic conditions (Funamori et al., 1997; Singh et al., 1998; Dubrovinsky and Dubrovinskaia, 2004), non-hydrostaticity can affect line positions and width, but not produce line splitting. Pseudo-splitting can be observed only in the integrated pattern and only when three factors are combined: strong uniaxial stress (e.g. elliptical Debye-Scherrer rings), strong preferred orientation of crystallites in two directions (e.g. bright spots on the nearest and furthest parts of the ellipse) and integration of the entire Debye-Scherrer ring. Line splitting, such as shown in Fig. 3.31, can only be the result of a reduction in crystal symmetry.

P-V data were fitted to a second-order Birch-Murnaghan isothermal equation of state (EOS) with values $K_{300}=158(5)$ GPa and $V_0=11.53(1)$ cm³/mol for the cubic structure and $K_{300}=170(7)$ GPa and $V_0=11.21(1)$ cm³/mol for the rhombohedral structure (Fig. 3.35). According to these parameters, the phase transition from a cubic to a rhombohedral structure appears to be a first order, but with the caveat that no form of EOS can describe P-V data accurately near the transition point.

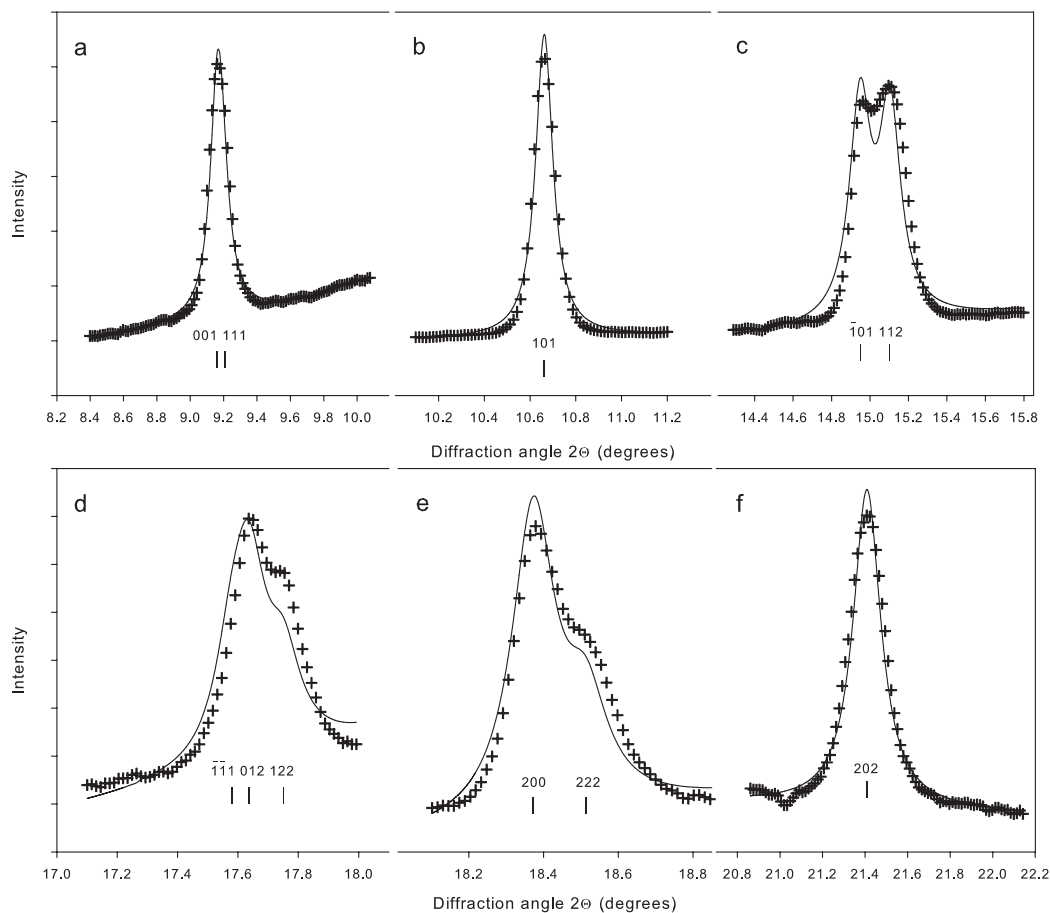


Fig. 3.34. X-ray diffraction patterns collected at 42(1) GPa showing splitting of former cubic reflections: a - 111_c ; b - 200_c ; c - 220_c ; d - 311_c ; e - 222_c ; and d - 400_c . Crosses - experimental intensity; solid lines - calculated for a rhombohedral structure with $\alpha \sim 60.4^\circ$. Ticks and indices below curves show the positions of rhombohedral reflections.

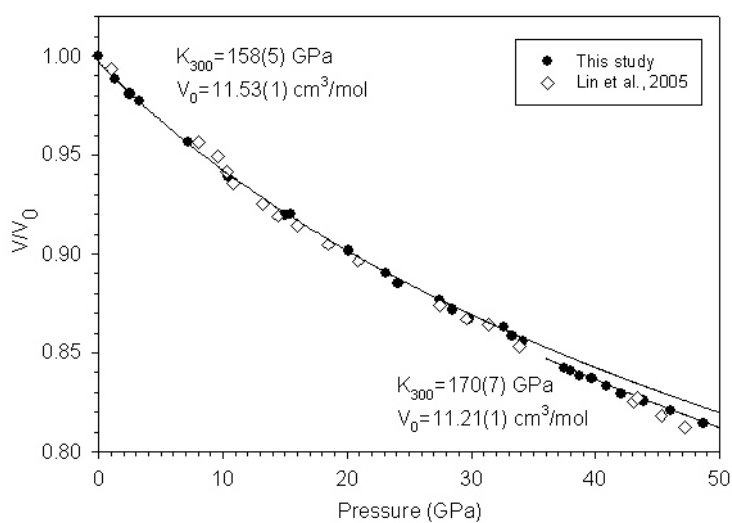


Fig. 3.35. Pressure-volume data for sample FP-1 (black circles). Fits to a 2nd-order Birch-Murnaghan equation of state are shown as solid lines. Data for $(\text{Mg}_{0.83}\text{Fe}_{0.17})\text{O}$ from Lin et al. (2005) are placed for comparison (open diamonds).

No pressure hysteresis in the phase transition was observed by XRD, and the diffraction pattern of the recovered sample was consistent with the ideal cubic structure.

Combined *in situ* X-ray powder diffraction, Mössbauer and XANES spectroscopy data on $(\text{Mg}_{0.8}\text{Fe}_{0.2})\text{O}$ unequivocally indicate a structural transition at 35(1) GPa and room temperature, where the high-pressure phase is interpreted on the basis of Rietveld refinements and line splitting analysis of image-plate data to be a rhombohedral structure. Mössbauer data show clearly the absence of magnetic splitting in spectra from the high-pressure phase to at least 56 GPa, which establishes the stability of the rhombohedral distortion in the absence of magnetic ordering. Similarly, the magnetic ordering transition in FeO was recently shown to occur independently of the rhombohedral structural transition at high pressure and room temperature (Kantor et al., 2004-I,II). This decoupling of the rhombohedral distortion from magnetic ordering has important implications for understanding the fundamental interactions in transition metal monoxides. Firstly, the nature of the structural distortion at low temperatures and at high pressures should be re-examined: if the structural transition is not driven by magnetization, another type of interatomic interaction or particular aspects of metal-oxygen chemical bonding may be responsible. Secondly, magnetoelastic coupling in the transition metal monoxides may not be as strong as previously thought (Struzhkin et al., 2001), so that rapid mode softening might not be connected with magnetic interactions, but only with the structural phase transition.

The composition $x_{\text{Fe}}=0.2$ is the lowest iron concentration in $(\text{Mg,Fe})\text{O}$ so far where a cubic-to-rhombohedral phase transition has been reported (Fig. 3.36). However comparison of results from different laboratories is complicated by two factors: (1) experimental resolution must exceed a certain value in order to detect the transition; and (2) the effect of non-hydrostatic stress on the phase transition. Hence the observation that no phase transition occurs in the compositions $x_{\text{Fe}}=0.4$ (Shu et al., 1998-II) and $x_{\text{Fe}}=0.6$ (Lin et al., 2003; Richet et al., 1989) could also be interpreted to indicate that experimental resolution was not sufficient to observe the transition. For example in the present study the presence of the transition could not be confirmed using only the integrated X-ray diffraction patterns (see above). Also, the presence of overlapping peaks from the pressure medium, e.g. NaCl (Lin et al., 2003) can also reduce experimental resolution.

Non-hydrostatic stress likely affects the pressure of the structural transition in $(\text{Mg,Fe})\text{O}$. Previous experiments have already demonstrated that the degree of non-hydrostaticity affects the structural transition pressure in FeO (Dubrovinsky et al., 2000-I), and comparison of previous experimental results for $(\text{Mg,Fe})\text{O}$ show a trend to increasing

transition pressure as the degree of non-hydrostatic stress in the experiment is reduced (Fig. 3.36). Non-hydrostatic stress can also change the nature of the transition, e.g. a second-order transition becomes a tricritical under stress in MnO (Bloch et al., 1975).

The observed high-pressure X-ray diffraction patterns indicate a lowering of crystal symmetry, and cannot be described as a cubic phase under non-hydrostatic stress as discussed in the previous section. On the other hand, the cubic-to-rhombohedral transition could be driven by uniaxial stress; in other words, the transformation could be stress induced. Since the degree of pseudo-cubic lattice distortion is known, a strain tensor can be easily calculated. However in order to transform the strain tensor into a stress tensor, the full single-crystal elastic tensor is required, which is unknown for $(\text{Mg}_{0.8}\text{Fe}_{0.2})\text{O}$ ferropericlase under high pressure. In order to make estimations of stress tensor components, I used elastic constants of pure MgO, which are well determined at high pressure (Zha et al., 2000). This calculation shows that a uniaxial stress of about 3 GPa is required to produce a corresponding ($\alpha = 60.5^\circ$) rhombohedral distortion of the cubic lattice at 40 GPa. The magnitude of this stress is within values expected for DAC experiments conducted without a pressure medium (Merkel et al., 2002); hence stress development could be a driving mechanism for the phase transition. However the electronic structure is also a factor, because no evidence of a rhombohedral distortion has been observed in pure MgO (Duffy et al., 1995; Merkel et al., 2002) even at extreme pressures and under high uniaxial stress.

On the basis of this study, I have clearly shown that 20 mol% FeO is sufficient to induce a rhombohedral distortion in $(\text{Mg},\text{Fe})\text{O}$ at a confining pressure of ~ 35 GPa in the presence of uniaxial stress. It is also clear from Mössbauer spectroscopy that the rhombohedral distortion of $\text{Mg}_{0.8}\text{Fe}_{0.2}\text{O}$ is not associated with long-range magnetic ordering. A rhombohedral distortion in ferropericlase with mantle composition ($\text{Mg}_{0.8}\text{Fe}_{0.2}\text{O}$) could influence physical properties of the Earth's lower mantle, since such a phase transition is accompanied by a rapid C_{44} mode softening (Sumino et al., 1980) and by a decrease of sound wave velocities.

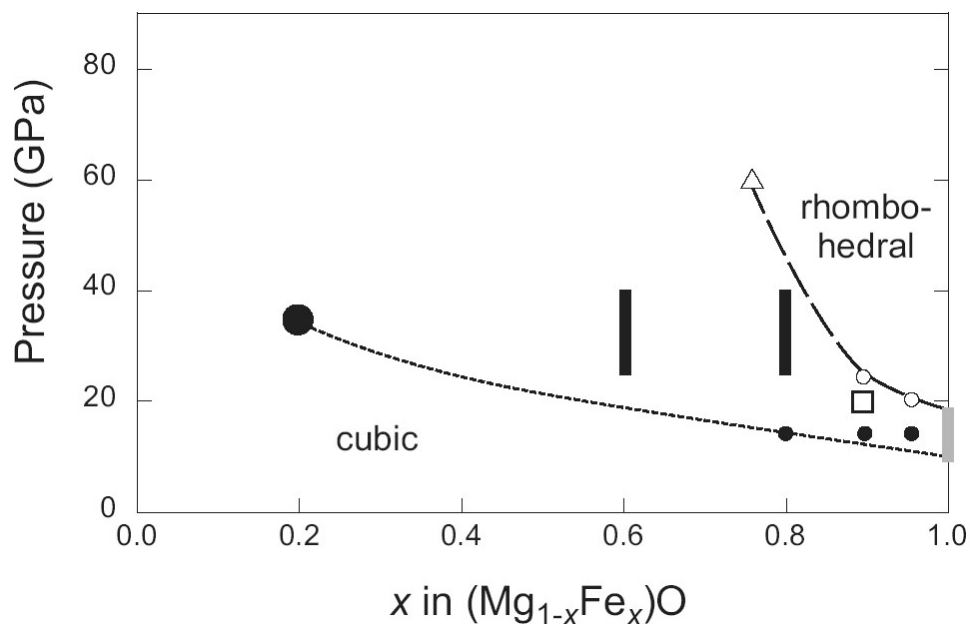


Fig. 3.36. Phase diagram for $(\text{Mg,Fe})\text{O}$ at room temperature showing the cubic-rhombohedral phase boundary. Solid symbols represent experiments where non-hydrostatic stress is large, while open symbols indicate experiments where a pressure medium was used and non-hydrostatic stress is inferred to be less. Small solid circles – *Kondo et al.*, 2004; black bars and open circles – *Shu et al.*, 1998-II; triangle – *Lin et al.*, 2003; square – *Mao et al.*, 2002; large solid circle – this work; grey bar – range of transition pressures observed in FeO using different types of pressure media (*Shu et al.*, 1998-I; *Yagi et al.*, 1985). The dotted line indicates the inferred phase boundary for experiments conducted under conditions of large non-hydrostatic stress, while the dashed line indicates the boundary inferred for experiments where non-hydrostatic stress is significantly less. Results from experiments where no cubic-rhombohedral transition was observed are not shown on the plot due to the ambiguity of whether experimental resolution was sufficient to distinguish the rhombohedral distortion (see text).

III.5. Pressure-induced spin crossover in ferropericlasite

Iron, being a transition metal with uncompleted d-electron shell, can exist in different spin states. The Fe^{2+} ion has a $3d^6$ electronic configuration, and six electrons are distributed over five d-orbitals. For a free ion all of these orbitals have equal energy. In a ligand field of octahedral symmetry the degeneracy is removed, and orbitals are split into two E_g orbitals with higher energy and three T_{2g} levels with lower energy, which are separated by an amount Δ_o (the O subscript stands for “octahedral” splitting). I will use the Δ_o notation for the octahedral crystal field splitting in order to distinguish from the Mössbauer quadrupole splitting Δ . Electronic occupation of d-orbitals depends on the magnitude of Δ_o . In a weak field Δ_o is small, and the energy gain from unpaired electrons overcomes the crystal-field splitting and a high-spin configuration with four unpaired electrons exists (Fig. 3.37.a). In a strong field Δ_o is higher with respect to the electron-pairing energy and electrons occupy lower-energy levels. This state is called low-spin with no unpaired electrons (Fig. 3.37.b).

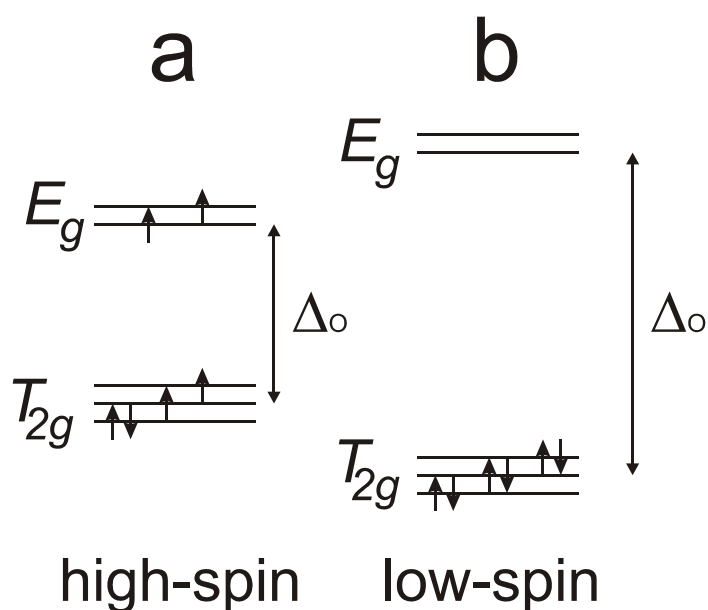


Fig. 3.37. Energy levels of Fe^{2+} in an octahedral field. a) – weak field (high-spin state) and b) – strong ligand field (low-spin state).

The crystal-field splitting describes the d-electron energy levels only in a pure ionic state. The ligand field theory expresses the energy levels of a partly filled d-shell in terms of two types of parameters: the orbital energy differences Δ_o and the integrals of interelectronic repulsion. These integrals are described by the empirical Racah parameters, and the resulting energy levels (known as Tanabe-Sugano diagrams) are quite complex for a Fe^{2+} octahedral compound. Racah parameters reflect the degree of metal-ligand bond covalency, and a low-

spin state could be stabilised even with a small value of Δ_O in the case of strongly covalent chemical bonding. Both crystal-field splitting and Racah parameters depend on thermodynamic parameters, and the spin state of iron can be changed by varying temperature or pressure. Such a transition is known as a spin transition or spin crossover and occurs in many metal-organic and other compounds. Physical properties can change dramatically upon spin crossover. Sometimes there is a strong density change (by a few percent), optical property changes, and even structural transitions caused by iron spin crossover. In low-spin Fe^{2+} there are no unpaired electrons and magnetic moments, and hence transformation to the low-spin state causes also a loss of magnetism.

The main iron-bearing minerals in the Earth (olivine and its high-pressure modifications, pyroxenes, ferropicicase and silicate perovskite) contain iron in a high-spin state at ambient conditions. However, high pressure in the Earth's interior could induce a spin-pairing transition in all these materials, which can have a significant effect on the properties of corresponding phases. Possible iron spin crossover in the main lower-mantle phases silicate perovskite and ferropicicase has been a subject of numerous experimental and theoretical studies. Here I present some results concerning spin crossover in low-iron containing ferropicicase, the second most abundant mineral in the Earth's lower mantle.

Three ferropicicase samples were used in this study (Fe5, Fe13 and Fe20), and sample synthesis description is given in section III.3. Mössbauer spectra of these samples were collected up to 105 GPa, and at high pressures clear changes that are consistent with spin crossover were observed (Fig. 3.38). Above ~ 50 GPa a new component appears in the Mössbauer spectra of ferropicicase. This new component has virtually zero quadrupole splitting and an isomer shift somewhat smaller than the high-spin component. This is typical for low-spin Fe^{2+} : when there are no unpaired electrons, the charge distribution becomes much more symmetrical and the electrical field gradient (EFG) becomes essentially zero because of the disappearance of the valence electrons EFG contribution. The total charge (electron) density at the Fe nucleus increases, and this is the reason for the IS decrease. The absolute change of the isomer shift (Fig. 3.39) is, however, relatively small (appr. 0.17 mm/s) compared to those (~ 0.5 mm/s) usually observed for iron-organic complexes (Gütlich et al., 1978).

In order to prove that this change is indeed due to a spin change of iron, the charge densities for high- and low-spin Fe^{2+} in (Mg,Fe)O were calculated. The calculations details and supercell configurations are described in section III.3. There was no significant difference in charge density for the isolated Fe ion, and for 2Fe and 3Fe clusters. Calculations

were made for the cell parameter $a = 4.25, 4.00, \text{ and } 3.80 \text{ \AA}$ and for high- and low-spin iron electronic configurations. According to the Eq. 2.4, the isomer shift depends not only on the electron density, but also on the difference of the mean squared radii of the ground and excited nuclear states. The latter value could not be calculated or measured directly, and for practical usage a simple relationship $\Delta\delta = \alpha \times \Delta\rho$ is used, where $\Delta\delta$ is the change in isomer shift, and $\Delta\rho$ is the change in electron density. Calibration of the coefficient α is straightforward: the electron density for several Fe compounds can be calculated *ab initio*, and isomer shifts can be measured experimentally. However, depending on which theoretical method and compounds are used, the value of α can be significantly different. Literature values vary from -0.11 to $-0.62 \text{ bohr}^3 \times e^{-1} \times \text{mm} \times \text{sec}^{-1}$ (Table III.5.1). We calculated also the charge density for α -Fe, since experimental values of the centre shift reported here are given relative to α -Fe. I used only the α -Fe value and one ferroperricite calculation at zero pressure in order to calibrate the α coefficient. The obtained value of $-0.32 \text{ bohr}^3 \times e^{-1} \times \text{mm} \times \text{sec}^{-1}$ agrees fairly well with many previous determinations (see Table III.5.1). All other values of IS were obtained directly from the calculations and show perfect agreement with the experiment (Fig. 3.39).

On compression at ambient temperature, in all three ferroperricite samples the low-spin component gradually increases with increasing pressure, and the amount of the high-spin component decreases accordingly (Fig. 3.40). The high-spin and low-spin fractions were calculated from the absorption areas of the subspectral components, assuming equal Debye-Waller factors of the HS and LS Fe ions. In fact this is not true, but this difference is usually neglected (Gütlich et al., 1978). The studied samples were highly enriched with the ^{57}Fe isotope and the effective Mössbauer thickness was much higher than ideal. The high thickness of the absorber results in significant internal multiple absorption, which could significantly distort the relative areas of the two subspectral components in the mixed spin region. Thickness corrections can be accounted for using a full transmission integral calculation (Cranshaw, 1974). We used NORMOS software (a commercially available fitting program written by R.A. Brand and distributed by Wissenschaftliche Elektronik GmbH, Germany) to perform simultaneous full transmission integral calculations and non-linear least-squares spectrum fitting. The thickness of the source is also higher than in conventional experiments due to the higher concentration of ^{57}Co in a point source, but thickness effects in the source are much smaller compared to those in the absorber. At a source age of six months, which is when the measurements reported in this work were made, the dimensionless effective thickness of the source is less than 2. After correction for thickness effects the

linewidth (full width at half maximum) of the LS component decreases from 0.81 mm/s to 0.40 mm/s, which is only slightly greater than the linewidth recorded for iron metal using the same source. The relative subspectral components areas are not significantly affected by thickness effects no more than 10-15%.

The range over which high- and low-spin states coexist is remarkable: for the Fe5 sample it is about 30 GPa, and more than 50 GPa for the Fe20 sample (Fig. 3.40). Such a broad region of spin crossover cannot be attributed to pressure gradients in the DAC. With several small ruby chips placed in different parts of the sample chamber, pressure gradients could be measured and were not higher than 5-7 GPa.

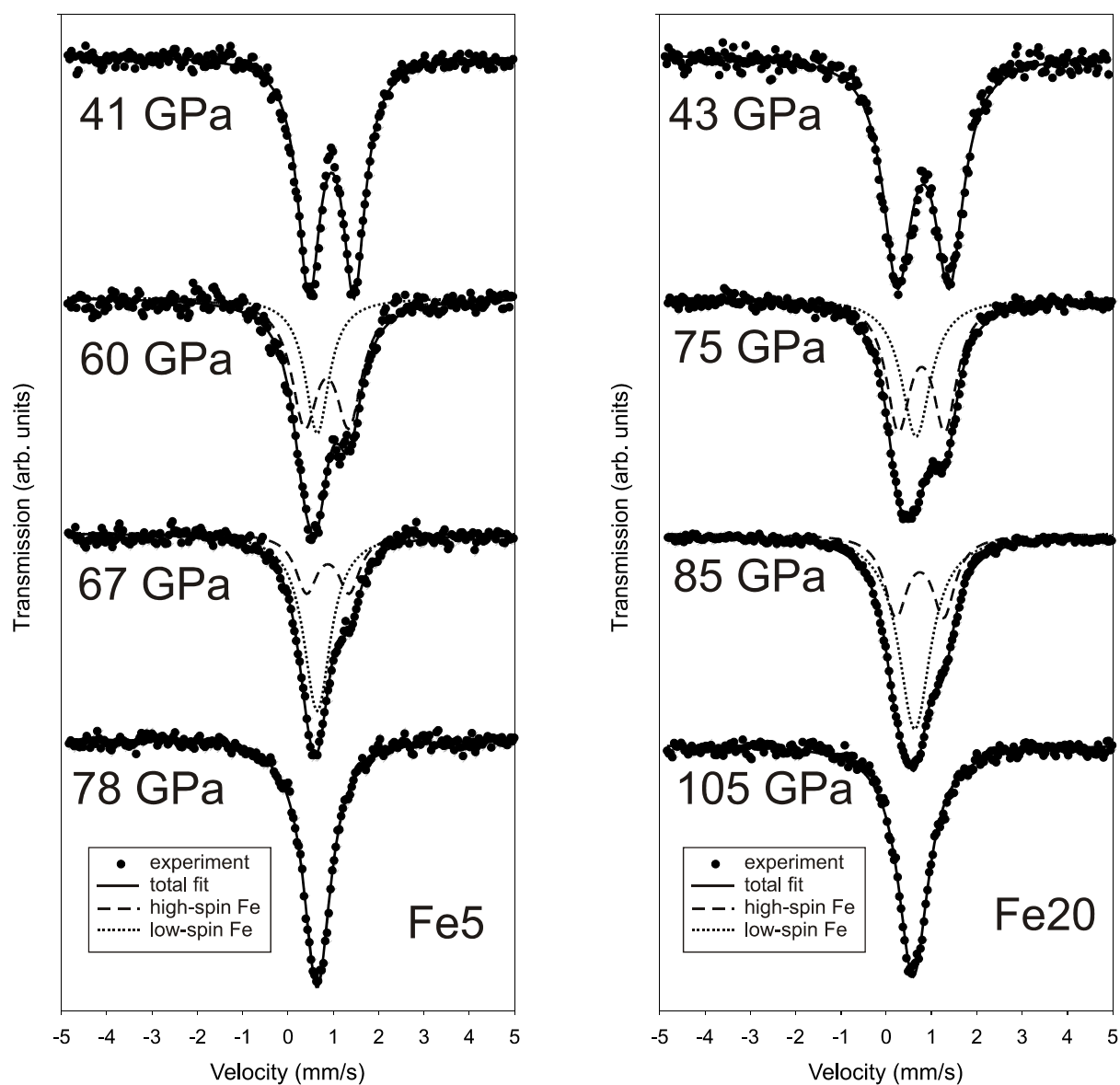


Fig. 3.38. Room temperature Mössbauer spectra of Fe5 (left) and Fe20 (right) ferropericlase samples upon spin crossover. Dashed lines show the high-spin component and dotted lines show the low-spin component in the spectra.

Table 3.2. Conversion parameter α for ^{57}Fe determined by different authors.

α (bohr ³ $\times e^{-1}\times\text{mm}\times\text{sec}^{-1}$)	Author (s)	Year
-0.11	Simanek and Sroubek	1967
-0.13	Pleiter and Kolk	1971
-0.15	Simanek and Wong	1968
-0.15	Sharma and Sharma	1972
-0.17	Kündig	1976
-0.19	Wakoh and Yamashita	1968
-0.20	Danon	1966
-0.23	Duff	1974
-0.28	Moyzis and Drickamer	1968
-0.33	McNab et al.	1971
-0.34	Trautwein et al.	1973
-0.37	Ingalls	1967
-0.38	Walch and Ellis	1973
-0.51	Walker et al.	1961
-0.62	Uher and Sorensen	1966
-0.32	Present work	

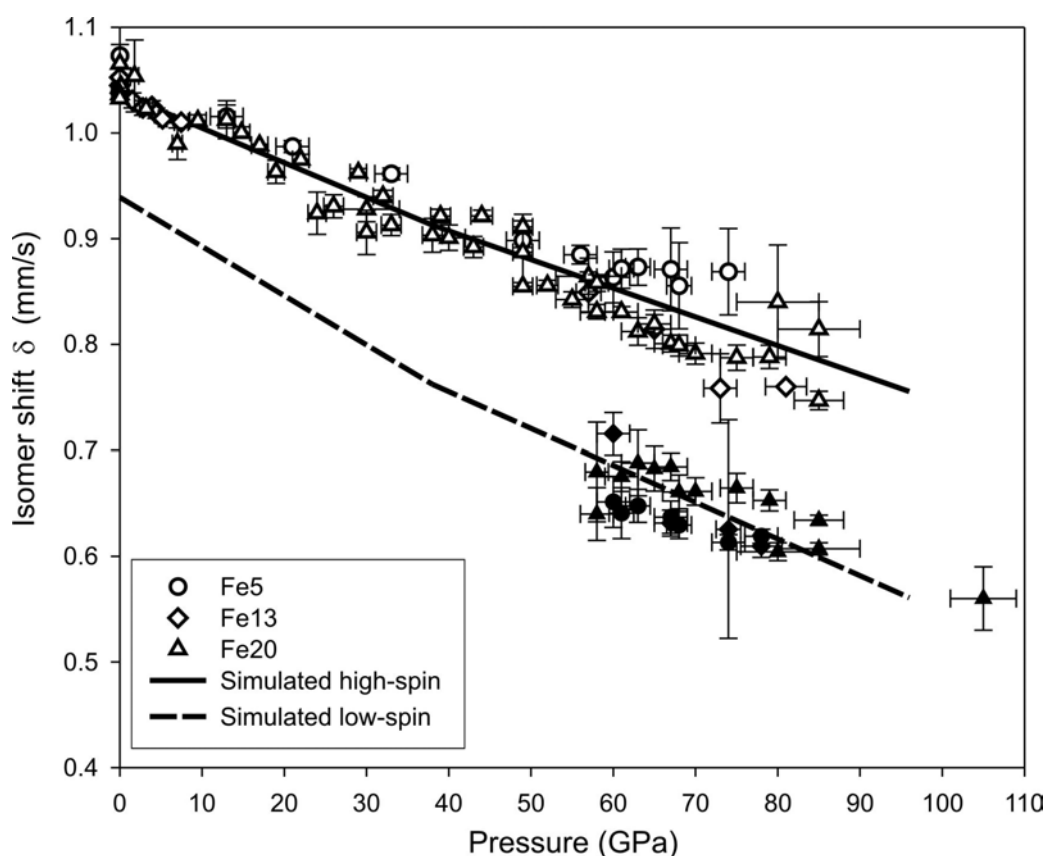


Fig. 3.39. Pressure dependence of ferropericlasite isomer shift (values are given relatively to $\alpha\text{-Fe}$). Open and closed symbols are for high- and low-spin components, respectively. Circles, diamonds and triangles are for Fe5, Fe13, and Fe20 samples, respectively. Solid and dashed lines show the results of *ab-initio* simulations.

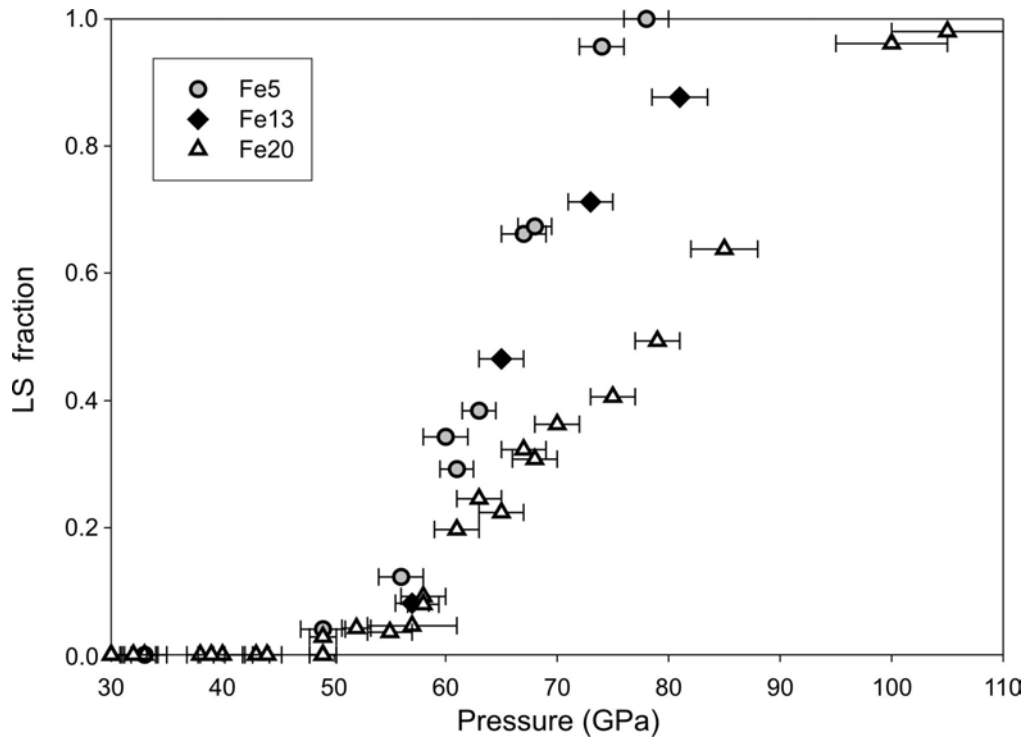


Fig. 3.40. Low-spin fraction in ferropericlase as a function of pressure at room temperature. Circles, diamonds and triangles are for Fe5, Fe13, and Fe20 samples, respectively.

In order to understand these results on spin crossover in ferropericlase, a brief digression into the physics of this phenomenon in general should be made. Spin crossover in ferropericlase is often discussed in terms of a phase transition. A number of studies are focused on a determination of the volume (density) collapse, and the magnitude of seismic wave velocity discontinuity associated with the spin transition. The question of whether it is a first- or a second-order transition is also discussed (Lin et al., 2005; Speziale et al., 2005; Tsuchiya et al., 2006; Sturhahn et al., 2006). However, spin crossover is not necessarily a phase transition. In order to apply a thermodynamic theory of phase transitions, there should be two distinct phases – a high-spin and a low-spin phase. In the case of two or more possible different states of an atom (in this case high- or low-spin electronic configuration), all the states have always (at any finite temperature) a certain non-zero probability. Every energy level or quantum state of an atom, however high an energy level is populated, as described by the Boltzmann thermal population function. This means that in any Fe^{2+} compound and under any thermodynamic conditions, there are some iron ions in a high-spin and some in a low-spin state. Usually, one state is dominating and the other state has negligible population, and a compound is considered to be either high- or low-spin. However, there can be a continuous change in spin probability between these two states. The term “spin crossover” reflects this

particular idea: at some particular P, T -conditions the low-spin probability and the high-spin probabilities are equal. Different molecules or ions within the same crystal exist in different spin states while the crystal is still a single phase (Bolvin and Kahn, 1995). When both spin states of iron coexist in significant amounts in a single crystal, they cannot be considered as two distinct phases. However, the physical properties and chemical bonding in high- and low-spin Fe compounds can be significantly different, giving rise to a real phase transition. If any structural changes occur upon spin crossover, it should be described as a phase transition. In case there is a volume discontinuity or changes in symmetry of a crystal, spin crossover can be described in terms of a phase transition. Three principal cases are shown schematically in Fig. 3.41. If no phase transition occurs in the system, the high-spin fraction changes continuously (Fig. 3.41.a). In such a case the choice of the thermodynamic limits of a “high-spin”, “low-spin” and transition region is purely arbitrary. For instance, one can call assign a “high-spin” state if there are less than 1% of low-spin populated iron atoms, or 0.1%, or 5%. In this study I use a simple criterion based on the Mössbauer spectroscopy detection limits. If the amount of low- (high-) spin component is below the detection limit (2 - 5%), I assign it to be a high- (low-) spin state. The spin crossover point is exactly the point where the abundance of high- and low-spin are equal, but nothing particular occurs in the system at this point. In the case of a second-order phase transition associated with spin crossover (Fig. 3.41.b), the picture will be slightly different: a certain discontinuity in high-spin abundance is observed at the transition point. A strong hysteresis is unlikely in these two cases. Finally, there could be a first-order transition coupled with the spin transition (Fig. 3.41.c). In first order phase transitions a finite region of metastability exists (shown with the dashed line). The resulting (observed experimentally) abundance of high-spin Fe would show a hysteresis loop (dashed-dotted line) due to the presence of a metastable phase near the transition point. Examples of all three cases for the pressure-induced spin transition of iron can be found. For example, case “a” (no phase transition) exists for Fe^{2+} impurities in MnS_2 (Barger et al., 1971) and is more common for dilute Fe solid solutions in which iron does not play a dominating role in crystal structure formation. Case “b” (second-order phase transition coupled with spin crossover) was probably observed in a 1,10-phenanthroline complex (Thompson et al., 2004). A typical example of the “c” type – the first order transition with hysteresis is the α - to ϵ -iron transition (Taylor et al., 1991), where high-spin body-centred cubic iron transforms to low-spin hexagonal close packed ϵ -iron.

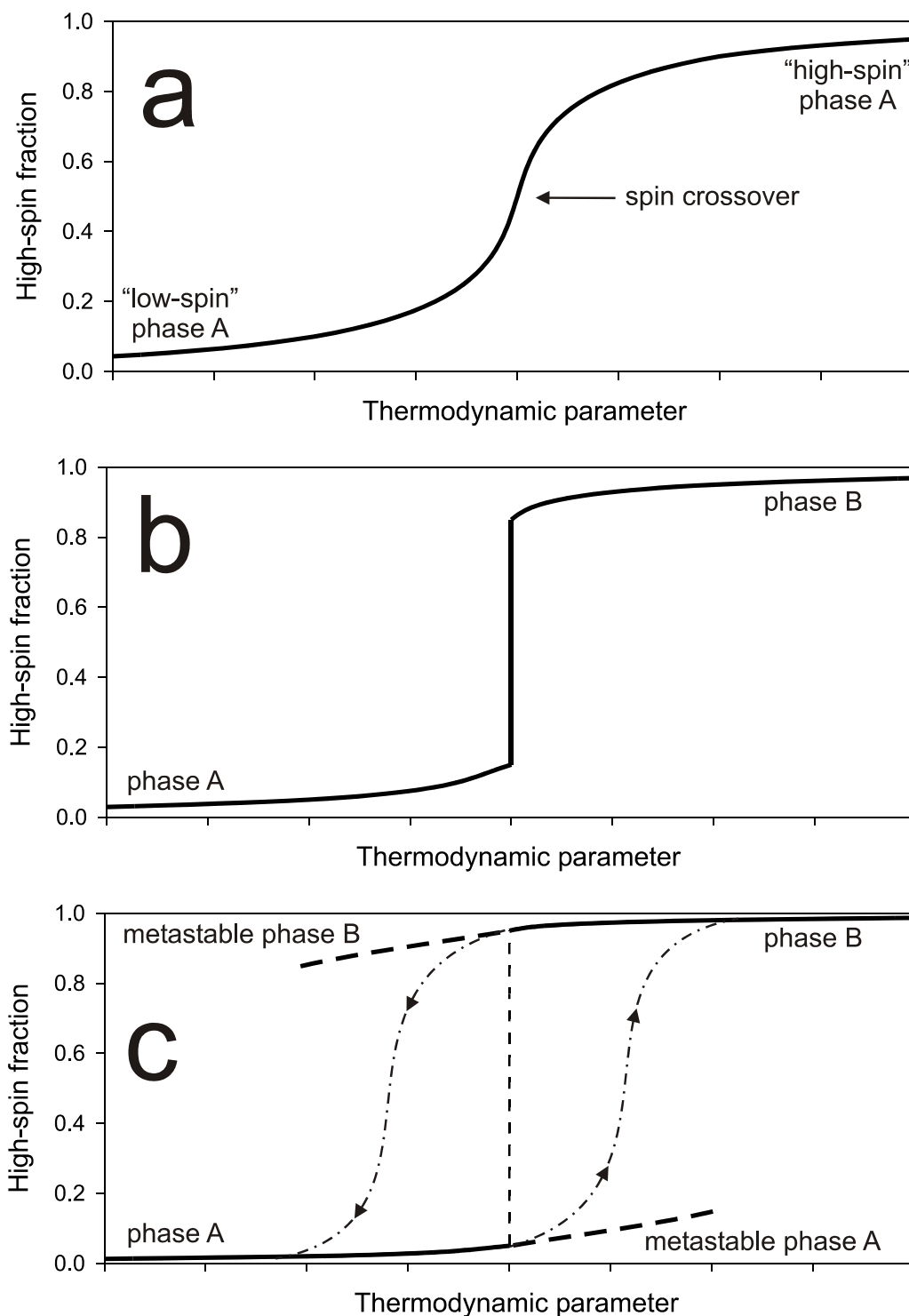


Fig. 3.41. Schematic changes of high-spin abundance upon a spin transition. The thermodynamic parameter could be either temperature or pressure, or both. a) – spin crossover without phase transition; “high-spin” and “low-spin” are the same phase. b) – spin crossover and a second-order phase transition. Two distinct phases can be found, one with low-spin dominating (phase A) and another with high-spin dominating (phase B). c) – spin crossover and a first-order transition. Due to the metastability of phase A above the transition point and phase B below the transition point, a hysteresis loop in the high-spin abundance appears.

My experimental observations allow the interpretation of spin changes in ferroperricite at high pressure as a spin crossover without phase transition. The broad region of significant high- and low-spin states coexistence and the continuous LS fraction change is characteristic for “a” type transitions. Since no symmetry or structural change occurs in ferroperricite above spin crossover, the possibility of a “b”-type transition can be ruled out. It is possible still to have a first-order isostructural transition, in the case of two (pseudo-) cubic phases with different densities. In this case in the pressure range of the HS and LS states coexistence, two phases with different volumes should coexist, which has never been observed in any experiment. Therefore, pressure-induced spin crossover in ferroperricite is unlikely to be a phase transition.

I would like to note that this is not simply a semantic question. A phase transition of first order should incorporate a latent heat of a transformation and the first derivative of the free energy should have a discontinuity. A second-order phase transition implies continuous changes of the first derivative, but a discontinuity in the second energy derivative (for example, continuous volume change but discontinuity in bulk modulus upon compression). If there is no phase transition, all thermodynamic functions including heat capacity change continuously upon spin crossover. In particular, the compression curve of ferroperricite should not be described as two separate equations of state for high- and low-spin phases, but as a single equation with (possibly) anomalous compression in some pressure range. A two-equation of state model with a gradual change from one curve to another (Lin et al., 2005) can give a good analytical representation, but is ill-founded.

Since there is no phase transition in ferroperricite and the system can be considered as being in thermal equilibrium, the high-spin and low-spin population should follow in the simplest model of Boltzmann distribution

$$\frac{\psi_{LS}}{\psi_{HS}} = \exp \frac{-\Delta E}{kT} \quad (3.13),$$

where ψ_{LS} and ψ_{HS} are relative fractions of low- and high-spin molecules (atoms) in the crystal, ΔE is the energy difference between high- and low-spin state, k is the Boltzmann constant and T is absolute temperature. ΔE is a function of thermodynamic parameters and should change its sign with varying thermodynamic parameters to satisfy spin crossover conditions. When $\Delta E = 0$ populations of high- and low-spin Fe are equal, and this point is called spin crossover. In a pressure-induced spin crossover ΔE changes with pressure at constant temperature, passing through zero at some given crossover pressure. Usually the energy difference between two phases or two electronic states, in this case ΔE , changes

almost linearly with pressure, at least in the vicinity of the critical pressure. Our *ab initio* calculations also prove this suggestion as shown below. The character of spin crossover (i.e. its broadness) therefore depends on temperature and the slope of ΔE with pressure. The latter should not change significantly with temperature, and only the crossover pressure could be temperature dependent.

Low-temperature measurements can give additional important information concerning the physical properties of the spin crossover, because the temperature contribution to the Boltzmann function vanishes to zero. Experimental facilities in the Bayerisches Geoinstitut do not allow low-temperature Mössbauer spectroscopic measurements in the DAC; however, some literature data are available. Low-temperature data at 10 K for $(\text{Mg}_{0.8}\text{Fe}_{0.2})\text{O}$ were collected up to 80 GPa by Speziale et al., (2005). At low-temperature the Fe20 sample is antiferromagnetically ordered in the high-spin state. The high-spin component is therefore a superposition of several closely overlapped sextets, while the low-spin component, similarly to the room temperature observations, is a single line. In such a case near the end of the transition the uncertainty of the high-spin fraction is very high, since the small area is distributed over a large velocity range. In particular, the Fe20 Mössbauer spectrum at 80 GPa and 10 K can be fitted relatively well as a pure low-spin spectrum with a single line, but if a high-spin sextet is added to the model, it would give more than 35 % of the total spectral absorption. In any case, the width and pressure of the spin crossover at 10 K is virtually the same as at 300 K (Fig. 3.42).

In case where 300 K data are fitted to the simple Boltzmann distribution model with a particular experimentally determined pressure slope of ΔE , at 10 K this model predicts spin crossover to occur over a few GPa pressure range (model 1 in Fig. 3.42). Similarly, if the low-temperature data are fitted to this model with a small pressure slope of ΔE , at 300 K this fit predicts an enormously broad transition, such that at ambient pressure there should be already more than 40 % of a low-spin population (model 2 in Fig. 3.42). Therefore, a simple model cannot be applied to describe spin transitions in ferropericlase.

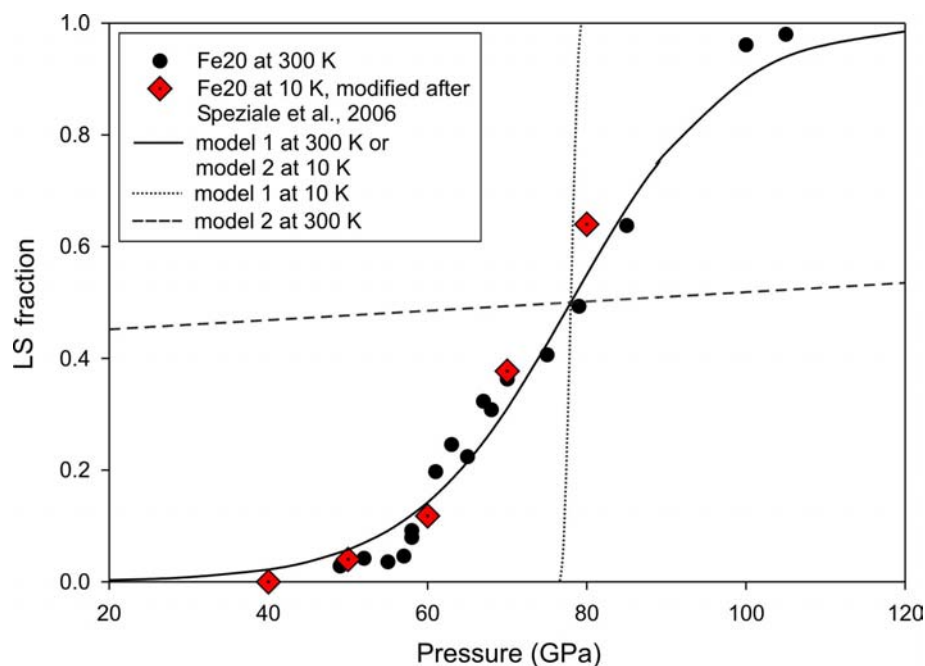


Fig. 3.42. Pressure evolution of the low-spin fraction in the Fe20 sample. Circles are data points at 300 K and diamonds at 10 K (data from Speziale et al., 2005; re-analysed). The solid line shows a simple Boltzmann population model either for 300 K (corresponding 10K-curve is a dotted line) or for 10 K (corresponding 300K-curve is a dashed line), see text for details.

The only way to interpret the fact that the experimental transition width remains virtually the same for 10 K and 300 K is that spin crossover passes through several steps. If there are different types of Fe ions in the crystal, they could have different critical pressures. Such a behaviour (step-like spin transition) is known for many metal-organic complexes, for example $[\text{Fe}(\text{2-pic})_3]\text{Cl}_2 \times \text{EtOH}$ (Köppen et al., 1982). This idea can be illustrated with a simple model. Let us suggest that there are four different types of iron (Fe^{A} , Fe^{B} , Fe^{C} , and Fe^{D}) in the structure with the crossover pressures 50, 60, 70 and 80 GPa, respectively, and in equal amounts of 25 %. The total ψ_{LS} would be as is shown in Fig. 3.43.a. Each type of atom goes through the transition independently, and the total low-spin fraction increases over a broader range. The temperature effect on the transition width is therefore much smaller (Fig. 3.43.b). At a low temperature of 10 K the transition is going through four sharp steps, but the total transition width is large. At 300 K each of these steps are smoothed by the temperature contribution to the Boltzmann function (Eq. 3.13), but the total transition width remains virtually the same. Even at 800 K the transition does not become much broader. At higher temperatures, however, the temperature population effect is dominating, and at 2400 K (temperature close to the lower mantle-core boundary) it becomes much broader, occupying the entire pressure range of the mantle.

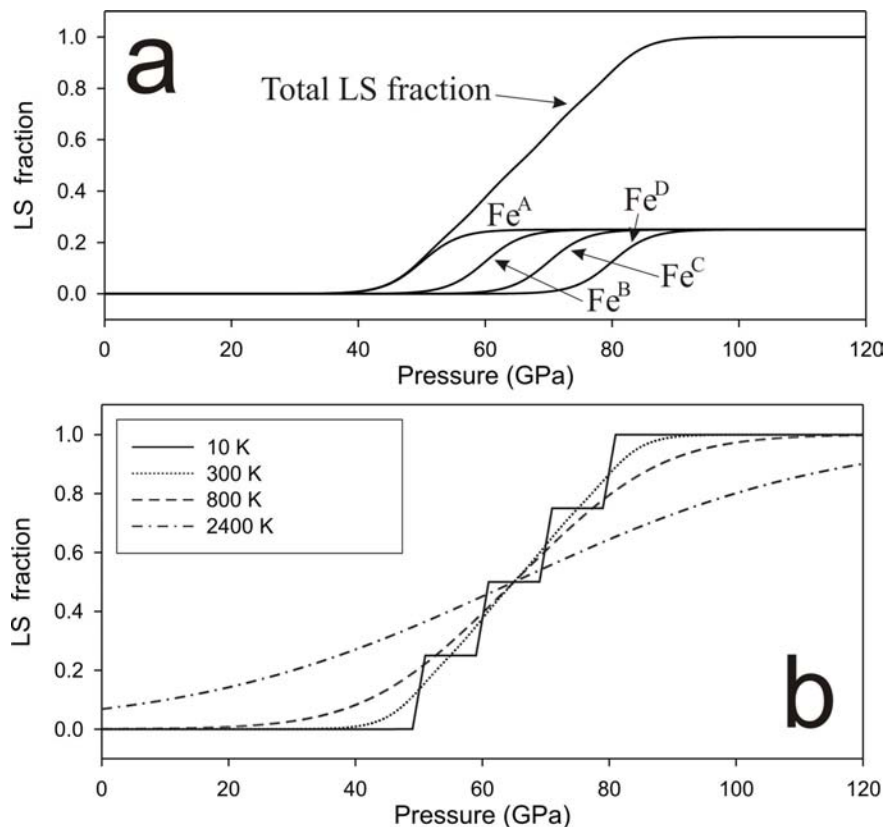


Fig. 3.43. Step-like spin crossover. a) schematic cartoon showing four separate steps for Fe^A to Fe^D undergoing spin crossover one after another and the total sum of LS fraction. b) temperature effect on step-like spin crossover. Solid curve for 10 K; dotted line – 300 K; dashed line – 800 K; dashed-dotted line – 2400 K.

The nature of these steps is not trivial to interpret. My suggestion is, and it is supported by our *ab-initio* calculations, that Fe ions in different local surroundings can have different critical pressures of spin crossover. An isolated Fe²⁺ ion transforms to the low-spin state relatively easily. When another Fe ion is in its first coordination shell a significant electronic exchange between Fe ions appears. This electronic exchange stabilizes the high-spin state relative to the low-spin state. This idea is supported by static *ab-initio* calculations (Fig. 3.44). The critical pressure is different for different Fe clusters: it is about 20 GPa for the isolated Fe ion, while for a 2Fe cluster it is about 40 GPa. The pressure slope of ΔE remains virtually the same. Simulated low-spin fractions in different Fe clusters and for different temperatures (according to Eq. 3.13) are shown in Fig. 3.45.

The height of each step of the spin transition depends on the relative abundance of different Fe clusters. Different cluster abundances are defined by the composition and short-range order (see section III.5.3). Separation (pressure difference) between these steps is

controlled by the strength of electronic exchange between neighbouring Fe ions. Electronic exchange interactions normally decrease with increasing temperature (Lotgering and Diepen, 1976; Taran and Rossman, 2002). The total fraction of low-spin Fe^{2+} ions depends therefore not only on pressure, temperature and composition, but also on the short-range order, a phenomenon that is often ignored in solid solutions.

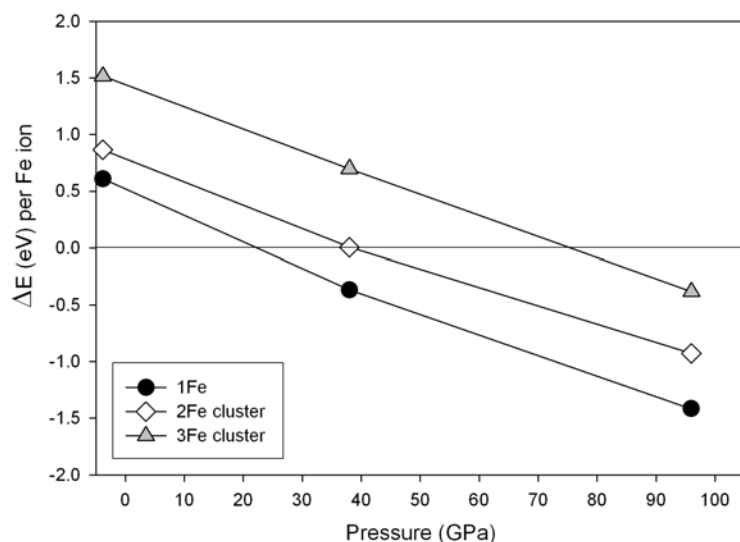


Fig. 3.44. Calculated energy difference between the high- and low-spin state of Fe in different Fe clusters.

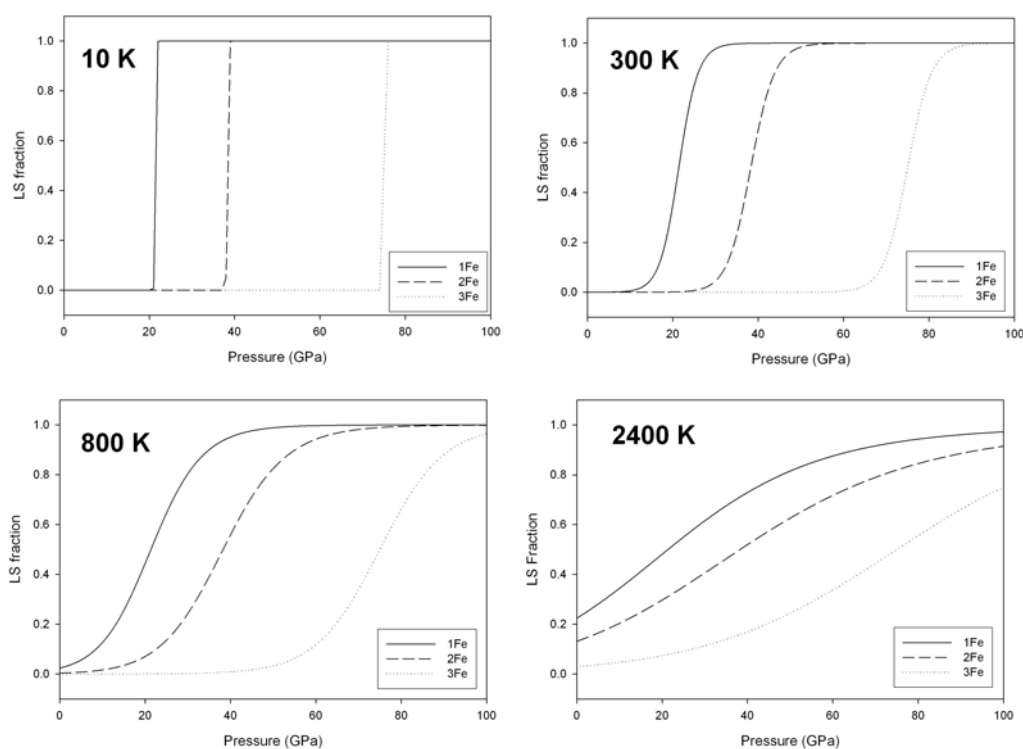


Fig. 3.45. LS fraction at different temperatures from *ab-initio* calculations. Only the temperature contribution to the Boltzmann statistics was taken into account.

The temperature effect requires additional consideration. A “normal” temperature effect shifts the critical point to higher pressures. This is the effect of thermal expansion on one hand and of higher entropy contribution (the electronic entropy of the high-spin state is higher than that of the low-spin state) on the other hand. Temperature also increases the width of the transition region according to Boltzmann statistics, so the “beginning” of the transition would occur at lower pressures and the transition “finish” would shift to higher pressures. The decrease of exchange interactions gives a different effect: the width of different steps decreases, and the critical pressure for different Fe clusters approach that of an isolated Fe ion. As a result, the total transition width could even decrease from the high-pressure side with increasing temperature. The temperature effect on spin crossover in ferroperricite contains several competing contributions, and if they completely annihilate each other, temperature could have no effect on the total spin crossover in ferroperricite.

Several high-temperature Mössbauer spectroscopic measurements were performed for the Fe₅ and Fe₂₀ samples up to 750 K using a resistively heated DAC. The observed temperature dependence of the spin crossover is remarkable: for the Fe₂₀ sample almost no temperature effect on crossover pressure and transition width was observed (Fig. 3.46.a). For the Fe₅ sample increasing temperature results in a slight decrease of the crossover pressure, while the transition width remains virtually the same (Fig. 3.46.b). These features can be explained only within the step-like spin crossover with each step following Boltzmann statistics, as described above.

In terms of applications to the Earth’s lower mantle properties, high temperature (2000 – 2400 K) would cause the spin transition in ferroperricite to be very broad and to occur over the entire depth range of the mantle. Even if electronic exchange interactions completely disappeared at these temperatures and the transition occurred in a single step, the broadness of the transition at these temperatures would be enormous. Therefore, no pronounced discontinuities in any physical property of ferroperricite are expected at lower mantle conditions. Indeed, no strong seismic waves anomalies are known in the mantle. It is remarkable that the same conclusion was made based on very different assumptions and model (Sturhahn et al., 2006).

At room temperature or lower temperatures and especially for low Fe concentrations, some anomalies in compression of ferroperricite can be observed. These anomalies should not be described as volume discontinuities or gradual transitions from one equation of state of the “high-spin” state to another of the “low-spin” state, as proposed in the literature (Lin et

al., 2005; Speziale et al., 2005), but as an anomalous (non-linear) K' behaviour with increasing pressure. I believe that no simple equation of state (such as the commonly used Birch-Murnaghan EOS) can describe the compression behaviour of ferropericlase upon spin crossover.

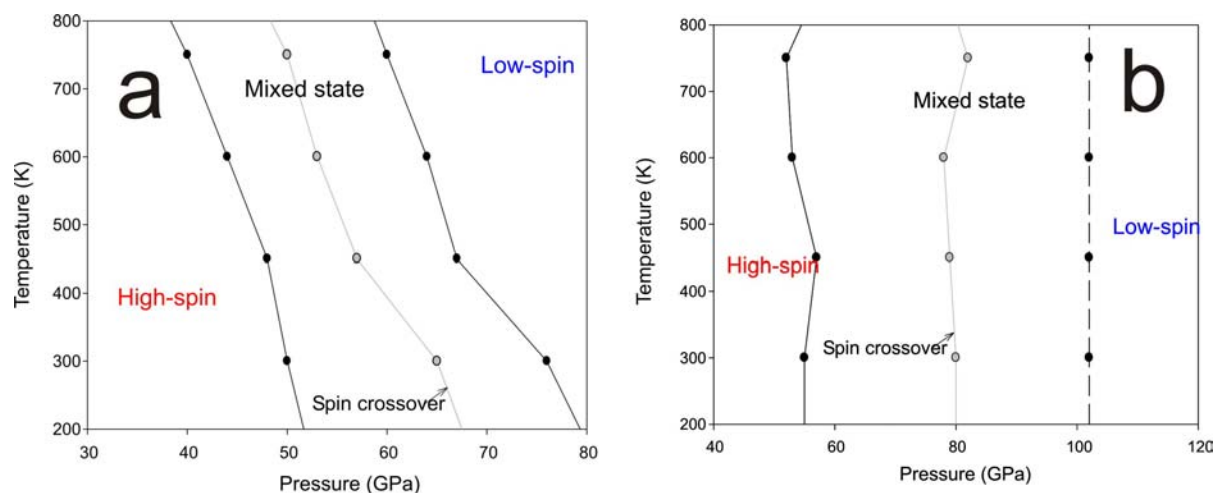


Fig. 3.46. Temperature dependence of spin crossover in Fe5 (a) and Fe20 (b) ferropericlase samples. Boundaries are drawn at the point where low-spin or high-spin states are no longer detectable.

The nature of the driving force of the spin transition in ferropericlase is also not trivial to understand. A recent optical absorption spectroscopic study of ferropericlase containing 12 mole % iron shows that the spin-pairing transition is caused not by increasing crystal-field splitting, but by a strong increase of chemical bonding covalency (Kepler et al., 2007). In particular, the measured crystal-field splitting in the low-spin state Δ_0 was $10\,546\text{ cm}^{-1}$, which is not very different to those of many Fe^{2+} bearing minerals at ambient conditions, while the Racah parameter B value (376 cm^{-1}) is more than twice as small than its free-ion value of 1060 cm^{-1} . A strong covalency increase could also explain the discrepancy between conventional Mössbauer spectroscopic studies (Speziale et al., 2005; Kantor et al., 2006) and X-ray emission spectroscopic (XES) studies (Badro et al., 1999; Lin et al., 2005) which show a much narrower transition width. Mössbauer spectra are not sensitive to the chemical bond covalency, while it could significantly distort XES spectra (Tyson et al., 1999). Optical absorption measurements also show that the radiative thermal conductivity of ferropericlase would not change significantly with the spin transition, reducing only by about 15 % (Kepler et al., 2007).

These results show the importance of short-range order and local structure in the (Mg,Fe)O solid solution, especially for understanding of spin crossover in ferropericlase.

Some recent *ab-initio* simulations do not take these effects into account, and the results obtained are not therefore reliable. For example, the recent work of Tsuchiya et al. (2006) assumes that Fe ions should be positioned as far as possible from each other in (Mg,Fe)O, which is contradictory both to our experimental observations and calculated free energies for different types of iron arrangements. The quantitative *ab-initio* simulations of spin crossover in ferropericlase should be done within the cluster variation approach or some other technique that accounts for different clusters and local structure in the solid solution.

The proposed model also predicts, in particular, that for very low iron concentrations (at the ppm level or less) and at low temperatures spin crossover would occur relatively sharply and at relatively low pressures (about 30 GPa), which could be in future verified experimentally. Another interesting prediction is that for low-iron containing ferropericlase, a detectable amount of the low-spin component could be probably observed even at ambient pressure at temperatures higher than 2000 K.

IV. Conclusions

The present study shows several new important results of high-pressure and high-temperature properties of both FeO oxide and (Mg,Fe)O solid solution with mantle-like composition. A large variety of experimental techniques have been used in this study: X-ray and neutron diffraction as well as X-ray absorption and Mössbauer spectroscopic methods. High-pressure experiments were performed using a diamond anvil cell (DAC) apparatus that allows coverage of the whole range of pressures of the Earth's lower mantle. DACs were adapted for the present study by fitting platinum internal resistive heaters. Resistive heating overcomes many of the disadvantages of laser heating, where temperatures can be maintained within narrow limits over long periods of time, stresses are reduced, heating is relatively homogeneous, and moderate temperatures are easily accessible. The current apparatus allows heating in air up to 1000 K.

This new methodology of *in situ* high-pressure and high temperature ^{57}Fe Mössbauer spectroscopy allow experimental data to be obtained about the valence, electronic and spin state of iron in Earth relevant materials.

I have determined the magnetic and structural phase boundary of non-stoichiometric wüstite up to 73 GPa and 1100 K. The structural phase boundary of a cubic-to-rhombohedral transition obtained in this study is generally consistent with that reported previously. The transition boundary between paramagnetic and antiferromagnetically ordered phases is determined for the first time and differs significantly from that suggested by Badro et al. (1999), although decrease of the Néel temperature at very high pressures is possible (by analogy with MnO and EuO). In the entire studied P, T range magnetization was observed at lower pressures (or higher temperatures) than the rhombohedral distortion.

The phase diagram of MnO was studied by means of powder neutron diffraction up to 9 GPa and temperatures down to 5 K. Below 3.5 GPa the magnetic ordering transition coincides with the lattice distortion transition, and the transition temperature increases with increasing pressure. Above 3.5 GPa the magnetic ordering (Néel) temperature decreases slowly with pressure, while the temperature of the structural transition continues to increase, and a new field (rhombohedral paramagnetic phase) appears in the diagram. The reason for the structural distortion can be explained from the point of view of close packing of non-spherical metal ions, and the interplay between the main free energy contributions explains the phase diagram topology of both FeO and MnO. Under certain conditions magnetic

ordering could induce rhombohedral distortion, although it not the only possibility, and combination of two different structural states (cubic and trigonal) and two different electronic states (paramagnetic and antiferromagnetic) gives in total four possible phases.

These considerations imply that the displacive transition in transition metal monoxides is not a purely magnetostriction effect. Previously reported experimental observations of elastic constant softening in the vicinity of structural transitions in transition metal monoxides allow the suggestion that the transition is driven by the phonon instability. *Ab-initio* calculations also support this general conclusion (Fang et al., 1999).

The detailed investigation of the FeO crystal structure under high pressure revealed that at pressures above ~ 70 GPa there is another displacive transition in FeO from trigonal to the monoclinic phase. A possible high-pressure monoclinic phase of FeO was previously supposed (eg. Fei, 1996), but never before unequivocally proved experimentally. The high-pressure monoclinic phase of FeO is somewhat similar to those observed at low temperatures and ambient pressure in nearly stoichiometric FeO (Fjellvag et al., 2002; Dobson, *private communication*), but not identical. The phase diagram of FeO seems to be much more complicated than previously thought, and FeO stoichiometry is also an important factor for determining phase stability fields.

One of the most important conclusions of the first part of this study devoted to the high-pressure behavior of FeO is that trigonal distortion is not necessarily coupled with magnetic ordering. This implies that trigonal distortion could occur even in a very diluted (Mg,Fe)O solid solution in the paramagnetic state. Our combined X-ray diffraction, Mössbauer and X-ray absorption spectroscopic study of $\text{Mg}_{0.8}\text{Fe}_{0.2}\text{O}$ ferropicrlase shows indeed a trigonal distortion at a pressure of about 35 GPa and room temperature. The experiments were performed without any pressure transmitting medium and strong non-hydrostatic stresses could exist in the powder sample. The observed high-pressure X-ray diffraction patterns, however, indicate a lowering of crystal symmetry, and cannot be described as a cubic phase under non-hydrostatic stress. On the other hand, the cubic-to-rhombohedral transition could be driven by uniaxial stress; in other words, the transformation could be stress-induced.

On the basis of my experimental results, it was clearly shown that 20 mol% FeO is sufficient to induce a rhombohedral distortion in (Mg,Fe)O at a confining pressure of ~ 35 GPa in the presence of uniaxial stress. It is also clear from Mössbauer spectroscopy that the rhombohedral distortion of $\text{Mg}_{0.8}\text{Fe}_{0.2}\text{O}$ is not associated with either long- or short-range magnetic ordering. A rhombohedral distortion in ferropicrlase with mantle composition

($\text{Mg}_{0.8}\text{Fe}_{0.2}\text{O}$) could influence physical properties of the Earth's lower mantle, since such a phase transition could be accompanied by a rapid C_{44} mode softening (Sumino et al., 1980) and by a decrease of shear wave velocities. There are no direct experimental measurements for such anomalies in ferropericlase and no such features have been observed in the lower mantle in seismological records. High temperature stabilizes the high-symmetry cubic phase, so this transition is likely not relevant for the lower mantle. On the other hand, this transition is very important for interpreting the experimental high-pressure data on this material, because a major fraction of experiments are performed at room temperature, and stress conditions are never hydrostatic at these pressures (above 30 GPa).

The detailed analysis of Mössbauer spectra of ferropericlase with different compositions (5 – 20% of Fe) revealed that there is a distribution of Fe^{2+} hyperfine parameters (specifically, quadrupole splitting). From the analysis of quadrupole splitting distribution it is possible to characterize the local atomic structure in the (Mg,Fe)O solid solution according to the methodology, suggested in present work. Short-range order was found to increase dramatically with increasing pressure, especially for the lower-Fe samples. These changes of the local atomic environment were found to be irreversible, and the samples quenched from high pressure show different Mössbauer spectra than those quenched from ambient pressure and high temperature. The tendency for Fe clusterization was also confirmed by *ab-initio* simulations. In the simulated supercell a clear dependence of enthalpy on short range order was discovered, and the configurations with Fe ions located closer to each other are more stable. Simple estimations of Gibbs free energy, with the configurational and excess vibrational entropy taken into account, also confirm that significant deviations from the random cation distribution could exist also at high temperatures in (Mg,Fe)O. This tendency for Fe clusterization could also be responsible for a possible high-pressure and high-temperature decomposition of (Mg,Fe)O (Dubrovinsky et al., 2000-I).

An important implication of pressure-induced Fe ions clusterization is that certain physical properties of (Mg,Fe)O solid solution could be dependent on the sample history. Establishing of equilibrium short-range order requires redistribution of atoms in the crystal lattice and therefore is kinetically controlled. For example, samples quenched from high pressures and those quenched from high temperature have different short-range order and different free energies. Most synthetic samples of (Mg,Fe)O are synthesized at ambient pressure and high temperature, and some properties measured on these samples are not relevant for “high-pressure” ferropericlase, existing in the mantle. Interestingly, the strong

tendency for clusterization in high-spin Fe^{2+} ions disappears if the Fe^{2+} ion exists in the low-spin state, as shown by *ab-initio* simulations.

The spin transition of Fe^{2+} in $(\text{Mg,Fe})\text{O}$ was studied mainly by means of Mössbauer spectroscopy. Under high pressure (above ~ 50 GPa) a low-spin absorption component appears in the Mössbauer spectra. Relative changes of the hyperfine parameters agree with the spin transition. A decrease of isomer shift (implying an increase of electron density at the Fe nuclei) and a vanishing of quadrupole splitting (implying almost complete disappearance of electrical field gradients) are expected to occur in the case of a high- to low-spin transition of Fe^{2+} in an octahedral ligand field. Moreover, the absolute magnitude of these changes agrees perfectly with the results of *ab-initio* calculations.

The spin transition region was found to be remarkably broad. The higher the iron content, the broader was the observed transition region. For $(\text{Mg}_{0.95}\text{Fe}_{0.05})\text{O}$ the transition width is about 20 GPa, while it is more than 50 GPa for $(\text{Mg}_{0.80}\text{Fe}_{0.20})\text{O}$ ferropericlase. Such an extremely broad transition region, coupled with the absence of any symmetry changes or pronounced volume collapse in Mg-rich members of $(\text{Mg,Fe})\text{O}$ solid solution, leads to the conclusion that spin crossover in ferropericlase is not a phase transition. In such a case, the relative fraction of high- and low-spin iron ions is controlled by the Boltzmann thermal distribution and depends on absolute temperature and the energy difference between high- and low-spin states. The fact that the transition width is virtually the same at 10 K (Speziale et al., 2005) and 300 K (this study) could be explained only if the transition is completed in several steps. These steps could reflect different local surroundings of Fe ions in the $(\text{Mg,Fe})\text{O}$ structure. If there are Fe ions in the next-nearest-neighbor shell, the high-spin state is stabilized to higher pressures. This conclusion was supported by *ab-initio* simulations. This interpretation of spin crossover in ferropericlase also explains the observed compositional dependence of the crossover pressure and transition width.

High-temperature measurements show that up to 750 K there was no significant increase of the transition width, while the crossover pressure remains almost the same for $(\text{Mg}_{0.80}\text{Fe}_{0.20})\text{O}$ and decreases with increasing temperature for $(\text{Mg}_{0.95}\text{Fe}_{0.05})\text{O}$. High-temperature observations are fully consistent with the proposed model: the onset of the transition is shifted to lower pressures due to increasing thermal contribution to the Boltzmann statistics of the spin population, and decreasing pressure separation between separate steps due to decreasing Fe-Fe exchange interactions. The extrapolation of the present model to lower mantle conditions results in a very broad spin crossover that occupies nearly the entire depth range of the Earth's lower mantle. The average spin state of Fe would change

continuously and smoothly throughout the entire lower mantle, and no drastic discontinuities could be assigned to spin crossover in ferropericlase.

In summary, I can state the following:

- 1) A new methodology of high-pressure and high-temperature *in situ* Mössbauer spectroscopic measurements has been developed and tested on the examples of FeO and (Mg,Fe)O. This setup allows coverage of the entire pressure range of the Earth's mantle and temperature range up to at least 750 K.
- 2) The phase diagram of FeO was found to be more complex than was previously thought. A cubic to trigonal distortion does not coincide with magnetic ordering in the entire P, T -range. Phase boundaries between cubic and trigonal and paramagnetic and antiferromagnetic phases were determined.
- 3) A new monoclinic phase of FeO was observed at pressures above 70 GPa, implying even more complex phase relations in this challenging material.
- 4) A trigonal distortion was observed for the first time in a (Mg_{0.8}Fe_{0.2})O ferropericlase sample around 35 GPa and room temperature under non-hydrostatic conditions. Although it is not clear yet if this phenomenon is relevant for the Earth's mantle, it is important for correct interpretation of room-temperature experimental measurements.
- 5) Detailed analysis of ferropericlase Mössbauer spectra allow estimations of the local atomic structure in the (Mg,Fe)O solid solution. The degree of short-range order changes dramatically with pressure, and clear signs of Fe ion clusterization were observed. These results were supported also by *ab-initio* simulations.
- 6) Pressure-induced spin crossover in ferropericlase does not show features characteristic for a phase transition. On the contrary, it can be understood as thermally equilibrated high- and low-spin states coexisting in the same phase. All the features, including the compositional and temperature dependences of the crossover pressure and transition width, can be explained by the proposed model.
- 7) Finally, the implications of spin crossover in ferropericlase in the Earth's mantle are the following: there are no density or elastic property discontinuities associated with this transformation. Also, there are no dramatic changes in thermal radiative conductivity in ferropericlase due to spin crossover (Keppler et al., 2007). There are probably also no rapid changes in

Fe/Mg partitioning between ferropericlase and (Mg,Fe)SiO₃ perovskite, since the spin state of iron in ferropericlase changes continuously throughout the entire lower mantle depth.

Finally, I would like to acknowledge many people, who also participate this study. My supervisors, C.A. McCammon and L.S. Dubrovinsky, have provided me with their supervision, support and numerous advises throughout my study. My teachers – V.S. Urusov, D.Yu. Pushcharovsky, Yu.K. Egorov-Tis'menko and many others showed me the incredible world of science and give me my skills in many fields. Many people from different countries assisted me with theoretical *ab initio* calculations: G. Steinle-Neumann, N. Skorodumova, R. Ahuja, M. Mattezini, J. Almeida. I want to thank all the scientific and technical employees of Bayerisches Geoinstitut for their help and assistance, and personally (in alphabetical order) T. Boffa-Balaran, F. Heidelbach, E. Holbig, A. Kantor, A. Kurnosov, and A. Kuznetsov. Many people outside BGI also assisted me in experiments performing, and I would like to thank here also I. Goncharenko, S. Pascarelli, G. Aquilanti, W. Crichton and M. Hanfland. This study was done under financial support of the Deutsche Forschungsgemeinschaft (German Science Foundation) under project number MC 3/13-3.

Bibliography

- Abd-Elmeguid M.M. and Taylor R.D. (1990) Onset of valence and magnetic instabilities in the ferromagnetic semiconductor EuO at high pressures. *Physical Review B* **42**, 1048-1051.
- Aksenov V.L., Kuzmin A.Zu., Purans J., and Tyutyunnikov S.I. (2001) EXAFS Spectroscopy at Synchrotron-Radiation Beams. *Physics of Particles and Nuclei* **32**, 675-708.
- Angel R.J. and Hugh-Jones D.A. (1994) Equations of state and thermodynamic properties of enstatite pyroxenes. *Journal of Geophysical Research* **99**, 19777-19783.
- Anisimov V.I., Zaanen J., and Andersen O.K. (1991) Band theory and Mott insulators: Hubbard U instead of Stoner I . *Physical Review B* **44**, 943-954.
- Ankudinov A.L., Bouldin C.E., Rehr J.J., Sims J., Hung H. (2002) Parallel calculation of electron multiple scattering using Lanczos algorithms. *Physical Review B* **65**, 104107.
- Ankudinov A.L., Ravel B., Rehr J.J., Conradson S.D. (1998) Real-space multiple-scattering calculation and interpretation of x-ray-absorption near-edge structure. *Physical Review B* **58**: 7565-7576.
- Anthony J. W., Bideaux R.A., Bladh K.W., Nichols M.C. (1997) *Handbook of Mineralogy, volume III - Halides, Hydroxides, Oxides*. Mineral Data Publishing, Tucson, 628 p.
- Badro J., Fiquet G., Guyot F., Rueff J.P., Struzhkin V.V., Vankó G., and Monaco G. (2003) Iron partitioning in Earth's mantle: Toward a deep lower mantle discontinuity. *Science* **300**, 789-791.
- Badro J., Struzhkin V.V., Shu J., Hemley R.J., Mao H.K., Kao C.C., Rueff J.P., Shen G. (1999) Magnetism in FeO at Megabar Pressures from X-Ray Emission Spectroscopy. *Physical Review Letters* **83**, 4101-4104.
- Bargeron C.B., Avinor M., and Drickamer H.G. (1971) The Effect of Pressure on the Spin State of Iron(II) in Manganese(IV) Sulfide. *Inorganic Chemistry* **10**, 1338-1339.
- von Barth U., and Grossmann G. (1982) Dynamical effects in x-ray spectra and the final-state rule. *Physical Review B* **25**, 5150-5179.
- Bloch D., Hermann-Ronzaud D., Vettier C., Yelon W.B., and Alben R. (1975) Stress-Induced Tricritical Phase Transition in Manganese Oxide. *Physical Review Letters* **35**, 963-967.
- Bolvin H., and Kahn O. (1995) Ising model for low-spin high-spin transitions in molecular compounds; within and beyond the mean-field approximation. *Chemical Physics* **192**, 295-305.
- Bowen H.K., Adler D., and Auken B.H. (1975) Electrical and optical properties of FeO. *Journal of Solid State Chemistry* **12**, 355-359.

- Broussard L. (1969) The disproportionation of wüstite. *Journal of Physical Chemistry* **73**, 1848-1854.
- Brown J.M. (1999) The NaCl pressure standard. *Journal of Applied Physics* **86**, 5801-5808.
- Bruno M.S. and Dunn K.J. (1984) Stress analysis of a beveled diamond anvil. *Review of Scientific Instruments* **55**, 940-943.
- Burns R.G. (1993) *Mineralogical Applications of Crystal Field Theory* (second edition). Cambridge University Press, 551 p.
- Chen G., Liebermann R.C., Weidner D.J. (1998) Elasticity of Single-Crystal MgO to 8 Gigapascals and 1600 Kelvin. *Science* **280**, 1913-1916.
- Cranshaw T.E. (1974) The deduction of the best values of the parameters from Mossbauer spectra. *Journal of Physics E* **7**, 122-124.
- Dadashev A., Pasternak M.P., Rozenberg G.Kh., and Taylor R.D. (2001) Applications of perforated diamond anvils for very high-pressure research. *Review of Scientific Instruments* **72**, 2633-2637.
- Danon J., *Application of the Mössbauer Effect in Chemistry and Solid State Physics*. International Atomic Energy Agency, Vienna, 1966.
- Ding Y., Liu H., Somayazulu M., Meng Y., Xu J., Prewitt C.T., Hemley R.J., Mao H.K. (2005) Zone-axis x-ray diffraction of single-crystal Fe_{1-x}O under pressure. *Physical Review B* **72**, 174109.
- Dmitriev V.P., Kuznetsov A.Yu., Machon D., Weber H.-P., and Tolédano P. (2003) Phase transition mechanisms in lanthanide elemental crystals. *Europhysics Letters* **61**, 783-789.
- Dobson D.P., Cohen N.S., Pankhurst Q.A., Brotholt J.P. (1998) A convenient method for measuring ferric iron in magnesiowüstite MgO-Fe_{1-x}O. *American Mineralogist* **83**, 794-798.
- Drury M.R. and Fitz Gerald J.D. (1996) Grain boundary melt films in an experimentally deformed olivine-orthopyroxene rock: implications for melt distribution in upper mantle rocks. *Geophysical Research Letters* **23**, 701-704.
- Dubrovinskaia N. and Dubrovinsky L. (2003) Whole-cell heater for the diamond anvil cell. *Review of Scientific Instruments* **74**, 3433-3437.
- Dubrovinsky L., Dubrovinskaya N. (2004) Angle-dispersive diffraction under non-hydrostatic stress in diamond anvil cells. *Journal of Alloys and Compounds* **375**, 86-92.
- Dubrovinsky L.S., Dubrovinskaia N.A., Saxena S.K., Annersten H., Hålenius E., Harryson H., Tutti F., Rekh S., Le Bihan T. (2000-I) Stability of Ferropicicase in the Lower Mantle. *Science* **289**, 430-432.

Dubrovinsky L., Dubrovinskaia N., Saxena S., LiBehan T. (2000-II) X-ray diffraction under non-hydrostatic conditions in experiments with diamond anvil cell: wüstite (FeO) as an example. *Material Sciences and Engineering A* **288**, 187-190.

Dubrovinsky L., Dubrovinskaia N., Kantor I., McCammon C., Crichton W., Urusov V. (2005) Decomposition of ferropicriolite ($Mg_{0.80}Fe_{0.20}O$) at high pressures and temperatures. *Journal of Alloys and Compounds* **390**, 41-45.

Dudarev S.L., Botton G.A., Savrasov S.Y., Humphreys C.J., and Sutton A.P. (1998) Electron-energy-loss spectra and the structural stability of nickel oxide: An LSDA+U study. *Physical Review B* **57**, 1505-1509.

Dufek P., Blaha P., and Schwarz K. (1995) Determination of the Nuclear Quadrupole Moment of ^{57}Fe . *Physical Review Letters* **75**, 3545-3548.

Duff K.J. (1974) Calibration of the isomer shift for ^{57}Fe . *Physical Review B* **9**, 66-72.

Duffy T.S., Hemley R.J., and Mao H.K. (1995) Equation of State and Shear Strength at Multimegabar Pressures: Magnesium Oxide to 227 GPa. *Physical Review Letters* **74**, 1371-1374.

Dziewonski A.M. and Anderson D.L. (1981) Preliminary Reference Earth Model. *Physics of the Earth and Planetary Interior* **25**, 297-356.

Dziewonski A.M., Hales A.L., and Lapwood E.R. (1975) Parametrically simple Earth model consistent with geophysical data. *Physics of the Earth and Planetary Interior* **10**, 12-48.

Eekhout S.G., De Grave E., McCammon C.A., Vochten R. (2000) Temperature dependence of the hyperfine parameters of synthetic $P2_1/c$ Mg-Fe clinopyroxenes along the $MgSiO_3$ - $FeSiO_3$ join. *American Mineralogist* **85**, 943-952.

Evans R.J., Rancourt D.G., Grodzinski M. (2005) Hyperfine electric field gradients and local distortion environments of octahedrally coordinated Fe^{2+} . *American Mineralogist* **90**, 187-198.

Fang Z., Solovyev I.V., Sawada H., and Terakura K. (1999) First-principles study on electronic structures and phase stability of MnO and FeO under high pressure. *Physical Review B* **59**: 762-774.

Fei Y., Crystal chemistry of FeO at high pressure and temperature (1996) in *Mineral Spectroscopy: A Tribute to Roger G. Burns*. Edited by M.D. Dyar, C. McCammon, and M.W. Schaefer, 243-254.

Fei Y. and Mao H.K. (1994) In situ determination of the NiAs phase of FeO at high pressure and temperature. *Science* **266**, 1678-1680.

Fjellvag H., Hauback B.C., Vogt T., and Stolen S. (2002) Monoclinic nearly stoichiometric wüstite at low temperatures. *American Mineralogist* **87**, 347-349.

Funamori N., Funamori M., Jeanloz R., Hamaya N. (1997) Broadening of x-ray powder diffraction lines under nonhydrostatic stress. *Journal of Applied Physics* **82**, 142-146.

Fyfe W.S. (1960) The possibility of *d*-electron coupling in olivine at high pressures. *Geochemical et Cosmochimical Acta* **19**, 141-143.

Gale J.D. (1997) GULP - a computer program for the symmetry adapted simulation of solids. *Journal of Chemical Society: Faraday Transactions* **4**, 629-637.

Goncharenko I.N. (2004) Neutron diffraction experiments in diamond and sapphire anvil cells. *High Pressure Research* **24**, 193-204.

Goncharov A.F., Struzhkin V.V., and Jacobsen S.D. (2005) Reduced radiative conductivity of low-spin (Mg,Fe)O in the lower mantle. *Science* **312**, 1205–1208.

Gramsch S.A., Cohen R.E., and Savrasov S.Y. (2003) Structure, metal-insulator transitions, and magnetic properties of FeO at high pressures. *American Mineralogist* **88**, 257-261.

Green D.H., Falloon T.J. (1998) Pyroline: A Ringwood Concept and Its Current Expression. In: *The Earth's Mantle*, ed. I. Jackson, pp. 311-378. Cambridge University Press.

Greenwood N.N. and Gibb T.C., *Mössbauer Spectroscopy*, Chapman and Hall, London (1971).

Guo Q.Z., Mao H.K., Hu J., Shu J., and Hemley R.J. (2002) The phase transitions of CoO under static pressure to 104 GPa. *Journal of Physics: Condensed Matter* **14**, 11369-11374.

Gütlich P., Link, R., Trautwein A., *Mössbauer Spectroscopy and Transition Metal Chemistry*, Springer-Verlag, Berlin (1978).

Haavik C., Stolen S., Hanfland M., Catlow C.R.A. (2000) Effect of defect clustering on the high-pressure behaviour of wüstite. High-pressure X-ray diffraction and lattice energy simulations. *Physical Chemistry - Chemical Physics* **2**, 5333-5340.

Hammersley A.P., Svensson S.O., Hanfland M., Fitch A.N., Hausermann D. (1996) Two-dimensional detector software: From real detector to idealised image or two-theta scan. *High Pressure Research* **14**, 235-248.

Hart S.R. and Zindler A. (1986) In search of a bulk Earth composition. *Chemical Geology* **57**, 247-267.

Harte B., and Harris J.W. (1994) Lower mantle mineral associations preserved in diamonds. *Mineralogical Magazine A* **58**, 384-385.

Hedin L., and Lundqvist B.I. (1971) Explicit local exchange-correlation potentials. *Journal of Physics C* **4**, 2064-2083.

Hogrefe A., Rubie D.C., Sharp T.G., and Seifert F. (1994) Metastability of enstatite in deep subducting lithosphere. *Nature* **372**, 351-353.

- Hohenberg P., Kohn W. (1964) Inhomogeneous Electron Gas. *Physical Review* **136**, B864-B871.
- Huber G.K., Syassen K., and Holzapfel W.B. (1977) Pressure dependence of 4f levels in europium pentaphosphate up to 400 kbar. *Physical Review B* **15**, 5123-5128.
- Ingalls R. (1967) Isomer Shift of Fe57 in Iron. *Physical Review* **155**, 157-165.
- Jackson D.D., Aracne-Ruddle C., Malba V., Weir S.T., Catledge S.A., and Vohra Y.K. (2003) Magnetic susceptibility measurements at high pressure using designer diamond anvils. *Review of Scientific Instruments* **74**, 2467-2471.
- Jacobsen S.D., Lin J.F., Angel R.J., Shen G., Prakapenka V.B., Dera P., Mao H.K., and Hemley R.J. (2005) Single-crystal synchrotron X-ray diffraction study of wüstite and magnesiowüstite at lower-mantle pressures. *Journal of Synchrotron Radiation* **12**, 577-583.
- Jacobsen S.D., Reihmann H.-J., Spetzler H.A., Mackwell S.J., Smyth J.R., Angel R.J., and McCammon C.A. (2002) Structure and elasticity of single-crystal (Mg,Fe)O and a new method of generating shear waves for gigahertz ultrasonic interferometry. *Journal of Geophysical research* **107**, 2037-2051.
- Jaffe J.E., Snyder J.A., Lin Z., Hess A.C. (2000) LDA and GGA calculations for high-pressure phase transitions in ZnO and MgO. *Physical Review B* **62**, 1660-1665.
- Jagoutz E., Palme H., Baddenhausen H., Blum K., Cendales M., Dreibus G., Spettel B., Lorenz V., Wänke H. (1979) The abundance of major, minor and trace elements in the earth's mantle as derived from primitive ultramafic nodules. In: *Proceedings of the 10-th Lunar and Planetary Science Conference*, pp. 2031-2050. Elmsford, NY: Pergamon Press.
- Jayaraman A. (1983) Diamond anvil cell and high-pressure physical investigations. *Reviews of Modern Physics* **55**, 65-108.
- Kantor A.P., Jacobsen S.D., Kantor I.Yu., Dubrovinsky L.S., McCammon C.A., Reichmann H.J., and Goncharenko I.N. (2004-I) Pressure-Induced Magnetization in FeO: Evidence from Elasticity and Mössbauer Spectroscopy. *Physical Review Letters* **93**, 215502.
- Kantor I.Yu., McCammon C.A., and Dubrovinsky L.S. (2004-II) Mossbauer spectroscopic study of pressure-induced magnetisation in wiistite (FeO). *Journal of Alloys and Compounds* **376**, 5-8.
- Kantor I., Dubrovinsky L., McCammon C., Kantor A., Pascarelli S., Aquilanti G., Crichton W., Mattesini M., Ahuja R., Almeida J., and Urusov V. (2005-I) Pressure-induced phase transition in Mg_{0.8}Fe_{0.2}O ferropericlyase. *Physics and Chemistry of Minerals* **33**, 35-44.
- Kantor I.Yu., Dubrovinsky L.S., McCammon C.A. (2005-II) Mössbauer spectroscopy at elevated pressures and temperatures: Spin transition in (Mg_{0.8}Fe_{0.2})O ferropericlyase. *Proceedings of the Joint 20th AIRAPT – 43rd EHPRG International Conference on High Pressure Science and Technology*, T5-P101. Available online at http://bibliothek.fzk.de/zb/verlagspublikationen/AIRAPT_EHPRG2005/Posters/P101.pdf

- Kantor A.P., Dubrovinsky L.S., Dubrovinskaia N.A., Kantor I.Yu., Goncharenko I.N. (2005-III) Phase transitions in MnO and FeO at low temperatures: A neutron powder diffraction study. *Journal of Alloys and Compounds* **402**, 42-45.
- Kantor I.Yu., Dubrovinsky L.S., McCammon C.A. (2006) Spin crossover in (Mg,Fe)O: A Mössbauer effect study with an alternative interpretation of x-ray emission spectroscopy data. *Physical Review B* **73**, 100101.
- Kennett B.L.N. and Engdahl E.R. (1991) Traveltimes for global earthquake location and phase identification. *Geophysical Journal International* **105**, 429-465.
- Kennett B.L.N., Engdahl E.R., and Buland R. (1995) Constrains on the velocity structure in the Earth from travel times. *Geophysical Journal International* **122**, 108-124.
- Keppler H., Kantor I., Dubrovinsky L.S. (2007) Optical absorption spectra of ferropicriase to 84 GPa. *American Mineralogist* **92**, 433-436.
- Kizler P. (1992) X-ray-absorption near-edge structure spectra for bulk materials: Multiple-scattering analysis versus a phenomenological approach. *Physical Review B* **46**, 10540-10546.
- Koch F. and Cohen J.B. (1969) The defect structure of Fe_{1-x}O. *Acta Crystallographica B* **25**, 275-287.
- Kondo T., Ohtani E., Hirao N., Yagi T., and Kikegawa T. (2004) Phase transitions of (Mg,Fe)O at megabar pressures. *Physics of the Earth and Planetary Interior* **201**, 143-144.
- Kondo T., Ohtani E., Yagi T., Kikegawa T. (2002) In-situ X-ray Study of (Mg,Fe)O Under High Pressure and Temperature. *Journal of Conference Abstracts* **7**, 57.
- Kondo T., Yagi T., Syono Y., Noguchi Y., Atou T., Kikegawa T. and Shimomura O. (2000) Phase transitions of MnO to 137 GPa. *Journal of Applied Physics* **87**, 4153-4159.
- Köppen H., Müller E.W., Köhler C.P., Spiering H., Meissner E., and Gütlich P. (1982) Unusual spin-transition anomaly in the crossover system [Fe(2-pic)₃]Cl₂×EtOH. *Chemical Physics Letters* **91**, 348-352.
- Kresse G., Furthmüller J. (1996) Efficient iterative schemes for *ab initio* total-energy calculations using a plane-wave basis set. *Physical Review B* **54**, 11169-11186.
- Kündig W. (1976) Electron densities and isomer shift. *Hyperfine Interactions* **2**, 113-125.
- Kuzmin A., Mironova N., and Purans J. (1997) The influence of pd mixing and magnetic interactions on the pre-edge peak intensity at the Co (Ni) K absorption edge in Co(Ni)_cMg_{1-c}O solid solutions. *Journal of Physics: Condensed Matter* **9**, 5277-5286.
- Leider H.R. and Pipkorn D.N. (1968) Mössbauer effect in MgO:Fe⁺²; low-temperature quadrupole splitting. *Physical Review* **165**, 494-500.

- Lin J.-F., Heinz D.L., Mao H.K., Hemley R.J., Devine J.M., Li J., and Shen G. (2003) Stability of magnesiowüstite in Earth's lower mantle. *Proceedings of National Academy of Sciences USA* **100**, 4405-4408.
- Lin J.F., Struzhkin V.V., Jacobsen S.D., Hu M.Y., Chow P., Kung J., Liu H., Mao H.K., Hemley R.J. (2005) Spin transition of iron in magnesiowüstite in the Earth's lower mantle. *Nature* **436**, 377-380.
- Long G.J. and Grandjean F. (1991) Mössbauer effect, magnetic and structural studies of wüstite, Fe_{1-x}O . *Advances in Solid-State Chemistry* **2**, 187-221.
- Lotgering F.K. and van Diepen A.M. (1976) Electron exchange between Fe^{2+} and Fe^{3+} ions on octahedral sites in spinels studied by means of paramagnetic Mössbauer spectra and susceptibility measurements. *Journal of Physics and Chemistry of Solids* **38**, 565-572.
- Lytle F.W., Gregor R.B., and Panson A.J. (1988) Discussion of x-ray-absorption near-edge structure: Application to Cu in the high- T_c superconductors $\text{La}_{1.8}\text{Sr}_{0.2}\text{CuO}_4$ and $\text{YBa}_2\text{Cu}_3\text{O}_7$. *Physical Review B* **37**, 1550-1562.
- Mao H.K., Bell P.M., Dunn K.J., Chrenko R.M., and Devries R.C. (1979) Absolute pressure measurements and analysis of diamonds subjected to maximum static pressures of 1.3-1.7 Mbar. *Review of Scientific Instruments* **50**, 1002-1009.
- Mao H.K., Shu J., Fei Y., Hu J.Z., and Hemley R.J. (1996) The wüstite enigma. *Physics of the Earth and Planetary Interior* **96**, 135-145.
- Mao W., Shu J., Hu J., Hemley R., and Mao H.K. (2002) Displacive transition in magnesiowüstite. *Journal of Physics: Condensed Matter* **14**, 11349-11354.
- Mao H.K., Xu J., and Bell P.M. (1986) Calibration of the ruby pressure gauge to 800 Kbar under quasihydrostatic conditions. *Journal of Geophysical Research* **91**, 4673-4678.
- Mazin I.I., Fei Y., Downs R., and Cohen R.E. (1998) Possible polytypism in FeO at high pressures. *American Mineralogist* **83**, 451-457.
- McCammon C.A. (1992) Magnetic properties of Fe_xO ($x > 0.95$). Variation of Néel temperature. *Journal of Magnetism and Magnetic Materials* **104-107**, 1937-1938.
- McCammon C. (1993) Effect of Pressure on the Composition of the Lower Mantle End Member Fe_xO . *Science* **259**, 66-68.
- McCammon C.A. and Liu L.-G. (1984) The effects of pressure and temperature on nonstoichiometric wüstite, Fe_xO : The iron-rich phase boundary. *Physics and Chemistry of Minerals* **10**, 106-113.
- McCammon C., Peyronneau J., and Poirier J.-P. (1998) Low ferric iron content of $(\text{Mg,Fe})\text{O}$ at high pressures and temperatures. *Geophysical Research Letters* **25**, 1589-1592.

- McCammon C.A., and Tennant C. (1996) High-pressure Mössbauer study of synthetic clinoferrite, FeSiO₃. in “*Mineral Spectroscopy: A Tribute to Roger G. Burns*”, Special Publication No. 5, Geochemical Society, Houston, 281-288.
- McDonough W.F. and Sun S.-S. (1995) The composition of the Earth. *Chemical Geology* **120**, 223-253.
- McNab T.K., Micklitz H., and Barrett P.H. (1971) Mössbauer Studies on ⁵⁷Fe Atoms in Rare-Gas Matrices between 1.45 and 20.5 K. *Physical Review B* **4**, 3787-3797.
- Meng Y., Shen G., and Mao H.K. (2006) Double-sided laser heating system at HPCAT for in situ x-ray diffraction at high pressures and high temperatures. *Journal of Physics: Condensed Matter* **18**, S1097-S1103 (2006).
- Merkel S., Wenk H.R., Shu J., Shen G., Gillet P., Mao H.K., and Hemley R.J. (2002) Deformation of polycrystalline MgO at pressures of the lower mantle. *Journal of Geophysical Research* **107**, 2271-2288.
- Merrill L. and Bassett W.A. (1974) Miniature diamond anvil pressure cell for single crystal x-ray diffraction studies. *Review of Scientific Instruments* **45**, 290-294.
- Minervini L. and Grimes R.W. (1999) Defect clustering in wüstite. *Journal of Physics and Chemistry of Solids* **60**, 235-245.
- Molenda J., Stoklstrókosa A., Znamirowski W. (1987) Transport Properties of Ferrous Oxide Fe_{1-y}O at High Temperature. *Physica Status Solidi B*, **142**, 517-529.
- Monkhorst H.J. and Pack J.D. (1976) Special points for Brillouin-zone integrations. *Physical Review B* **13**, 5188-5192.
- Morelli A. and Dziewonski A.M. (1993) Body-wave traveltimes and a spherically symmetric P- and S-wave velocity model. *Geophysical Journal International* **112**, 178-194.
- Morimoto N., Akimoto S., Koto K., and Tokonami M. (1970) Crystal structures of high pressure modifications of Mn₂GeO₄ and Co₂SiO₄. *Physics of the Earth and Planetary Interior* **3**, 161-165.
- Morosin B. (1970) Exchange Striction Effects in MnO and MnS. *Physical Review B* **1**: 236-243.
- Morozov M., Brinkmann Ch., Lottermoser W., Tippelt G., Amthauer G., Kroll H. (2005) Octahedral cation partitioning in Mg, Fe²⁺-olivine. Mössbauer spectroscopic study of synthetic (Mg_{0.5}Fe²⁺_{0.5})₂SiO₄ (Fa₅₀). *European Journal of Mineralogy* **17**, 495–500.
- Moyzis J.A. and Drickamer H.G. (1968) Effect of Pressure on the Isomer Shift of Fe⁵⁷ in the bcc Phase. *Physical Review* **171**, 389-392.
- Mrowec S., Podgorecka A. (1987) Defect structure and transport properties of non-stoichiometric ferrous oxide. *Journal of Materials Science* **22**, 4181-4189.

- Murakami M., Hirose K., Kawamura K., Sata N., Ohishi Y. (2004) Post-Perovskite Phase Transition in MgSiO₃. *Science* **304**, 855-858.
- Murakami M., Hirose K., Ono S., Tsuchiya T., Isshiki M., Watanuki T. (2004) High pressure and high temperature phase transitions of FeO. *Physics of the Earth and Planetary Interiors* **146**, 273-282.
- Nasu S. (1994) High pressure Mössbauer spectroscopy using a diamond anvil cell. *Hyperfine Interactions* **90**, 59-75.
- Newkirk J.B., Smoluchowski R., Geisler A.H., and Martin D.L. (1951) Phase Equilibria in an Ordering Alloy System. *Journal of Applied Physics* **22**, 290-298.
- Oganov A.R. (2002) *Computer Simulation Studies of Minerals*. Ph.D Thesis, University College of London.
- Oganov A.R., Dorogokupets P.I. (2003) All-electron and pseudopotential study of MgO: Equation of state, anharmonicity, and stability. *Physical Review B* **67**, 224110.
- Oganov A.R., Gillan M.J., Price G.D. (2003) *Ab initio* lattice dynamics and structural stability of MgO. *Journal of Chemical Physics* **118**, 10174-10182.
- Oganov A.R. and Ono S. (2004) Theoretical and experimental evidence for a post-perovskite phase of MgSiO₃ in Earth's D" layer. *Nature* **430**, 445-448.
- Okamoto T., Fujii H., Hidaka Y., and Tatsumoto E. (1967) Effect of Hydrostatic Pressure on the Néel Temperature in FeO and CoO. *Journal of the Physical Society of Japan* **23**, 1174-1174.
- O'Neill H.St.C. and Palme H. (1998) Composition of the Silicate Earth: Implications for Accretion and Core Formation. In: *The Earth's Mantle*, ed. I. Jackson, pp. 3-127. Cambridge University Press.
- Palme H. and Boynton W.V. (1993) Meteoritic constraints on conditions in the solar nebula. In: *Protostars and Planets III*, ed. E.H. Levy and J.I. Lunine, pp. 979-1004. University of Arizona Press, Tucson.
- Palme H., Larimer J., and Lipschutz M.E. (1988) Moderately volatile elements. In: *Meteorites and the Early Solar System*, ed. J.F. Kerridge and M.S. Matthews, pp. 436-461. University of Arizona Press, Tucson.
- Palme H., Nickel K.G. (1985) Ca/Al ratio and the composition of the Earth's upper mantle. *Geochemical et Cosmochemical Acta* **49**, 2123-2132.
- Pascarelli S., Mathon O., and Aquilanti G. (2004) New opportunities for high pressure X-ray absorption spectroscopy using dispersive optics. *Journal of Alloys and Compounds* **362**, 33-40.

- Pasternak M.P., Taylor R.D., Jeanloz R., Li X., Nguyen J.H., and McCammon C.A. (1997) High Pressure Collapse of Magnetism in $\text{Fe}_{0.94}\text{O}$: Mössbauer Spectroscopy Beyond 100 GPa. *Physical Review Letters* **79**, 5046-5049.
- Perdew J.P., Burke K., Ernzerhof M. (1996) Generalized Gradient Approximation Made Simple. *Physical Review Letters* **77**, 3865-3868.
- Piermarini G.J. and Block S. (1975) Ultrahigh pressure diamond-anvil cell and several semiconductor phase transition pressures in relation to the fixed point pressure scale. *Review of Scientific Instruments* **46**, 973-979.
- Pleiter F. and Kolk B. (1971) The contact density of conduction electrons in iron and the isomer shift of ^{57}Fe . *Physics Letters B* **34**, 296-298.
- Price G.D. (1983) The nature and significance of stacking faults in wadsleyite, natural β - $(\text{Mg,Fe})_2\text{SiO}_4$ from the Peace River meteorite. *Physics of the Earth and Planetary Interior* **33**, 137-147.
- Rehr J.J. and Albers R.C. (2000) Theoretical approaches to x-ray absorption fine structure. *Reviews of Modern Physics* **72**, 621-654.
- Rekhi S., Dubrovinsky L.S., and Saxena S.K. (1999) Temperature-induced ruby fluorescence shifts up to a pressure of 15 GPa in an externally heated diamond anvil cell. *High Temperatures – High Pressures* **31**, 299-305.
- Remsberg A.R. and Liebermann R.C. (1991) A study of the polymorphic transformations in Co_2SiO_4 . *Physics and Chemistry of Minerals* **15**, 498-506.
- Richet P., Mao H.K., Bell P.M. (1989) Bulk moduli of magnesiowustites from static compression measurements. *Journal of Geophysical Research* **94**, 3037-3045.
- Ringwood A.E. (1962) A model of the upper mantle. *Journal of Geophysical Research* **67**, 857-866. A model of the upper mantle. 2. *Journal of Geophysical Research* **67**, 4473-4477
- Ringwood A.E. (1975) *Composition and Petrology of the Earth's Mantle*. New York: McGraw-Hill.
- Ringwood A.E. (1979) *Origin of the Earth and Moon*. Berlin: Springer-Verlag.
- Ringwood A.E. and Major A. (1996) Synthesis of Mg_2SiO_4 - Fe_2SiO_4 spinel solid solution. *Earth and Planetary Science Letters* **1**, 241-245.
- Rooksby H.P. (1948) A note on the structure of nickel oxide at subnormal and elevated temperatures. *Acta Crystallographica* **1**, 226-227.
- Roth W.L. (1960) Defects in the crystal and magnetic structures of ferrous oxide. *Acta Crystallographica* **13**, 140-149.
- Saito S., Nakahigashi K., and Shimomura Y. (1966) X-Ray Diffraction Study on CoO . *Journal of Physical Society of Japan* **21**, 850-860.

Sata N., Shen G., Rivers M.L., and Sutton S.R. (2002) Pressure-volume equation of state of the high-pressure B2 phase of NaCl. *Physical Review B* **65**, 104114.

Sata N. (2002) High pressure studies on Fe_xO : Quasi-isothermal compression experiments and applications to the Earth's core. Ph.D. Thesis, University of Tokyo.

Saxena S.K., Chatterjee N., Fei Y., and Shen G. *Thermodynamic Data on Oxides and Silicates. An Assessed Data Set Based on Thermochemistry and High Pressure Phase Equilibrium*. Berlin, Springer-Verlag (1993).

Seehra M.S. and Giebultowicz T.M. (1988) Magnetic structures of fcc systems with nearest-neighbor and next-nearest-neighbor exchange interactions. *Physical Review B* **38**, 11898-11900.

Sharma R.R. and Sharma A.K. (1972) Isomer Shifts of Fe^{57} in Fe_2O_3 and Rare-Earth Iron Garnets. *Physical Review Letters* **29**, 122–124.

Sharp T.G. and Rubie D.C. (1995) Catalysis of the olivine to spinel transformation by high clinoenstatite. *Science* **269**, 1095-1098.

Shu J., Mao H.K., Hu J., Fei Y., and Hemley R.J. (1998-I) Single-crystal X-ray diffraction of wustite to 30 GPa hydrostatic pressure. *Neues Jahrbuch für Mineralogie - Abhandlungen* **172**, 309-323.

Shu J., Mao H.K., Hu J., Fei Y., and Hemley R.J. (1998-II) High-Pressure Phase Transition in Magnesiowustite ($\text{Fe}_{1-x}\text{Mg}_x$)O. *EOS Transactions of American Geophysical Union* **79** (17); Spring Meeting Suppl.: M21A-01.

Shull C.G., Strauser W.A., and Wollan O.E. (1951) Neutron Diffraction by Paramagnetic and Antiferromagnetic Substances. *Physical Review* **83**, 333-345.

Šimánek E. and Šroubek Z. (1967) Overlap Contribution to the Isomer Shift of Iron Compounds. *Physical Review* **163**, 275-279.

Šimánek E. and Wong A.Y.C. (1968) Calibration of the Fe^{57} Isomer Shift. *Physical Review* **166**, 348–349.

Simons B. (1980) Composition – Lattice Parameter Relationship of the Magnesiowüstite Solid Solution Series. *Carnegie Institution of Washington Yearbook* **79**, 376-380.

Singh A.K., Mao H.K., Shu J., and Hemley R.J. (1998) Estimation of Single-Crystal Elastic Moduli from Polycrystalline X-Ray Diffraction at High Pressure: Application to FeO and Iron. *Physical Review Letters* **80**, 2157-2160.

Smart J.S. and Greenwald S. (1951) Crystal Structure Transitions in Antiferromagnetic Compounds at the Curie Temperature. *Physical Review* **82**, 113-114.

- Spain I.L. (1977) Ultrahigh pressure apparatus and technology, in: *High Pressure Technology, vol. 1 Equipment design, materials, and properties*, editors Spain I.L. and Paauwe J. Marcel Dekker, New York, p. 395.
- Speziale S., Zha C.-S., Duffy T.S., Hemley R.J., Mao, H.-K. (2001) Quasi-hydrostatic compression of magnesium oxide to 52 GPa: Implications for the pressure-volume-temperature equation of state. *Journal of Geophysical Research* **106**, 515-528.
- Speziale S., Milner A., Lee V.E., Clark S.M., Pasternak M.P., and Jeanloz R. (2005) Iron spin transition in Earth's mantle. *Proceedings of National Academy of Sciences USA* **102**, 17918-17922.
- Srivastava U.C. and Nigam H.L. (1973) X-ray absorption edge spectrometry (XAES) as applied to coordination chemistry. *Coordination Chemistry Reviews* **9**, 275-310.
- Struzhkin V.V., Mao H.K., Hu J., Schwoerer-Böhning M., Shu J., Hemley R.J., Sturhahn W., Hu M.Y., Alp E.E., Eng P., and Shen G. (2001) Nuclear Inelastic X-Ray Scattering of FeO to 48 GPa. *Physical Review Letters* **87**, 255501.
- Sturhahn W., Jackson J.M., and Lin J.-F. (2006) The spin state of iron in minerals of Earth's lower mantle. *Geophysical Research Letters* **32**, L12307.
- Sumino Y., Kumazawa M., Nishizawa O., and Pluschkell W. (1980) The elastic constants of single-crystal Fe_{1-x}O, MnO and CoO, and the elasticity of stoichiometric magnesiowüstite. *Journal of Physics of Earth* **28**, 475-495.
- Sung C.M. and Burns R.G. (1976) Kinetics of high-pressure phase transformations: implications to the evolution of the olivine-spinel transition in the downgoing lithosphere and its consequences on the dynamics of the mantle. *Tectonophysics* **31**, 1-31.
- Taran M.N. and Rossman G.R. (2002) High-temperature, high-pressure optical spectroscopic study of ferric-iron-bearing tourmaline. *American Mineralogist* **87**, 1148-1153.
- Taylor R.D., Pasternak M.P., and Jeanloz R. (1991) Hysteresis in the high pressure transformation of bcc- to hcp-iron. *Journal of Applied Physics* **69**, 6126-6128.
- Thompson A.L., Goeta A.E., Real J.A., Galetc A., and Muñoz M.C. (1994) Thermal and light induced polymorphism in iron(II) spin crossover compounds. *Chemical Communications* 1390-1391.
- Trautwein A., Regnard J.R., Harris F.E., Maeda Y. (1973) Isomer-Shift Calibrations Using Multivalent States of ⁵⁷Fe in KMgF₃. *Physical Review B* **7**, 947-951.
- Tsatskis I. (1998) Quadratic short-range order corrections to the mean-field free energy. *Journal of Physics: Condensed Matter* **10**, L683-L689.
- Tsuchiya T., Wentzcovitch R.M., da Silva C.R.S., and de Gironcoli S. (2006) Spin Transition in Magnesiowüstite in Earth's Lower Mantle. *Physical Review Letters* **96**, 198501.

Tyson T.A., Qian Q., Kao C.C., Rueff J.P., de Groot F.M.F., Croft M., Cheong S.W., Greenblatt M., Subramanian M.A. (1999) Valence state of Mn in Ca-doped LaMnO₃ studied by high-resolution Mn K_{β} emission spectroscopy. *Physical Review B* **60**, 4665-4674.

Uher R.A. and Sorensen R.A. (1966) Structure Effects in the Charge Radius of Spherical Nuclei. *Nuclear Physics* **86**, 1-46.

Urusov V.S., Dubrovinsky L.S. *Computer modelling of structure and properties of minerals*. Moscow State University Press: Moscow, 200 pp. (in Russian) (1989).

Urusov V.S., Tauson V.L., and Akimov V.V. (1997) *Solid State Geochemistry*. GEOS: Moscow, 500 pp. (in Russian).

Vaughan P.J. and Coe R.S. (1981) Creep mechanism in Mg₂GeO₄: effects of a phase transition. *Journal of Geophysical Research* **86**, 389-404.

Vos W.L. and Schouten J.A. (1991) On the temperature correction to the ruby pressure scale. *Journal of Applied Physics* **69**, 6744-6746.

Wakoh S. and Yamashita J. (1968) Internal Field and Isomer Shift of Metallic Iron and Nickel. *Journal of the Physical Society of Japan* **25**, 1272-1281.

Walch P.F. and Ellis D.E. (1973) Covalency versus Overlap Distortion in the Mössbauer Isomer Shift. *Physical Review B* **7**, 903-907.

Walker L.R., Wertheim G.K., and Jaccarino V. (1961) Interpretation of the Fe⁵⁷ Isomer Shift. *Physical Review Letters* **6**, 98-101.

Wang Y., Gasparik T., and Liebermann R.C. (1993) Modulated microstructure in synthetic majorite. *American Mineralogist* **78**, 1165-1173.

Wang Y., Guyot F., and Liebermann R.C. (1992) Electron microscopy of (Mg,Fe)SiO₃ perovskite: evidence for structural phase transitions and implications for the lower mantle. *Journal of Geophysical Research* **97**, 12327-12347.

Wang Y., Perdew J.P. (1991) Correlation hole of the spin-polarized electron gas, with exact small-wave-vector and high-density scaling. *Physical Review B* **44**, 13298-13307.

Wänke H., Dreibus G., Jagoutz E. (1984) Mantle chemistry and accretion history of the Earth. In: *Archean Geochemistry*, ed. A. Kröner, pp. 1-24. Berlin: Springer-Verlag.

Warren B.E. (1968) X-ray Diffraction. Addison-Wesley, Massachusetts, USA, 381 p.

Waychunas G.A., Dollase W.A., Ross II C.R. (1994) Short-range order measurements in MgO-FeO and MgO-LiFeO₂ solid solutions by DLS simulation-assisted EXAFS analysis. *American Mineralogist* **79**, 274-288.

Weidenschilling S.J. (1998) Formation processes and time scales for meteorite parent bodies. In: *Meteorites and the Early Solar System*, ed. J.F. Kerridge and M.S. Matthews, pp. 348-371. Tucson: University of Arizona Press.

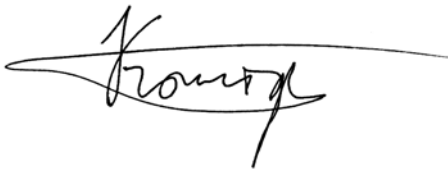
- Welberry T.R. and Christy A.G. (1997) Defect distribution and the diffuse X-ray diffraction pattern of wüstite, Fe_{1-x}O . *Physics and Chemistry of Minerals* **24**, 24-38.
- Wentzcovitch R.M., Karki B.B., Cococcioni M., deGironcoli S. (2004) Thermoelastic Properties of MgSiO_3 -Perovskite: Insights on the Nature of the Earth's Lower Mantle. *Physical Review Letters* **92**, 018501.
- Willis B.T.M. and Rooksby H.P. (1953) Change of structure of ferrous oxide at low temperature. *Acta Crystallographica* **6**, 827-831.
- Wood J.A. and Morfill G.E. (1988) A review of solar nebula models. In: *Meteorites and the Early Solar System*, ed. J.F. Kerridge and M.S. Matthews, pp. 348-371. Tucson: University of Arizona Press.
- Woodward R.L. and Masters G. (1991) Global upper mantle structure from long-period differential travel times. *Journal of Geophysical Research* **96**, 6351-6378.
- Yagi T., Suzuki T., Akimoto S.I. (1985) Compression of wüstite ($\text{Fe}_{0.98}\text{O}$) to 120 GPa. *Journal of Geophysical Research* **90**, 8784-8788.
- Yang H. and Ghose S. (1994) In-situ Fe-Mg order-disorder studies and thermodynamic properties of orthopyroxene ($\text{Mg,Fe}_2\text{Si}_2\text{O}_6$). *American Mineralogist* **79**, 633-643.
- Yoo C.S., Maddox B., Klepeis J.-H.P., Iota V., Evans W., McMahan A., Hu M.Y., Chow P., Somayazulu M., Häusermann D., Scalettar R.T., and Pickett W.E. (2005) First-Order Isostructural Mott Transition in Highly Compressed MnO. *Physical Review Letters* **94**, 115502.
- Yusa H., Akaogi M., and Ito E. (1993) Calorimetric study of MgSiO_3 garnet and pyroxene: heat capacities, transition enthalpies, and equilibrium phase relations in MgSiO_3 at high pressures and temperatures. *Journal of Geophysical Research* **98**, 409-422.
- Zabinsky S.I., Rehr J.J., Ankudinov A., Albers R.C., Eller M.J. (1995) Multiple-scattering calculations of x-ray-absorption spectra. *Physical Review B* **52**, 2995-3009.
- Zha C.S., Mao H.K., Hemley R.J. (2000) Elasticity of MgO and a primary pressure scale to 55 GPa. *Proceedings of National Academy of Sciences USA* **97**, 13494-13499.
- Zhang J. (2000) Effect of Defects on the Elastic Properties of Wüstite. *Physical Review Letters* **84**, 507-510.
- Zou G., Mao H.K., Bell P.M. and Virgo D. (1980) High-pressure experiments on the iron oxide wüstite (Fe_{1-x}O). *Carnegie Institution of Washington Yearbook* **79**, 374-376.

Erklärung

Hiermit erkläre ich, dass ich die vorliegende Arbeit selbständig verfasst und keine anderen als die von mir angegebenen Quellen und Hilfsmittel benutzt habe.

Ferner erkläre ich, dass ich nicht anderweitig versucht habe, mit oder ohne Erfolg, eine Dissertation einzureichen und auch keine gleichartige Doktorprüfung an einer anderen Hochschule endgültig nicht bestanden habe.

Bayreuth, im Februar 2007

A handwritten signature in black ink, appearing to read 'Kantor', with a long horizontal flourish extending to the right.

Innokenty Kantor.